MASSEY UNIVERSITY
TE KUNENGA KI PŪREHUROA
UNIVERSITY OF NEW ZEALAND

Geothermal exploration using hyperspectral and thermal remote sensing – Inferring shallow hydrology of the Waiotapu Geothermal Field, New Zealand

A thesis presented in partial fulfilment of the requirements of the degree of

Doctor of Philosophy

In

Earth Sciences

At Massey University (Manawatū Campus),

Palmerston North, New Zealand

By

Cecilia Rodriguez-Gomez

2023

Abstract

Geothermal areas can exhibit a series of surface manifestations (e.g. mineral alteration and deposition, thermal anomalies, hot springs, and characteristic plant species) which can be directly detected with remote sensing techniques within the visible, near-infrared, and thermal ranges. These surface manifestations are, to some extent, a reflection of the subsurface activity. There is a wealth of techniques, including geological, geophysical, and geochemical methods, which can be used to explore and monitor geothermal areas; however, remote sensing techniques from airborne and spaceborne platforms can provide a cost-effective alternative. In many cases, geothermal areas are densely covered by vegetation which can further increase the time and cost of exploration. However, vegetation has the capability to reflect the environment it lives in. Here, we propose vegetation can be utilised as a proxy for subsurface geothermal activity using a combination of hyperspectral (VNIR/SWIR), thermal infrared, and LiDAR imagery with rock/soil and plant elemental concentration values. These techniques are used in geothermal areas but have rarely been employed to analyse plants growing in the area. At Waiotapu Geothermal Field, less than 10% of the surface is directly exposed, areas where the hyperspectral airborne successfully identified three main lithologies and alteration minerals; acid-sulphate alteration, "mixed" alteration, and silica-sinter deposition. While plants cover the remaining 90% of the surface, with kanuka shrub (*kunzea ericoides* var. *microflora*) as the dominant species in soils >40 °C. As such, kanuka was selected for our investigation and four geothermally relevant elements were chosen (Ag, As, Ba, and Sb). In areas with near-neutral high-chloride springs with a significant upflow (e.g. Champagne Pool), Ag, As, and Sb are enriched in rock/soil samples and are uptaken by kanuka plants. Whereas high Ba concentrations were found in plants living in peripheral areas where water mixing is taking place. The foliar element concentration zonation maps were successfully developed through classification using Random Forest and regression with Kernel Partial Least Squares. Employing ICPMS data and laboratory, airborne, and satellite hyperspectral (VNIR/SWIR) remote sensing data to create models to predict the foliar element concentrations. The results correspond well with the geology and thermal profile of Waiotapu Geothermal Field. Additionally, thermal anomalies selected from airborne TIR broadband imagery were studied using point pattern analysis such as randomness test-statistics, to map their preferred patterns and orientation, which appear to be controlled by subsurface permeability and water flow. This research opens new opportunities for geothermal exploration and monitoring through plants using hyperspectral imaging, which can overcome the limitations of geothermal exploration methods in densely vegetated areas.

“Ehara taku toa i te toa takitahi, engari he toa takitini”

“I come not with my own strengths but bring with me the gifts, talents and strengths of my family, tribe and ancestors”

Photo of Wai-O-Tapu, “sacred waters”. Exhibiting views towards Primrose Terrace (front), silica sinter deposition (back left) and Champagne Pool (back right). In the surroundings, kanuka growing near the manifestations and further back pine plantation is visible. Photo credit: Cecilia Rodriguez-Gomez

Dedication

To my mother, infinite source of strength and inspiration.

Acknowledgements

The completion of this PhD thesis would not have been the great journey it was without all the people who formed part of my life, before and throughout these years. First, a world of thanks to Gabor Kereszturi who was not only the best chief-supervisor I could have dreamt of but has become a dear friend, I admire his endless passion, patience and energy. I can say without a doubt that my PhD journey has been possible and enjoyable due to him, gracias totales. All my co-supervisors and external advisors played key roles within different areas of this multidisciplinary research. A heartfelt thanks to Paramsothy Jeyakumar, "Jeya", for his lovely way of explaining basic concepts about the way of plants and the encouraging words for the present and future goals. I am grateful for Reddy Pullanagari's openness and readiness to share knowledge and solutions regarding image processing and modelling. I am thankful for Melody Whitehead's ideas and brainstorming which gave this research a different perspective. Thank you to Jonathan Procter, "Jon", for his support and constructive comments. A sincere thank you to Stuart Mead, for his refreshing and creative ideas, great chicken stories and overall support for anything he could help me to understand better. Special thanks to Kate Arentsen, a woman who counts like many more, so many thanks for arranging and solving any type of situation.

I am forever grateful for the support from GNS Science group since before the PhD started and throughout. It has been one of the greatest joys of my life to be part of your geothermal team, a place where I feel at home. Thank you to Chris Bromley, who opened his doors as a friend, mentor and boss, for teaching me to not be afraid to start endeavours for which I don't feel quite ready. Infinite thanks to Rob Reeves, for his trust, fun times under any circumstance, planning ahead for dessert and all the support throughout this PhD and in my previous years, his advice has always been and will continue to be a guide for me. Gracias to Andrew Rae, for sharing his knowledge so openly, his jokes, great times and support on the field and for suggesting I go to Massey and use their hyperspectral sensor.

This journey wouldn't have been as special and certainly would have been much harder without the support of my fellow students, colleagues, and various friends. Between culinary endeavours, spontaneous and planned trips, great music, diverse sports, wonderful horses, extraordinary star-gazing, and random to insightful conversation, their company became part of my life and essential for my growth and well-being, from the bottom of my heart, ngā mihi. This includes but is not limited to: Rupsa, Bernhard, Charline, Bogs, Natalie, Carlos, Ramola, Daniel, Anna and Sarah Palmer, Kirsty and Ben. Other physically far but always close to my heart humans include Andrea, Bárbara and Poyo, you are my chosen family. Special gracias to Ger, my long-distance emotional support, listener of all my problems, solution-seeker and permanent connection to my original land, México, thank you for all your love.

This research was financed by the Royal Society of New Zealand, Te Apārangi, through the Catalyst Fund (CSG-MAU1705) and Massey University, School of Agriculture and Environment (PhD Scholarship). It was

possible to conduct this research due to the sampling permits given by Ngati Tahu – Ngati Whaoa Runanga Trustees (40/2015) and the Department of Conservation (DOC) (78428-GEO) sampling permits. As well as field access to surrounding areas of Waiotapu Geothermal Field from Timberlands Limited. I am deeply grateful to Colin Dunn Consulting Inc for the chemical concentration analyses at Acme Labs – Bureau Veritas, Vancouver, Canada.

Last but not least, I want to thank my family for being the wind beneath my wings and leading me by example.

Table of contents

List of Figures

List of Tables

Abbreviations

µm	Micrometres
Ag	Silver
As	Arsenic
ASTER	Advanced Spaceborne Thermal Emission and Reflection Radiometer
Au	Gold
B	Boron
Ba	Barium
Ca	Calcium
$CaCO_3$	Calcium carbonate
Cd	Cadmium
Cl	Chlorine
CLR	Centred Log-Ratio
CO2	Carbon dioxide
CO3	Carbon trioxide
DEM	Digital Elevation Model
DSM	Digital Surface Model
e.g.	*Exempli grati*, used for "for example"
ECOSTRESS	ECOsystem Spaceborne Thermal Radiometer Experiment on Space Station
ENVI	Environment for Visualising Images
Fe	Iron
FLIR	Forward-Looking Infrared
FWHM	Full Width at Half Maximum
GIS	Geographic Information Systems
H_2O	Water
H_2S	Hydrogen sulphide
HCO_3	Bicarbonate
HS	Hyperspectral
i.e.	*id est*, used for "that is to say"
ICP-MS	Inductively Coupled Plasma – Mass Spectrometer
K	Potassium
KDE	Kernel Density Estimates
KPLS	Kernel Partial Least Squares
LiDAR	Light Detection and Ranging
LOOCV	Leave-One-Out Cross Validation
LR	Log-ratio
LSCV	Least-Squares Cross Validation
LWIR	Longwave Infrared
Ma	Millions of years ago
MAE	Mean Absolute Error

Mg	Magnesium
MSE	Mean Square Error
MW	Megawatts
Mwe	Megawatts electric
MWt	Megawatts thermal
Myr	Million years
Na	Sodium
NDVI	Normalised Differential Vegetation Index
NH_4	Ammonium fluoride
nm	Nanometres
NZD	New Zealand Dollars
OA	Overall Accuracy
OH	Hydroxide
PCA	Principal Component Analysis
PhD	Philosophiae Doctor, Doctor of Philosophy
PLS	Partial Least Squares
ppm	Parts Per Million
PRISMA	PRecursore IperSpettrale della Missione Applicativa
RF	Random Forest
RGB	Red Green Blue
RMSE	Rooted Mean Square Error
S	Sulphur
SAM	Spectral Angle Mapper
SAMSE	Summed-Asymptotic Mean Squared Error
Sb	Antimony
SEM	Scanning Electron Microscopy
SiO_2	Silicon dioxide
SO_2	Sulphur dioxide
SO_4	Sulphate
SVM	Support Vector Machine
SWIR	Shortwave Infrared
TAC	Thermal Anomaly Candidates
Ti	Titanium
TIR	Thermal Infrared
TVZ	Taupo Volcanic Zone
UAV	Unmanned Aerial Vehicle
USA	United States of America
VIS	Visible
VNIR	Visible and Near Infrared
XRD	X-ray Diffraction

1 Introduction

1.1 Geothermal systems

Geothermal systems are generally characterised by high geothermal gradients (Henley & Ellis, 1983; Moeck, 2014), and each system can be shaped by a particular set of properties, including surface manifestations (e.g. hot springs, mud pools, geysers, steaming grounds, fumaroles, and in some cases characteristic communities of plant species) (Van der Meer et al., 2014; Reeves & Rae, 2016; Hewson et al., 2020; Qudsi & Noor, 2022), host rock (e.g. permeability, porosity, mineralogy, hydrology) (Patterson et al., 2018; Heap et al., 2019; Gallagher et al., 2020), heat source (e.g. shallow intrusion, active magmatism) (Moeck, 2014; Pan et al., 2021) and water properties (e.g. temperature, pH) (Van der Meer et al., 2012; Shoedarto et al., 2021; Achmad & Salam, 2022). The geological component is vastly controlled by the plate tectonic processes and associated volcanism/magmatism, while the hydrological settings are more locally controlled and heterogeneous (Moeck, 2014; Wilson & Rowland, 2016; Han et al., 2018; Gallagher et al., 2020).

Depending on these variables, geothermal systems can be divided broadly into convection-dominated (e.g. hydrothermal) and conduction-dominated (e.g. hot dry rock) systems (Moeck, 2014; Gomez-Ortiz et al., 2019; Heap et al., 2019; Kraal et al., 2021).

a) Convection-dominated systems: Often formed over a heat source (i.e. magmatic rising plume), which reaches an underground water body and by convection creates a reservoir, where the ‘parental’ water is heated and rises to the surface (Shoedarto et al., 2020; Chambefort, 2021). The fluid movement is greatly controlled by regional and local faults and fracturing, as well as rock porosity and permeability structures (Niederau et al., 2019; Milicich et al., 2020a; Kraal et al., 2021). Based on the geological controls there are convection-dominated systems of active magmatism (i.e. volcanic; e.g. Java, Indonesia), plutonic (i.e. recent plutonism; e.g. Larderello, Italy; Geysers, USA) and of the active extensional domain (e.g. Western Turkey; East African Rift; Upper Rhine graben) (Brogi et al., 2003; Moeck, 2014; Liu et al., 2021). The Taupo Volcanic Zone in New Zealand belongs to the latter, characterised by extensional setting with active magmatism (Simpson & Bignall, 2016; Wilson & Rowland, 2016). More details on convection-dominated systems and their exploration have recently been reviewed by Jolie et al., (2021).
b) Conduction-dominated systems: They occur mainly under passive plate tectonic settings, such as intracratonic basins (e.g. Paris Basin; Habanero, Australia) and orogenic belt (e.g. Unterhaching, Germany) (Procesi et al., 2019; Sengelen et al., 2019; Xu et al., 2022). Typically geologic controls are litho- or biofacies of sedimentary rock with faults and fractures, lacking seismicity (Moeck, 2014). Many of the conduction-dominated systems come with their own set of challenges, such as deeper wells and host rock with lower permeability (Kumari & Ranjith, 2019). Conduction-dominated geothermal systems have

recently been reviewed, and more details can be found in Kumari & Ranjith, (2019) and Procesi et al., (2019).

The rising fluids in convection-dominated systems interact with the host rock to develop assemblages of mineral alteration, mineral deposition, springs and pools of different chemistry (e.g. acid-sulphate, high-chloride near-neutral, alkaline-bicarbonate) (Bégué et al., 2017; Wang et al., 2020; Shoedarto et al., 2021; Ndikubwimana et al., 2022). Those indicate specific formation environments with a distinct range of temperature and pH in which distinct mineral associations can be formed (Table 1.1):

a) Acid, sulphate-rich waters leading to acid-sulphate alteration can be formed by steam rising above the groundwater table level oxidising to H_2S, mineralogy depends on the fluid temperature and pH conditions (Aguilera et al., 2016; Idroes et al., 2019; Ünal Ercan et al., 2022). These are typically replacing primary plagioclases, pyroxene, amphibole and glass (Aguilera et al., 2016; Simpson & Bignall, 2016; Maza et al., 2021). Acid-sulphate springs are generally low in chloride content and pH values, and can form mud pools and fumaroles (Ellis & Mahon, 1967; Barbier, 2002; Mardiati et al., 2020). Microbe communities are relevant in acid-sulphate area as they are linked to As and Fe processes (Inskeep et al., 2004; Jiang et al., 2016).
b) Near-neutral, chloride-rich waters coming from the deep reservoir are called ‘parental’ fluids (i.e. experienced little wall rock-fluid interactions), they rise all the way to the surface via fractures and connected pore spaces (Pan et al., 2021; Shoedarto et al., 2021). These waters are characterised by their high content of Cl, Na, Si, F, NH_3, As, Li, Rb, Cs and Ba elements and compounds (Pirajno, 2009; Wang et al., 2018; Sasaki et al., 2021, McCleskey et al., 2022). The surface manifestation of near-neutral water is associated with springs and outflows that can form clear pools, silica sinter terraces and occasional geysers (Kratt et al., 2004; Gallagher et al., 2020; Ünal Ercan et al., 2022). They are prone to develop microbial mats, which colours depend on the water temperature, chemistry and microbes and algae (Lynne & Campbell, 2004; Das & Thakur, 2021; Gong et al., 2022).
c) Alkaline, bicarbonate-rich waters are common in geological settings with carbonate rocks and can deposit travertine in terraces, similar to those of silica sinter (Barbier, 2002; Pirajno, 2009; Capezzuoli et al., 2014; Ndikubwimana et al., 2022). They are usually indicative of peripheral zones, where CO_2-rich steam condensates or mixes with shallow sub-surface waters (Henley & Ellis, 1983; Maza et al., 2021). Typical mineralisation includes calcite, aragonite and dolomite (Maza et al., 2021; Wei et al., 2021; Ndikubwimana et al., 2022).

Table 1.1. Mineral associations in different formation environments. Modified from Kratt et al., 2004; and Pirajno, 2009.

Environment	Resulting mineralogy
Acid, sulphate-rich	Kaolinite, smectite, illite, alunite, jarosite, cristobalite, gypsum, opal, native sulphur, quartz and sulphides
Near-neutral, chloride-rich	Silica polymorphs (silica sinter, opal, quartz)
Alkaline, Bicarbonate	Calcite, aragonite, dolomite

Surface and shallow subsurface features are the targets of exploration and monitoring campaigns in geothermal systems (Abuzied et al., 2020; Qudsi & Noor, 2022). There are three main branches of exploration techniques; geological, geophysical and geochemical (Deon et al., 2019; Savitri et al., 2021). The geological techniques target the identification of typical (alteration) mineral assemblages, mapping surface manifestations and identifying regional structural controls (Abuzied et al., 2020; Meng et al., 2021) to infer reservoir properties and potential (Jolie et al., 2021; Meng et al., 2021). The geochemical techniques, include water chemical analysis, geothermometers, and isotope analysis (Chenaker et al., 2018; Kuwatani et al., 2020), to establish the source of heat and water (Chambefort, 2021; Wei et al., 2021). These analyses can be applied to fluids from hot pools, water springs, streams, diluted thermal fluids and groundwater wells (Moeck, 2014; Wang et al., 2021; Wei et al., 2021). These studies allow for the fluid chemistry, fluid paths, temperature at depth and subsurface interaction with the host rock to be studied and understood (Bobos & Williams, 2017; Pan et al., 2021; Wei et al., 2021). The geophysical techniques using electric and magnetic surveys altogether can be used to establish the boundary of the geothermal system and map the fluid paths (i.e. higher resistivity) (Cherkose & Saibi, 2021; Hacıoğlu et al., 2021) and mineralogy changes provoked by the hot fluid-rock interaction (i.e. demagnetisation) (Cherkose & Saibi, 2021; Achmad & Salam, 2022; Basantaray & Mandal, 2022), while seismic surveys can determine structural controls and host rock properties (i.e. locating faults which can serve as fluid channels) (Zhou et al., 2021; Okamoto et al., 2022).

Technology has vastly propelled the evolution of geothermal exploration methods. Remote sensing techniques which belongs to the geophysical techniques, can map the surface extent and temperature profiles of geothermal systems, are one of the fields that have been subject to extensive developments (e.g. hyperspectral satellites, InSAR (Liu et al., 2021; Qudsi & Noor, 2022)). Remote sensing is more cost and time-efficient than other field surveys (e.g. surface feature and mineralogy identification, ground geophysical techniques) (Abubakar et al., 2017; Meng et al., 2021). Furthermore, optical remote sensing (e.g. optical, thermal) can capture a synoptic view of the Earth's surface with associate spatial, spectral and temporal information. The wealth of such a stream of information, however, has not reached its full potential for improving geothermal exploration and monitoring (Abubakar et al., 2017; Romaguera et al., 2018). Thus, a synergistic combination of remote sensing and other

geology/geochemical approaches can hold significant benefits to understanding shallow and near-surface geological processes occurring within geothermal systems.

1.2 Remote sensing

Remote sensing refers to the study of an object without physical contact (Clark, 1999; Bakker et al., 2009). Remote sensors can be mounted on spaceborne (e.g. satellites), airborne (e.g. planes and drones) and hand-held platforms (e.g. on the field or laboratory). These platforms can carry a variety of equipment/sensors including sensors covering different ranges from the electromagnetic spectrum (e.g. visible (350-700 nm) (VIS), near-infrared (700-1,300 nm) (NIR), short wave infrared (1,300-2,500 nm) (SWIR) and longwave infrared, which in this document we will refer to as thermal infrared (7,500–13,000 nm) (TIR). These sensors can acquire data in different bandwidths [i.e. broadband (>100 nm) and narrowband with >100 bands also known as hyperspectral (<50 nm)], and different spatial resolutions (e.g. centimetres to hundreds of meters), enabling the application of different types of studies. For material identification (e.g. mineral, plant species) narrowband hyperspectral is ideal; as it allows the detection of small spectral absorption features (Van der Meer et al., 2012; Abubakar et al., 2017; Qudsi & Noor, 2022), which can remain undetected with broadband sensors.

Instruments in the VNIR/SWIR range (350-2,500 nm) can detect electronic and vibrational processes occurring at the atomic level of minerals/substances (e.g. Hunt, 1977). These can be diagnostic for sulphates (e.g. alunite, jarosite and gypsum), phyllosilicates (e.g. kaolinite, illite, smectite and micas) and carbonates (e.g. calcite and siderite), by identifying absorption features related to O-H, H_2O, CO_3 and NH_4 (Gupta & Roy, 2007; Van der Meer et al., 2014; Savitri et al., 2021). In the TIR region emissivity from an object measured by typically broadband sensors (Thermal Infrared, TIR), can successfully identify thermal anomaly locations and obtain relative temperatures (Reeves & Sanders, 2019; Weldeyohannes et al., 2022). This capacity has broad applications in geothermal areas such as the retrieval of surface temperature (Abubakar et al., 2017; Marwan et al., 2021; Romaguera et al., 2018), calculations of heat output or heat flux (Heasler & Jaworowski, 2018; Morifuji et al., 2021; Seward et al., 2022), and monitoring temperature changes on surface (Nishar et al., 2016; Reeves & Rae, 2016; Silvestri et al., 2020). However, hyperspectral TIR remote sensing can also be used in geothermal areas for mineral identification, such as silicates, sulphates, oxides and clay minerals (Vaughan et al., 2003; Kruse et al., 2011; Kraal et al., 2018; Laukamp et al., 2021). More particularly the TIR region is ideal, in the geothermal exploration context, to identify silica-bearing minerals, as silica-bearing minerals only have absorption features in the TIR region, due to the characteristic Si-O stretching vibration within the silicate structure (Vaughan et al., 2005; Kruse, 2014; Hecker et al., 2019). For these technologies which rely on the information provided by directly detecting rock/soil or thermal anomalies, vegetation is usually an impediment (Freski et al., 2021).

There are other types of remote sensing techniques with active sensors, such as Light Detection and Ranging (LiDAR) and Interferometric Synthetic Aperture Radar (InSAR). Both these techniques are applied to geothermal exploration to identify ground changes, such as ground deformation (Maghsoudi et al., 2018; Liu et al., 2021), landslides (Pawluszek-Filipiak & Borkowski, 2020), subsidence (Cigna et al., 2019), active faulting (Falorni et al., 2011), lithology mapping (Freski et al., 2021). These applications are relevant for geothermal monitoring, providing information on potential hazards and changes in the subsurface caused by fluid extraction and reinjection at geothermal power plants (Falorni et al., 2011; Cigna et al., 2020). In areas with vegetation cover, LiDAR presents an advantage, as it has the capacity to "see" through vegetation and create digital surface models in areas where other techniques might not be able to give information from the ground (Hecker et al., 2017; Ramdhan, 2019).

Most remote sensing-based exploration and monitoring techniques in geothermal areas focus on studying the ground or the subsurface (e.g. mineral identification, ground deformation, ground temperature, thermal anomaly identification, active fault mapping, magnetic mapping) (Van der Meer et al., 2014). Regardless, remote sensing has rarely been applied to observe plants living in geothermal areas (Vaughan et al., 2020), which can work as a proxy for surface and subsurface processes. Broadband/multispectral and narrowband/hyperspectral remote sensing targeting plants and crops have extensive literature (see more details in (Cisternas et al., 2020; Pôças et al., 2020; Sishodia et al., 2020)). Such data combined with geostatistics can highlight plant nutrient levels (Maes & Steppe, 2019; Sishodia et al., 2020; Giovos et al., 2021) and health indicator indices (Xue & Su, 2017; Giovos et al., 2021). Indices such as The Normalised Difference Vegetation Index (NDVI) along with other vegetation indices from Landsat imagery were applied to Peut Sagoe, Indonesia, Shandong, China and the Main Ethiopian Rift to extract land surface emissivity changes (Liu et al., 2021; Weldeyohannes et al., 2022; Zaini et al., 2022). The decrease in heat output at Karapiti, New Zealand was interpreted from the increase of healthy vegetation, which can be retrieved from an NDVI map such as Landsat imagery (Mia et al., 2012). Seward et al., (2018) categorised vegetation types at the same location (i.e. Karapiti), and correlated them with the type of heat output (i.e. conductively, steam-heated and high-heat). Agreement between surface temperature and NDVI maps has been identified in Indonesia with Landsat imagery (Putri et al., 2021) and with an UAV (Marwan et al., 2021). Vegetation has been used as an indicator of geothermal features occurrence along with surface roughness in West Java, Indonesia (Saepuloh et al., 2021). The use of remote sensing to study vegetation living in geothermal areas has increased, but there is more information which can be given by vegetation than what has been explored so far.

Vegetation can not only reflect the effects of heated ground, but it can uptake elements in significant quantities (e.g. accumulator and hyperaccumulator species), which can affect their physical and chemical properties (Dunn, 2011; Rascio & Navari-Izzo, 2011; Wang et al., 2018). For example, metal-induced physical and chemical changes to plant tissues have been studied in pot studies (e.g. Rathod et al., 2015, 2018; Li et al.,

2019; Kazberuk et al., 2021; Nebeská et al., 2021), and are mainly applied for remediation and mining purposes (Rathod et al., 2015; Chakraborty et al., 2021; Yin et al., 2021). Regardless, high concentrations of Ag, Au, As and Sb have been detected previously in plants living in geothermal areas of New Zealand (Dunn, 2011; Dunn & Christie, 2019), along with visible physical changes (e.g. shorter height, horizontal growth of their roots) (Boothroyd, 2009; Van Manen & Reeves, 2012), highlighting an area of opportunity for remote sensing techniques to be applied in geothermal areas.

1.3 Research gap and objectives

Hyperspectral (VNIR/SWIR) remote sensing has been identified as a tool for geothermal exploration to some extent. Regardless, the geothermal literature indicates that hyperspectral-based studies have mostly targeted bare ground exposure (Calvin & Pace, 2016; Qudsi & Noor, 2022) and/or drill cores (Kamau et al., 2020; Kraal et al., 2021), avoiding targeting plant cover which is typically seen as an obstacle for exploration. However, a handful of field studies have focused on plants growing within geothermal areas (de Lange, 2014; Smale et al., 2018), but the employed remote sensing techniques has been limited to NDVI (Mia et al., 2012) and its relation to surface soil temperatures (Seward et al., 2018). The plant cover within a geothermal field can be significant, limiting our ability to provide seamless maps of geothermal systems and for any remote sensing methods to be applied. This highlights the importance to understand and investigate the viability of plants to work as pathfinders for subsurface processes in geothermal areas.

Waiotapu Geothermal Field is a geothermal system located in the Taupo Volcanic Zone of New Zealand, a region known for its high thermal activity. Like many other geothermal areas in New Zealand and the world (e.g. Indonesia, México or Caribbean Islands) (Flores-Armenta & Gutiérrez-Negrín, 2011; Nasruddin et al., 2016; Koon Koon et al., 2020), it displays a variety of surface manifestations characteristic from convective geothermal systems (e.g. steaming grounds, fumaroles, geysers, silica sinter deposits and hydrothermally altered minerals) (Lloyd, 1959; Hedenquist, 1991; Simpson & Bignall, 2016; Wilson & Rowland, 2016) and has a dense vegetation cover (Mongillo, 1994; Burns & Leathwick, 1995; Burns et al., 2013). Furthermore, since the 1980s when it became a “Protected” site, only non-invasive methods are allowed for its “exploration”. Hence, it is an ideal candidate for testing new hyperspectral-based methods that are non-invasive and can be carried out remotely.

To address the identified limitations of remote sensing methods for vegetated geothermal fields, the following research objectives were proposed:

1) To characterise surface alteration and deposition types in geothermal systems using hyperspectral (VNIR/SWIR) remote sensing and ground exploration techniques.
2) To develop a new remote sensing approach for chemical fingerprinting of geothermal activity using plant cover.

3) To quantify thermal manifestations and their preferred spatial occurrence using thermal infrared remote sensing.

We hypothesise that plant spectral responses (kanuka in New Zealand) can serve as a proxy for subsurface activity in geothermal areas. This is a novel geothermal exploration perspective which is of relevance to areas with dense plant cover around the world, the geothermal energy potential left untapped is very large and it is a renewable energy which will play a key role in the future (Jolie et al., 2021; Soltani et al., 2021; Ahmed et al., 2022).

1.4 Thesis structure

This thesis presents novel methodologies to explore subsurface activity in geothermal areas via direct detection of barren surface and alteration, plant interactions with the subsurface activity (i.e. heat, element depletion or excess) and spatial analysis of heat distribution. The methodology applies analysis of hyperspectral (VNIR/SWIR), thermal infrared and LiDAR imagery in combination with rock/soil and plant samples. The thesis is composed mainly of published papers (Chapter 3) or manuscripts submitted for publication (Chapters 4 and 5) in international peer-reviewed journals. Therefore, some chapters contain repetition of core concepts (e.g. hyperspectral and thermal infrared remote sensing, geological setting) and previous research. As such, each chapter works as an independent manuscript which provides the relevant context to understand the material presented and a detailed description of the data post-processing and methodology. Even though each of the three main chapters stands alone, all of them are oriented to understating subsurface processes taking place in Waiotapu Geothermal Field, and directly or indirectly build upon each other. Chapter 6, provides a synthesis of the main chapters and their findings along with some recommendations on utilising hyperspectral remote sensing for geothermal explorations. All references are located at the end of the thesis in Chapter 7.

This thesis starts with an introductory chapter and literature review (Chapter 1-2) which recapitulate previous research related to subsequent Chapters (3, 4 and 5) which involve novel research. Chapter 2 contains five subtopics *Waiotapu Geothermal Field*, *Hyperspectral remote sensing*, *Remote sensing application at geothermal fields*, *Thermal infrared remote sensing* and *Biogeochemistry*.

Chapter 3 exemplifies the implementation of hyperspectral remote sensing in Waiotapu Geothermal field, becoming the first documented application of hyperspectral remote sensing to geothermal areas in New Zealand. Lithological maps were created with the use of Spectral Angle Mapper (SAM) and Support Vector Machine (SVM) supervised classification. To complement the airborne data, 75 rock/soil samples were acquired from field. These samples were analysed for their element concentrations and detailed mineral identification with Inductively Coupled Plasma Mass Spectrometry (ICP-MS), Scanning Electron Microscopy (SEM) and Energy Dispersive X-ray Spectroscopy. Three main groups of mineral assemblages were selected from the image classifications, including acid-sulphate alteration (characterised by mud-pools), mixed alteration caused by sulphur-chloride

waters, and silica deposition (Champagne Pool as the main high-chloride near-neutral water source for silica deposition). Furthermore, thermal infrared imagery confirmed spatial heterogeneity and overall higher surface temperatures for the acid-sulphate alteration zones. This study reinforces the use of hyperspectral (VNIR/SWIR) remote sensing as a tool for first reconnaissance and monitoring in geothermal areas, when bare ground exposure is significant.

Chapter 4 successfully relates element concentrations (e.g. As, Ba and Sb) from kanuka shrub (*kunzea ericoides* var. *microflora*) samples with spectral signatures retrieved from laboratory, airborne and spaceborne hyperspectral (VNIR/SWIR) data to create prediction models and distribution maps (not direct concentration measurements). Prediction models (classification and regression models) correlate the elemental concentration with subtle changes in the spectral signature of plants, to analyse which environmental variables might be affecting the plant in different manners. The models were developed with Kernel Partial Least Squares Regression and Random Forest Classification, to create element maps of Waiotapu Geothermal Field. The northern region has higher quantities of barium bioavailable for kanuka, while the central-southern region has high concentrations of arsenic, antimony and silver uptaken by the plant. These two main regions coincide with the ones identified in Chapter 3 and with the elemental concentrations of soil/rock samples. Furthermore, plant physical changes were compared to independent TIR imagery and LiDAR-based plant height. This study is the first of its kind, proving the potential of plants to work as proxies to understand the subsurface processes in geothermal areas and assist in exploration and monitoring surveys. It is not only a non-invasive technique but it can be employed in geothermal areas with dense plant cover.

Chapter 5 focuses on novel applications of point pattern analyses of selected thermal anomalies detected through TIR imagery within Waiotapu Geothermal Field. Thermal anomalies were delineated manually for spatial point pattern analysis to assess their distribution and orientation. While regional structural controls seem to be present, near-surface (<200 m) fractures, alteration and overall permeability appear to play a relevant role in the distribution of thermal anomalies at Waiotapu Geothermal Field. The north and the south of the system as in the previous two chapters could be identified by their differences in thermal anomaly's spatial distribution and temperatures. In the north, higher temperatures (>47 C°, derived from Chapter 3), low density of thermal anomalies and separation within clusters is present, while the south/central region presents overall lower temperatures (<47 C°), higher density of thermal anomalies and clustering at all distances. Waiotapu Geothermal Field has an orientation close to that of the near active faults (i.e. Ngapouri and Paeroa Faults, N40°E-N55°E and N45°E - N60°E, respectively) and that of the Taupo Volcanic Zone (TVZ) (N45°E). Further studies are recommended to understand the spatial patterns in geothermal areas, but this study exemplifies a novel application for thermal infrared imagery within geothermal areas.

Chapter 6 presents the discussion and conclusions, divided into *Geological model for Waiotapu Geothermal Field, Implications for geothermal exploration, future work and new directions* and *Conclusions*. It compiles the information from Chapters 3, 4 and 5 in a synthesised manner, highlighting novel findings, their linkage to previous studies and perspectives for future research.

2 Literature Review

2.1 Waiotapu Geothermal Field

2.1.1 Geology, alteration and surface features

Waiotapu Geothermal Field is located in the northeastern part of the Taupo Volcanic Zone (TVZ), The TVZ is an intra-arc continental rift between the Australian and Pacific Plates, with overall NNE-SSW orientation, causing high volcanic and geothermal activity from shallow and deep magmatic intrusions (Seebeck et al., 2014; Wilson & Rowland, 2016). Waiotapu Geothermal Field is one of the ~20 geothermal systems within the TVZ, with a surface area of ~18 km^2 and a heat flow of ~500 MW (Figure 2.1) (Benseman et al., 1963; Hedenquist & Browne, 1989; Bibby, Glover, et al., 1995). The TVZ basement consists of weakly metamorphosed Mesozoic rock broadly referred to as 'greywacke', more specifically Torlesse Composite Terrane, Kaweka Terrane subunit (Hedenquist, 1991; Milicich et al., 2020).

The basement rock is overlaid by thick rhyolitic ignimbrite deposits occasionally intercalated by lacustrine sediments (Steiner, 1963; Grindley et al., 1994). The host rock directly underneath Waiotapu Geothermal Field is also mostly comprised of pyroclastic deposits, including welded ignimbrite and unlithified tephras. Its broadly rhyolitic composition has a primary mineralogy with plagioclase feldspar, pyroxene and Fe-Ti bearing oxides (e.g. magnetite) with alteration products of quartz polymorph (e.g. opal and cristobalite) and K-feldspar and locally chlorite, calcite, epidote, pyrrhotite, titanite, zeolites, leucoxene, and apatite (Hedenquist & Browne, 1989). Two ignimbrites have reached Waiotapu Geothermal Field, forming the bulk part of the host-rock: including the lenticular ignimbrite, Waiotapu Ignimbrite formed between 0.6 and 0.7 Ma (Wood, 1994; Houghton et al., 1995) and the biotite-bearing quartzose ignimbrite, Rangitaiki Ignimbrite which is 0.32 to 0.38 Myr old (Steiner, 1963; Grindley et al., 1994; Ritchie, 1996).

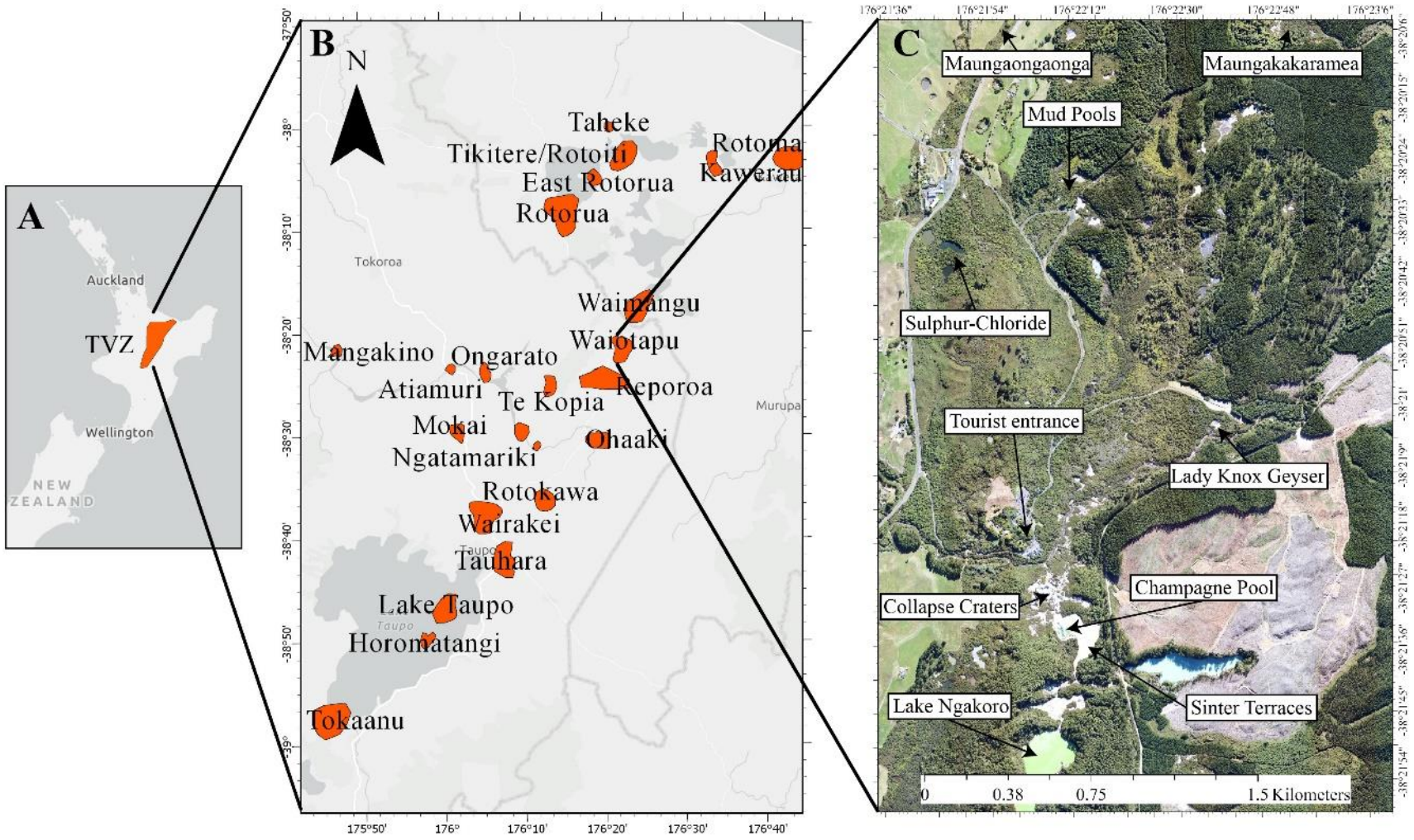

Figure 2.1. Overview of the Taupo Volcanic Zone with location for geothermal areas and close-up of Waiotapu Geothermal Field. A) TVZ location within the North Island of New Zealand. B) Main geothermal areas of the TVZ. C) An enlarged area of Waiotapu Geothermal Field on a true-colour airborne imagery.

The host rock (i.e. ignimbrites) shows strong anisotropy in permeability with high horizontal up to 990 × 10^{-15} m^2 and low vertical permeability up to 45 × 10^{-15} m^2 (Kaya et al., 2014). The ignimbrites are interlayered with lacustrine sediments, such as the Huka Falls Formation (Wood, 1994). Sediments are composed of rhyolitic pumice and other pyroclastic materials, silicified by hydrothermal action (Lloyd, 1959). This layer acts as a spatially discontinuous litho-cap layer of the hydrothermal system, with low vertical permeability of 1.17-9.90 × 10^{-15} m^2 (Risk et al., 1994).

Table 2.1. Chemical features of some hot springs at Waiotapu Geothermal Field. Data adopted from (Lloyd, 1959; Hedenquist & Browne, 1989; Pope & Brown, 2014).

Feature	Temperature [°C]	pH	Na [mg/kg]	Cl [mg/kg]	SiO_2 [mg/kg]	HCO_3 [mg/kg]	SO^-_4 [mg/kg]	Type
Champagne Pool	~76	~6	~1118	~1934	~495	~62	~70	Deep upflow
Lady Knox Geyser	~98	~7	~581	~911	~432	~34	~151	Deep upflow
Chloride-rich waters	60-100	~6-8.5	~701	~1800	~203	~17	~75	Deep upflow
Acid-sulphate waters	50-99	~2-5	<300	<200-	<200	<30	125-2800	Heated groundwater
Sulphur-chloride waters	~99	~2.5	~32	~200	~308	-	~338	Heated groundwater
Bicarbonate-chloride waters	70 - 99	4-6.5	~341	200 - 500	~264	Up to 500	~183	Periphery of system

Waiotapu Geothermal Field hosts a variety of surface manifestations, including geysers, fumaroles, steaming grounds, collapse craters, hot springs, mud pools, high-chloride pools and silica sinters (Table 2.2) (Grange, 1937; Lloyd, 1959; Hedenquist & Browne, 1989). Hot spring's temperatures range from 60 to 100°C, while their pH values vary from acidic (i.e. < 6) in sulphur-chloride and bicarbonate-chloride waters, to neutral pH (6 – 7)) in chloride-rich waters (Table 2.1). The heat source (from a magmatic plume (Rowland & Sibson, 2004)) has been located in the northern parts close to the south of Mount Maungakakaramea and Mount Maungaongaonga (Figure 2.1). The magmatic intrusions heat a high-chloride fluid reservoir located at 1-4 km deep with >200 °C (Hedenquist, 1991). The depth and location have been constrained by early exploration drilling and core related bulk rock geochemistry, isotope geochemistry and petrology (Wilson, 1963). The rising geothermal fluids with basic pH and a high chloride content (1,250 ppm) (Giggenbach, 1995; Hedenquist, 1982), flow mostly to the south in a horizontal manner (Kaya et al., 2014), with a vertical to horizontal permeability ratio

of 1:40, representative of the TVZ (Rowland & Simmons, 2012). Permeability is associated with faulting, host rock's pore space and pore connectivity (Rowland & Simmons, 2012) which altogether can promote fluid flow controlling the alteration intensity and type of hydrothermal minerals (Browne, 1978).

Table 2.2. Surface manifestations at Waiotapu Geothermal Field.(More details in (Hedenquist & Browne, 1989; Giggenbach et al., 1994).

Feature	Temperature [°C]	Formation Area
Champagne Pool	~76	Central area
Lady Knox Geyser	~98	Central area
Fumaroles	~99	North and central area
Steaming grounds	>25	Central area
Collapse craters	>25	Central area
Mud pools	50-98	Northern area
Silica sinter forming fluids	<50	Central and southern area

Little evidence exists for active faulting directly crossing the system, but Waiotapu Geothermal Field resembles the TVZ orientation (NE-SW) (Rowland et al., 2007). The closest mapped active fault zone is the Paeroa Fault, ~10 km Southwest, extending from the Ngapouri Fault southward to the northern rim of Reporoa caldera (Wood, 1994) and in the southern most area it is dissected by ring faults from the northern margin of the Reporoa caldera (Nairn et al., 1994). At Waiotapu Geothermal Field, faulting and fractures can increase some vertical permeability while the host rock has a high intrinsic horizontal permeability, allowing fluids to moving to south and west from the heat source (Hedenquist, 1982; Mongillo, 1994; Wood, 1994; Hadfield et al., 2001; Kaya et al., 2015), to finally drain into the Waiotapu Stream, which flows to the south and joins the Waikato River (Lloyd, 1959). Mineral deposition sealing faults has been documented to be lowering the host-rock's permeability at Waiotapu Geothermal Field (Wood, 1994). Its anisotropic permeability prevented Waiotapu Geothermal Field from being exploited commercially for heat and electricity production (Wilson, 1963), and now the geothermal system is classified as "Protected" by the Waikato Regional Council.

The most common occurring alteration type is the acid-sulphate alteration in the Waiotapu Geothermal Field, which is predominant in the northern region with surface occurrence of mud pools. In contrast, the water table located closer to the surface in the southern parts causing alteration-induced (e.g. dissolution of glassy groundmass and pumiceous deposits) collapsed craters within the variously altered host rock (Hedenquist & Henley, 1985; Hedenquist & Browne, 1989). The former alteration type is typically argillic caused by raising

vapour from reservoir condensing near surface when reaching meteoric water forming a suite of secondary minerals including cristobalite, kaolinite, alunite, sulphides and native sulphur associations (Table 2.3) (Hedenquist, 1991). The latter alteration towards the southern areas, is characterised by intermingling alteration mineral associations due to the circulation of chloride-rich fluids. The minerals related to chloride-rich fluids form albite/adularia/epidote/chlorite alteration occurring at temperatures as low as 180 °C, with recrystallized groundmass rich in quartz polymorphs, pyrite, pyrrhotite, titanite, leucoxene, calcite and limonite, sphalerite and galena (Hedenquist & Browne, 1989) (Table 2.3). Occurrence of alteration minerals in the north comprises an assemblage of kaolinite, alunite, cristobalite, native sulphur and fine pyrite, dominant within the top 50 m but reaching depths of 200 m from 100 to 100 °C (Hedenquist & Browne, 1989) (Table 2.3). This assemblage of minerals is caused by acid-sulphate waters, in the north which with higher elevations can result in mud pools whereas in the south, closer to the water table, it has caused collapse craters due to large scale dissolution of the glassy and pumiceous volcanics of the host rock (Hedenquist & Henley, 1985; Hedenquist & Browne, 1989).

Table 2.3. Main minerals documented at Waiotapu Geothermal Field. (More details in (Hedenquist & Browne, 1989; Pope & Brown, 2014)).

Primary Mineral	Alteration / secondary mineral	Location	Depth	Process
Plagioclase feldspar (Albite, oligoclase, andesine)	Albite/ oligoclase	Phenocrysts replacement and vein filling	>200 m	Replacing andesine, more abundant than adularia
	Adularia	Phenocrysts replacement and vein filling	>100 m	Replacing andesine. May result from boiling
	White mica (muscovite to illite)	Phenocrysts replacement and vein filling	<300 m	Replacing andesine
	Chlorite	Phenocrysts replacement and vein filling	>200 m	Major alteration product of biotite or pyroxenes
	Epidote	Phenocrysts replacement and vein filling	>350 m	Replacing adularia
	Zeolite	Phenocrysts replacement and vein filling	<400 m	Reaction of volcanic rocks to alkaline groundwater
	Quartz	Phenocrysts replacement, disseminated, vein and fracture filling	Throughout	Ubiquitous as recrystallization of glass
	Calcite	Phenocrysts replacement and vein filling	>150 m	Deposition from a boiling fluid
Pyroxene	Epidote	Phenocrysts replacement and vein filling	>250 m	Replacing adularia
	Chlorite	Fracture and vein filling	>200 m	Major alteration product of biotite or pyroxenes
	Pyrite	Fracture and vein filling	>50 m	
	Titanite	Disseminated	>100 m	Late overprint, associated with leucoxene
	Quartz	Phenocrysts replacement, disseminated, vein and fracture filling	Throughout	Ubiquitous as recrystallisation of glass
Biotite	Epidote	Phenocrysts replacement and vein filling	>250 m	Replacing adularia
	Chlorite	Phenocryst replacement	>200 m	Major alteration product of biotite or pyroxenes
Fe-Ti Oxides (e.g.	Leucoxene (e.g. rutile, titanite)	Disseminated	>100 m	Alteration product from magnetite
	Titanite	Disseminated	>100 m	Late overprint, associated with leucoxene

magnetite, ilmenite)				
Alkalis + Silica	Alunite	Disseminated, fracture and vein filling	<200 m	Leached from alkali and silica by hot, acid water, by acid-sulphate steam-heated waters
	Kaolinite	Disseminated, fracture and vein filling	<200 m	Leached from alkali and silica by hot, acid water, by acid-sulphate steam-heated waters
	Amorphous silica	Disseminated	Throughout	Ubiquitous as recrystallisation of glass
	Quartz	Phenocrysts replacement, disseminated, vein and fracture filling	0 and deeper	Ubiquitous as recrystallisation of glass
	Calcite	Fracture and vein filling	>150 m	Deposition from a boiling fluid
	Quartz	Phenocrysts replacement, disseminated, vein and fracture filling	Throughout	Ubiquitous as recrystallisation of glass
Groundmass	Titanite	Disseminated	>100 m	Late overprint, associated with leucoxene
	Pyrite	Disseminated, fracture and vein filling	>50 m	Alteration from pyrrhotite
	Calcite	Fracture and vein filling	>150 m	Deposition from a boiling fluid
	Zeolite	Fracture and vein filling	<400 m	Reaction of volcanic rocks to alkaline groundwater
	White mica (muscovite to illite)	Phenocrysts replacement and vein filling	<300 m	Late overprint
	Chlorite	Phenocryst replacement	>200 m	Major alteration product of biotite or pyroxenes
	Leucoxene	Disseminated	>100 m	Alteration product from magnetite
	Pyrrhotite	Fracture and vein filling	200-400 m	From highly reducing conditions, now being replaced by pyrite

Local lowering of the water table derived from pressure changes and hydrothermal eruptions, caused changes of mineralisation indicating cooling, based on fluid inclusion studies (Hedenquist, 1982; Hedenquist & Browne, 1989). Heat also appears to have decreased with time, implied by minerals such as epidote, which formation temperature is around 240 °C, but is now found at 200 – 220 °C (Hedenquist, 1991; Simpson & Bignall, 2016). Another example of the system's evolution is that of andesine being replaced by albite, later by adularia and finally by white mica (muscovite), this has been interpreted to be due to an increase of water-rock circulation (Hedenquist & Browne, 1989). This increased water-rock circulation from incursion of marginal steam-heated waters, causes cooling by dilution, which has caused a decrease on pH and an increase on CO_2 (Hedenquist, 1982). There are also former silica sinter deposition and alteration about 1 km west and southwest of lake Ngakoro and 400 m north of Champagne Pool (Hedenquist, 1991; Lloyd, 1959). Champagne Pool one of the most well-known surface features at Waiotapu Geothermal Field resulted from a ~900 year-old hydrothermal eruption, forming a low rimmed crater made of ejected breccias (Gallagher et al., 2020). Today, this hosts silica sinter terraces to the south, enriched in gold and silver with native sulphur and antimony sulphides (Simmons et al., 2016). It is one of several other hydrothermal eruptions linked to intrusion and arrest of magma (Nairn et al., 2005).

Water chemistry at Waiotapu Geothermal Field can be broadly divided into three classes, acid-sulphate, sulphate-chloride and chloride-rich, with a minor prescence of bicarbonate-chloride waters (Table 2.1) (Lloyd, 1959). Acid-sulphate waters have a pH of 2–5 and low temperatures varying from 50 to 99 °C, and their acidity is governed by surface oxidation of hydrogen sulphide (Lloyd, 1959). The sulphate present in geothermal systems of the central TVZ is originated from multiple sources: sulphate in equilibrium with H_2S, descending surface steam-heated fluids with H_2S oxidation, or sulphate reduction from magmatic SO_2 (Chambefort, 2021). At Waiotapu Geothermal Field, the sulphate-chloride waters differ from the acid-sulphate ones in that the former contain up to 200 [mg/kg] of chloride anions (Table 2.1), while the later contain up to that amount. Such waters are less affected by rainfall than sulphate-acid waters and emerge at water table level, similar to chloride-rich springs (Lloyd, 1959). The chloride-rich waters contain the chloride anion up to 1800 mg/kg, are near neutral 6 to 8.5 pH and temperatures range between 60 and 100 °C. Chloride-rich waters often deposit silica sinters, Waiotapu Geothermal Field has documented old series of sinter deposits indicating a wider surface discharge in the past (Lloyd, 1959). The present iso-chloride lines have been delineated by Lloyd, 1959 with Champagne Pool as the chloride maximum. Finally, bicarbonate waters appearing gradually, reaching its highest at the south-eastern side of Lake Ngakoro, these springs have temperatures between 70 and 90 °C. They are formed by carbon dioxide attacking the host rock at shallow depth (Lloyd, 1959). Recent water chemistry studies have shown that changes in the shallow portion of the system have significant effect in water chemistry changes within decade scale, controlling components such as SO^{-}_{4}, Mg or Ca (Pope & Brown, 2014). Whereas components such as Na and B are conservative and seem to be controlled by the deep reservoir (Pope & Brown, 2014).

2.1.2 Geophysical studies

Waiotapu Geothermal Field and the surrounding geothermal areas have been investigated extensively with seismic (Davy & Caldwell, 1998; Eberhart-Phillips et al., 2008; Bannister et al., 2013), resistivity (Healy & Hochstein, 1973; Risk et al., 1994; Bibby et al., 1998; Heise et al., 2010), magneto-telluric (Heise et al., 2008; Bertrand et al., 2012; Bannister et al., 2013), magnetic (Gerard & Lawrie, 1952; Hochstein & Soengkono, 1997; Soengkono, 2011, 2016) and aerial thermal infrared methods (Mongillo, 1994; Reeves & Sanders, 2019).

The TVZ heat source is interpreted to be driven by shallow mid-crustal intrusions that fuel discrete heat sources such as plumes under each individual geothermal field or groups of fields. These have been imaged with magneto-telluric techniques (Bertrand et al., 2012) and are supported by numerical models (Kissling & Weir, 2005; Kaya et al., 2014). The heat in the TVZ comes from a region of partial melting, where seismicity is largely restricted to the top 8 km of crust, indicating a brittle-ductile transition (Hurst et al., 2016). Seismic surveys at Waiotapu Geothermal Field have shown levels of activity distinctive of geothermal areas (i.e. seismic noise amplitude >1.0 μm/s with no diurnal variation), caused by changes of phase at depths <300 m (Whiteford, 1995). Gravity anomalies have also been studied in the region (Modriniak & Studt, 1959), where variations of thickness suggest shallower basement rocks and a depression between Taupo and White Island/Whakaari with Paeroa Fault as western boundary, regardless, no specific interpretations were made.

Magnetic anomalies can identify areas of demagnetization and reveal hydrothermal alteration and its areal extent (Soengkono, 2016; Bertrand et al., 2022) in geothermally altered areas. From an airborne magnetic survey an area of demagnetization (i.e. of 0.5 A/m) of ~5 km^2 was delineated (Hochstein & Soengkono, 1997; Soengkono, 2001). A resistivity survey with Schlumberger array showed an enclosed resistivity boundary of 10 Ωm over an area of 10 km^2. This is interpreted to be caused by hot fluids rising which enable hydrothermal alteration. Furthermore, it is inside a bigger resistivity boundary of 30 Ωm along with Reporoa, Waikite and Waimangu geothermal areas (Healy & Hochstein, 1973; Bibby et al., 1994). This apparent connection derived from such resistivity survey (Bibby et al., 1995) has been interpreted to indicate a deeper connection amongst these areas. Although, this is highly debated, evidence from spatial distribution heat output predicted by numerical models (Kissling & Weir, 2005; Kaya et al., 2014), geochemical studies (Giggenbach et al., 1994) and isotope data (Stewart, 1994) indicate those areas are separate hydrothermal systems. With Waikite being an outflow from Waiotapu Geothermal Field (Kaya et al., 2014).

Two airborne thermal infrared surveys have previously been collected at Waiotapu Geothermal Field, covering 8,000 to 12,000 nm wavelength domains. The first airborne thermal infrared survey detected known warm lakes, springs, streams and warm grounds, but it also found previously unreported surface features in the Southeast of Lake Ngakoro (Mongillo, 1994). It also provided information of the overall alignment of surface features, providing evidence for fault control at Waiotapu Geothermal Field with a Northeast orientation

(Mongillo, 1994). Recently, a second airborne thermal infrared survey took place, also utilising non-geothermal water bodies to empirically calibrate for temperature (Mongillo, 1994; Reeves & Sanders, 2019). This survey found that surface features generally agree with previously mapped ones. Furthermore, these types of data allow for hazard identification, district planning and monitoring over time (Reeves & Sanders, 2019).

2.1.3 Surface plant cover

The extreme ground conditions (e.g. low soil pH, high ground temperatures) present at many geothermal areas of the TVZ can host plant communities that have adapted to such extreme conditions. The geothermal ecosystems commonly include a combination of ferns (e.g. *Hypolepis* species), moss species (e.g. *Campylopus pyriformis*), liverworts (e.g. *Chiloscyphus semiteres*) and shrubs (Given, 1980; Van Manen & Reeves, 2012; Smale et al., 2018). These species can live in acidic soils, extremely acidic soils, in proximity to steam, with nutrient excess or deficiency, water and/or soil with high contents of heavy metals and metalloids (Given, 1980; Burns & Leathwick, 1995; Boothroyd, 2009). *Kunzea ericoides* var. *microflora* (i.e. referred to as kanuka hereafter) is a thermotolerant vascular species endemic to geothermal areas of New Zealand that can live with soil temperatures above 40°C (Burns, 1997; Van Manen & Reeves, 2012). The height of kanuka is generally related to the near-surface (root zone) soil temperature with smaller plants in hotter soils (Burns, 1997; Muukkonen, 2005; Smale et al., 2018) and has also been documented to uptake and translocate non-essential elements such as arsenic, cadmium, antimony and silver (Dunn & Christie, 2020).

2.2 Hyperspectral (VNIR/SWIR) remote sensing

2.2.1 Principles of remote sensing

Remote sensing is the process of collecting information from an object in a remote manner (i.e. without physical contact), measuring electromagnetic radiation in different ranges and spectral resolutions. In broad terms it can be divided in active and passive sensors. Active sensors provide their own source of illumination many of them operating in the microwave portion of the electromagnetic spectrum (e.g. synthetic apretur radar), and other regions of the spectrum (e.g. NIR, LiDAR). This enables them to operate at any time and penetrate the atmosphere under most conditions. Passive sensors in the contrary, require a naturally occurring source of energy (e.g. reflected or re-emitted Sun's energy, thermal infrared emitted energy), and most of them operate in the visible, infrared and thermal infrared portions of the electromagnetic spectrum (e.g. hyperspectral radiometer, sounder, spectroradiometer) (Lillesand & Kiefer, 1979; Van der Meer & de Jong, 2001; Jensen, 2015).

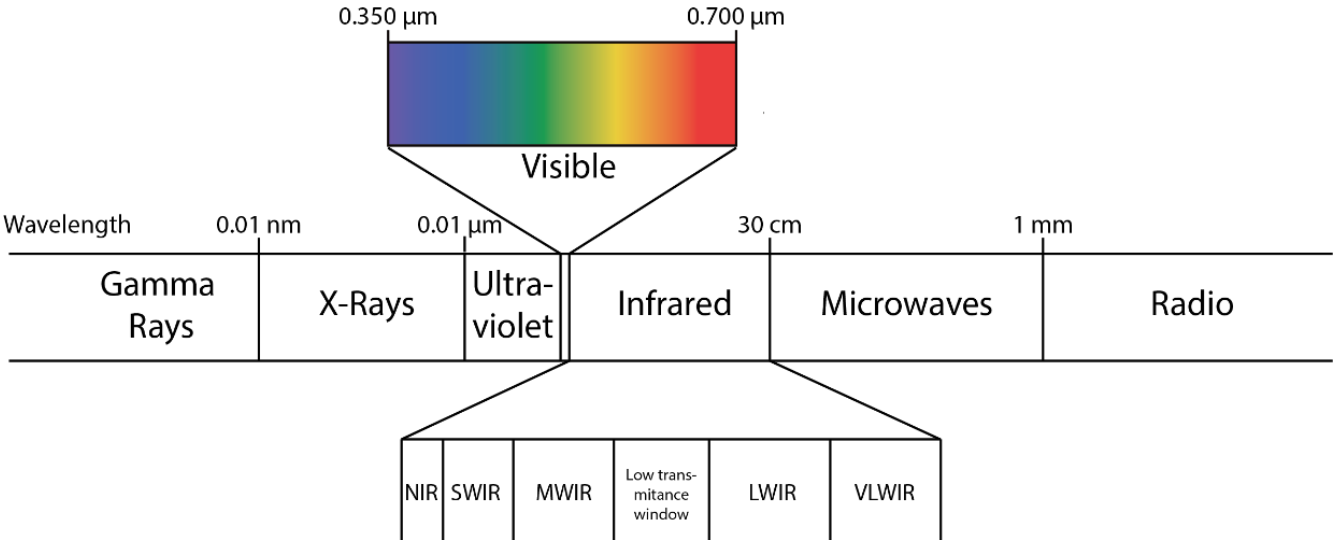

Figure 2.2. Electromagnetic spectrum regions.

Optical sensors (Figure 2.2), measure radiation that is either emitted by the Sun and reflected back from a ground object (e.g. typically in the visible (VIS), near (NIR) and short wavelength (SWIR) regions), or emitted by ground objects (e.g. VIS-NIR, but typically in the longer wavelength domains depending on the object's temperature). The energy of the electromagnetic spectrum behave in accordance with the basic wave theory (Lillesand & Kiefer, 1979), travelling as sine waves with interacting electrical and magnetic oscillation and modelled as particles called photons (Bakker et al., 2009), explained with Maxwell's equations (Eismann, 2012). This classical model can be further extended by quantum mechanics for the complex index of refraction of resonant spectral features to electrical and mechanical characteristics of the material's atomic composition (Eismann, 2012).

Hyperspectral also called image spectroscopy is a subset of optical remote sensing which "samples" the electromagnetic spectrum at many hundreds of narrow (~10 nm) and contiguous spectral bands (Goetz et al., 1985), representing a cube of information with two spatial dimensions (Figure 2.3, X and Y-axis) and one dimension representing the spectral response (Figure 2.3, Z-axis) for each of the bands in each pixel of the image (Eismann, 2012; Borengasser et al., 2013).

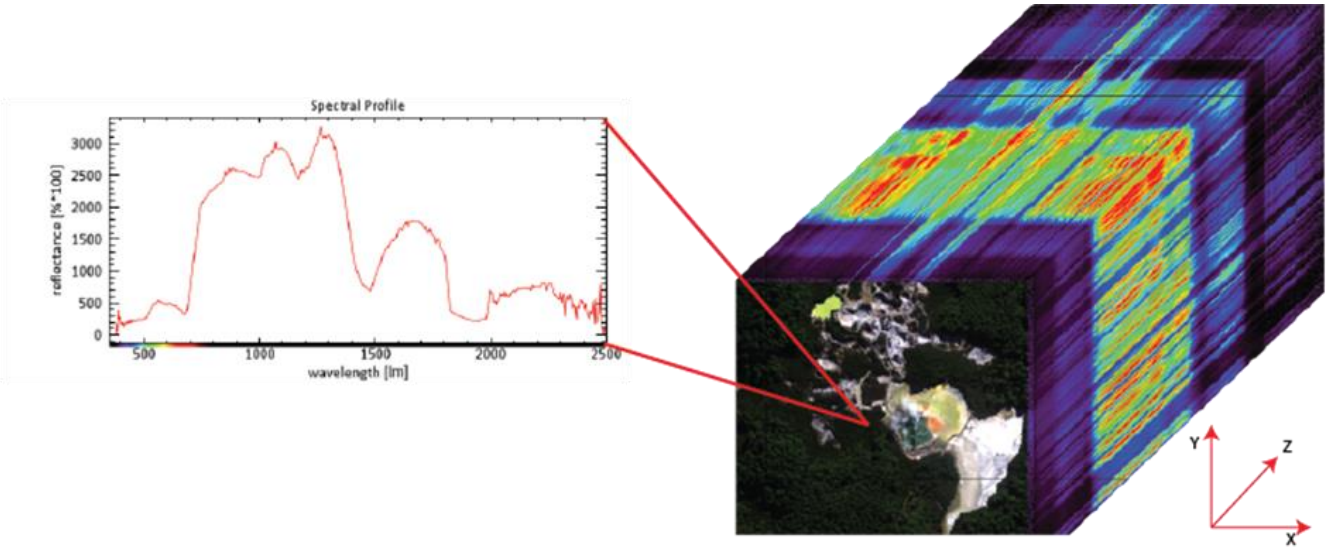

Figure 2.3. Spectral profile from a pixel of a hyperspectral data cube, representing three dimensions of data. (X and Y - spatial domain, Z - spectral domain).

Reflectance spectra represent a combination of physical and chemical information of the ground objects, and objects can be identified based on their spectral reflectance profile that is shaped by the material's reflectance, absorption and transmitting properties (e.g.Bakker et al., 2009). These properties are derived from physical relationships between the spectrum of reflected or emitted light, vibrational and electronic processes, as well as microscopic surface and volumetric properties (Clark, 1999; Bakker et al., 2009; Eismann, 2012).

The visible (VIS) region (350–700 nm, Figure 2.2) includes blue, green and red colours. Our eyes can see in this region, but are not capable to detect all the physical and chemical processes that take place while energy interacts with matter (i.e. electronic transition and charge transfer processes associated with transition metals Fe, Ti, Cr) (Clark, 1999; Van der Meer & de Jong, 2001). Some of the properties are influenced by chemical bonds (Card et al., 1988; Clark, 1999), crystal structure (Van der Meer & de Jong, 2001) and grain size (Clark et al., 2003), which can then be characteristics of certain minerals, providing the capability of hyperspectral data to distinguish and map ground mineral composition (Van der Meer et al., 2012; Asadzadeh & de Souza Filho, 2016). For plant studies, indices in this region have been widely applied due to the fact that healthy vegetation strongly absorbs solar radiation in the red spectral region while strongly scattering in the NIR region (Gobron et al., 2000). VIS region of plants is highly dominated by the absorption properties of pigments in the palisade mesophyll (e.g. chlorophyll-a, chlorophyll-b, B-carotene), chlorophyll being the most important one (Van der Meer & de Jong, 2001; Jensen, 2015). Chlorophyll is the first pigment to degrade causing an increase of reflectance within red wavelengths, followed by the carotenoids increasing the reflectance within blue wavelengths (Sanches et al., 2013). This region has displayed changes when high concentrations of As are present in the soil (Rathod et al., 2018) and in overall stressful environments (Carter, 1993).

The near infrared (NIR) region (700–1,300 nm, Figure 2.2) reflects broad and shallow absorption features due to electronic transition and charge-transfer processes associated with metal ions (e.g. Fe, Cr, Co, Ni) (Eismann, 2012; Van der Meer et al., 2012). Giving the capacity to identify minerals with iron content, such as hematite (Van der Meer et al., 2012). For example, Fe^{+3} bearing minerals have two absorption features in the NIR range (~700-900 nm) (Van der Meer, 2004; Bakker et al., 2009). For plants, the VIS-NIR region, where the red edge is located and scattering in the spongy mesophyll takes place, is very relevant for plant health studies (Van der Meer & de Jong, 2001; Slonecker et al., 2009; Weng, 2009; Xia et al., 2014; Elarab et al., 2015; Iriel et al., 2015; Jensen, 2015). Due to the stretching and bending vibrations of molecular bonds (e.g. C-O, O-H, C-H, N-H bonds) (Curran, 1989; Van der Meer et al., 2012), the concentration of the chemical constituents (Card et al., 1988; Curran, 1989), water content (Buitrago et al., 2016; Shi et al., 2016), leaf structure (Fourty et al., 1996; Féret et al., 2011), pigmentation content (Bakker et al., 2009), leaf thickness (Sellers, 1985; Rock et al., 2017) and species composition (Hope et al., 1993; Rock et al., 2017) can be identified. Throughout this document we will refer to the visible and the near-infrared region as VNIR.

The short wave infrared (SWIR) region (1,300–2,500 nm, Figure 2.2) has been applied for mineral exploration in the past (Hook & Rast, 1990; Madani & Emam, 2011; Fagbohun et al., 2015), due to its capacity to differentiate amongst surface minerals (e.g. Hunt, 1977). As well as in geothermal exploration (Kratt et al., 2010; Reath & Ramsey, 2013; Van der Meer et al., 2014; Govil, 2017). The presence or lack of water and hydroxyl, carbonate and sulphate determine absorption features in the SWIR region, caused by vibrational processes (Van der Meer et al., 2012). At ~1,400 nm and ~1,900, there is a molecular water absorption feature, at ~1,400 nm an absorption feature due to O-H, Al-OH has an absorption feature at ~2,200, Mg-OH at ~2,300 nm and $CaCO_3$ presents absorption features ~2,320 and ~2,350 nm. Detecting minerals like illite, kaolinite, halloysite or dickite with absorption features around 2,200 nm (Eismann, 2012). Another application for SWIR has been in vegetation mapping and quantifying the chemical composition of vegetation (Drake et al., 1999; Pullanagari et al., 2017), also many indices and ratios indicating the health state of vegetation occur in this range (i.e. water absorption). Reflectance in this region is mainly determined by the free water in the leaf tissue with absorption features at ~1,450 and ~1,950 nm (Bakker et al., 2009). Another two examples relevant to plant absorption features in SWIR include lignin (~1,750 nm) and cellulose (~2,172) (Kokaly, 2001; Serrano et al., 2002).

2.2.2 Data acquisition, pre-processing and corrections

Hyperspectral data can be acquired from different platforms: ground, airborne and space. Ground platforms include handheld sensors (usually point spectrometers) utilized in field and laboratories. There are also air-and space-borne platforms which refer to sensors acquiring data from air- (e.g. airplanes) and space-crafts (e.g. space shuttles or satellites) respectively, these are within the range of image spectrometers (Bakker et al., 2009; Eismann, 2012).

The large volumes of data from hyperspectral acquisition have the potential for better identification and characterisation of materials. However, this often makes data processing complex and challenging. The data processing workflow generally follows as:

1) Radiometric corrections and sensor noise: This includes the conversion of the raw digital number (DN) values read by the sensor into radiance (SI unit watts per square meter, per steradian, per micron (or nanometer)): Radiance data is often subject to noise due to detector malfunctions (Bakker et al., 2009; Honkavaara et al., 2009). Such as shot noise (random pixels which were not recorded), line drop-out (a detector that goes off and therefore an entire line will lack information), bad line start (sensors that start reading at a different time than the rest, pushing all the readings), line striping (a detector goes out of radiometric adjustment, recording differently than the others) (e.g. (Saxena et al., 2020). The techniques to improve these malfunctions are not a standard techniques (i.e. only required when the sensor is having problems) and are also known as 'image restoration'. Shot-noise or random noise in a pixel is replaced by the interpolated DN from surrounding pixels, continuous wavelet analysis or other filtering techniques (Feng et al., 2018; Owotogbe et al., 2019). Line drop-out requires the calculation of the average DN value of each line and the scene average, this is compared to all the lines with a designated threshold to identify defective lines and replace them (Rasti et al., 2018). Line stripping is very common and can be corrected with 'histogram matching' from all the other detectors (Meza et al., 2011; Rasti et al., 2018), it is still a relevant subject for remote sensing which keeps growing with newer techniques to denoise imagery (Li et al., 2022; Wang et al., 2022).

2) Atmospheric correction: Solar reflected radiance data are highly sensitive to Sun elevation and azimuth, ground topography and atmospheric scattering, atmospheric water content and trace gases (Sun et al., 2021). Therefore, any optical remote sensing image needs to be atmospherically corrected before applications (Schläpfer & Richter, 2002; Gao et al., 2009). There is relative atmospheric correction based on ground reflectance properties (e.g. vicarious and empirical calibration (Brook & Dor, 2011; Coppo et al., 2017; Hook et al., 2020)), using field-based spectroscopy approaches like tarp and targets. While on the other hand, there is absolute physical modelling-based atmospheric correction, employing radiative transfer modelling to quantify scattering and absorption (Tuominen & Lipping, 2014; Gao et al., 2020; Carmon et al., 2022). Models include the moderate resolution atmospheric transmission (MODTRAN) (Adler-Golden et al., 1999; Gao et al., 2009; Silvestri et al., 2020; Heller Pearlshtien et al., 2021), Second Simulation of the Satellite Signal in the Solar Spectrum (6S) (Vermote et al., 2006; Yan et al., 2018), ACORN (San & Süzen, 2010; Calin et al., 2021); FLAASH (ENVI, 2009; Yang et al., 2021) ENVI's Fast Line-of-sight Atmospheric Analysis of Spectral Hypercubes and ATCOR (Richter & Schläpfer, 2016; El Alem et al., 2021). The latter uses look-up tables (LUT) of atmospheric correction functions dependent on scan angle, relative azimuth angle between a scan line and solar azimuth, and terrain elevation (Jensen, 2015; Richter & Schläpfer, 2016).

3) Geocoding: This process relates each pixel of the image to a "true" position on the ground via georectification (Purkis & Klemas, 2011). Geocoding can project the image into a user-specified coordinate system while minimizing geometric distortions (Jensen, 2015). Allowing the remote sensing data to be linked with other thematic geospatial data (e.g. vector data) in Geographic Information Systems (GIS) platform (Warner et al., 2009). Geocoding can also include mosaicking operation which is a process of stitching individual images together (Nishar et al., 2016; Hewson et al., 2020; Marwan et al., 2021).

2.2.3 Post-processing

Remotely sensed data enhancement algorithms are applied to improve the spectral quality of the image, reduce the computational burden by data reduction or segregate noise in the data. Some of the most popular methods include (Table 2.4):

1. Data reduction: Principal Component Analysis, which transforms the original data into a substantially smaller set of uncorrelated variables that represent most of the information present in the original dataset (Li et al., 2018). Minimum Noise Fraction, is a linear transformation which consists of two separate PCA rotations (Green et al., 1988; Luo et al., 2016). Both can also be applied for noise reduction (Luo et al., 2016; Nyahucho, 2020).
2. Data transformation: First and second-order derivatives that can reduce the influence of illumination and eliminate background signal error (Cao et al., 2018; Chu et al., 2022). Log-transform which can enhance the spectral differences (Cao et al., 2018). Centred Log-Ratio (CLR) transformation which prepares data for standard statistical approaches (Aitchison, 2008; Muriithi, 2015). Band ratios have been used in a wide range of applications (e.g. agriculture, mineral detection, and food technology) (Madani & Emam, 2011; Van der Meer et al., 2014; Ulusoy, 2016; Tian et al., 2021). Scaling and centring, to equalize between input data variables (length of the vectors and its standard deviation) (Grahn & Geladi, 2007). Z-score, to standardise or normalise values by subtracting the mean and dividing by its standard deviation (Singer & Kouda, 2001). Spectral smoothing is also achieved through the use of filters, such as least squares based filter Savitzky-Golay, one of the most important and widely used filters for smoothing the data (Savitzky & Golay, 1964; Pan et al., 2015; Hou et al., 2018). Derivative filters, are also used with the goal of retrieving spectral details and reducing the signal-to-noise ratio (Tsai & Philpot, 1998; Pan et al., 2015). One downside of smoothing filters is the possibility of artificial broad absorption features, or missing important narrow absorption features (Gao et al., 2009). Also, at frequencies above the cut-off, some filters (e.g. Savitzky-Golay) have poor noise compression, which has led to other filters being tested, like finite impulse response filters which have improved results (Schmid et al., 2022).
3. Endmember extraction: endmembers are the spectra that linearly combined can explain all the other spectral signatures in the data (Kruse et al., 2011; Somers et al., 2011) and can be used for image

classification. It can be performed manually by selecting areas with pure materials or selecting the endmember spectra from a multidimensional data cloud (i.e. n-Dimensional scatter plot), in other cases a fully automated endmember determination is applied (Eismann, 2012). Pixel Purity Index which aids to obtain the most spectrally pure pixels (Qu et al., 2014).

Table 2.4. Post-processing methods and their impact on further analytical methods.

Post-processing method	Impact on analytical methods
Data reduction	Can reduce computational requirements, but there is potential for information loss.
Data transformation	Enhance data for easier manipulation and information extraction for further analysis. On the other hand, which transformation is chosen can be highly data dependant, requiring some a priori expert knowledge.
Endmember extraction	Enables accurate classifications and unmixing. However, if there is not enough spectral separation between endmembers it can lead to inaccuracies within analytical methods.
Spectral smoothing	Noise reduction, as well as improvement within further analytical methods (classification). Regardless there is the possibility of oversmoothing, leading to loss of information and inaccuracies.

2.2.4 Analytical methods

Spectral analytical techniques can be grouped in various manners, including date of emergence, presumed randomness, type of data they are applied to, the way pixels are treated, the need for training data and data representation fashion (Asadzadeh & de Souza Filho, 2016). Here we present a taxonomic tree organised by the basis on which a priori reference data are needed or not (Figure 2.4). It is also worth noting there are ensemble classifiers that take into account several classifiers to allocate a class label for a given pixel.

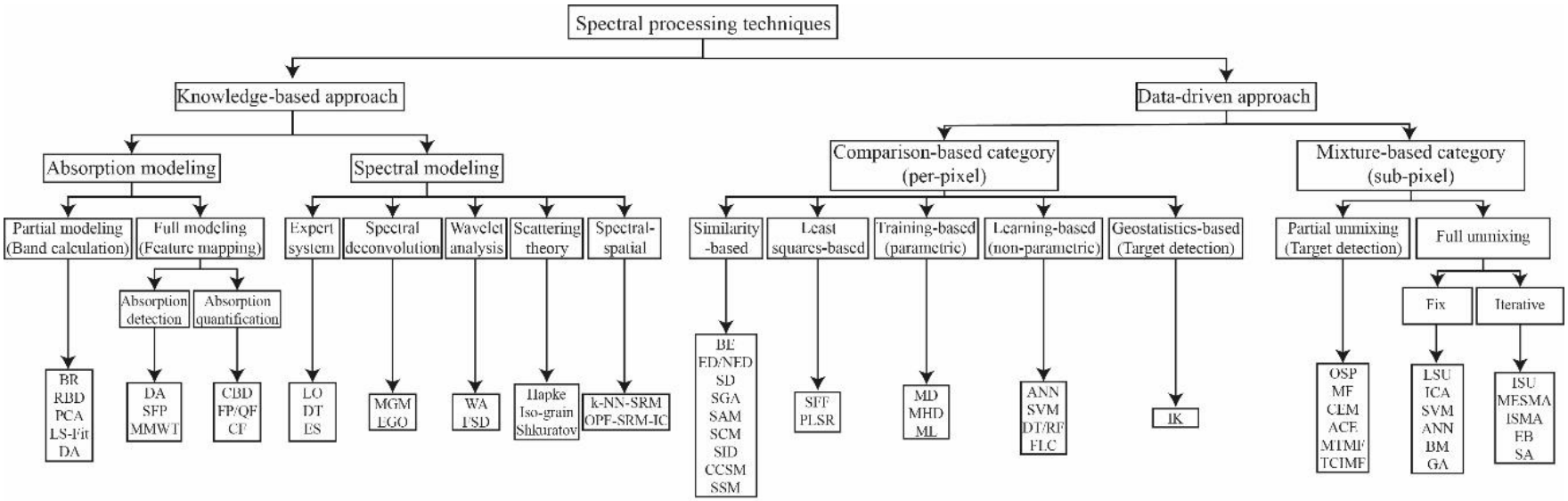

Figure 2.4. Taxonomic tree of spectral processing techniques organised by a priori reference required or not. Modified from (Asadzadeh and de Souza Filho, 2016b)*. The acronyms used in the tree and throughout the text are:* ***BR****: band ratio,* ***RBD****: relative absorption band- depth,* ***PCA****: principal component analysis,* ***LS-fit****: least-square fitting,* ***DA****: derivative analysis,* ***SFP****: spectral fingerprints,* ***MMWT****: maximum modulus wavelet transform,* ***CBD****: continuum band-depth,* ***FP****: fitted polynomial,* ***QF****: quadratic fitting,* ***CF****: curve fitting,* ***LO****: logical operator,* ***DT****: decision tree,* ***ES****: expert systems,* ***MGM****: modified Gaussian model,* ***EGO****: exponential Gaussian optimization,* ***WA****: wavelet analysis,* ***FSD****: Fourier self-deconvolution,* ***Hapke****: Hapke (bidirectional) scattering theory,* ***Iso-grain****: Iso-grain scattering theory,* ***Shkuratov****: Shkuratov scattering theory,* ***k-NN-SRM****: k-nearest neighbors-statistical region merging,* ***OPF-SRM-IC****: optimum-path forest-statistical region merging,* ***BE****: binary encoding,* ***ED****: Euclidean distance,* ***NED****: normalized Euclidean distance,* ***SD****: spectral distance,* ***SGA****: spectral gradient angle,* ***SAM****: spectral angle mapper,* ***SCM****: spectral correlation mapper,* ***SID****: spectral information divergence,* ***CCSM****: cross-correlogram spectral match,* ***SSM****: spectral similarity mapper,* ***SFF****: spectral feature fitting,* ***PLSR****: partial least square regression,* ***MD****: minimum distance,* ***MHD****: Mahalanobis distance,* ***ML****: maximum likelihood,* ***ANN****: artificial neural network,* ***SVM****: support vector machines,* ***DT****: decision tree,* ***RF****: random forests,* ***FLC****: fuzzy logic classifier,* ***IK****: indicator kriging,* ***OSP****: orthogonal subspace projection,* ***MF****: matched filtering,* ***CEM****: constrained energy minimization,* ***ACE****: adaptive coherence estimator,* ***MTMF****: mixture tuned matched filtering,* ***TCIMF****: target-constrained interference-minimized filter,* ***LSU****: linear spectral unmixing,* ***ICA****: independent component analysis,* ***SVM****: support vector machines,* ***ANN****: artificial neural network,* ***BM****: Bayesian model,* ***GA****: genetic algorithm,* ***ISU****: iterative spectral unmixing,* ***MESMA****: multiple endmember spectral mixture analysis,* ***ISMA****: iterative spectral mixture analysis,* ***EB****: endmember bundles,* ***SA****: simulated annealing*

Classification algorithms quantify similarities or dissimilarities of spectra, grouping pixels with similar spectra together (Grahn & Geladi, 2007) and are often applied to distinguish between different land surface cover types (Lv & Wang, 2020). Spectral classifiers are data-driven and create approximations between unknown pixel spectra and labelled training data. Classification methods can broadly be divided into two types: supervised (Ghamisi et al., 2017), which rely on the existence of labelled samples and unsupervised/clustering, where there are minimal user inputs. There are also approaches that share commonalities between supervised and unsupervised methods, called semisupervised, such as transductive support vector machine methods for classification (Bruzzone et al., 2005). These are beyond the scope of the thesis, but extensive review papers on semi-supervised methods can be found in the literature (Lv & Wang, 2020; Riese et al., 2020; Wang et al., 2021).

Image classification using a supervised approach has long been used through ENVI workflow tool. This includes selecting a classification method from unsupervised and supervised methods. Unsupervised classification methods cluster the pixels based on statistics, calculating the class mean iteratively until all pixels are classified (the user can select the number of classes). Supervised classification methods require training data and the selection of an algorithm (e.g. Maximum likelihood, Minimum distance, Spectral Angle Mapper and Mahalanobis Distance) (Li et al., 2020).

Maximum likelihood Classifier is a supervised, non-linear classification method (Lv & Wang, 2020). It computes second-order statistics mean, standard deviation and covariance from the training data to classify through a maximum probability criterion (Nidamanuri, 2020). It is a fast computational classification method compared to Support Vector Machine or Neural Network classifiers (Huang et al., 2002). However, it does require the training data to be normally distributed to provide good results (Lv & Wang, 2020).

Spectral Angle Mapper (SAM), measures the similarity of an image pixel to a reference spectrum and calculates the angle between two spectra, treating them as vectors in a space with dimensionality equal to the number of input bands (Debba et al., 2005; Asadzadeh & de Souza Filho, 2016). Its straightforward approach and availability, as well as its indifference to illumination variations, have made this a widely used algorithm (Crósta et al., 1998; Hecker et al., 2008). However, SAM's performance is highly dependent on the reference spectrum (Hecker et al., 2008; Zhang & Li, 2014). Its simplicity which in some applications is ideal, is also its downside, as it is incapable of detecting small differences between mineral species (Crósta et al., 1998).

Spectral Machine learning approaches have been widely applied to hyperspectral data (Gewali et al., 2018), which has been the subject of intense research and development, especially over the past

10 years. These methods are superior in terms of accuracy over classical spectral methods such as the Spectral Angle Mapper (Zhang & Li, 2014). Broadly speaking, machine learning utilises concepts from multivariate statistical approaches and it has been increasingly applied to hyperspectral images for both classification and regression. When improved accuracy is required, multivariate statistical methods are used (Torres & Amigo, 2020). These calculate a correlation between a set of independent samples (i.e. two data matrices X and Y) measures to predict the values for unknown samples (Grahn & Geladi, 2007). Here, a brief overview is provided covering the most popular machine learning methods:

1. Random Forest (RF) is an ensemble classifier that produces multiple decision trees from randomly selected input samples, effectively dealing with big datasets and high co-linearity (Belgiu & Drăgu, 2016; Xia et al., 2014).
2. Support Vector Machine (SVM), a non-parametric machine learning algorithm based on statistical learning theory, which constructs a model of a linear or non-linear hyperplane in a multidimensional space which best separates the labelled classes (Melgani & Bruzzone, 2004; Varshney & Arora, 2004; Gewali et al., 2018). In terms of classification accuracy and computational time, SVMs are much more effective, seem more effective than traditional pattern recognition approach and exhibit low sensitivity to the Hughes phenomenon (Melgani & Bruzzone, 2004), as well as higher accuracies than other methods (Huang et al., 2002).
3. Partial Least Squares (PLS) has been widely used in chemometric studies involving spectroscopy signals related to any type of target variables (e.g. chemical concentration, mineral chemical contents, soil properties) (Gomez et al., 2008; Slonecker et al., 2009; Pullanagari et al., 2016; Rathod et al., 2018; Stafford et al., 2018). PLS combine features from Principal Component Analysis and multiple regression, and it is effective for very large sets of independent variables (Wold et al., 2001; Abdi, 2003). While the Principal Component Regression finds the maximum variance, PLS regression takes advantage of covariance between both predictor and target variables (Abdi, 2003). There are many variations of PLS, including Kernel-PLS (Rosipal & Trejo, 2002). K-PLS is a regularised least squares regression in a Kernel Hilbert Space, which allows for non-linear models (Rosipal & Trejo, 2002; Blanchard & Krämer, 2010). With advantages such as the utilisation of fewer and qualitatively different components than for example, Principal Component Regression (Rosipal & Trejo, 2002). One downside is that there is still no clear ‘stopping’ rule, as to how bit the kernel must be, as this also appears to be data dependent (Blanchard & Krämer, 2010).
4. Deep Learning methods have a great discriminative ability (Cao et al., 2020). However, its success is greatly linked to numerous training (labelled) samples, which can be time

consuming and expensive (Cao et al., 2020; Liu et al., 2017). One of the deep learning methods which has gained a lot of success for hyperspectral classification is Convolutional Neural Network (CNN), therefore plenty of CNN-based methods have emerged, such as deep CNN, contextual deep CNN, and others (Krizhevsky et al., 2017; Acquarelli et al., 2018). These methods can learn quickly (Wang et al., 2022), but there is also a risk of overfitting (Chu et al., 2022) and it also requires usage expertise (Mäyrä et al., 2021).

Both classification and regression analysis require various degrees of training and independent validation data that has not been used in the model development (Molinaro et al., 2005; Lyons et al., 2018). Validation methods for classification and regression have often been used, including:

1. Training and Test Split, is also known as the learning-test split of the holdout method (McLachlan, 1992). It creates a single partition based on a predetermined ratio (e.g. 80-20% for training and validation, respectively) (Molinaro et al., 2005). It is a popular method which uses little computational power, but it has two sources of bias including each observation contribute only to either the training or testing set and if the learning set is small, the test set error for the model tends to over-estimate the model error on the full dataset (Molinaro et al., 2005; Pawluszek-Filipiak & Borkowski, 2020; An et al., 2021).
2. Cross validation is also known as k-fold cross validation and can vary to leave-one-out cross-validation (LOOCV) or Monte Carlo cross-validation (MCCV) (Molinaro et al., 2005). They have the benefit of testing all data once whereas other validation methods (Bootstrapping or Monte Carlo) do not (Lyons et al., 2018). LOOCV has not been favoured over k-fold in cases where the sample size is large, due to computational burden (Molinaro et al., 2005). The variation of different partitioning methods can introduce a variety of adverse effects on the predictive model, including covariate shift (Moreno-Torres et al., 2012), over- or under-sampling (Blagus & Lusa, 2015) and computational burden (Molinaro et al., 2005).
3. Bootstrapping, is a resampling technique which belongs to the Monte Carlo family methods (Efron & Tibshirani, 1993; Berrar, 2019). It resamples the data repeatedly and can be adapted to other sampling schemes easily (Fox, 2002; An et al., 2021). Along with LOOCV it has been found to give some of the smallest biases (Molinaro et al., 2005; Berrar, 2019). However, it is prone to overestimate the prediction error (Molinaro et al., 2005).

The assessment of model performance can be benchmarked using error metrics (Foody, 2008), this measure how well the model fits to the data you used to create the model (Hughes & Fisher, 2022). In general, the model tends to improve the more variables you can include, but this is usually an unrealistic approach and it can also cause overfitting (Hughes & Fisher, 2022). There is a wide

range of error metrics which assist to determine the accuracy of classification and regression models. One of the simplest ways of assessing a model's performance is through an error matrix, an effective way of summarising the agreement between the map and reference classifications (Stehman & Foody, 2019). Overall accuracy, calculated from the error matrix is the sum of entries on the main diagonal of the error matrix, providing a very coarse assessment (Foody, 2020). R-square or R^2 has been widely used and suggested as a standard metric for regression model evaluation (Chicco et al., 2021), not having the interpretability limitations of Mean Square Error (MSE), Rooted Mean Square Error (RMSE) or Mean Absolute Error (MAE). These error metrics (i.e. MSE, RMSE and MAE) share a downside, their values can range from zero to infinity, therefore a single value does not give enough information on the model´s performance (Chicco et al., 2021). MSE and MAE evaluate the accuracy and quality of fit in terms of the distance between the regression and the actual training points (Sammut & Webb, 2011; Wang & Lu, 2018). MSE variation RMSE is one of the most popular error metrics, it is related to MSE and will be identical to an ordering based on MSE (Kelley & Lai, 2011). MAE has a variation in its percentage form, Mean Absolute Percentage Error (MAPE) RMSE is better to represent performance when the expected error distribution is Gaussian than MAE (Chai & Draxler, 2014). There are plenty of papers which review, criticise and support different error metrics, which in many cases is data dependent (e.g. (Willmott & Matsuura, 2005; Foody, 2009; Olofsson et al., 2014; Chai & Draxler, 2014; Stehman & Foody, 2019; Foody, 2020).

2.2.5 Application at geothermal fields

The application of hyperspectral remote sensing VNIR and SWIR has been widely applied for mineral identification in geothermal exploration. An extensive review can be found in (Thompson et al., 1996; Gupta & Roy, 2007; Van der Meer et al., 2014; Savitri et al., 2021) The VNIR/SWIR section of the electromagnetic spectrum can indicate a variety of minerals including sulphates (e.g. alunite, jarosite and gypsum), phyllosilicates (e.g. kaolinite, illite/smectite and micas), and carbonates (e.g. calcite and siderite). Due to the absorption features related to O-H, H_2O, CO_3, SO_2 and NH^4 (Clark et al., 1990; Nash et al., 2004; Poulet et al., 2005; Calvin & Pace, 2016), such hyperspectral datasets have traditionally been used for mineral mapping (Kereszturi et al., 2018; Rajan Girija & Mayappan, 2019; Pour et al., 2021).

Key mineral phases associated with hydrothermal processes can be mapped using laboratory and airborne hyperspectral imagery. Sulphate minerals, such as alunite, have been identified in different geothermal fields by a broad absorption at ~2,160 nm and a shallower one at ~2,320 nm with spaceborne platforms such as Advanced Spaceborne Thermal Emission and Reflection Radiometer (ASTER) (Rowan et al., 2006). Airborne platforms like Airborne Visible/Infrared

Imaging Spectrometer (AVIRIS) (Kruse et al., 2011). As well as hand-held Fourier Transform Infrared spectroscopy (FTIR) (Littlefield & Calvin, 2014).

Phyllosilicates (e.g. kaolinite, illite/smectite and micas) can also be detected with VNIR/SWIR techniques. By absorption features at 1,400 and 2,200 nm due to vibration modes in the hydroxyl functional groups (e.g. Al-OH) (Notesco et al., 2016; Kamau et al., 2020) There are atmospheric water absorption bands near 1,400 nm (Clark et al., 1990), therefore this wavelength cannot be used to infer mineralogy (Van der Meer & de Jong, 2001). Clay mineral identification has been done with spaceborne platforms such as ASTER (Kratt et al., 2010; Mardiati et al., 2020), and airborne platforms like HyMap and ProSpecTIR. And by hand-held FTIR (Littlefield & Calvin, 2014), Terraspec (Mauriohooho et al., 2014) and Specim sensors (Kamau et al., 2020). Carbonates present an absorption feature at 2,300 nm, due to carbonate ions (Littlefield & Calvin, 2014; Notesco et al., 2016) and they have been identified with ASTER spaceborne platform and with HyMap airborne platform (as tufa in Pyramid Lake Basin, USA) (Kratt et al., 2010).

It is worth mentioning that the identification of silicate minerals, including silica-bearing minerals, baryte or adularia is not ideal in the VNIR/SWIR region of the electromagnetic spectrum. It can be easily detected with thermal infrared techniques, see Chapter 2.4. Regardless, some studies have detected opal (Kratt et al., 2009; Littlefield & Calvin, 2014) in the VNIR/SWIR regions with airborne platforms.

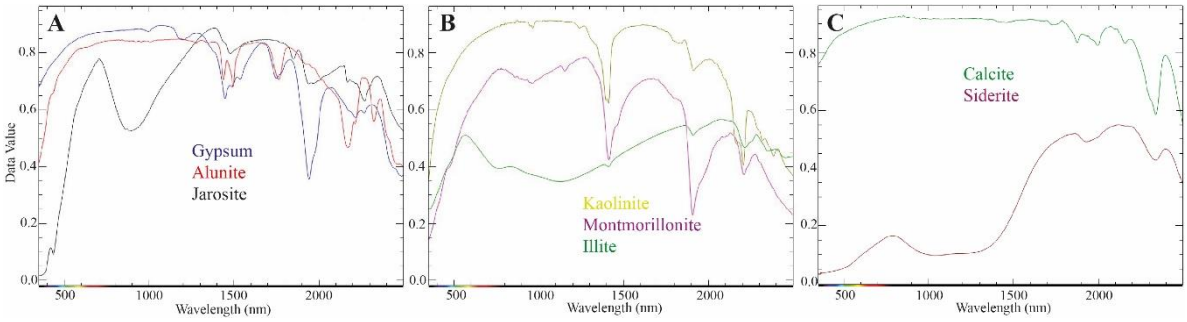

Figure 2.5. Spectral signature for minerals characteristic of geothermal areas within the VNIR/SWIR spectral range.

2.3 Thermal infrared remote sensing

Thermal Infrared (TIR) is the term commonly used within the remote sensing community to refer to the region of the electromagnetic spectrum which detects emitted heat (Haselwimmer & Prakash, 2013; Mia et al., 2012). Any object emits thermal energy if its temperature is above absolute zero (0 K or -273.15 °C) (Prakash, 2000). The radiated energy from the surface's object is determined by its temperature and emissivity (more details in (Hapke, 1993; Prakash, 2000)). The emitted

radiation in typical geothermal settings is measured between ~7,500 and 13 ,000 nm, referred to as the Long Wave Infrared (LWIR) region, which in this document we will refer to as thermal infrared (TIR). TIR radiation can then be converted to temperature, thus TIR has often been used to assess geothermal areas by mapping thermal anomalies (Haselwimmer & Prakash, 2013; Van der Meer et al., 2014). Spectral emissivity can also be used to detect material composition, and therefore can aid in mapping some hydrothermal and rock-forming minerals, such as feldspars, quartz/silica, baryte and adularia (Hecker et al., 2019; Ninomiya & Fu, 2019). A synthesised review for both applications can be found in (Abubakar et al., 2017).

Radiance is the product of the radiance leaving the surface and the atmosphere's transmittance, plus upwelling radiation from the atmosphere (more details in Ninomiya et al., 2005). Accordingly, the emitted energy is especially affected by the Earth's atmospheric transmittance (Ninomiya & Fu, 2019), and is also influenced by meteorological conditions, topography, and other natural phenomena (e.g. convection from air currents, volcanic activity) (Romaguera et al., 2018; Gemitzi et al., 2021). For geothermal applications, the crucial part is to separate the inherent heat of the geothermal source from other heat sources (i.e. indirect or direct solar heating effects or human built structures) (Savage et al., 2010). Other applications to heat anomaly detection have been applied in volcanology settings, to do temporal change analysis, point pattern analysis or hazard forecasting (Connor & Hill, 1995; Cigna et al., 2020).

For mineral identification, characteristic absorption features between 8,200 and 10,000 nm are located within atmospheric windows that can be used. For example, the Si-O fundamental molecular vibrations can be diagnostic for silica-bearing rocks/minerals due to cation substitution taking place (more detail in (Salisbury et al., 1991; Hapke, 1993)). Such absorption features make it also possible to identify other rock-forming minerals, such as feldspar, carbonates, sulphates and phosphates (Rowan et al., 2006; Aslett et al., 2018; Hecker et al., 2019). For example, the detection of silicate minerals preferred in this thermal infrared region, as they do not tend to have diagnostic absorption features within the VNIR and SWIR (Hecker et al., 2010; Feng et al., 2018). There is vast information on mineral identification for this spectral region, some examples can be found in (Vaughan et al., 2003; Hecker et al., 2010; Schodlok et al., 2016).

2.3.1 Data acquisition and calibration

Thermal infrared data acquired in a laboratory were the first measurements which showed the importance of TIR for geology, demonstrating its potential to complement VNIR and SWIR (Lyon & Green, 1975; Hewson et al., 2020; Mardiati et al., 2020). The measured crystal orientation influences the resulting spectra in such measurements, which can give the transmitted, reflected or

emitted energy (Hecker et al., 2010; Notesco et al., 2016). Transmission is one of the most studied, it requires little material and gives excellent information on the absorbance with easy interpretation, it has been applied mainly to quantitative mineralogy (King et al., 2004; Hecker et al., 2010). Diffuse reflectance (also known as Diffuse Reflectance Infrared Fourier Transform Spectroscopy, DRIFTS), is well suited for powdered samples, giving a high signal to noise (King et al., 2004; Hutengs et al., 2018). Directional-hemispherical reflectance, or DHR, use a collimated beam of light directed to the sample and measure the reflected energy (Hapke, 1993). It is practical for terrestrial uses, as it can indeed give emissivity spectra for minerals and rocks (Salisbury et al., 1991; Hecker et al., 2010; Hutengs et al., 2018). Lastly, the emissivity of a material is its emitting ability compared to a black body (Lillesand et al., 2015). In laboratory measurements, the energy emitted inherently by the sample is obtained by heating it up to 100 °C and with the use of a calibrated black body target (Ruff et al., 1997; Virtue et al., 2021). A black body is a near-perfect emitter and absorber of electromagnetic energy, similar to how the Sun, water or vegetation behave (Young et al., 2002; Ninomiya & Fu, 2019), which can give opportunities for ground truthing airborne surveys (Reeves & Sanders, 2019; Weldeyohannes et al., 2022).

TIR can be acquired at any time of the day with handheld (FTIR instruments), airborne (TIMS, FLIR, AisaOWL, MASTER) or satellite platforms (ASTER, Landsat 8 and 9, MODIS, ECOSTRESS) (e.g. Bedell et al., 2017). The radiation at the surface is only one of the ways heat is transferred to the atmosphere, there is also, air convection, air conduction and steam advection, but radiation is the only component which TIR imagery can detect (Seward et al., 2018; Liu et al., 2021). For geothermal areas, it is preferable to acquire data during the night, due to the significant interference from the solar heated ground (Reeves & Sanders, 2019; Sekertekin & Arslan, 2019). Therefore, night acquisitions (i.e. two hours after sunset or before dawn) assist to minimize the effect of the Sun's radiation and improve thermal contrast (Seward et al., 2018; Weldeyohannes et al., 2022). Atmospheric and radiometric corrections can be applied for airborne and spaceborne acquisitions, due to the contamination of atmospheric conditions, by subtracting atmospheric effects (e.g. absorption, upward emission and scattering of Earth's surface radiation) (Vermote et al., 2006; Young et al., 2002). These corrections can take into account types of sensor, meteorological visibility, date and time, sun zenith and azimuth angles, amongst others (Haselwimmer & Prakash, 2013; Seward et al., 2018; Ninomiya & Fu, 2019). In some cases, typically of airborne acquisitions, radiometric calibrations are applied to convert the sensor recorded Digital Number (DN) into at-surface radiances (Vaughan et al., 2010). Later a radiance additive scaling factor is applied to compute the spectral radiance, which is later converted to brightness temperatures (Darge et al., 2019; Gemitzi et al., 2021). When it is possible for heat surveys, calibration with field temperatures (e.g. non-geothermal water

bodies) at the time or close to the time of acquisition is recommended. Field temperatures provide a ground truth with kinetic temperature to calibrate the values from the sensor (Coolbaugh et al., 2007; Reeves & Sanders, 2019). It is also important to consider other parameters which can affect the values retrieved in thermal infrared surveys (apart from the effect of the Sun's energy), such as altitude (Gutiérrez et al., 2012), land cover (Gemitzi et al., 2021), meteorological conditions (Chan et al., 2018) and soil humidity (Hulley et al., 2010).

2.3.2 Thermal infrared and its geothermal applications

The first airborne survey using single channel broadband bandwidth (>100 nm) TIR in a geothermal area to map surface thermal anomalies was in 1970, in Long Valley and the Salton Sea, USA (Hodder, 1970). In New Zealand it was ~20 years later in Waiotapu Geothermal Field, finding thermal anomalies never documented before and estimating the heat output (Mongillo, 1994). The first satellite surveys focused on geothermal were using Landsat and SPOT to map structures influencing geothermal processes (Deroin et al., 1995). The uses of thermal infrared for geothermal exploration have grown a lot since then, as their benefits greatly surpass the limitations and challenges of its use, encompassing diverse applications:

1) Surface temperature: Generated by calculating the Land Surface Temperature (LST), which is a robust and cost-effective technique to detect thermal anomalies (Romaguera et al., 2018), using a variety of algorithms (Abubakar et al., 2017; Sekertekin & Arslan, 2019). LST can assist to delineate active surface extensions as well as structural features (Hodder, 1970; Mongillo, 1994; Calvin et al., 2015; Lloyd et al., 2016; Seward et al., 2018). It has also been used as a first reconnaissance tool to detect geothermal potential with satellite platforms such as Landsat (China (Qin et al., 2011), Japan (Mia et al., 2014; Tian et al., 2015) and ASTER (Bradys Hot Springs, USA (Coolbaugh et al., 2007)). And in some cases as a multi-temporal study with satellite platforms, such as MODIS (Aegean region (Zouzias et al., 2011)), Landsat (Taiwan (Chan et al., 2018), Greece (Gemitzi et al., 2021), Peut Sagoe in Indonesia (Zaini et al., 2022), Japan (Mia et al., 2013)), Meteostat Second Generation (Kenyan Rift (Romaguera et al., 2018) or ECOSTRESS (Italy (Silvestri et al., 2020)). Airborne platforms such as GEOSCAN (Waiotapu and Waimangu, New Zealand (Mongillo, 1994)), DigiTHERM (Silali, Kenya (Mutua et al., 2013)), AHS (Spain (Sobrino et al., 2006)). Recently the use of unmanned aerial vehicles (UAV) has also grown with studies in Italy (Silvestri et al., 2020), Indonesia (Marwan et al., 2021), Iceland (Bjornsson et al., 2019) and New Zealand (Harvey & Luketina, 2014). In some cases of airborne and spaceborne acquisitions, the first step to other applications involves calculating the LST from the

acquired data, the theoretical basis for this application can be found in (Abubakar et al., 2017a).

2) Heat output: Surface heat flux calculations with a variety of methods can constrain geothermal reservoir models (Mongillo, 1994; Bromley et al., 2011; Haselwimmer et al., 2013; Heasler & Jaworowski, 2018). Radiative heat flux represents the heat emitted by radiation from the ground plus indirect (re-radiated) solar radiation effects (Vaughan et al., 2012). In geothermal areas, radiative heat flux is the function of heat transfer rates from the depth to the surface by fluid convection and conduction without indirect radiation (Watson et al., 2008). Heat flux calculations have been achieved from satellite platforms, including Landsat (Japan (Morifuji et al., 2021), Yellowstone, USA (Watson et al., 2008)) and ASTER (Yellowstone, USA (Vaughan et al., 2012). Hand-held and airborne platforms can also be useful and provide much higher resolution data. These have been applied using FLIR sensors to a range of geothermal systems, including Pilgrim Hot Springs, Alaska (Haselwimmer et al., 2013) and Yellowstone, USA (Jaworowski et al., 2010), Waimangu, New Zealand (Seward et al., 2022). With UAVs in Wairakei, New Zealand (Nishar et al., 2016), and UAVs using Optris sensors in Mexico (Carbajal-Martínez et al., 2021).

3) Monitoring features: In non-exploited areas, developed reservoirs or in the vicinity of urban areas (Reeves & Rae, 2016; Zaini et al., 2022). Temporal change detection is often based on two or more TIR image acquisitions of different times (Sekertekin & Arslan, 2019; Gemitzi et al., 2021). This can then reveal thermal changes indicative of variations in the production if the resource is being exploited, geological structures or geothermal hazards (Allis, 1979, 1981; Bromley et al., 2010; Haselwimmer et al., 2013; Reeves & Rae, 2016). A variety of platforms and revisit times have been used when monitoring a geothermal area, a study compared three spaceborne platforms (e.g. ECOSTRESS, ASTER and Landsat 8), finding high compatibility between the three (Silvestri et al., 2020). With ECOSTRESS providing higher spatial resolution and shorter revisit time, representing an improvement over the other two platforms (Silvestri et al., 2020). ECOSTRESS satellite is quite recent but a variety of other satellite platforms have been used, including Landsat (Karapiti, New Zealand (Mia et al., 2012), New Zealand (Seward et al., 2018)), Advanced Spaceborne Thermal Emission and Reflection Radiometer (ASTER) (Yellowstone National Park, USA (Vaughan et al., 2012a, 2020)). Airborne platforms have also been widely used with sensors like the Forward Looking Infrared (FLIR) (New Zealand (Seward et al., 2018), USA (Haselwimmer et al., 2013; Jaworowski et al., 2013)). The use of UAVs like in other applications is also

increasing, being applied to geothermal areas like Parco delle Biancane, Italy (Silvestri et al., 2020) or Seulawah Volcano, Indonesia (Marwan et al., 2021). UAVs can provide regular monitoring with good results (Harvey & Luketina, 2014; Nishar et al., 2016; Marwan et al., 2021). This technique has proven its capability to calculate heat loss, with the potential of becoming a key tool for geothermal applications (Harvey et al., 2016).

In the case of narrowband hyperspectral TIR, mineral detection and mapping have been the main focus of the applications. Besides readily mappable minerals using VNIR and SWIR, TIR domain con further detect silica-bearing minerals and phosphates, elements representative of geothermal areas (Van der Meer et al., 2012; Calvin et al., 2015; Ninomiya & Fu, 2019). Due to the emissivity caused by the vibration modes of Si-O, S-O and C-O (Notesco et al., 2016). For this application with TIR data, SEBASS airborne platform have been the most used, in areas with scarce vegetation (Reath & Ramsey, 2013; Ninomiya & Fu, 2019; Hewson et al., 2020).

Sulphate minerals including alunite and jarosite have characteristic absorption bands in both VNIR/SWIR and TIR regions (Kruse et al., 2011; Laukamp et al., 2021). Alunite at 9,000 nm and jarosite at 9,100 nm and a broader feature around 9,800 nm, as well as at 10,990 nm (Bishop & Murad, 2005; Rowan et al., 2006) can be diagnostic for mapping surface alteration within geothermal fields (Kruse et al., 2011; Kraal et al., 2018). Oxide minerals such as goethite present a doublet absorption feature within 11,000-13,000 nm (Eismann, 2012) aiding accurate identification. Those have been the subject of mapping studies using airborne platforms, such as the Spatially Enhanced Broadband Array Spectrograph System (SEBASS) (Salton Sea, USA (Reath & Ramsey, 2013) and other geothermal areas of USA (Vaughan et al., 2003, 2005)). Also with hand-held platforms like FTIR (Bishop & Murad, 2005; Calvin et al., 2015).

Clay minerals including kaolinite, montmorillonite, illite/smectite, have spectral features at 8,840, 9,400, 9,900, 10,500 and 11,000 nm (Rowan et al., 2006; Eisele et al., 2015; Abera, 2018). Identification has been proven with airborne platforms such as MODIS/ASTER airborne simulator (MASTER) and SEBASS (Steamboat Springs, USA (Vaughan et al., 2005)) and Airborne Hyperspectral Scanner (AHS) in Czech Republic (Notesco et al., 2014). As well as ground FTIR sensors in Australian samples (Eisele et al., 2015) and laboratory measurements resampled to ASTER satellite parameters (Rowan et al., 2006) with good results.

Silicate minerals, such as quartz and its polymorphs, present absorption features between 8,000-9,000 nm, including a characteristic narrow doublet feature at 8,600 nm (Sabins, 1999; Eismann, 2012; Kruse, 2014). Identification has been proposed via satellite platforms like ASTER

(Cuprite Nevada, USA (Kruse, 2014) and Reko Diq, Pakistan (Rowan et al., 2006)). As well as with airborne platforms like Thermal Infrared Multispectral Scanner (TIMS) (Cuprite Nevada, USA (Hook et al., 1992)), Hyperspectral Thermal Emission Spectrometer (HyTES) (Davis-Schrimpf, USA (Qudsi & Noor, 2022)) and SEBASS (USA, (Vaughan et al., 2003). Feldspars of different compositions can be distinguished only with thermal infrared, as shown by laboratory analyses (Hecker et al., 2010; Nyahucho, 2020). For example, alkali feldspars can be differentiated along the 12,500-14,300 nm, where microcline shows two spectral features while albite show four spectral features (Salje et al., 1989; Zhang et al., 1997; Hecker et al., 2010).

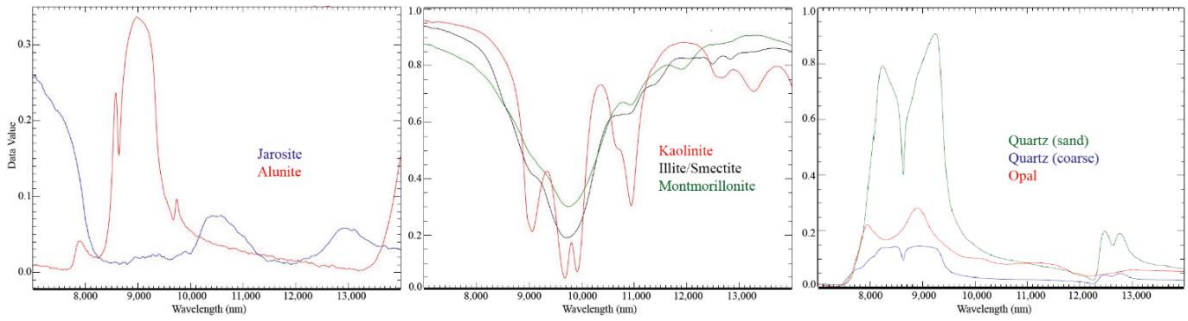

Figure 2.6. Spectral signature for minerals characteristic of geothermal areas within the narrowband TIR spectral range. Y-axis data value corresponds to reflectance.

2.4 Plant biogeochemistry

There is a wealth of information which can be retained by plant chemistry, yet, utilization of this source of information in geothermal and mineral exploration as well as remediation, has only started to take place in the last 50 years (Dunn, 2011; Cohen et al., 2021). Biogeochemistry involves the analysis of plant tissues to assess mineralization, bedrock composition and structure, chemistry of soils, and groundwater (Cohen et al., 1987; Kovalevsky, 1987) with the assumption that plant chemistry can be related to such underlying systems, due to their extensive root system, which "samples" large volumes of soil and groundwater (Cohen et al., 1987). Biogeochemistry is often completed in the field and samples are analysed in the laboratory by standard wet chemistry methods, such as Inductively Coupled Plasma Mass Spectrometry (ICP-MS) (Maity et al., 2011; Müller et al., 2013; Zhao et al., 2015; Wang et al., 2017), Inductively Couples Plasma Optical Emission Spectroscopy (ICP-OES) (Shtangeeva et al., 2011; Dunn & Christie, 2019), X-ray absorption spectroscopy (XAS) (Shahid et al., 2017), and X-ray fluorescence spectrometry (XRF) (Rincheval, 2019; Cohen et al., 2021). Toxic elements such as Ag, As, Ba, Cd, Hg, Pb, Sb, Ti and Zn can be uptaken by plants and eventually cause plant stress (Sridhar et al., 2005; Tschan et al., 2009; Cox et al., 2016; Farooq et al., 2016; Li et al., 2018; Sleimi et al., 2021). These elements are transferred via

their root system to the rest of the plant (Bech et al., 1997; Dunn, 2011; Shahid et al., 2017). Naturally, each area has different ambient chemical and environmental conditions for plants, which may favour the migration of elements, solution, diffusion, electrochemical cells, bacterial movements and others (for more detail please refer to (Dunn, 2011; Kovalevsky, 1987)). In the same manner, plant species are characterised by various rates of element uptake and transfer mechanisms (Wójcik et al., 2014; Rincheval, 2019).

Geothermal fields present a variety of conditions that can manifest stress in plants, including high temperatures, acidic and nutrient-depleted soils, elevated amounts of chemical elements (e.g. Ag, As, Sb) and water stress (Way & Hall, 2001; Van Manen & Reeves, 2012; Pippucci et al., 2015). Plants living in geothermal areas have been reported to show physical changes such as growth inhibition (e.g. smaller height, slower growth, lower plant density) (Burns, 1997; Bateson et al., 2008; Saepuloh et al., 2021; Zaini et al., 2022). Chemically, plants decrease their photosystem efficiency, which can damage their biomembranes and stomatal conductance (Manzo et al., 2013; Pippucci et al., 2015). Spectral changes in stressed geothermal vegetation have been attributed mainly to high temperatures (Burns, 1997; Mia et al., 2014; Putri et al., 2021; Saepuloh et al., 2021; Zaini et al., 2022). Nevertheless, high concentrations of Sb, S, As and Cd, also cause changes in spectral properties of the plant canopy (e.g. red-edge shifting towards the blue due to decreasing chlorophyll contents (Manzo et al., 2013; Rathod et al., 2018)), however, these relationships have mostly been proven only in controlled experiments (Féret et al., 2011; Noomen et al., 2006; Rathod et al., 2013; Shi et al., 2016; Rathod et al., 2018). The uptake of certain elements (e.g. As, Sb, U) is also of interest for mineral exploration, as arsenic is known to mineralize with gold and uranium. The uptake of arsenic, antimony and cadmium has also been studied for remediation purposes (Kovalevsky, 1987; Craw et al., 2007; Rascio & Navari-Izzo, 2011; Feng et al., 2013; Rathod et al., 2013). Acidic conditions and high native element concentrations have been remotely detected using Normalised Difference Vegetation Indices (Way & Hall, 2001; Mia et al., 2012, 2014) and Red Edge shifts (Way & Hall, 2001). While water stress detected by changes in the infrared region (e.g. 900-970 nm) (Hunt & Rock, 1989; Champagne et al., 2001; Poblete et al., 2020; Zeng et al., 2022), can assist to determine near-surface wetness conditions (Harris et al., 2005) or drought effects (Hunt et al., 1994).

Leaf pigments in the palisade mesophyll, chlorophyll a, b and B-carotene can be detected in the visible range (VIS, 350–700 nm) (Sims & Gamon, 2002; Sanches et al., 2013; Jensen, 2015). Leaf chlorophyll is one of the first pigments to degrade, causing a reflectance increase within red wavelengths and when carotenoids degrade, an increase in leaf reflectance within blue wavelengths takes place (Van der Meer & de Jong, 2001). Scattering in the spongy mesophyll, stomatal closure

and damage to cellular membranes is detected in the near infrared (NIR, 700 – 1,300 nm) (Suwa et al., 2008; Kabata-Pendias, 2010; Finnegan & Chen, 2012; Jensen, 2015). Changes in these two regions (VIS-NIR) have been associated with metal and thermal stress (Slonecker et al., 2009; Rathod et al., 2015, 2018). Leaf water content changes can be detected around 940–2,600 nm (Jensen, 2015), with maximum sensitivity around 940, 1,450, 1,940 and 2,500 nm (Carter, 1993; Champagne et al., 2001). Furthermore, TIR has been found to indicate water stress using indices like the Crop Water Stress Index (CWSI) or the Leaf Water Content (LWC) (Sepulcre-Cantó et al., 2006; Berni et al., 2009; Poblete et al., 2020).

High temperature environments can also cause stress in plants detectable through remote sensing. As an indicator of the occurrence and drought severity (Bhuiyan et al., 2017; Dhawale & Paul, 2018), the effect of extreme climate changes (Ryu et al., 2020; Morfopoulos et al., 2022) or urban land surface temperatures (Worku et al., 2021). The physical effect of elevated soil temperatures on plants has been reported in other field studies, as plant height decreases as soil temperature increases in geothermal areas (Given, 1980; Burns & Leathwick, 1995; Smale et al., 2018), and roots start growing in a horizontal manner (Van Manen & Reeves, 2012).

In New Zealand, geothermally heated soils have a combination of endemic vegetation including, kanuka (*kunzea ericoides*), moss (from the *Campylopus* spp.), liverworts (of the *Dicranoloma* spp.) and lichens (*Caladonia capitellata* and *Cladia leptoclada*) (Given, 1980; Burns & Leathwick, 1995; Burns, 1997; Smale & Fitzgerald, 2015; Beadel et al., 2018). One of the dominant species is kanuka, a bush with the capacity to live in hot and acidic soils depleted of nutrients (Moyersoen & Beever, 2004). Partially benefit from a relation with Pisolithus ectomycorrhizas fungi, which associates with kanuka on hot (50 °C at 8 cm depth), highly acidic and N depleted soils (Moyersoen & Beever, 2004; Orlovich & Cairney, 2004), possibly assisting kanuka (Robinson et al., 2006) as other bacteria and fungi do with other plants, to uptake elements beyond their natural barrier (Kovalevsky, 1987; Macur et al., 2004; Liu et al., 2006; Filella et al., 2007; Feng et al., 2013). Kanuka's chemical concentration for elements characteristic of near-neutral waters in geothermal areas (e.g. Waiotapu) has been studied before, finding high concentrations of Au, As, and Sb (Dunn & Christie, 2019). Vegetation and fungi are not the only biological entities of relevance in geothermal areas, there are also lichen species that uptake trace elements (e.g. As, B and Hg) (Burns & Leathwick, 1995; Loppi & Bargagli, 1996; Bennett & Wetmore, 1999) and resist hot grounds (Glime & Iwatsuki, 1990; Fahselt, 1995; Ward et al., 2000). Microorganisms in water springs with thermophilic capacities (Brock, 1978) or the capability to oxidize and reduce elements (e.g. sulphur compounds, iron ions, manganese ions) (Sand, 2003; Hetzer et al., 2007). These microbial life forms reflect the origin of life on Earth and a

possible analogue for other planets (Russell & Hall, 1997; Preston et al., 2008; Pirajno, 2009), adding relevance to understanding their behaviour in such environments.

3 Chapter 3. “Lithological mapping of Waiotapu Geothermal Field (New Zealand) using hyperspectral and thermal remote sensing with ground exploration techniques”

- This chapter has been submitted, reviewed and published in *Geothermics* (Elsevier), under the same title. DOI: 10.1016/j.geothermics.2021.102195

  Contributing authors:

  - **Cecilia Rodriguez-Gomez** (School of Agriculture and Environment, Massey University, Palmerston North, New Zealand): Conceptualisation, Methodology, Programming, Investigation, Formal analysis, Visualisation, Writing – Original Draft, Writing – Review & Editing.
  - **Gabor Kereszturi** (School of Agriculture and Environment, Massey University, Palmerston North, New Zealand): Conceptualisation, Methodology, Investigation, Writing – Review & Editing, Supervision, Funding acquisition, Project administration.
  - **Robert Reeves** (GNS Science, Wairakei Research Centre, Taupo, New Zealand): Supervision, Investigation, Writing – Review & Editing.
  - **Andrew Rae** (GNS Science, Wairakei Research Centre, Taupo, New Zealand): Supervision, Investigation, Writing – Review & Editing.
  - **Reddy Pullanagari** (MAF digital Lab, School of Food and Advanced Technology, Massey University, Palmerston North, New Zealand): Supervision, Investigation, Writing – Review & Editing.
  - **Paramsothy. Jeyakumar** (School of Agriculture and Environment, Massey University, Palmerston North, New Zealand): Supervision, Investigation, Writing – Review & Editing.
  - **Jonathan Procter** (School of Agriculture and Environment, Massey University, Palmerston North, New Zealand): Supervision.

3.1 Introduction

Geothermal exploration has aimed to spatially and temporarily characterise geothermal surface features linked to their subsurface hydrogeological system. When characterising surface alteration types various techniques have been used in the past, such as geological techniques (Calvin et al., 2015; Giordano et al., 2013; Lagat, 2007; Mauriohooho et al., 2014; Simpson & Rae, 2018), geochemical techniques (Blasco et al., 2018; Bobos & Williams, 2017; Burgos, 1999; Harvey et al., 2017), and geophysical techniques (Bibby et al., 1994; Calvin et al., 2005; Hochstein & Soengkono, 1997; Mongillo, 1994; Reeves & Rae, 2016; Seward et al., 2018). However, it is often a combination of these exploration techniques that provides extensive and in-depth information on geothermal systems.

Remote sensing can support delineation of hydrothermal alteration zones and minerals, thermal anomalies and tectonic features, by employing classification algorithms, regressions models and image threshold approaches (Han et al., 2018; Haselwimmer & Prakash, 2013; Rajesh, 2004; Reeves & Rae, 2016; Van der Meer et al., 2012; Vaughan et al., 2010; Watson et al., 2008; Yang et al., 2000). Geothermal development represents a significant investment cost, with a considerable 42% of the total cost being related to exploration (Jennejohn, 2009; Shortall et al., 2015). Remote sensing techniques can effectively reduce the cost and time of initial reconnaissance surveys of larger areas faster and cheaper than ground-based mapping alone (Bakker et al., 2009; Bedell et al., 2017; El Bouazouli et al., 2019; Jones et al., 2010; Noorollahi et al., 2005; Rathod et al., 2013). Furthermore, remote sensing technology can reach countries where the economic and location circumstances inhibit geothermal exploration surveys.

Optical remote sensing techniques measure electromagnetic energy reflected, emitted or scattered by an object without physical contact (Bakker et al., 2009; Clark, 1999). In particular, hyperspectral remote sensing has a great value due to their narrow and contiguous bands, which can be used to characterise alteration mineralogy in scarcely vegetated geothermal systems (Hellman & Ramsey, 2004; Kratt et al., 2006). Visible-Near Infrared (350-1,300 nm, VNIR) and Shortwave Infrared (1,300-2,500 nm, SWIR) hyperspectral sensors acquire spectral information, which allows for the detection of sulphates (e.g. alunite, jarosite, gypsum), phyllosilicates (e.g. kaolinite, montmorillonite, illite, micas) and carbonates (e.g. calcite, siderite) (Calvin et al., 2015; Kereszturi et al., 2020; Kratt et al., 2006; Swayze et al., 2014; Van der Meer et al., 2018; Zhang & Li, 2014). Silica, opal and quartz are other relevant and distinctive mineralisation products of geothermal areas that have particular absorption features in the Thermal Infrared (TIR) region of the spectrum, detectable with hyperspectral sensors (Aslett et al., 2018; Feng et al., 2018; Vaughan et al., 2003). The

identification of these minerals along with their spatial distribution, in combination with surface temperature data, can reveal the spatial extension of the hydrothermal system, subsurface hydrogeology, and energy production potential (Calvin & Pace, 2016; Nash et al., 2004; Wisian et al., 2001).

This study aims to delineate surface hydrothermal alteration patterns using ground and airborne hyperspectral (350-2,500 nm, VNIR/SWIR), and single channel broadband TIR (7,500-13,000 nm) remote sensing data over the Waiotapu Geothermal Field in New Zealand. The remote sensing approach proposed here is complemented by VNIR/SWIR spectroscopy, Inductively Coupled Plasma Mass Spectrometry (ICP-MS) for bulk rock composition, and Scanning Electron Microscopy (SEM)-Energy Dispersive X-Ray spectroscopy (EDX) from soil and rock samples, to characterise a heavily vegetated geothermal field. The ground data is to assist airborne remote sensing imagery classification and to understand the different mineral alterations and depositions occurring throughout the system. The combination of the analyses contributes to the understanding and monitoring of Waiotapu Geothermal Field, by a non-invasive surface exploration approach.

3.2 Geological Setting

The Waiotapu Geothermal Field is located in the Taupo Volcanic Zone (TVZ) and is the largest out of the more than 20 geothermal systems within the TVZ based on surface feature area extension (~18 km^2) and heat flow (~500 MW) (Figure. 3.1) (Barker et al., 2020; Benseman et al., 1963; Bibby, Glover, et al., 1995; Hedenquist, 1991; Hedenquist & Browne, 1989; Hochstein, 2007; Kaya et al., 2015; Lloyd, 1959; Milicich et al., 2020). The TVZ basement consists of a sedimentary weakly metamorphosed rock referred to as ‘greywacke’, more specifically Torlesse Composite Terrane, subunit Kaweka Terrane (Milicich et al., 2020), overlaid by extensive layers of ignimbrite and sediments (Grindley et al., 1994; Steiner, 1963). The TVZ is characterised by extensive rhyolitic and basaltic volcanism and associated geothermal activity due to the overall high geothermal gradient. The volcanic activity is related to the subduction of the Pacific plate under the Australian plate, also causing normal faulting with a NE-SW orientation (Milicich et al., 2020; Wilson & Rowland, 2016).

Even though little evidence exists for active faulting at Waiotapu Geothermal Field, the alignments of surface manifestation of hot spring and explosion craters generally follow a NE-SW trend (Hedenquist & Henley, 1985; Mongillo, 1994). The closest mapped active fault zone is the Paeroa Fault, ~10 km Southwest, extending from the Ngapouri Fault southward to the northern rim of Reporoa caldera (Wood, 1994). Permeability is associated with faulting and fluid flow, which can be reflected in the intensity and type of mineral alteration (Browne, 1978). At Waiotapu Geothermal

Field, faulting and fractures can increase some vertical permeability while the host rock has a high intrinsic horizontal permeability, allowing fluids to move south and west from the heat source (Hadfield et al., 2001; Hedenquist, 1982; Kaya et al., 2015; Mongillo, 1994; Wood, 1994), to finally drain into the Waiotapu Stream, which flows to the south and joins the Waikato River (Lloyd, 1959).

Waiotapu is hosted by Oruanui and Rangitaiki Ignimbrite closest to the surface of a series of pyroclastic flows from rhyolitic eruptions (Cole, 1990; Ritchie, 1996; Wood, 1994). These are often interlayered with lacustrine sediments of the Huka Group Formation, which act as a litho cap of the hydrothermal system (Kaya et al., 2014). Deep chloride-rich fluid heats up and rises, interacting with groundwater which causes irregular acidic alteration patterns (Hedenquist, 1982; Hedenquist & Browne, 1989). The fluids and host rock interactions resulted in a variety of surface features, including steaming ground, fumaroles, collapse and hydrothermal eruption craters, silica deposits and sinters, mud pools, hot chloride pools, sulphur-chloride and bicarbonate-chloride springs (Grange, 1937; Hedenquist & Browne, 1989; Hunt et al., 1994; Lloyd, 1959).

Waiotapu Geothermal Field has often experienced changes in the groundwater table level due to pressure changes (more detail in (Hedenquist & Browne, 1989; Lloyd, 1959)), forcing a spatial shift in springs depositing sinter. Occasionally, hydrothermal eruptions can occur, including one of the most prominent surface features of Waiotapu Geothermal Field, the Champagne pool, now filled with chloride-rich thermal waters (Gallagher et al., 2020; Hedenquist & Browne, 1989). The Champagne pool currently deposits silica sinter enriched in, gold and silver with native sulphur and antimony sulphides on the rim (Simmons et al., 2016).

The argillic alteration from steam-heated waters occurs in the northern part of the system (Hedenquist & Browne, 1989) forming a suite of secondary minerals such as cristobalite, kaolinite, alunite, sulphides and native sulphur associations (Hedenquist, 1991). The southern part of the system hosts at the water table level, neutral pH high-chloride waters and silica sinter (Pirajno, 2009), which combine with the prevailing acid-sulphate features (Hedenquist, 1991).

Furthermore, the present surface cover is dominated by dense scrub vegetation (Cochrane et al., 1994; Deroin et al., 1995; Given, 1980; Mia et al., 2012), limiting hydrothermal lithological mapping to windows of rock outcrops proximal to geothermal surface features. The most abundant plant species are kanuka (*Kunzea ericoides var. microflora*), ferns (e.g. *Hypolepis* species) and some moss species (e.g. *Campylopus pyriformis)* (Beadel et al., 2018; Burns & Leathwick, 1995; Smale & Fitzgerald, 2015).

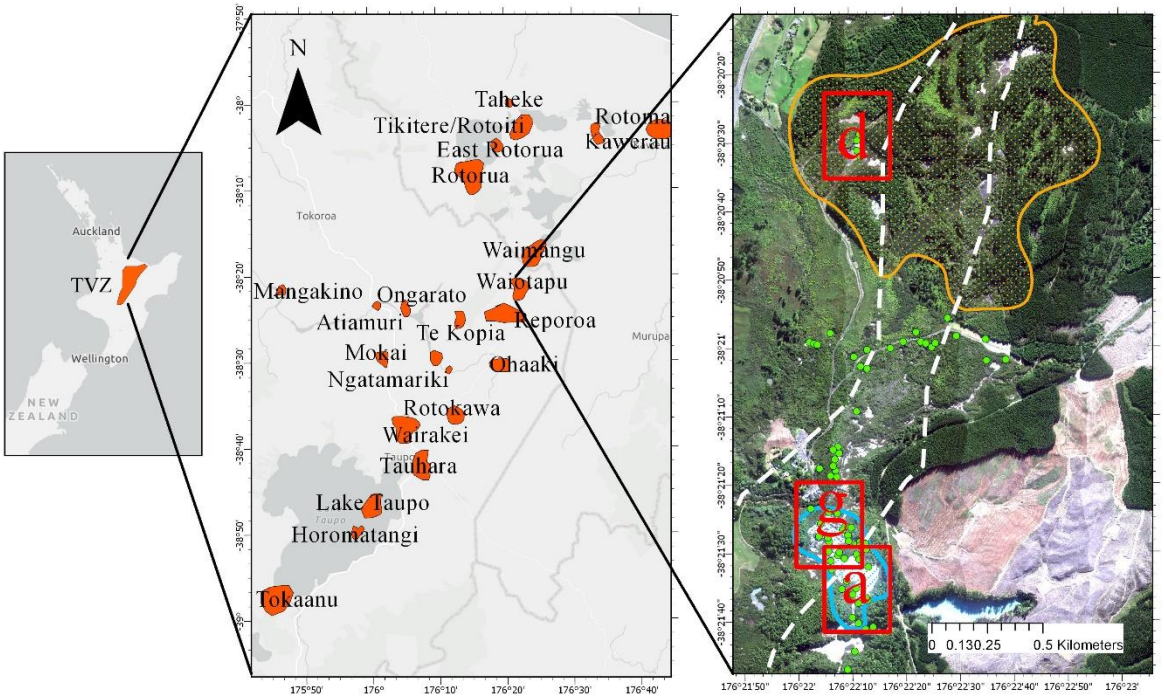

Figure 3.1. Waiotapu Geothermal Field location in New Zealand North Island, within the TVZ geothermal fields. White dash lines represent normal faults Ngapouri and Paeroa, green points sampling sites. Chloride-rich surface features located inside the blue filled area and acid-sulphate features are prominent inside the orange area. Red squares (a,d,g) refer to Figure 3.9 close-ups.

3.3 Data and Methods

3.3.1 Airborne Hyperspectral Data Collection and Instrumentation

Hyperspectral airborne imagery was captured using an AisaFENIX push-broom, full-spectrum instrument mounted on a Cessna 185 aircraft. It acquires data from 0.38 to 2.5 µm, collecting 448 spectral bands with a ground resolution of 1 m (for more details (Kereszturi et al., 2018; Pullanagari et al., 2016)). The aerial survey was carried out in a North-South direction between 11:20 to 12:59 local time on 13 April 2019 (UTC +12 hrs), with only 10 hours difference from the thermal infrared image acquisition flight at night.

The data pre-processing included radiometric corrections using CaliGeoPro, followed by atmospheric corrections in ATCOR-4 (Richter, 1998), and geo-rectification in PARGE (Schläpfer & Richter, 2002). The individual image strips were then mosaicked into a full data cube. Exposed soil and rock versus vegetation was selected using 0.4 as a threshold value for the Normalised Difference

Vegetation Index (NDVI). The airborne hyperspectral data had some noise due to atmospheric interferences (1.9-2.1 μm) which was removed, and a neighbourhood derivative spectral smoothing was applied.

3.3.2 Thermal Infrared Remote Sensing, Spatial Change Analysis

The airborne Thermal Infrared (TIR) image was captured on 13 April 2019 at night between 20:30 and 23:30, with a FLIR A615 TIR sensor by GNS Science (details in, Reeves & Sanders, 2019). The night acquisition can minimise solar heating and solar reflection effects on the ground surface (Seward et al., 2018). A linear temperature calibration from water bodies measured at the time of the TIR survey was applied to the image to get absolute temperature values (for more detail Reeves and Sanders, 2019). However, it is important to note as temperatures are calibrated to water, caution is advised when examining other surface temperatures (i.e. soil and rock). The thermal imagery was used to assess the surface temperature spatial change of soil and rock for different hydrothermally deposited and altered zones through qualitative analyses.

3.3.3 Image Classification

Supervised classification approaches were utilised in this study using training samples (Ghamisi et al., 2017). Labelled class data were selected as polygons using field observations, hyperspectral imagery and high-resolution RGB photographs. 10 Classes were selected (Table A1.3) based on field data and spectral variability; dry silica, wet silica, water, river water, other water, champagne pool outflow, host rock rich, kaolinite dry, kaolinite wet and soil with vegetation. A variety of water classes were selected as the suspended particles and the level of microbial contained in them create a range of spectral reflectance profiles (Table A1.3). Differentiation between dry and wet mineralogy groups was also relevant for a correct classification as water considerably affects the SWIR portion of the spectral signature. The labelled class data were then subsetted randomly, on polygonal bases into 70% for training and 30% to test the classification accuracy. We used per-class and overall accuracies along with confusion matrices to assess the accuracy and F1-score of each classification (Foody, 2020).

Two commonly used classification algorithms were used, Spectral Angle Mapper (SAM) and Support Vector Machine (SVM). SAM is a pixel-based technique which measures the similarity of an image pixel to a reference spectrum and calculates the angle between two spectra, treating them as vectors in a space with dimensionality equal to the number of input bands. SAM has been widely used for surface classifications with good results (Asadzadeh & de Souza Filho, 2016; Debba et al.,

2005; Kruse et al., 1993; Van der Meer, 2018), but does not take into account the spectral variability inherent from many rocks (Zhang & Li, 2014).

SVM is a non-parametric machine learning classification algorithm based on statistical learning theory. It constructs a model based on the training data that are used to make predictions about the unknown data sets. With a linear or non-linear hyperplane in a multidimensional space which best separates the labelled classes data (Gewali et al., 2018; Varshney & Arora, 2004). In this case, to create a non-linear decision boundary a radial basis function kernel was applied. SVM can produce a high classification accuracy regardless of small training data sets in comparison to the predicted data set (Mountrakis et al., 2011).

3.3.4 Rock and Soil Spectral, Chemical and Scanning Electron Microscope (SEM) Analysis

In total, 74 soil and rock samples were collected a week after the imagery, to complement and serve as ground truth information. Soil or rock samples were collected to represent features of Waiotapu Geothermal Field, including a range of typical mineral alteration styles (Figure 3.1). The 74 samples were left to dry at ambient temperature (~17 °C) for 2 to 3 days, ground and sieved through a 1 mm mesh before laboratory based spectral acquisition and chemical analyses. Analytical Spectral Devices (ASD) Fieldspec High Resolution 4 was used to obtain the light reflectance properties of all samples at Massey University, calibrated to a white surface reference after 3 spot-measurements each with 5 measurements which were averaged. The elemental chemical concentration analysis was carried out with an Inductively Coupled Plasma Mass Spectrometer (ICP-MS), retrieving the chemical concentration of 53 elements (Table A1.1). Geochemical data are typically expressed in a form of compositional data (e.g. proportions, percentages), these types of data are constrained and require a transformation such as Centred Log-Ratio (CLR) to be suitable for statistical approaches (Aitchison, 1986, 2008; Muriithi, 2015). CLR was applied, and after a PCA to the chemical concentration values, elements with similarities (Smith, 1988), co-variation (Hood et al., 2019; McKinley et al., 2016) and possibly correlated within the geothermal system were selected.

A subset of 6 samples was prepared for SEM-EDS analysis as polished rock slabs. The rock samples were cut, mounted onto glass slides and then grounded to a thickness between 0.6 and 1 mm and polished for SEM analysis. Afterwards, the samples were carbon-coated and imaged using ThermoFisher Scientific FEI Quanta 200 Environmental Scanning Electron Microscope. This equipment works in backscatter electron (BSE) mode under an accelerating voltage of 20 kV and a working distance of ca. 10 mm, at Manawatu Microscopy and Imaging Centre - Massey University.

3.4 Results

Waiotapu Geothermal Field encompasses a complex combination of geothermal surface features, to gain an improved understanding of the system, ground samples are studied to better interpret remote sensing imagery. Therefore, ground samples were analysed to obtain their spectral signature, mineral characterisation and chemical element concentration. The mineral classification and hydrogeological processes derived from these techniques were compared to the classification obtained from the hyperspectral imagery and associated with the thermal infrared imagery. This comparison allowed an extensive understanding of the hydrogeological system and how well it is reflected by remote sensing approaches.

3.4.1 Hydrothermal Alteration Types from Ground Samples

The analysed soil and rock samples show a series of primary and secondary minerals that were identified by their absorption features in the VNIR/SWIR parts of the electromagnetic spectrum (Table A1.2). Furthermore, the hydrothermal alteration mineralogy has also been cross-checked with SEM-EDS analysis on selected samples. The samples can be classified into three main groups; silica-dominated, ignimbrite-dominated (host-rock) and acid-sulphate alteration, based on their dominant alteration mineralogy and original lithologies.

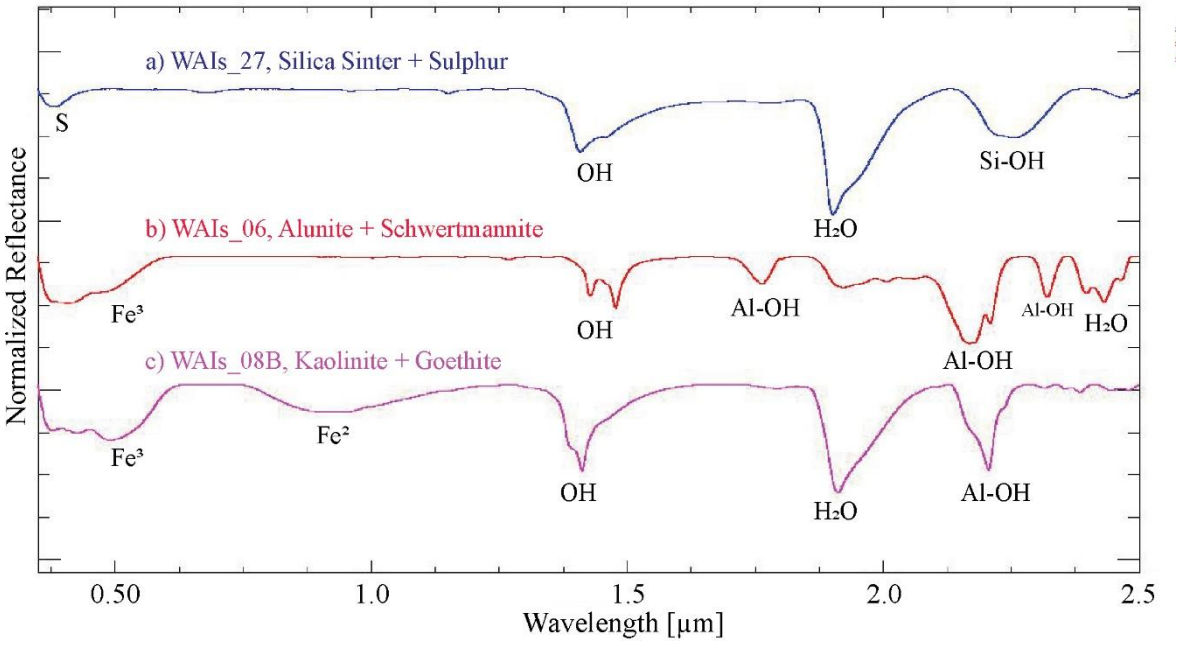

Figure 3.2. Spectral reflectance profiles for some mineral samples from Waiotapu.

The **silica-dominated group** includes quartz and its polymorphs with some minor native sulphur, which precipitates near chloride-rich features. Sample WAIs_27 from the silica sinter

terraces displays opal with the addition of the characteristic absorption feature of sulphur around 0.39 µm (Figure 3.2a). However, it is worth noting that silica-rich minerals can be limitedly detected by SWIR techniques due to their lack or broad absorption features. This group deposits from near-neutral pH chloride-rich waters spatially concentrated on the south of the system (Figure 3.1). Sinters are dominated by laminated layers of silica precipitates (Figure 3.3a), depositing silica in various rates and porosities, related to abiotic and biotic conditions of the environment (Handley et al., 2005). Some laminae from sample WAIs_27 include organic matter and silicified microbiome (Figure 3.3c-d). Northern areas of Champagne Pool, as well as south of silica sinter terraces, where Champagne Pool waters mix with Lake Whangioterangi have greater amounts of native sulphur precipitation on surface intermixed with quartz polymorphs neighbouring the near-neutral chloride-rich surface features (Figure 3.3b).

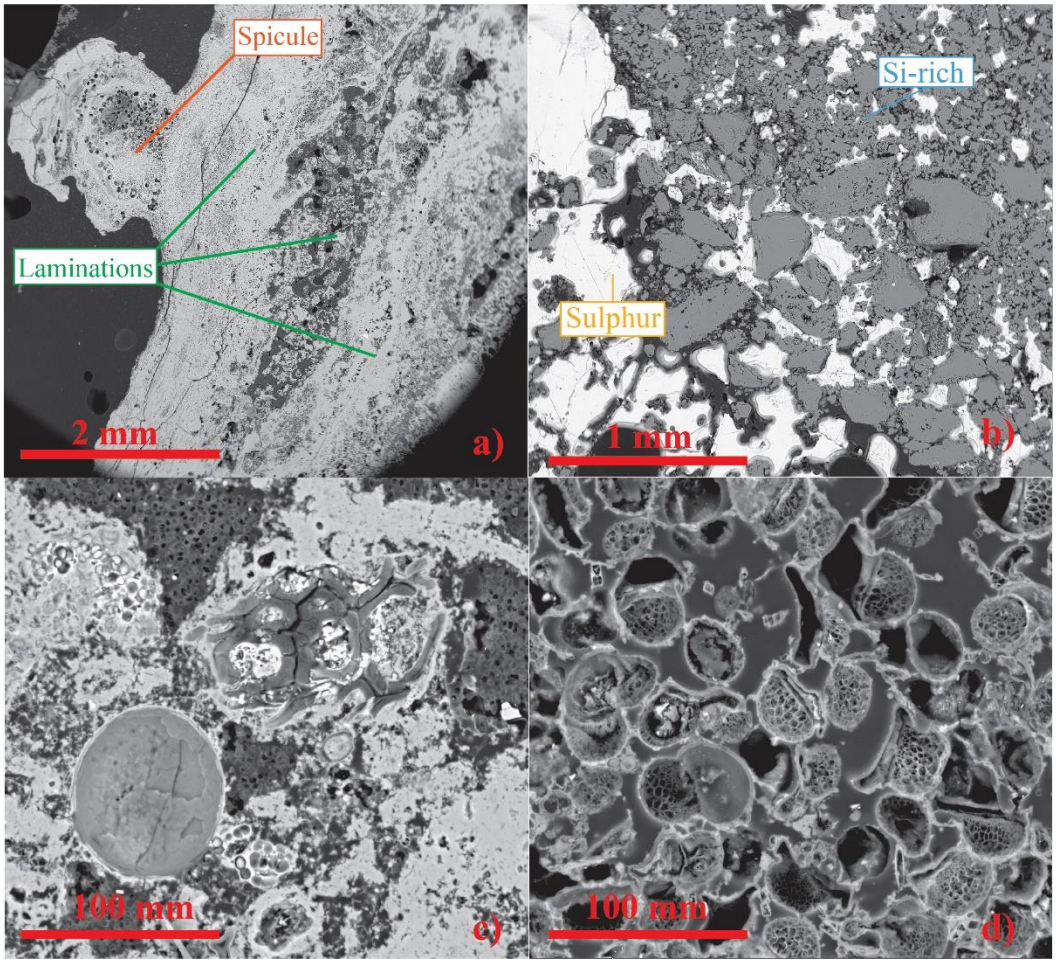

Figure 3.3. SEM from representative samples from the silica dominated region. a) Silica sinter sample displaying clear lamination and the formation of spicule on surface. b) Sample from a sulphur vent, formed by native sulphur and silica. c) Silica sinter sample containing microbiome matter. d) Silica sinter sample containing silicified microbiome.

The **ignimbrite-dominated group** comprises moderate to pervasively altered samples, with a range of opal/quartz polymorphs and phyllosilicate with occasional Fe oxides. Analysed sample WAIs_21 from Waiotapu Geothermal Field presents mild alteration, with extensive silicification and a homogeneous texture, encompassing quartz crystals (Figure 3.4). From spectroscopy analysis, we identify other samples that exhibit Fe oxide influence, observed in additional absorption features around 0.65 and 0.95 µm, corresponding to goethite and hematite minerals (Figure 3.2b) (Hunt & Ashley, 1979). The alteration to such minerals will be pH dependant, acidic (pH 0 to 4) and alkaline (pH = 10-14) favours the formation of goethite, while neutral pH favours the formation of hematite (Schwertmann & Murad, 1983). Both pH conditions exist within the fluids seen at Waiotapu (Giggenbach et al., 1994; Pope & Brown, 2014).

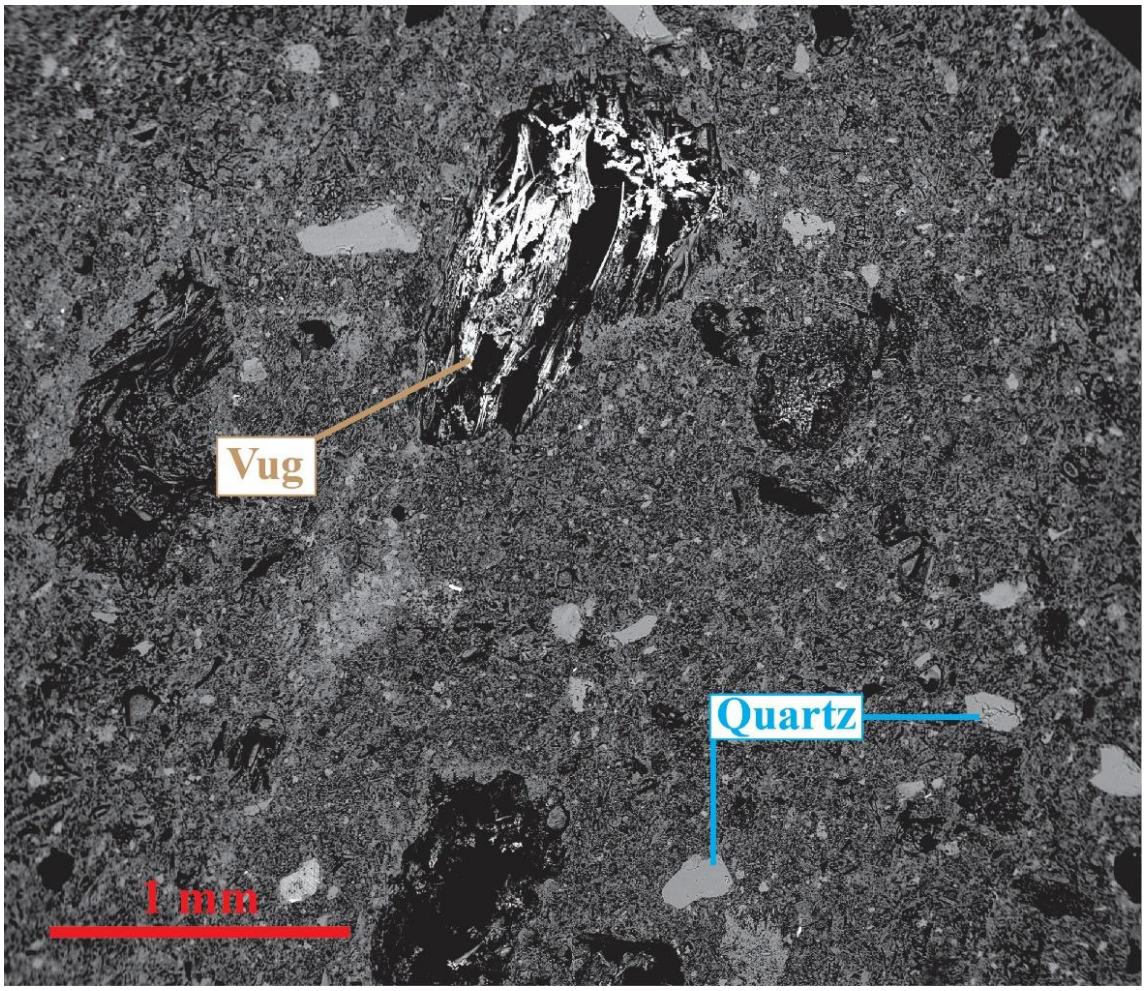

Figure 3.4. SEM-BSE image of sample WAIs_21, showing extensively silicified host rock with quartz crystals and vugs.

The **acid-sulphate alteration group** is typically characterized by kaolinite, alunite and jarosite alteration, mineral phases. These are formed by acid sulphate, steam-heated waters occurring

above the groundwater table (Dill, 2001; Hedenquist & Browne, 1989; Rye et al., 1992). From the spectroscopy analysis, we observe this mineral group shows typical absorption features show around 0.38, 0.43, 0.48, 0.94, 1.41, 1.91, 2.2 µm ±.02 µm (Figure 3.2a-b), consistent with phyllosilicates dominated by the kaolin group minerals from argillic alteration (John et al., 2008; Kereszturi et al., 2020; Sillitoe & Hedenquist, 2003). More details of absorption features and spectral matchings of samples on Table A1.2.

SEM imaging and energy-dispersive X-ray spectroscopy (EDS) from selected samples with different mineralogies display the complex acid-sulphate alteration taking place in Waiotapu Geothermal Field. These three samples reveal a variety of silica polymorphs in their possible form from the host rock but mostly forming the groundmass as recrystallized forms. A variety of alteration minerals have crystalized (alunite, baryte, Ti-rich, and pyrite) as pseudomorphs and by filling voids and fractures (Figure 3.6 and Table A1.2). Typically, alunite occurs void space with well-formed crystals of 10-200 µm across (Figure 3.5). The composition of alunite is typically potassium rich (Figure 3.5b-c).

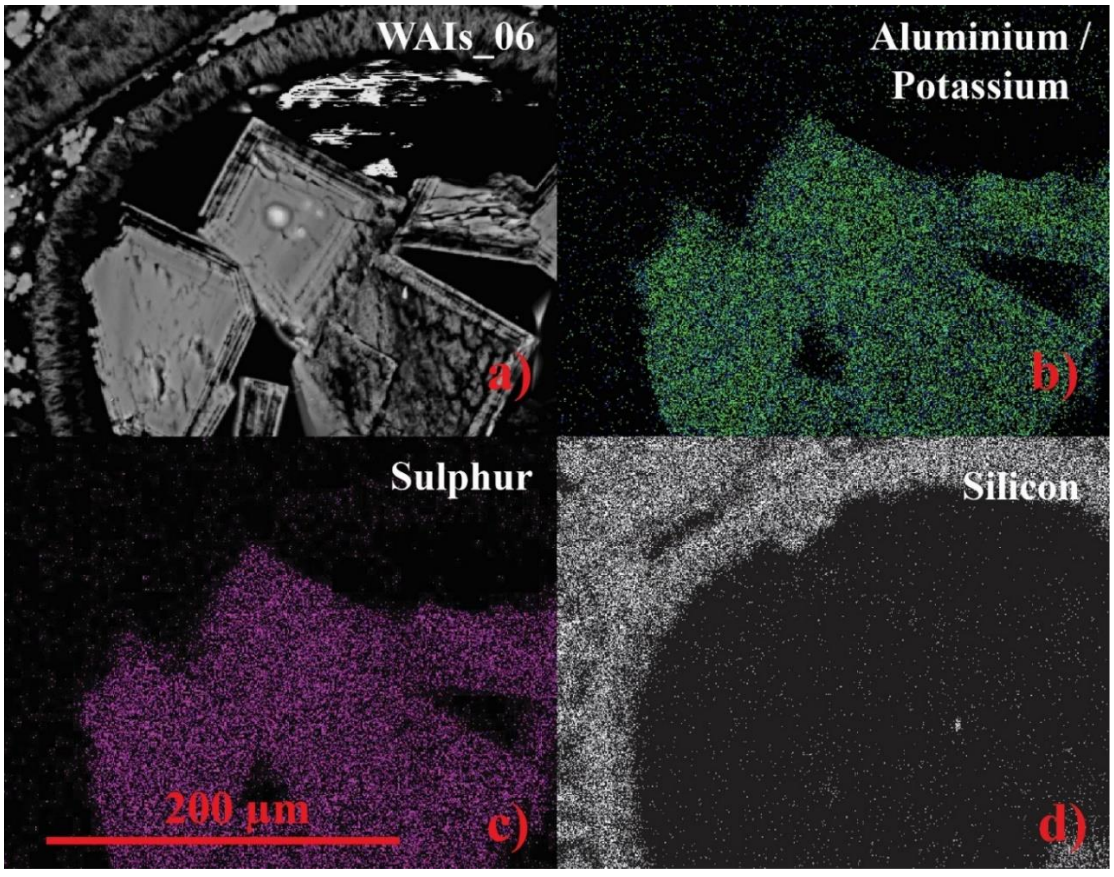

Figure 3.5. BSE image of the WAIs_06 sample showing well-developed void-filling alunite crystals (a) with EDS elemental maps for Al/K (b) S (c) and Si (d).

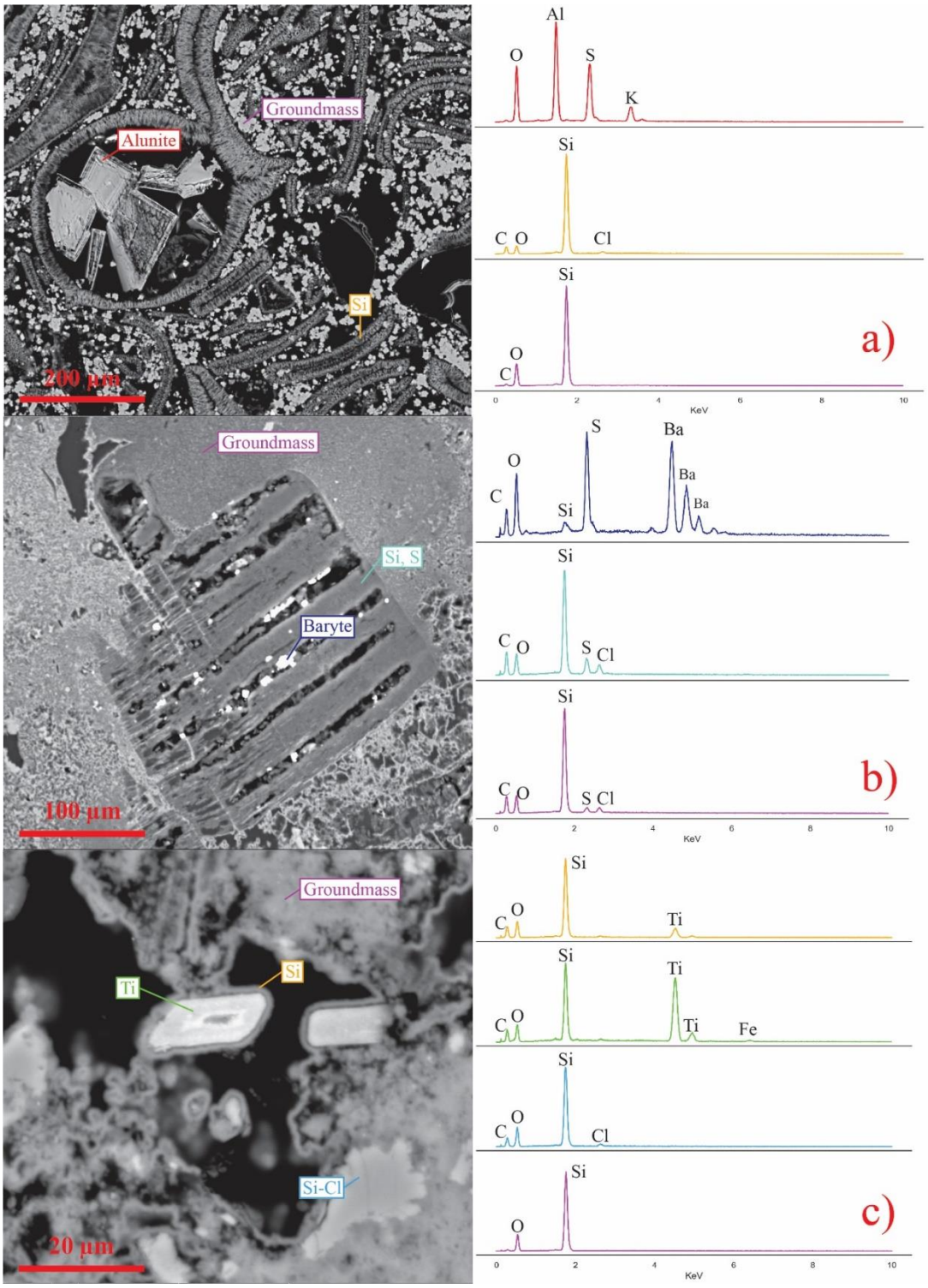

*Figure 3.6. SEM (left column) and EDS (right column) results for three samples representative from acid-sulphate alteration areas. Labelled EDS spots are colour coded. a) Sample WAIs_06 shows K-alunite crystals occupying voids with silica rich interior walls, as part of a recrystalised silica groundmass. b) Sample WAIs_22 shows silica and sulphur replacing a former crystal, with baryte precipitation occupying voids. c) Sample WAIs_*

Figure 3.6. 07 shows a Ti-rich alteration phase crystal with a silica rich rim, in a silica rich groundmass including quartz crystals.

3.4.2 Spatial pattern of elemental distribution and their co-occurrence

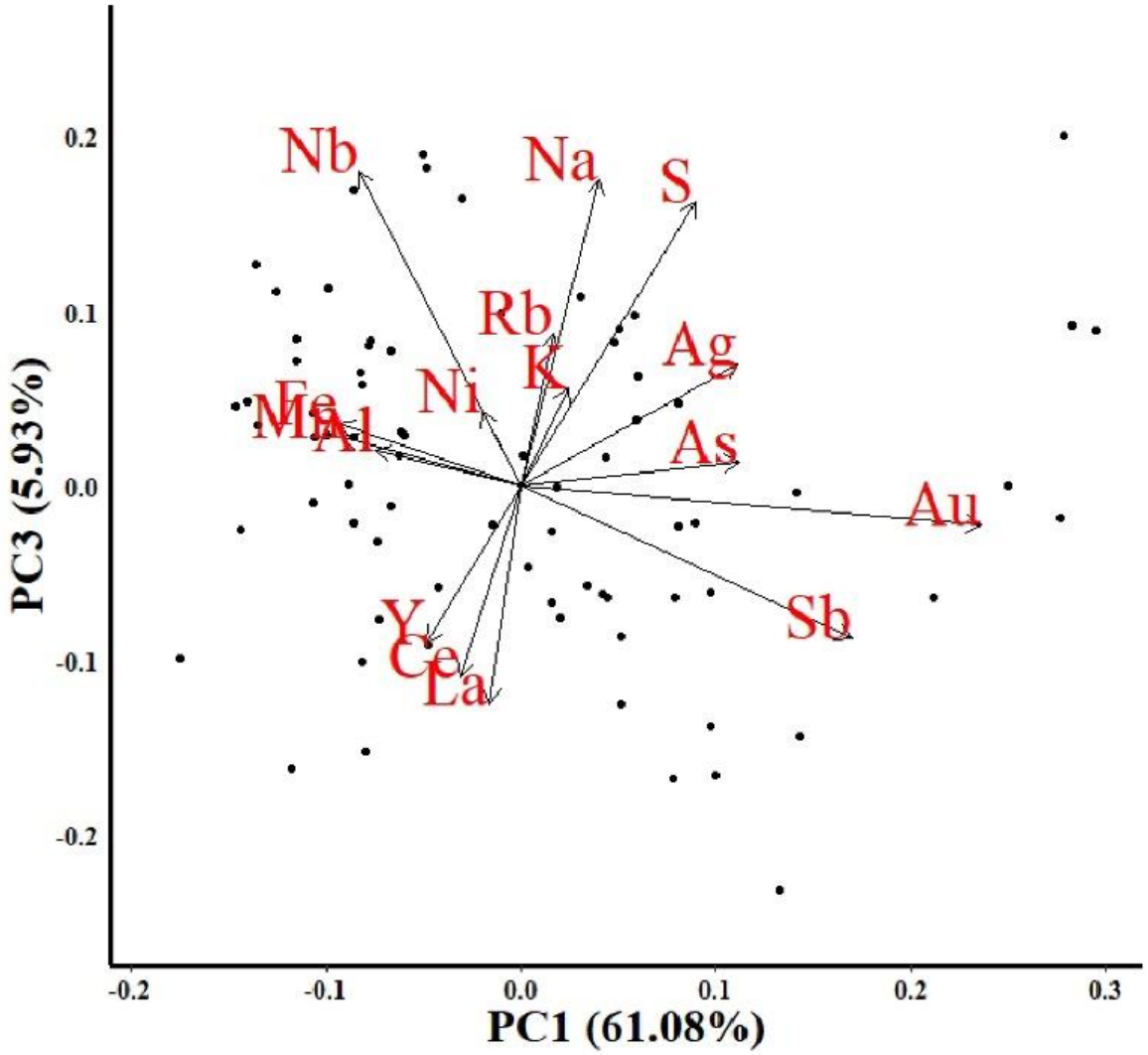

Figure 3.7. Principal Component Analysis of elemental compositions. Sb, Au, As, Ag and S can easily be grouped together along the PC1 positive direction.

The samples have been analysed for bulk chemical composition using ICPMS. The data returned 53 elements 36 of which are within detection limits (Table A1.1). Most of the elements did not show a high variance within samples, however, As (0.7 to >10000 mg/kg), Au (0.0001 to 3.28 mg/kg), and Sb (0.02 to 391 mg/kg) had large variance values and are elements associated within high-temperature geothermal systems (Hedenquist & Henley, 1985; Weissberg, 1969). Element concentrations were transformed using a Centred Log-Ratio (CLR) transformation, before analysing it with PCA. The PCA results show that Au, As, Sb and Ag are associated elements that follow a

similar behaviour and can be grouped together (Figure 3.7). Furthermore, those functional groups of elements also show spatial correlation when plotted as graduated circles depending on each element concentration (Figure 3.8). The spatial distribution shows higher concentrations around the southern part of the field, where the parent fluid (i.e. near-neutral pH, chloride-rich waters) reaches the surface. The most prominent example of such is Champagne Pool waters which flow downhill for about 250 m to Lake Whangioterangi outflow which flows into Lake Ngakoro (Figure 3.8).

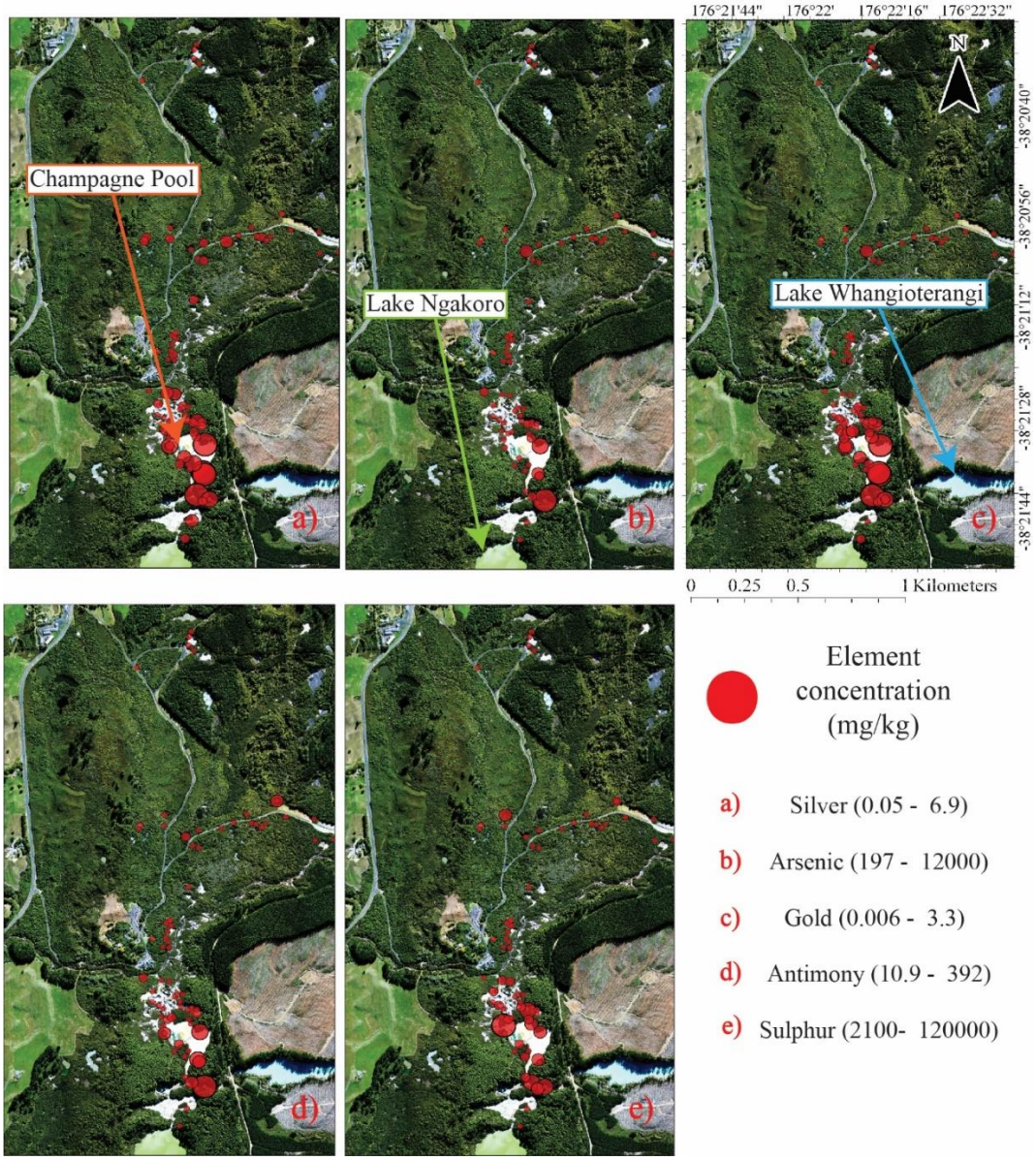

Figure 3.8. Waiotapu Geothermal Field spatial distribution of element concentrations (mg/kg) for silver (a), arsenic (b), gold (c), antimony (d) and sulphur (e). Element concentrations were measured with ICP-MS.

3.4.3 Remote Sensing Surface Characterisation and Thermal Spatial Distribution

The SAM and SVM image classifications both show high overall accuracies, with overall accuracies of 85.1% and 98.7% respectively. Both utilised the same training and testing data, which includes the three main hydrothermal mineral groups and a variety of water features (Table A1.3). The classifications were performed on a smoothed version of the hyperspectral imagery, mineral classes were selected with support of field observations and the mineralogical analysis of the collected ground samples. A variety of water classes were selected as great differences in colour and suspended sediment that affects the spectral reflectance considerably.

The easiest classes to discriminate by both algorithms are Soil / Vegetation, Dry Silica and Other Water (Tables 3.1 and 3.2). In contrast, Champagne Pool Outflow class is often misclassified as River Water, Other Water, by 0.22%, and 0.29% respectively in the SAM classification, and with Wet Silica and Wet Kaolinite classes, by 0.95% and 0.24% respectively in the SVM classification. This is principally due to the strong absorption of water in the SWIR region, which lowers the reflectance along this section of the spectrum (Table A1.3).

The lithological classes with regards to SVM display a more congruent spatial classification (Figure 3.8), as well as fewer misclassifications with other classes (Table 3.2). The training polygons for the Ignimbrite Dominated class are inherently mixed with different levels of mineral alteration, also their training spectral average displays similarities in absorption features around 0.90 and 1.40 µm, which could be causing confusion between Ignimbrite Dominated and Kaolinite Dry classes (Table 3.2). The most remarkable difference between SAM and SVM occurs within the kaolinite group, particularly visible in the mud pools located in the northern part of the system, correctly identified by SVM (Figure 3.9e-f).

Table 3.1. Error matrix for SAM, values are percentages and bold values show the percentage areas correctly classified.

Spectral Angle Mapper (SAM), Error Matrix (percentages)											
Class	Dry Silica	Wet Silica	Green Water	Water River	Champagne Pool Outflow	Ignimbrite Dominated	Dry Kaolinite	Wet Kaolinite	Soil / Vegetation	Other Water	Sum
Dry Silica	**8.79**	0.87	1.02	0.00	0.00	0.15	0.18	0.00	0.00	0.00	11.00
Wet Silica	0.00	**4.79**	0.00	0.00	0.00	0.00	0.00	0.04	0.00	0.00	4.83
Green Water	0.00	0.00	**11.18**	0.00	0.00	0.00	0.00	0.00	0.00	0.00	11.18
River Water	0.00	0.94	0.54	**6.97**	0.22	0.04	1.23	0.15	0.00	0.00	10.09
Champagne Pool Outflow	0.00	2.21	0.00	0.00	**8.13**	0.00	0.00	1.13	0.00	0.00	11.47
Ignimbrite Dominated	0.00	0.07	0.00	0.29	0.00	**10.09**	0.91	0.00	0.00	0.00	11.37
Dry Kaolinite	0.00	0.00	0.00	0.54	0.11	1.09	**4.94**	0.00	0.00	0.00	6.68
Wet Kaolinite	0.00	3.23	0.00	0.04	0.00	0.00	0.15	**6.50**	0.00	0.00	9.91
Soil / Vegetation	0.00	0.00	0.00	0.04	0.00	0.04	0.00	0.00	**8.17**	0.00	8.24
Other Water	0.00	0.00	0.00	0.00	0.29	0.00	0.00	1.85	0.00	**13.07**	15.21
Sum	8.79	12.13	12.75	7.88	8.75	11.40	7.41	9.66	8.17	13.07	100.00

Table 3.2. Error matrix for SVM, values are percentages and bold values show the percentage areas correctly classified.

Support Vector Machine (SVM), Error Matrix (percentages)											
Class	Dry Silica	Wet Silica	Green Water	Water River	Champagne Pool Outflow	Ignimbrite Dominated	Dry Kaolinite	Wet Kaolinite	Soil / Vegetation	Other Water	Sum
Dry Silica	**19.67**	0.00	0.00	0.00	0.00	0.00	0.00	0.00	0.00	0.00	19.67
Wet Silica	0.00	**11.45**	0.00	0.00	0.95	0.00	0.00	0.00	0.00	0.00	12.40
Green Water	0.00	0.00	**6.87**	0.00	0.00	0.00	0.00	0.00	0.00	0.00	6.87
River Water	0.00	0.00	0.00	**7.74**	0.00	0.00	0.08	0.00	0.00	0.00	7.82
Champagne Pool Outflow	0.00	0.00	0.00	0.00	**8.37**	0.00	0.00	0.00	0.00	0.00	8.37
Ignimbrite Dominated	0.08	0.00	0.00	0.00	0.00	**7.19**	0.00	0.00	0.00	0.00	7.27
Dry Kaolinite	0.00	0.00	0.00	0.16	0.08	0.16	**1.66**	0.32	0.00	0.00	2.37
Wet Kaolinite	0.00	0.00	0.00	0.00	0.24	0.00	0.00	**11.14**	0.00	0.00	11.37
Soil / Vegetation	0.00	0.00	0.00	0.00	0.00	0.08	0.00	0.00	**13.19**	0.00	13.27
Other Water	0.00	0.00	0.00	0.00	0.00	0.00	0.00	0.00	0.00	**10.58**	10.58
Sum	19.75	11.45	6.87	7.90	9.64	7.42	1.74	11.45	13.19	10.58	100.00

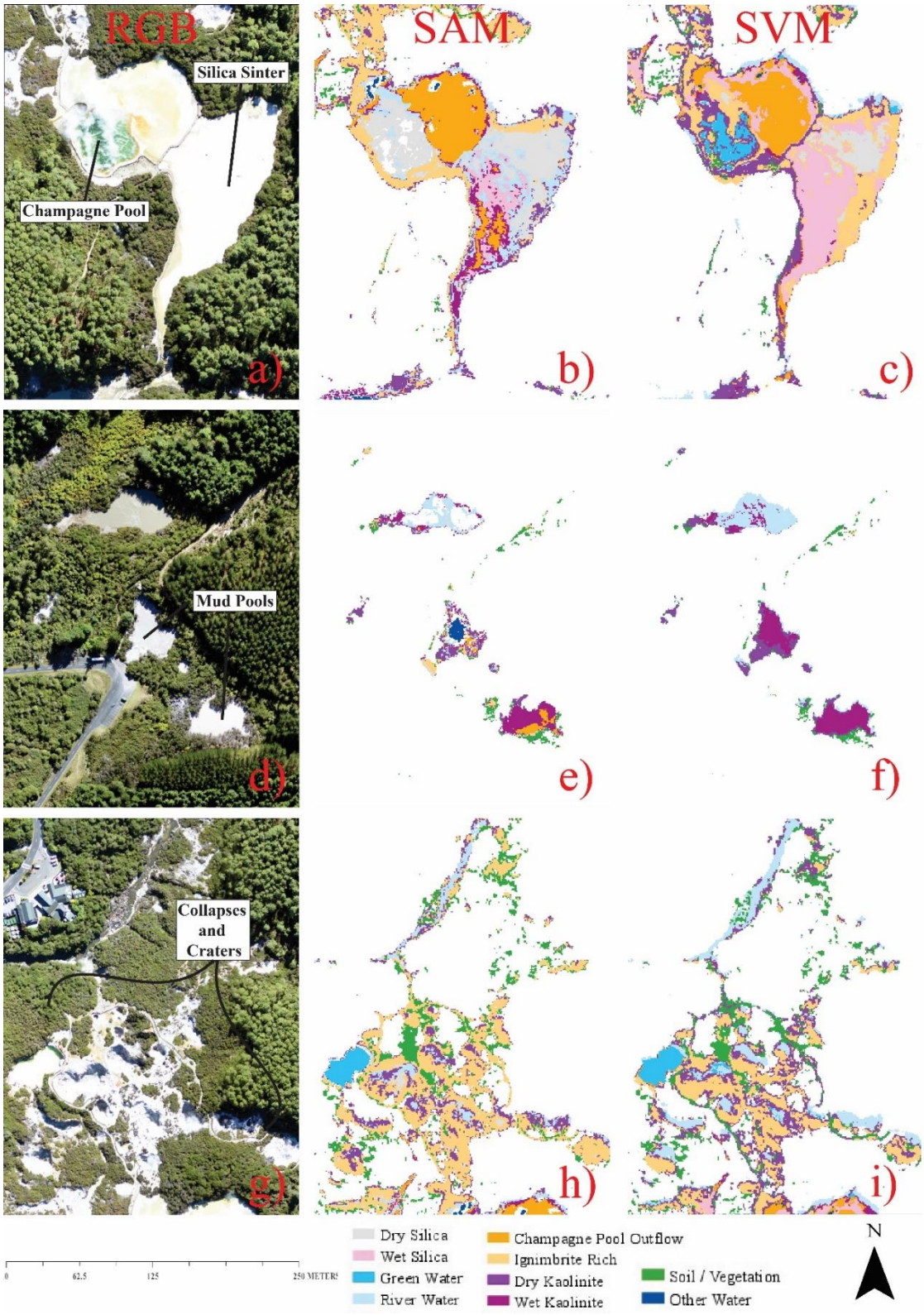

Figure 3.9. Classification images with SAM and SVM. a) Silica-dominated area with b) SAM classification and c) SVM classification. d) Acid-sulphate alteration area with e) SAM classification and f) SVM classification. g) Ignimbrite-dominated area with h) SAM classification and i) SVM classification.

Hydrothermal alteration and the resultant mineralogy are strongly pH and temperature dependent (Berger & Velde, 1992; Browne, 1978; Giggenbach, 1984; Henley & Ellis, 1983). The hyperspectral-based alteration maps and the airborne TIR data were compared on a class basis (Figure 3.10a-c). Where the mean values within each alteration class show relatively homogeneous values while temperature ranges increase from dry silica to acid sulphate-dominated alteration types (Figure 3.10d). Regardless of near neutral waters typically having higher temperatures than acid-sulphate waters, the acid-sulphate alteration areas display higher temperatures up to 100 °C (Figure 3.10d). These values can be linked to steaming grounds (100°C) more commonly adjacent to acid-sulphate water features than near neutral waters. The width of each class in the violin plot (Figure 3.10d) represents the frequency of temperature observations, revealing that wet silica areas form from uniformly cold water, while all other classes have a very broad range of temperatures. These observations are in agreement with in-site measurements at Waiotapu Geothermal Field, where near-neutral chloride water temperatures were 76°C to near boiling, while, mud pools waters measured temperatures from 27 to 99°C (Giggenbach et al., 1994; Hedenquist & Browne, 1989).

Table 3.3. Image Classification Accuracies by Surface Cover Types.

	Spectral Angle Mapper		**Support Vector Machine**	
Class	User's accuracy (%)	Producer's accuracy (%)	User's accuracy (%)	Producer's accuracy (%)
Dry Silica	100	79.87	100	99.6
Wet Silica	39.52	99.25	92.36	100
Green Water	85.79	100	100	100
River Water	87.67	69.06	98.99	98
Champagne Pool Outflow	91.06	70.89	100	86.89
Ignimbrite Dominated	88.54	88.82	98.91	96.81
Dry Kaolinite	66.67	73.91	70	95.45
Wet Kaolinite	59.08	65.57	97.92	97.24
Soil / Vegetation	100	99.12	99.4	100
Other Water	99.72	85.92	100	100

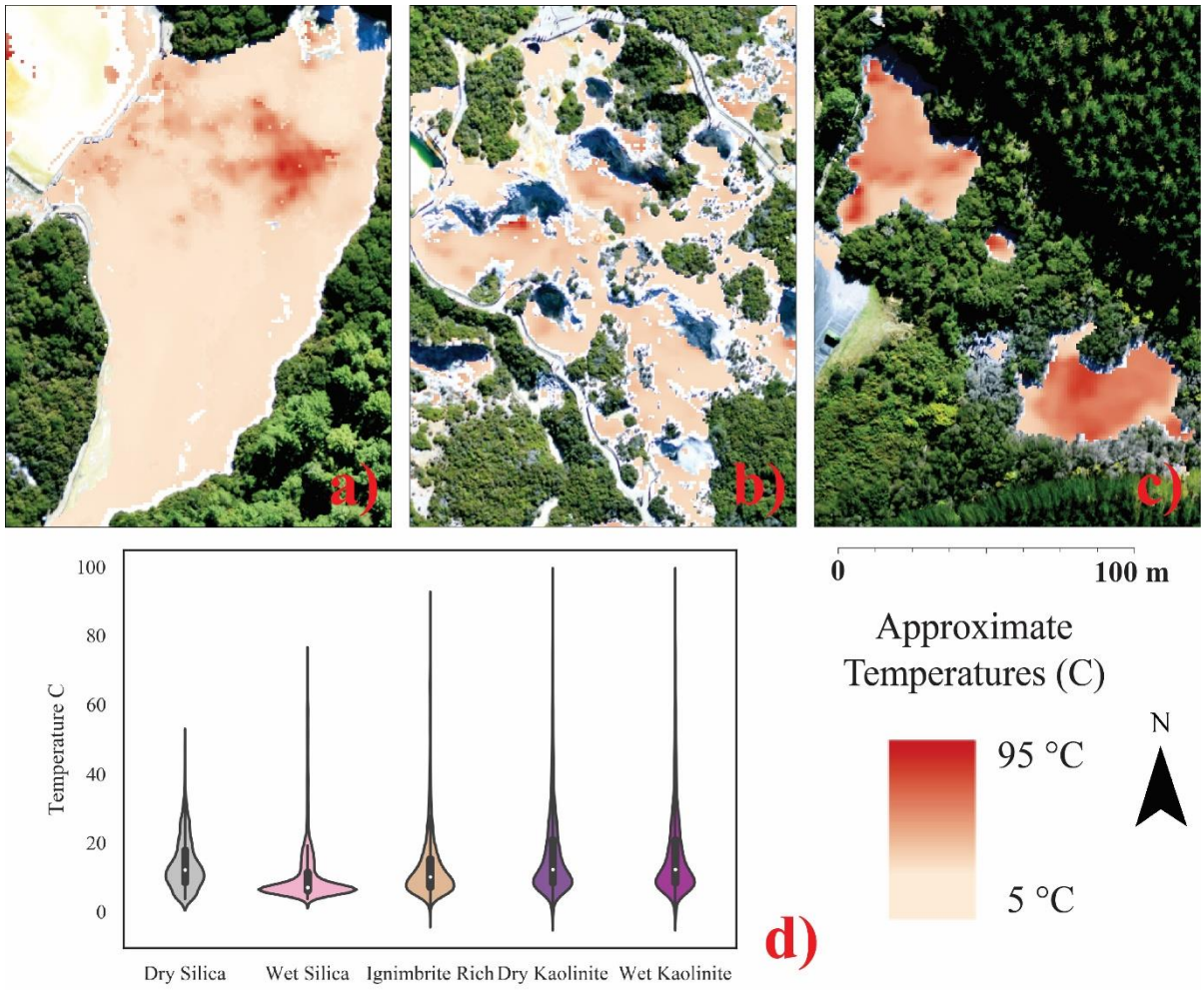

Figure 3.10. TIR data overlain on RGB imagery over the main bare rock occurrence in the Waiotapu Geothermal Field, corresponding to the same areas in Figure 3.9. a) Shows silica sinter deposition area. b) Ignimbrite dominated region with homogeneous heat distribution on surface. c) Mud pools with visible small zones of upwelling heat and water, where surface activity is taking place changing from 1-10 m. d) Violin plot displays the data distribution from the thermal infrared imagery, for each class as delineated by the SVM classification from the hyperspectral data and clipped out.

3.5 Discussion

3.5.1 Temporal Evolution and Hydrothermal Alteration of the Waiotapu Geothermal Field

Geological (e.g. mineral mapping, structural geology), geochemical (e.g. water and gas chemistry, stable isotope studies) and geophysical techniques (e.g. electromagnetic and gravity surveys) have been used to explore Waiotapu Geothermal Field since the 1950s (Lloyd, 1959), with the main purpose of assessing the system's energy potentials and understanding the hydrogeology.

Based on the hyperspectral image classification, the hydrothermal alteration at Waiotapu Geothermal Field has been mapped, contributing to the overall understanding of this geothermal area.

The hyperspectral remote sensing guided lithological mapping shows a strong spatial variability, with southern parts characterised by active silica sinter formation from the overflow of the chloride-rich waters (e.g. silica classes), while the northern part of the field is rich in acid sulphate alteration features (e.g. Figure 3.8d). The ignimbrite-dominated areas occur in between, encompassing broken silica sinter, interpreted to be remnants of ancient sinter forming areas with samples consistent with moderate to extensive silicification. The present distribution of lithological zones can be linked to the southward migration of chloride-rich fluid discharge, hydrothermal eruption craters caused by pressure changes in the system (Hedenquist & Browne, 1989; Kaya et al., 2015), an increase in CO_2 and a decrease in temperature (e.g. epidote found at sites with a present lower temperature than its formation) (Grindley et al., 1994; Simpson & Bignall, 2016).

The observed hydrothermal alteration minerals indicate a diverse paragenesis, controlled by pH, rock-water ratio and geothermal fluid temperatures (Mielke et al., 2014; Reyes, 1990; Wyering et al., 2014). The paragenesis of the observed hydrothermal alteration phases, such as silica and opal are consistent with precipitation from near neutral–pH, chloride–rich waters with temperatures below 75°C (Lynne, 2012) other minerals (e.g. kaolinite, alunite, jarosite) tend to form at temperatures close to 100°C, but at relatively shallow, near-surface parts of the geothermal system by acid-sulphate fluids.

Acid-sulphate alteration is caused by rising H_2S-rich hydrothermal fluids and microbial activity that can be detected on the surface or above the water table by sulphate minerals (e.g. alunite, gypsum, kaolinite). This process forms pervasively altered steam heated advanced argillic alteration patches (Hedenquist, 1991; Hedenquist & Browne, 1989). At Waiotapu Geothermal Field, changes in temperature, fluid-rock ratio and pH, cause propylitic alteration minerals, including illite, chlorite and epidote (Hedenquist & Browne, 1989; John et al., 2008). These alteration minerals are common in other ignimbrite hosted geothermal systems such as Yellowstone or Fish Lake Valley in the USA (Hellman & Ramsey, 2004; Littlefield & Calvin, 2014), major Olkaria in East Africa (Hewson et al., 2020) and Acoculco or Los Humeros in Mexico (Birkle et al., 2010; Canet et al., 2015).

The SEM and EDS data exhibit some of the complex alteration processes present in Waiotapu Geothermal Field, with extensive silicification and acid-sulphate alteration, typically for advanced argillic alteration with kaolinite, alunite, baryte, and Ti-rich as alteration products (Figure 3.4). The level and extent of alteration in geothermal systems are closely related to permeability, as fluids raise

to the surface through voids and fractures, altering the host rock and mobilizing elements (Dobson et al., 2003; John et al., 2008; Torres-Alvarado & Satir, 1998). Alunite is a common mineral from advanced argillic alteration along with kaolinite, well documented to indicate acidic conditions in Waiotapu Geothermal Field and the TVZ, (Hedenquist, 1991; Hedenquist & Browne, 1989; Simpson & Rae, 2018; White & Hedenquist, 1990), whereas Ti-rich alterations and baryte have not been mentioned in previous studies.

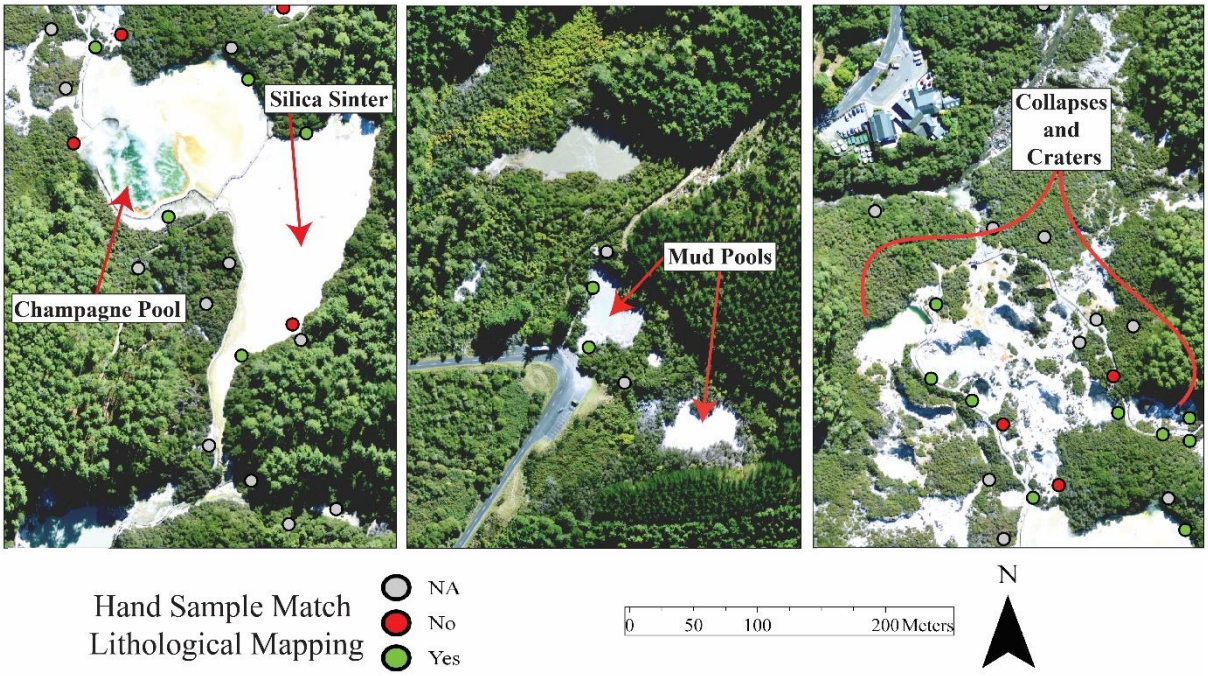

Figure 3.11. Classification images with SVM and classifications for hand samples.

Of the collected 74 hand samples, 35% are exposed in the hyperspectral image. Out of which 70% match the classified lithological type by SVM (Figure 3.11). This highlights the efficiency of remote sensing techniques. Extensive areas of silica sinter deposit in the southern area at water table level and predominant acid-sulphate alteration in the northern areas above the water table are visible in the image classification. Furthermore, pervasive acid-sulphate alteration patches scattered throughout Waiotapu Geothermal Field are also detected, displaying the complexity of the hydrothermal system. Presenting the practicality of remote sensing to classify partially vegetated geothermal areas and its capability to deliver information which assists in the hydrothermal alteration and evolution of the system.

3.5.2 Element Mobility and Distribution within Geothermal Systems

High chloride waters represent the deep parent fluid, which transports a range of elements (Fournier, 1989a; Lewis et al., 1997) through faults and fractures with elevated permeability (Nash

et al., 2004). Leaching elements such as arsenic (As), boron (B), fluoride (F), chromium (Cr), strontium (Sr), barium (Ba), antimony (Sb), lithium (Li), selenium (Se) thallium (Tl), and mercury (Hg) from the host rock, which deposit on subsurface and surface environments (Christensen et al., 1983; Henley and Ellis, 1983; Hetzer et al., 2007; Berger and Henley, 2011; Maity et al., 2011; Ullrich et al., 2013; Bundschuh and Maity, 2015; Want et al., 2018; Simpson and Christie, 2019; Heap et al., 2020).

Rock and soil samples proximal to the main near-neutral chloride-rich water upwelling areas (e.g. around the Champagne Pool), exhibit high concentrations of co-varying Ag, As, Au and Sb (e.g. Figure 3.7), while gradually decreasing concentration were measured over acid-sulphate dominated areas with prevalent steam-heated ground waters (Figure 3.8). Gold and silver are present in amorphous arsenic and antimony sulphides, most notably in the rim of Champagne Pool. The concentration of such elements is aligned with previous studies (Hedenquist and Henley, 1985; Giggenbach et al., 1994; Simpson and Bignall, 2016). Hence, spatial mapping through image classification can reveal active and ancient silica-dominated areas, representing preferred fluid pathways to the surface of geothermal fluid, as well as proxies for spatial mapping of the elemental distribution of some of these elements.

3.5.3 Image Classification for Surface Lithological Mapping

Many studies have mapped surface alteration minerals remotely, targeting specific minerals (i.e. alunite, kaolinite, jarosite) to delineate advanced argillic alteration and assess geothermal fields with minimum vegetation coverage (Crósta et al., 1998; Sabins, 1999; Debba et al., 2005; Swayze et al., 2014; Hoang and Koike, 2018), some reaching up to 92% overall accuracy. In our study, both classification algorithms identified the main surface features associated with hydrothermal alteration and depositions associated with different fluids with high accuracies (e.g. 98.7% for SVM classification). Even with the fact that the target classes are often mixed and soil/rock exposure is limited.

Table 3.4. Common minerals from geothermal areas, absorption features in µm. db - dobulet, br - broad, nr – narrow, lr – left right skewed, rs – right side skewed. Form (Clark, 1999; Clark et al., 1990, 2003; Lagat, 2007; Scott & Yang, 1997; Simpson & Rae, 2018; Van der Meer et al., 2014; Van der Meer et al., 2012), also based on the USGS Spectral Library

Imaging Spectroscopy		
Mineral	Absorption Features	Identification
Actinolite	0.674 (br) (Fe), 1.04, 1.39 (nr) (Mg-OH), 2.32 (nr) (Mg-OH), 2.39 (nr)	Indirect
Adularia	No particular absorption features in VNIR/SWIR	Indirect
Alunite	1.41 (db) (OH), 1.46 (OH), 1.77 (nr) (Sulphates?), 2.17 (db) (Al-OH), 2.33 (nr) (Al-OH)	Direct
Baryte	0.370 (br), 1.93 (br)	Indirect
Biotite	2.32 (Mg-OH), 2.39 (Mg-OH)	Indirect
Calcite	2.30 (lr) (CO_3), 2.55 (lr) (CO_3)	Direct
Chlorite	0.715 (br), 1.39 (nr), 2.25, 2.33	Indirect
Epidote	0.366, 0.457, 0.473, 0.616 (br), 1.36, 1.41, 1.55, 2.25 (nr) (Fe-OH), 2.34 (nr) (Fe-OH)	Indirect
Goethite	0.430 (db) (Fe), 0.650 (Fe), 0.973 (br) (Fe), 2.41	Direct
Gypsum	0.996 (br), 1.19 (br), 1.45, 1.49, 1.54, 1.75 (db), 2.20 (Al-OH)	Direct
Hematite	0.540 (db) (Fe), 0.880 (br)	Direct
Illite	1.41 (OH), 2.20 (br) (Al-OH), 2.34, 2.45 (Al-OH)	Direct
Jarosite	0.360 (br), 0.436 (nr), 0.898, 1.48 (OH), 1.85 (Sulphates?), 2.29 (Fe-OH), 2.40 (Fe-OH)	Direct
Kaolinite	0.967 (db), 1.24 (OH), 1.40 (db) (OH), 1.82, 1.85, 1.92 (rs), 2.20 (db) (Al-OH), 2.32, 2.39	Direct
Mica	1.40, 1.90 (H_2O), 2.20 (Al-OH), 2.35, 2.45	Direct
Montmorillonite	1.15, 1400 (db) (OH + H_2O), 1.90 (db) (H_2O), 2.20 (rs) (Al-OH)	Direct
Opal	1.40 (db), 1.90 (db) (H_2O), 2.20 (db) (br)	Direct
Prehnite	1.48 (nr), 1.92 (br), 2.24, 2.28, 2.35 (db)	Indirect
Pyrite	1.00 (br)	Indirect
Quartz	No particular absorption features in VNIR/SWIR	Indirect
Sulphur	0.370 (br)	Direct

The identification of minerals using remote sensing platforms is complex, as it is affected by the grain size, amount of materials present (e.g. pervasive alteration versus surface coating), reflectance angle and atmospheric effects which cause a high signal-to-noise ratio (Clark & Roush, 1984). Furthermore, some minerals (e.g. quartz) do not have any particular absorption feature in the

VNIR/SWIR region (Table 3.4). SAM can discriminate between unknown and labelled training data using measured spectral angles between them. This approach considers therefore only the shape of the spectral reflectance, regardless of its intensity. This has resulted in a decrease in the overall classification accuracy compared to SVM (e.g. 85.1% vs 98.7%). Furthermore, our ground samples indicate the dominance of silicification and silica-precipitation from overflowing fluids. These lithologies are dominated by spectrally featureless minerals (e.g. quartz, Table 3.4), causing the observed decrease in the classification results. The observed increase in classification accuracy by SVM (e.g. Wet Silica, Ignimbrite Dominated classes in Table 3.2) has the ability to incorporate not only spectral data (e.g. location and shape of the spectral reflectance profiles), but also light intensity changes among classes. Even though SVM has been proven to be less sensitive to Hughes phenomenon (i.e. training samples being relatively small compared to the number of bands) (Melgani & Bruzzone, 2004; Shao & Lunetta, 2012), it can result in overfitting (Bruzzone et al., 2005). However, the SVM results match in ~75% to the ground sampling data, highlighting that advanced machine learning based algorithms, such as SVM, can cope with spectrally featureless minerals, such as quartz. This can make them ideal for mapping geothermal areas dominated by silica sinter deposition and silicification alteration processes, improving our understanding of the geothermal systems.

Hyperspectral images through advanced image classification are well suited for mapping geothermal surface features and lithologies, however, they also have limitations. For example, the high spatial and spectral resolution can reduce some uncertainties but increase computational demand and processing complexity. Spectral mixing is a clear example of such complexity, in geothermal areas clay minerals tend to be mixed with other minerals which often share absorption features amongst them (Clark, 1999; Clark et al., 2003; Swayze et al., 2014). Furthermore, the bare ground pixels can also be mixed with the surrounding vegetation cover, resulting in a complex surface signature (Qu et al., 2014). These should be considered when selecting a training population. In this chapter/study, the thresholding approach using NDVI values gave favourable results, however, more advanced methods, such as semi-supervised algorithms (Ekanayake et al., 2018), can be applied in the future.

3.5.4 Role of Hyperspectral and Thermal Infrared Remote Sensing in Geothermal Exploration

Thermal infrared remote sensing represents a cost-effective technique to map and quantify temperature anomalies associated with surface geothermal features (e.g. fumaroles, hot springs, geysers, heated ground) to assess heat output, extension and temporal changes (Coolbaugh et al.,

2007; Haselwimmer & Prakash, 2013; Mongillo, 1994; Reeves & Rae, 2016; Romaguera et al., 2018). The surface temperature depends on several physical parameters (e.g. albedo, slope, compaction, grain size, thermal inertia), some of which are minimised by acquiring imagery at night (Calvin et al., 2005; Reeves & Rae, 2016). Furthermore, in our study, the temperatures were calibrated against water bodies on site while the flight takes place (Reeves & Sanders, 2019). With this in mind, estimated thermal data on soil and rocks can only be taken as an approximation and be used to detect spatial change, but not exact temperatures.

Earlier exploration studies have demonstrated the importance of hyperspectral remote sensing in geothermal exploration (Nash et al., 2004). This study extends the capability by combining the hyperspectral imagery derived surface classification with thermal infrared imagery to explore the thermal behaviour of lithological and hydrological classes (Figure 3.10). This approach can reveal spatially implicit formation conditions of silica-rich and acid-sulphate dominated zones within a geothermal field. This technique holds the potential to determine thermal behaviours from VNIR hyperspectral data or the identification of acid-sulphate regions from thermal aerial data.

Waiotapu Geothermal Field has seldom been explored in the last decade and hyperspectral remote sensing had not been carried out before. Regardless of the rock and soil exposure, conventional multispectral remote sensing is often too coarse resolution for assessing soil and rock exposures, and they are also lacking spectral bands to discriminate between (e.g. alunite vs kaolinite). The latter limitation can be overcome in the future by using new generation hyperspectral satellites such as PRISMA (Lopinto & Ananasso, 2013; Van der Meer et al., 2012) or upcoming SBG (Surface Biology and Geology) (Calvin & Pace, 2016; Kruse et al., 2011). This can lead to regional-scale mapping of geothermal surface manifestation, with improved spectral capability, but still with a limited spatial resolution of 30-60 m.

From the remotely sensed acquired imagery which includes most of the 18 km^2 of surface activity in Waiotapu Geothermal Field, only about 10% is exposed soil or water, the other 90% is largely covered by vegetation which hinders reflected electromagnetic radiation from the ground. Therefore, vegetation focused studies using hyperspectral technology can also be trialed in the future to detect proxies for subsurface activity. For example, the height and abundance are typically inversely related to heat output and heavy metal content as our ICPMS data show, which is in line with other observations from similar geothermal fields (Burns, 1997; Mia et al., 2014; Nash et al., 2003; Wang et al., 2018). These relationships should be explored by future studies in geothermal areas.

3.6 Conclusions

In this paper, image classification from airborne hyperspectral data of three main lithological classes; silica dominated, ignimbrite dominated, and acid-sulphate dominated was generated. An integrative analysis of Waiotapu Geothermal Field, including airborne hyperspectral VNIR and TIR imaging, laboratory spectroscopy, chemical concentrations, and SEM data was undertaken. Integration of VNIR hyperspectral and TIR remote sensing imagery along with chemical concentrations and spectral signatures from soil and rock samples helps identify the shallow mineral alterations and precipitates of Waiotapu Geothermal Field.

Most of the soil and rock samples analysed represent a mixture of minerals, with poorly crystallised kaolinite, ignimbrite host-rock and native sulphur widely present. These are concordant with the image classification, as kaolinite and host rock were detected together on exposed soil. The silica-rich deposits formed by near neutral chloride-rich waters have been classified successfully by the SVM algorithm, despite the lack of particular absorption features in the VNIR/SWIR domains. This might require further attention by future studies to utilise contextual spectral information to be incorporated in hydrothermal lithological mapping in geothermal areas.

Mapping of surface lithologies in geothermal areas can be improved by hyperspectral data combined with machine learning classification approaches. This is found to improve spatial distribution retrieval for spectrally featureless mineral phases, such as quartz.

Another important aspect to investigate is how chemical concentrations exposed the relation of high chemical concentrations of Ag, Au, As, and Sb with the spatial reach of near neutral high/chloride waters. The presence of these elements delineates the reach of such fluids and can become bioavailable to vegetation causing detectable spectral features. For geothermal systems that are largely covered by vegetation, hyperspectral imaging can also be applied to map vegetation anomalies as a proxy for geothermal activity at shallow depths.

MASSEY UNIVERSITY
TE KUNENGA KI PŪREHUROA
UNIVERSITY OF NEW ZEALAND

GRADUATE RESEARCH SCHOOL

STATEMENT OF CONTRIBUTION
DOCTORATE WITH PUBLICATIONS/MANUSCRIPTS

We, the candidate and the candidate's Primary Supervisor, certify that all co-authors have consented to their work being included in the thesis and they have accepted the candidate's contribution as indicated below in the *Statement of Originality*.

Name of candidate:	Cecilia Rodriguez-Gomez
Name/title of Primary Supervisor:	Gabor Kereszturi
In which chapter is the manuscript /published work:	Chapter 3

Please select one of the following three options:

(●) The manuscript/published work is published or in press

- Please provide the full reference of the Research Output:

Rodriguez-Gomez, C., Kereszturi, G., Reeves, R., Rae, A., Pullanagari, R., Jeyakumar, P. and Procter, J., 2021. Lithological mapping of Waiotapu Geothermal Field (New Zealand) using hyperspectral and thermal remote sensing and ground exploration techniques. Geothermics, 96: 102195. https://doi.org/10.1016/j.geothermics.2021.102195

( ) The manuscript is currently under review for publication – please indicate:

- The name of the journal:

- The percentage of the manuscript/published work that was contributed by the candidate:

- Describe the contribution that the candidate has made to the manuscript/published work:

( ) It is intended that the manuscript will be published, but it has not yet been submitted to a journal

Candidate's Signature:	Cecilia Rodriguez Gomez — Firmado digitalmente por Cecilia Rodriguez Gomez Fecha: 2022.12.05 12:15:57 -06'00'
Date:	05-dic-2022
Primary Supervisor's Signature:	Gabor Kereszturi — Digitally signed by Gabor Kereszturi Date: 2022.12.07 13:19:13 +13'00'
Date:	07-Dec-2022

This form should appear at the end of each thesis chapter/section/appendix submitted as a manuscript/ publication or collected as an appendix at the end of the thesis.

4 Chapter 4. “Remote exploration and monitoring of geothermal sources: A novel method for foliar element mapping using hyperspectral (VNIR/SWIR) remote sensing.”

This chapter has been submitted, reviewed and published in *Geothermics* (Elsevier), under the same title. DOI:

Contributing authors:

- **Cecilia Rodriguez-Gomez** (School of Agriculture and Environment, Massey University, Palmerston North, New Zealand): Conceptualisation, Methodology, Programming, Investigation, Formal analysis, Visualisation, Writing – Original Draft, Writing – Review & Editing.
- **Gabor Kereszturi** (School of Agriculture and Environment, Massey University, Palmerston North, New Zealand): Conceptualisation, Methodology, Investigation, Writing – Review & Editing, Supervision, Funding acquisition, Project administration.
- **Paramsothy Jeyakumar** (School of Agriculture and Environment, Massey University, Palmerston North, New Zealand): Supervision, Investigation, Writing – Review & Editing.
- **Reddy Pullanagari** (MAF digital Lab, School of Food and Advanced Technology, Massey University, Palmerston North, New Zealand): Supervision, Investigation, Writing – Review & Editing.
- **Robert Reeves** (GNS Science, Wairakei Research Centre, Taupo, New Zealand): Supervision, Investigation, Writing – Review & Editing.
- **Andrew Rae** (GNS Science, Wairakei Research Centre, Taupo, New Zealand): Supervision, Investigation, Writing – Review & Editing.
- **Jonathan Procter** (School of Agriculture and Environment, Massey University, Palmerston North, New Zealand): Supervision.

4.1 Introduction

Visible-Near infrared (350-1300 nm, VNIR) and Shortwave Infrared (1300–2500 nm, SWIR) hyperspectral remote sensing has been underutilized for monitoring geothermal resources globally. This is in part due to the economic burden hyperspectral (VNIR/SWIR) imagery acquisition has represented this far, and largely due to the obstacle imposed by dense plant cover at geothermal systems, which can hamper exploration by covering hydrothermal alteration patterns and geothermal surface features (e.g. warm ground, hot springs, silica sinter) (Mia et al., 2012; Rodriguez-Gomez et al., 2021). However, plant foliage can also reflect geothermal activity by responding to the local soil and water chemistry, nutrient availability, geothermal heat and gas emissions (Mia et al., 2012; Van Manen & Reeves, 2012). Plant spectral responses to the geothermal environment have been seldomly studied, presenting an opportunity to probe into geothermal systems by remotely characterising the vegetation in the area in a novel manner. This can further improve our conceptual understanding of plant-geothermal interactions and their role in geothermal exploration.

Plants can be subject to stress due to various extreme conditions, such as high temperatures, acidic and nutrient-depleted soils, elevated amounts of elements (e.g. silver-Ag, arsenic-As, antimony-Sb) and water stress (Pippucci et al., 2015). For instance, high concentrations of antimony, sulphur, arsenic and cadmium have caused changes in spectral properties of plant canopy (e.g. red-edge shifting towards the blue due to decreasing chlorophyll contents (Manzo et al., 2013; Rathod et al., 2018)), however, these relationships have mostly been proven only in controlled experiments (i.e. pot experiments). Elements such as Ag, As and Sb are related to the deep “parental” waters in geothermal areas (Wilson et al., 2012; Simmons et al., 2016), while other elements such as barium, are correlated to the mixing of groundwater with thermal waters (Dunn, 2007), and so their location is relevant in geothermal exploration. Theoretically, vegetation can offer new insights into shallow subsurface processes via fingerprinting element concentrations and their response to metals and metalloid in geothermal areas.

Waiotapu Geothermal Field, located in the Taupo Volcanic Zone (TVZ), New Zealand, has been well studied (Hedenquist, 1991; W. Giggenbach et al., 1994; Reeves & Sanders, 2019) and is an excellent test-ground to upscale the findings from such controlled laboratory experiments and develop new remote sensing monitoring methods. Waiotapu Geothermal Field has great natural variability of ground conditions (e.g. low to high soil pH and temperatures up to 90°C), with unique thermotolerant vascular species including *kunzea ericoides* var. *microflora* (i.e. kanuka) (Van Manen & Reeves, 2012). The height of kanuka has been previously related to the near-surface soil temperature where smaller plant height indicates hotter soils (Muukkonen, 2005; Smale et al., 2018).

Furthermore, it has also been previously documented to uptake and translocate non-essential elements (e.g. Ag, As, Cd, Sb) (Dunn & Christie, 2020). Approximately 90% of the areal surface at the Waiotapu Geothermal Field is covered by plants (Rodriguez-Gomez et al., 2021), with a ~10% dominated by kanuka, making this plant an ideal indicator species and proxy to link plant foliage and subsurface geothermal processes for the first time.

The research objective of this study is to develop a non-intrusive method for mapping geothermal activity in densely vegetated areas. By utilising advances in laboratory, airborne and satellite-based hyperspectral remote sensing and data analytics, we propose a new methodology by combining them with elemental composition data of kanuka foliage, rock and soil samples in a multivariate image classification framework. The resultant interpretations from the element anomaly maps derived from hyperspectral (VNIR/SWIR) data were supported by independent high-resolution airborne thermal infrared (TIR) imagery and light detection and ranging (LiDAR) data, as well as, existing geological data, to establish the causality of the mapped elemental anomalies at Waiotapu Geothermal Field, New Zealand (Figures 4.1-4.2).

4.2 Study Area

Waiotapu Geothermal Field forms part of the Taupo Volcanic Zone (TVZ), located in the North Island of New Zealand (Figure 4.1). Geothermal activity within the TVZ is associated with the subduction of the Pacific plate under the Australian plate (Hunt et al., 1994; Wilson et al., 1995; Kissling & Weir, 2005), subject to active extension in the overriding plate (Rowland & Sibson, 2004; Seebeck et al., 2014). The TVZ basement comprises indurated sedimentary rocks referred to as 'greywacke' (Milicich et al., 2020), overlain by a sequence of pyroclastic deposits, lavas and lacustrine sedimentary rocks (Steiner, 1963; Grindley et al., 1994). Many geothermal areas in the TVZ are formed by convective hydrothermal systems with a heated reservoir at depth (1-4 km) reaching temperatures above 200°C (Hedenquist, 1991; Kaya et al., 2014). The hot fluids interact with the host rock and groundwater, forming acid-sulphate, near-neutral high chloride and bicarbonate springs on the surface, exposing information about the subsurface activity (Pirajno, 2009).

Waiotapu Geothermal Field is one of the largest by surface features exposure of about 20 active geothermal areas in the TVZ (Figure 4.1A), with a surface area of ~18 km^2 and heat flow of ~500 MWt (Bibby, Glover, et al., 1995; Kaya et al., 2015). Seven wells drilled at Waiotapu Geothermal Field between 1957 and 1962 presented maximum temperatures of 195 °C with maximum depths of 1000 m (Giggenbach et al., 1994). Waiotapu is hosted by pyroclastic flows and lacustrine sediments

(Lloyd, 1959; Wood, 1994; Kaya et al., 2014), presenting surface features which include fumaroles, steaming ground, hydrothermal eruption craters, mud pools, hot chloride pools, acid-sulphate altered areas, silica and sinter deposits (Grange, 1937; Lloyd, 1959; Hedenquist & Browne, 1989; Hunt et al., 1994). Hot springs and explosion craters generally follow a NE-SW trend (Hedenquist & Henley, 1985; Mongillo, 1994) with the Ngapouri and Paeroa faults as the closest active mapped faults, located 1.5 km and 5 km to the northwest respectively (Nairn et al., 1994; Rowland & Simmons, 2012; Wood, 1994). Fluid from ~1 km depth is transported through faulting and associated fractures, offering vertical and horizontal permeability, allowing fluids to move south and west from the heat source (Hedenquist, 1982; Mongillo, 1994; Hadfield et al., 2001; Kaya et al., 2015). The thermal area drains into the Waiotapu Stream (Figure 4.1B), which joins the Waikato River to the south (Lloyd, 1959).

The extreme ground conditions (e.g. acidic soils, high temperatures) present at many geothermal areas of the TVZ can host rare communities of plant species that have adapted to these conditions. These geothermal ecosystems in the TVZ include a combination of ferns (e.g. *Hypolepis* species), moss species (e.g. *Campylopus pyriformis*), liverworts (e.g. *Chiloscyphus semiteres*) and shrubs (Given, 1980; Van Manen & Reeves, 2012; Smale et al., 2018). These species can live in extremely acidic soils, in proximity to steam, with nutrient excess or deficiency, water and/or soil with high contents of heavy metals and metalloids (Given, 1980; Burns & Leathwick, 1995; Boothroyd, 2009). *Kunzea ericoides* var. *microflora* (i.e. kanuka) is a thermotolerant vascular species endemic to geothermal areas of New Zealand that can live with soil temperatures above 40°C (Burns, 1997; Van Manen & Reeves, 2012). The height of kanuka is generally related to the near-surface soil temperature with smaller plants in hotter soils (Burns, 1997; Muukkonen, 2005; Smale et al., 2018) and has also been documented to uptake and translocate non-essential elements (e.g. Ag, As, Cd and Sb) (Dunn & Christie, 2020).

Approximately 90% of the areal surface at the Waiotapu Geothermal Field is covered by plants (Rodriguez-Gomez et al., 2021), with a ~10% dominated by kanuka. The high abundance of kanuka within geothermal systems makes this plant an ideal indicator species and proxy to link plant foliage and subsurface geothermal processes.

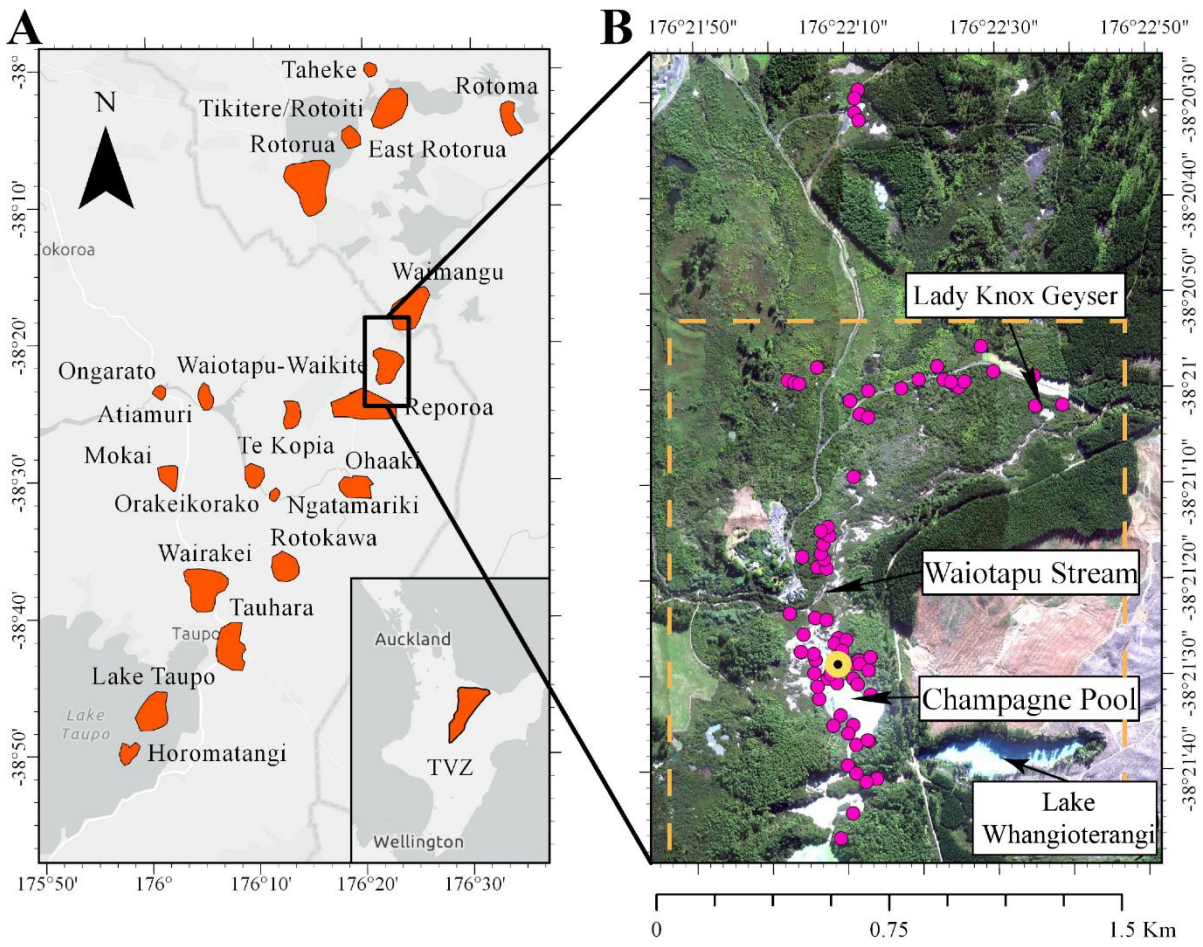

Figure 4.1 (A) Location map of Waiotapu Geothermal Field within the Taupo Volcanic Zone shown with other geothermal fields [modified from Bibby et al., 1995]. (B) Central part of the Waiotapu Geothermal Field. Pink dots show the ground sampling sites. On B) the yellow dashed rectangle represents the approximate location of Figures 4.6, 4.7 and 4.9. The yellow circle on B) represents the location for a rock/soil sample which had baryte mineralisation (Rodriguez-Gomez et al., 2021).

4.3 Materials and methods

4.4 Airborne and satellite hyperspectral data collection and instrumentation

An AisaFENIX sensor was used to capture an airborne hyperspectral (VNIR/SWIR) image (Tables 4.1 – 4.2) between 11:20 to 12:59 NZ Standard Time on 13 April 2019. From the raw data digital numbers were converted to at-sensor radiances with CaliGeoPro (Pullanagari et al., 2016). Radiance values were converted to reflectance values using Airborne Atmospheric and Topographic Correction Model, ATCOR (Richter, 1998), using a "flat terrain" mode with image-derived water vapour column 1 g/cm using bands at 1130 nm, initial visibility of 50 km, and rural aerosol model.

Followed by corrections of geometric inconsistencies performed in PARGE (Parametric Geocoding Software), with the use of ortho-photos acquired during the same flight with a Nikon D810 digital single-lens reflex camera (Schläpfer & Richter, 2002). A Savitzky-Golay (Savitzky & Golay, 1964) neighbourhood filter with a third-order polynomial smoothing (4 bands on each side) was applied to reduce noise caused by the sensor and atmospheric interferences.

Table 4.1. Input data characteristics at different acquisition scales. Abbreviation: FWHM – Full-width half maximum.

Scale	Laboratory-based (ASD FieldSpec)	Airborne-based AisaFENIX	Satellite-based (PRISMA)
Spatial Resolution (meter)	0.01	1	30
Number of Bands	2151	448	230
Spectral Sampling Interval (nm)	1.4/1.1 (VNIR/SWIR)	3.3/5.7 (VNIR/SWIR)	12
FWHM (nm)	1.4/2 (VNIR/SWIR)	3.2/12.2 (VNIR/SWIR)	12

The PRISMA (PRecursore IperSpettrale della Missione Applicativa) hyperspectral satellite provides VNIR/SWIR imagery (see Table 4.1 for instrument specifications) (Cogliati et al., 2021). One PRISMA tile (PRS_L2D_STD_20200304222315 _20200304222319_0001) was acquired on the 4th of March 2020 with L2D processing (i.e. geolocation, geocoded at surface reflectance, aerosol, water vapour map and cloud characterisation) was used. Figure A2.1 exemplifies visually the spatial and spectral differences between the airborne and satellite datasets.

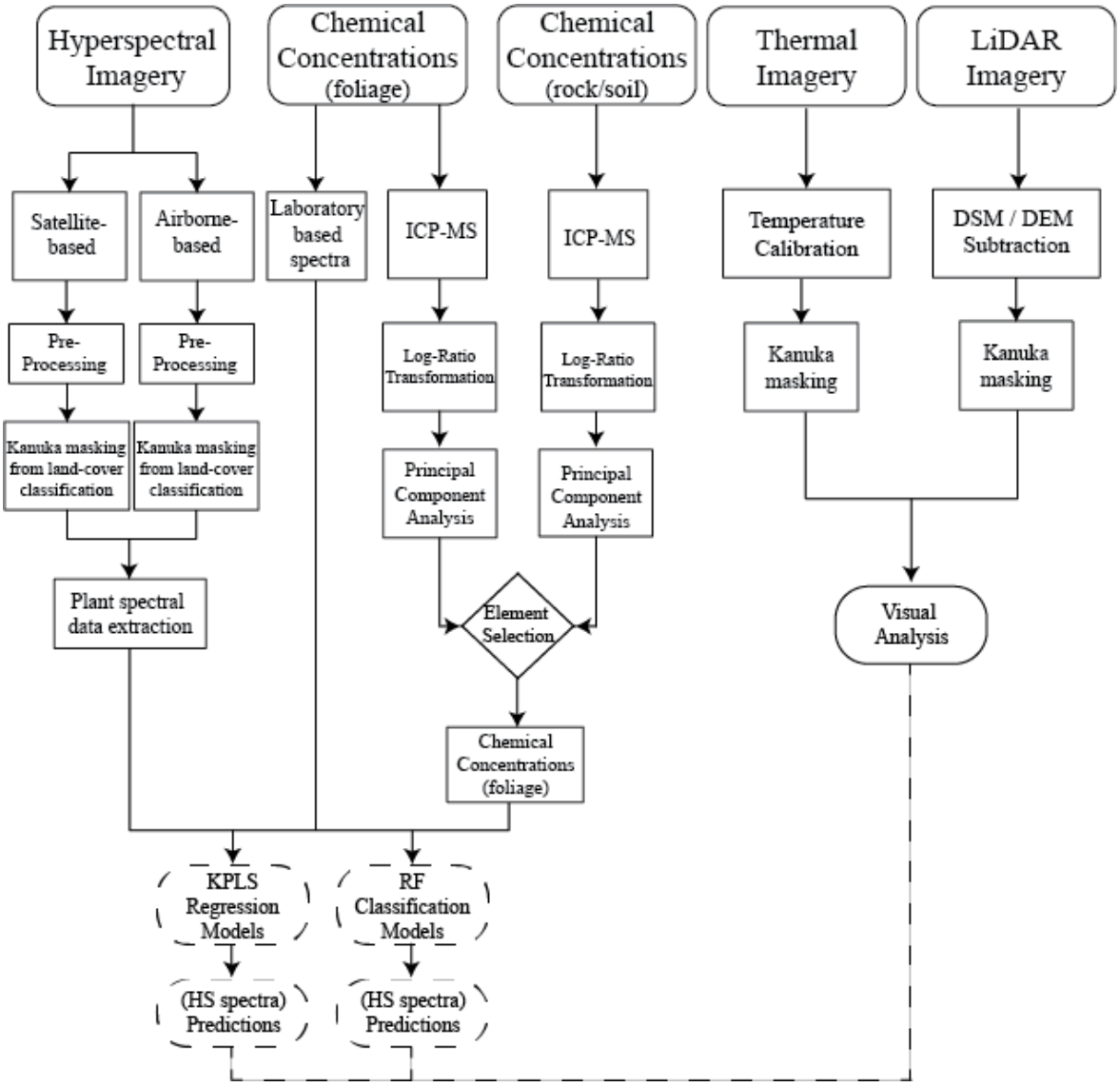

Figure 4.2. The applied processing and analytical workflow of the present study. Shown in the first row is the employed data, which includes 3 types of hyperspectral (VNIR/SWIR) data (laboratory, airborne and satellite-based), along with sample's elemental concentrations to generate distribution maps interpreted in the lights of independent LiDAR and TIR imagery.

4.4.1 Land surface cover classification

A Random Forest algorithm was utilised using labelled training samples to separate kanuka shrub spatial coverage from the other land surface cover classes (Table A2.1) (Ghamisi, Plaza, et al., 2017). Random Forest is an ensemble classifier that produces multiple decision trees from randomly selected samples (Belgiu & Drăgu, 2016). It effectively deals with large spectral datasets (Xia et al., 2014) with high co-linearity (Belgiu & Drăgu, 2016). It has been successfully applied to map tree species (Dalponte et al., 2013; Ghosh & Joshi, 2014; Cavallaro et al., 2015), hence this method was preferred in this study. Random Forest classification implemented in EnMAP-Box (van der Linden

et al., 2015) was used. The classification model was computed using 500 decision trees, gini coefficient as the impurity function and stopping criteria of 1 for minimum number of samples in a node and 0 as minimum impurity. This classification was used to retrieve the aerial extent of kanuka and used as a mask later (Figure A2.2).

4.4.2 Rock/soil and foliage analysis

A total of 74 rock/soil samples along with 77 kanuka foliage samples were collected one week after the airborne survey. The sampling was targeted to compare foliar elemental uptake from a variety of geothermal environments within Waiotapu Geothermal Field, and to provide a calibration/validation dataset. Plant samples only included foliage of kanuka shrub (*kunzea ericoides* var. *microflora*), the dominant shrub species in thermally active areas in New Zealand. At the field, 'combined' samples of multiple kanuka shrubs within a 3×3 m area were collected to capture underlying variability.

Foliage samples were dried for 24 to 36 hours at 40 °C. The leaves were separated from the stem, ground with a coffee grinder and sieved (2 mm mesh). Rock and soil samples were dried at 16-20 °C for 2 to 3 days, and then ground and sieved (1 mm mesh).

The ground samples have been analysed with an Inductively Coupled Plasma Mass Spectrometer (ICP-MS) at Bureau Veritas Mineral Laboratories, Vancouver, Canada (Figure 4.2). Obtaining concentrations higher than their detection level for 45 elements (Table A2.2), following the standard provided by Dunn and Christie (Dunn & Christie, 2020). The mineralogy and methods used for the rock/soil samples are presented in (Rodriguez-Gomez et al., 2021) and the lithological map retrieved from such samples is shown in Figure A2.3.

Reflectance between 350 and 2500 nm was collected from dried and ground samples with an ASD FieldSpec High Resolution 4 equipped with a contact probe (Figure 4.2). Each spectral measurement was calibrated against a white surface reference. An average from 3 spots, measured 5 times each, was obtained to create a single spectra measurement per sample, splice corrected.

The foliar and rock/soil datasets were transformed using Log Ratio (Aitchison, 1986) to convert the ICP-MS compositional data expressed in mg/kg into a suitable sample space to be analysed using standard statistical approaches (Aitchison, 1986; Muriithi, 2015). In this study, a Principal Component Analysis (PCA) was used to explore the underlying structure within the chemical compositions for both foliar and rock/soil datasets (Figure 4.4). PCA calculates eigenvectors and eigenvalues of a covariance matrix presenting differences and similarities of the data (McKinley

et al., 2016; Hood et al., 2019), exposing underlying patterns in high dimensionality data. Furthermore, Pearson-type linear correlation, was also used which can also be helpful in cross-examine multivariate datasets, revealing similarities and correlations (Waskom, 2021) (Figure A2.4).

4.5 Classification and regression for element zonation

The ground sample data and the hyperspectral data (VNIR/SWIR) were used to develop classification and regression frameworks for zoning element distribution within the Waiotapu Geothermal Field. The spectral data (in all scales; satellite, airborne or laboratory-based) were used here as explanatory variables (Table 4.1 and Figure 4.2), while the chemical composition data were used as target variables. All chemical concentrations were transformed using log-ratio transformation (Aitchison, 198) to be quasi-normally distributed before classification and regression.

Cross-validation has been suggested as one of the resampling methods with the smallest bias and mean square error (Berrar, 2019), and leave one out cross-validation can be computationally demanding, however, due to the small sample population (Molinaro et al., 2005) it was selected to train both classification and regression models. To assess the prediction overall accuracy (OA) and mean absolute error (MAE) were used for classification and regression, respectively.

For the classification, the ground sample's elemental concentrations were classified into three classes (low, medium and high) using standard deviation for each selected element (Figure 4.3). Due to the lack of information regarding elemental uptake of kanuka shrub living in geothermal areas a general scheme with three classes was selected. The classification was based on the distribution (n=77) of each indicator element (e.g., Ag, As, Ba, and Sb). Their distributions are normal after log-transformation, therefore, medium values correspond to "median" values of the population, while the low and high values showing the depleted and enriched areas, respectively. This is a robust way for mapping spatial associations of those indicator elements.

Two sets of classification were created (Figure 4.3): half standard deviation and one standard deviation. The results for half standard deviation are presented here (Table 4.3 and Figures 4.6-4.7), while, the results for one standard deviation are in the supplementary material. It is important to highlight that they both have similar spatial trends (e.g. Figures 4.6-4.7 and Figures 2.5-2.6). Random Forest classification algorithm was used to map element concentration classes. To tune the model parameter "mtry" (i.e. the number of variables which is randomly collected to be sampled in each split) was assigned as a sequential value from 1 to 150, with the highest overall accuracy value was taken as the optimal mtry value. While the number of trees and maximum depth parameters were kept constant, as 500 and none, respectively.

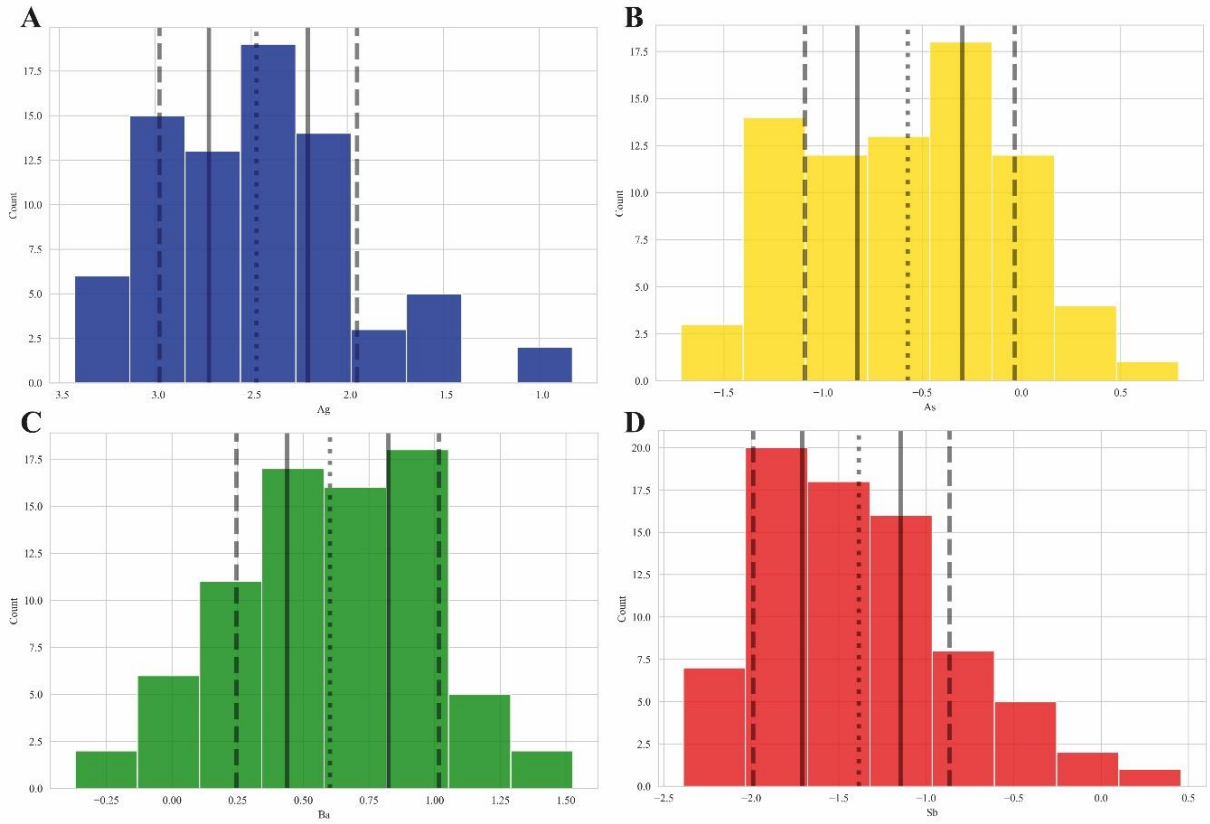

Figure 4.3. Foliar chemical concentration after a log-ratio transformation showing the mean (dotted line), half- (solid line) and one-standard deviation (dashed line). (A) Silver, (B) Arsenic, (C) Barium and (D) Antimony.

For each element's classification model, the important variables were retrieved following Hong et al., (2016). It considers two indices Mean Decrease Accuracy (MDA) and Mean Decrease Gini (MDG) extracted from the model. Utilising both indices considers not only the importance but also the impurity of the variable. These values were ranked and added to each other to compute a single total variable score and select the important wavelengths (Figure 4.8). Only the highest 10% was deemed as important and plotted in comparison to the average plant spectral reflectance for laboratory, airborne and satellite based spectral signatures (Figure 4.8).

For regression, Kernel Partial Least Squares (KPLS), an extension of the original Partial Least Squares multivariate statistical technique (Wold et al., 2001) was applied to the datasets (Table A2.3) (Figures A2.2-A2.3). KPLS transforms the original data to a high dimensional feature space using kernel functions for non-linear structure input data and linear PLS for feature extraction (Rosipal, 2003). It can be used to model relations between sets of observed variables and solve non-linear problems, which has been used for similar plant datasets before (Pullanagari et al., 2016; Chakraborty et al., 2021). The number of PLS were estimated based on the data using LOOCV, and the model with the least MAE was selected.

4.5.1 Thermal infrared and LiDAR data

Night-time airborne Thermal Infrared (TIR) imagery over the Waiotapu Geothermal Field was collected on 13 April 2019 with a FLIR A615 TIR camera, following Reeves & Sanders (2019). The survey flight altitude was 1-1.25 km above ground level. Resulting in a TIR image of ~0.7 m spatial resolution covering a total area of ~11 km^2. In-situ water temperatures were measured with a Yokogawa TX10 digital temperature meter which is connected to a K type thermocouple. The calibration measurements were taken at the same time as image acquisition to convert the airborne brightness values to absolute temperature (Reeves & Sanders, 2019). Because temperature values were calibrated against water bodies; temperature from other surfaces (i.e. rock/soil and foliage) with different emissivity must be used with caution as they will only be approximations (Rodriguez-Gomez et al., 2021).

The airborne LiDAR data were acquired in April 2019 and obtained from Land Information New Zealand (LINZ) Data Service as part of the Waikato – Reporoa and Upper Piako River LiDAR survey for Lincoln Agritech Limited. The survey was captured in New Zealand Transverse Mercator Projection with a spatial resolution of 1 m. The individual tiles of Digital Terrain Model (DTM) and Digital Surface Model (DSM) data were mosaicked together to form two single images, respectively, covering the area of interest. The DTM mosaic was then subtracted from the DSM model to obtain plant height.

The TIR and LiDAR datasets and their derivates provide approximate surface temperatures and plant height which have been studied previously at Waiotapu Geothermal Field (Burns, 1997; Van Manen & Reeves, 2012). Thus, they allow independent corroboration of the retrieved foliar element maps to further understand the effect of soil temperatures as well as the chemical uptake of plants growing in geothermal settings.

4.6 Results

4.6.1 Rock/Soil and foliar chemical relations

The bulk chemistry of rock/soil and foliar samples show 45 elements above the detection limit (Table A2.2) to which a log-ratio transformation was applied to normalize the compositional data. The PCA analysis and linear correlations showed silver (Ag), gold (Au), arsenic (As) and antimony (Sb) with similar behaviour in both rock/soil and foliar datasets, positively influencing PC1 (Figure 4.4), towards the samples closer to Champagne Pool (Figure 4.1). Champagne Pool in Waiotapu Geothermal Field, which name derives from the abundance of CO_2 bubbles coming to surface, is one of the largest focal points from where near-neutral high-chloride deep geothermal

water discharges to the surface (Figure 4.1). The upflow here is enriched in metals (e.g. Ag, Au) and metalloids (e.g. As, Sb) (Weissberg, 1969; Wilson et al., 2012; Simmons et al., 2016). Lady Knox Geyser is another area with near-neutral high-chloride waters (Figure 4.1); however, the acquired field samples from this area do not show high concentrations of Au, As and/or Sb (Figures A2.6-A2.7). This can be attributed to the smaller discharge in Lady Knox Geyser compared to Champagne Pool and the sampling locations being opposite to the groundwater flow direction.

In contrast, zinc (Zn), barium (Ba), and cadmium (Cd - only from foliar samples) showed the opposite behaviour in both rock/soil and foliar (Figure 4.4). The differences between rock/soil and foliar samples for Ba (large Ba concentrations in plant samples but not in rock/soil samples) visible in the PCA (Figure 4.4) are attributed to the type of rock/soil samples (e.g. northern area samples have a higher organic matter content while southern areas are mostly lithology-dominated). Ba concentration in foliage shows a clear opposite trend to Ag, As and Sb (Figure 4.4). The opposite trend seems to be correlate with the distance from Champagne Pool (Figure 4.4), with high Ba values occurring towards areas of water mixing further away from the Champagne Pool (Dunn, 2007a).

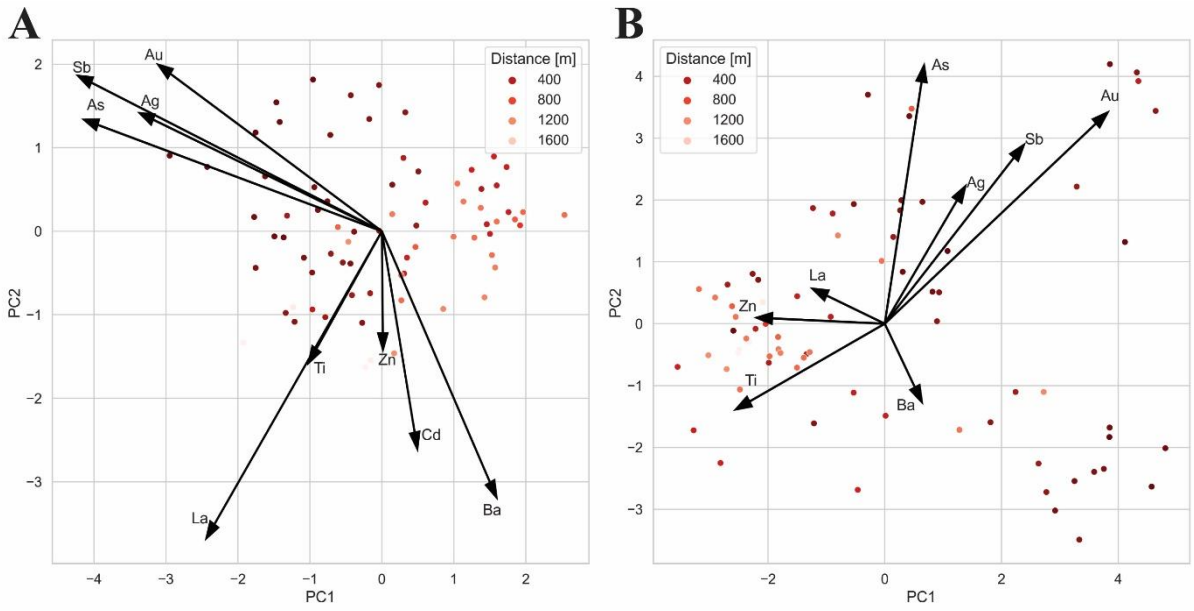

Figure 4.4. Score and loading plots of the Principal Component 1 (PC1) and Principal Component 2 (PC2) for (A) the foliar samples and (B) the rock/soil samples from Waiotapu Geothermal Field. Points are colour coded based on the distance from Champagne Pool.

The complexity of the geothermal system and furthermore, the diverse controls on the uptake of elements by plants (Shtangeeva et al., 2011; Farooq et al., 2016), is reflected in weak to moderate co-occurrence values between rock/soil and foliar chemical concentrations (Figure 4.5): Ag (Pearson R: 0.28 and p-value: <0.01), As (Pearson R: 0.17 and p-value: 0.01), Ba (Pearson R: -0.38 and p-

value: 0.18), and Sb (Pearson R: 0.40 and p-value: 0.18). Inter-elemental correlations with Pearson R for rock/soil and foliar chemical concentrations are shown in Figure A2.4. The low to moderate correlation is not unexpected, other studies have also presented that elemental concentrations between soil and plant samples do not exactly co-vary, due to chemical and biological factors, such as variations in pH and bacterial richness, as well as temperature differences (Borovička et al., 2006; Shtangeeva et al., 2011; Crowther et al., 2019; Sleimi et al., 2021; Ubeynarayana et al., 2021). Furthermore, the element uptake rates can vary amongst plant species and are dependent on their broader environment such as the soil pH (e.g. (Khan et al., 2015; Shahid et al., 2017)).

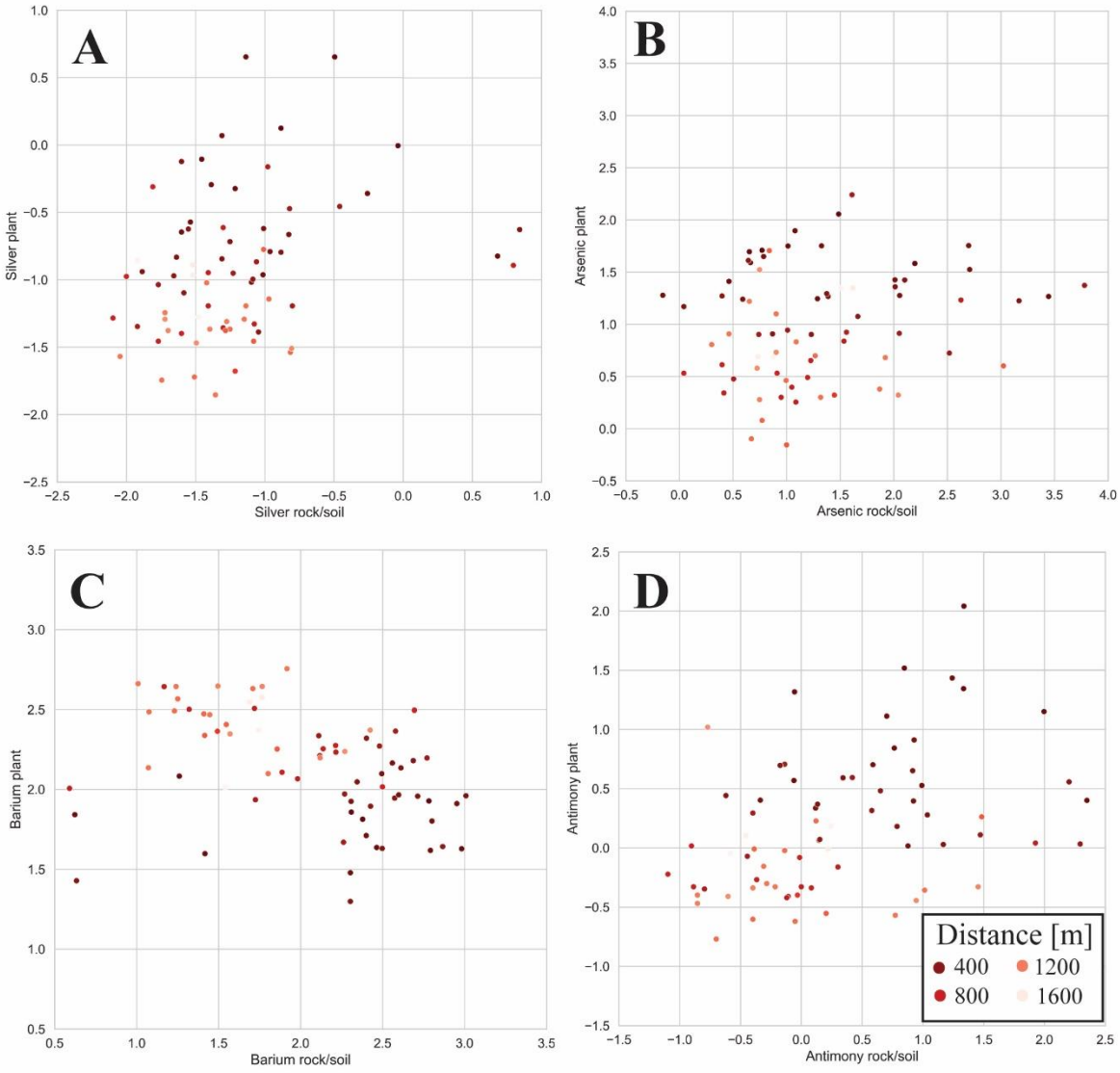

Figure 4.5. Scatterplots of log-ratio transformed chemical concentrations for foliage (y-axis) against rock/soil (x-axis), colour coded by the distance from Champagne Pool in meters. (A) Silver, (B) Arsenic, (C) Barium and (D) Antimony.

Overall rock/soil samples showed higher elemental concentrations than the foliar samples (Table 4.2). In this case, the bioaccumulation ratio was element-specific and non-linear, reflecting the complexity of the geothermal system and how the interrelations between rock/soil and foliar vary greatly throughout Waiotapu Geothermal Field. On average, higher bioaccumulation ratios were present in Ag and Ba, while As and Sb bioaccumulation ratios were significantly lower (Table 4.2). This can potentially indicate a barrier in the rhizosphere caused by mycorrhizal associations, which assist the plant obtaining nutrients and filtering toxic elements (Moyersoen & Beever, 2004). Some measured elemental concentrations in foliar samples are well above the toxic level tolerated in other species (Table 4.2), pointing to their potential as stress factors for plant growth in geothermal environments. Spectrally the kanuka samples show differences between high concentration and low concentration samples which are most prominent in 400-1500 nm and 1700 to 2200 nm (e.g. Figure 2.7).

Table 4.2. Chemical concentration ranges for rock/soil and foliar samples for silver, arsenic, barium, and antimony, phytotoxic levels for other plant species and bioaccumulation ratios from site samples.

Element	Rock/Soil [mg/kg]		Foliage [mg/kg]		Phytotoxic level [mg/kg] (other plant species)	Bioaccumulation Ratio
	Minimum	Maximum	Minimum	Maximum		Average (all samples)
Silver (Ag)	0.01	6.95	0.0003	0.15	3.8 in leaves (Wang et al., 2017)	0.15
Arsenic (As)	0.7	12000	0.019	6.21	0.003 in leaves (Wallace et al., 1980)	0.06
Barium (Ba)	3.9	1018.3	0.42	33.65	137 in soil (Suwa et al., 2008b)	0.14
Antimony (Sb)	0.02	392	0.04	2.87	0.15 in leaves (Shtangeeva et al., 2011b)	0.052

4.6.2 Classification and regression models

The classification on laboratory-based spectral data on the foliage samples showed overall accuracy (OA) between 0.41 and 0.47 with LOOCV without removing any outliers to keep complexity (Table 4.3). The airborne-based spectral data classification showed an improved overall

accuracy between 0.45 and 0.57 after LOOCV (Table 4.3). Satellite-based spectral data classification had an overall higher accuracy between 0.57 and 0.66 after LOOCV (Table 4.3). Higher OA values from the airborne- and satellite-based data are possibly caused by the hyperspectral image being partially sensitive to canopy structure information (Croft et al., 2014; Almeida et al., 2021; Zeng et al., 2022) and samples larger area due to their larger spatial resolutions. Any outliers in the training/validation datasets can significantly lower the overall accuracy when LOOCV is used (Molinaro et al., 2005; Berrar, 2019), regardless, outliers were kept as they represent the high variability in the system.

Table 4.3. Classification overall accuracy values for laboratory-based, airborne-based and satellite-based random forest models. Class-wise error and error matrix is included in the supplementary data.

Element	Overall Accuracy		
	Laboratory-based	Airborne-based	Satellite-based
Silver (Ag)	0.41	0.45	0.58
Arsenic (As)	0.43	0.57	0.63
Barium (Ba)	0.45	0.5	0.66
Antimony (Sb)	0.47	0.48	0.57

Airborne and satellite-based classification maps, showed good agreement between the observed spatial distributions of the samples, despite their large contrast in spatial resolutions (1 m versus 30 m). Classification maps for As, As and Sb indicate high concentrations near Champagne Pool, whereas Ba is enriched further away from the Champagne Pool (Figures 4.6-4.7).

The satellite-based classification models and predictions in conjunction with the ICP-MS foliar chemical data were performed to test the upscaling capability of this method for satellite imagery (Figure 4.7). The same area of kanuka coverage from the airborne-based image was employed as a mask to extract the kanuka covered pixels from the co-registration (Root Mean Square Error of 1.5 m) satellite image. The satellite-based classification models showed overall accuracy between 0.57 and 0.66, slightly higher than the airborne-based predictions (Table 4.3).

The performance of the regression models in laboratory and airborne-based datasets was deficient, with R^2 values between 0.02 to 0.26 and 0.17 to 0.23, respectively. Intriguingly, the maps are spatially congruent; regardless of unsatisfactory performance (e.g. see Table 2.4, Figure 2.5 and S6).

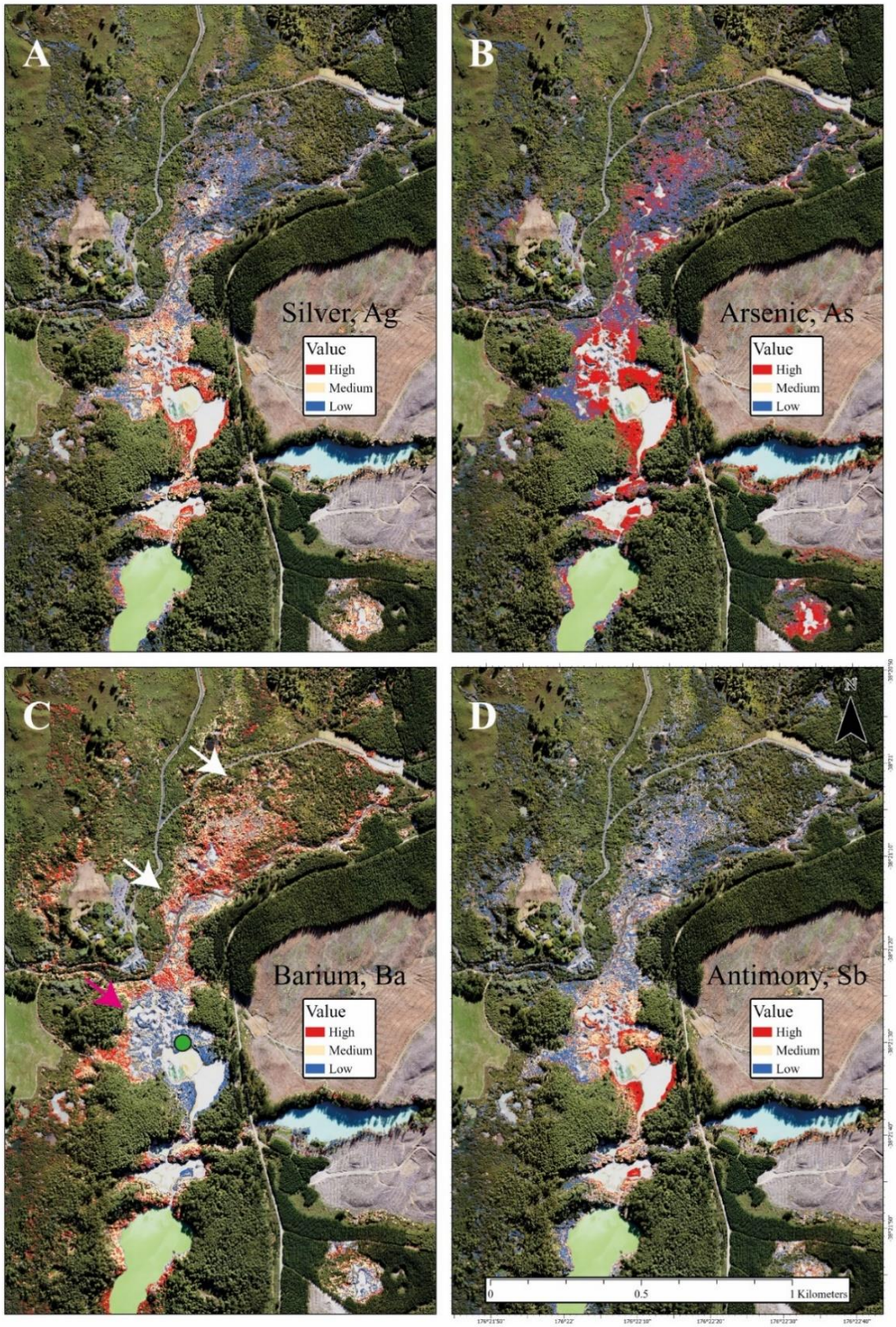

Figure 4.6. Predictions for silver (A), arsenic (B), barium (C), and antimony (D) concentration in plants from airborne-based imagery (high, medium, and low). (C) White arrows point to inferred groundwater mixing and low pH. Pink arrow points to high sulphate areas where barium is not bioavailable to plants. Green circle is the location of rock/soil sample_022 which has baryte crystals (Rodriguez-Gomez et al., 2021a).

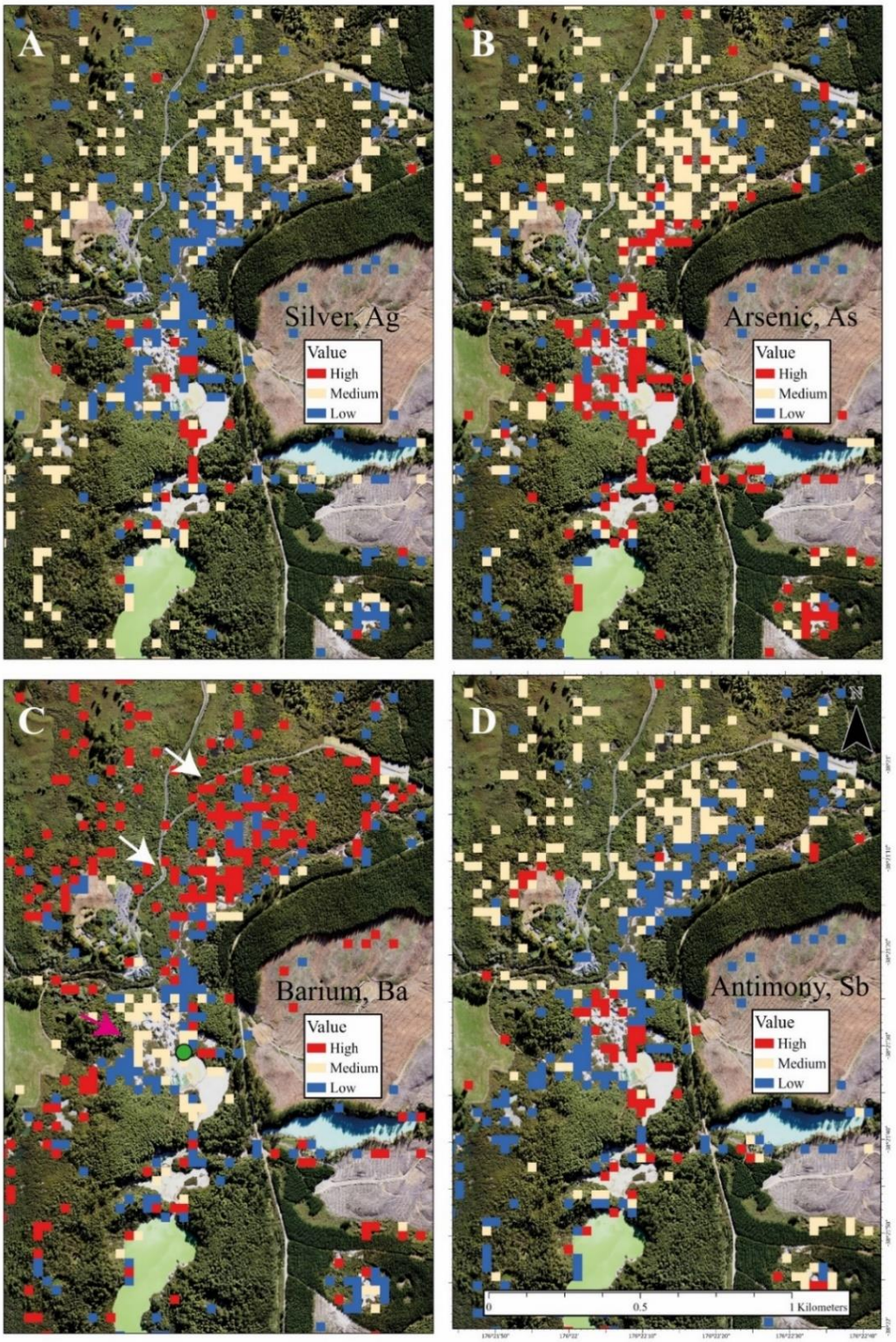

Figure 4.7. Predictions for silver (A), arsenic (B), barium (C), and antimony (D) concentration in plants from satellite-based imagery (high, medium, and low). (C) White arrows point to inferred groundwater mixing and low pH. Pink arrow points to high sulphate areas where barium is not bioavailable to plants. Green circle is the location of rock/soil sample_022 which has baryte crystals (Rodriguez-Gomez et al., 2021a).

From the classification models of laboratory, airborne and satellite-based datasets, the MDA and MDG values from each element's model were extracted, ranked and added to compute a single total variable score and select the important wavelengths (Figure 4.8), following Hong et al., 2016. Only the highest 10% was deemed as important and plotted in comparison to the average plant spectral reflectance for laboratory, airborne and satellite-based spectral signatures (Figure 4.8). Most of the selected important wavelengths are in the visible range for all datasets, and >1000 nm for the laboratory-based dataset (Figure 4.8).

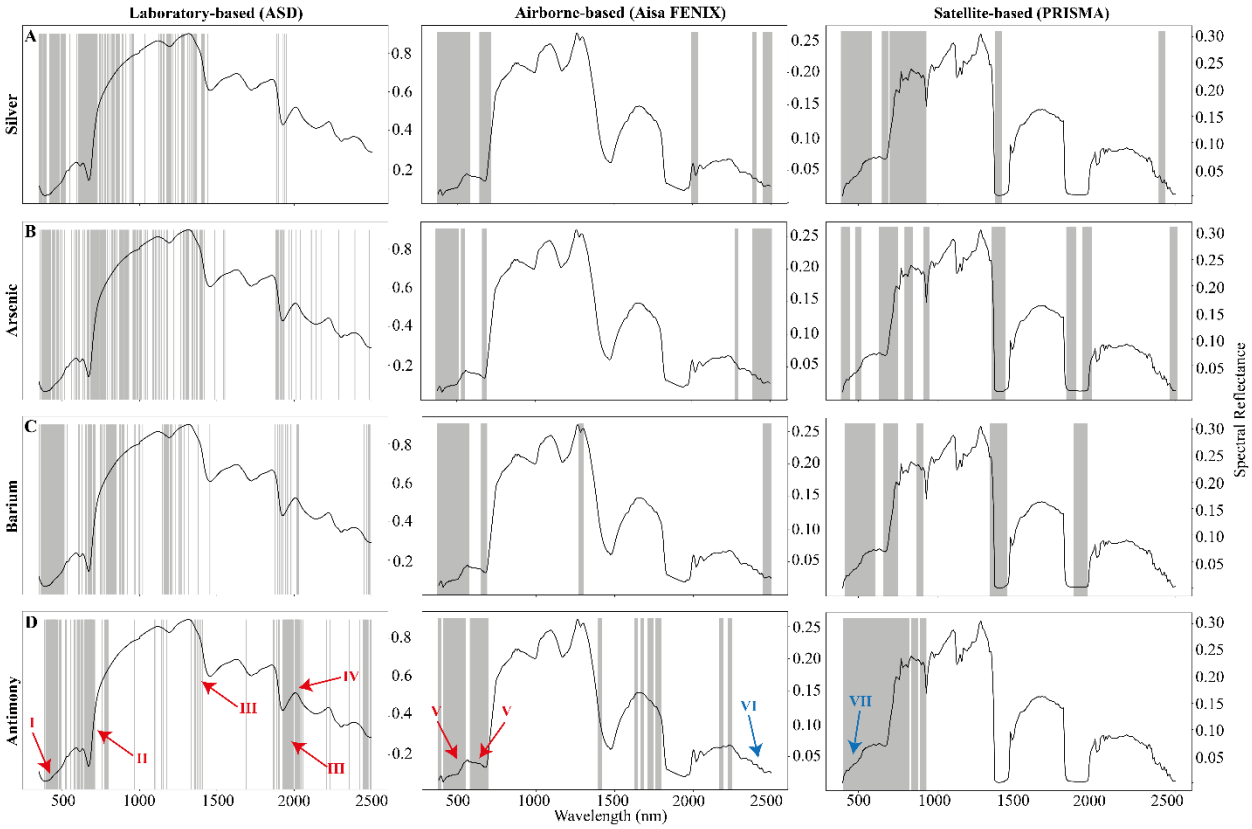

Figure 4.8. Important wavelengths derived from random forest classification models, shown per element (rows) for laboratory-, airborne and satellite-based (columns). (A) Silver, (B) Arsenic, (C) Barium and (D) Antimony. The presented plant spectral reflectance shown is the average spectral reflectance from all field sample sites as measured by laboratory equipment (ASD FieldSpec), airborne (AisaFENIX) and satellite (PRISMA). Red arrows point to significant absorption features (I) chlorophyll and carotenoid-related absorption(~452 nm), (II) Red edge region (680 – 750 nm), (III) Metal-induced stress ~1370 - 1570 nm and ~1825 - 2170 nm, (IV) water content ~ 2000 nm, (V) degradation of foliar pigments 470 – 510 nm and at 550 – 750 nm. Blue arrows point to noisy regions of the spectra (VI) <400 nm and (VII) > 2450 nm.

4.6.3 Spatial distribution of canopy height and approximate surface temperatures

The elemental distribution maps generated from elemental ICP-MS measurements and hyperspectral (VNIR/SWIR) spectra (airborne and satellite) can be compared with the LiDAR-derived plant height and TIR-based approximate ground temperature maps, only within the kanuka land cover type (Figure 4.9). Both datasets correlate well with geothermal activity and provide independent corroboration for the generated elemental distribution maps. The two datasets showed a trend between decreasing canopy height and increasing approximate surface temperature within a clear boundary (Figure 4.9C). This observation is consistent with previous studies (Burns & Leathwick, 1995; Muukkonen, 2005; Van Manen & Reeves, 2012). The abundance of shorter plants at low temperatures is interpreted to be due to young plants that have not reached full canopy height and some misclassification of kanuka for rock/soil (~3% misclassification, error matrix in Table A2.1).

Furthermore, Ag, As and Sb present similar behaviour in terms of plant height (Figure 2.10). The areas with high elemental distribution of these three elements tend to manifest as “shorter” kanuka plants, while the low elemental distributions often co-occur with “taller” kanuka plants. On the other hand, Ba presents the opposite behaviour (Figure 2.10).

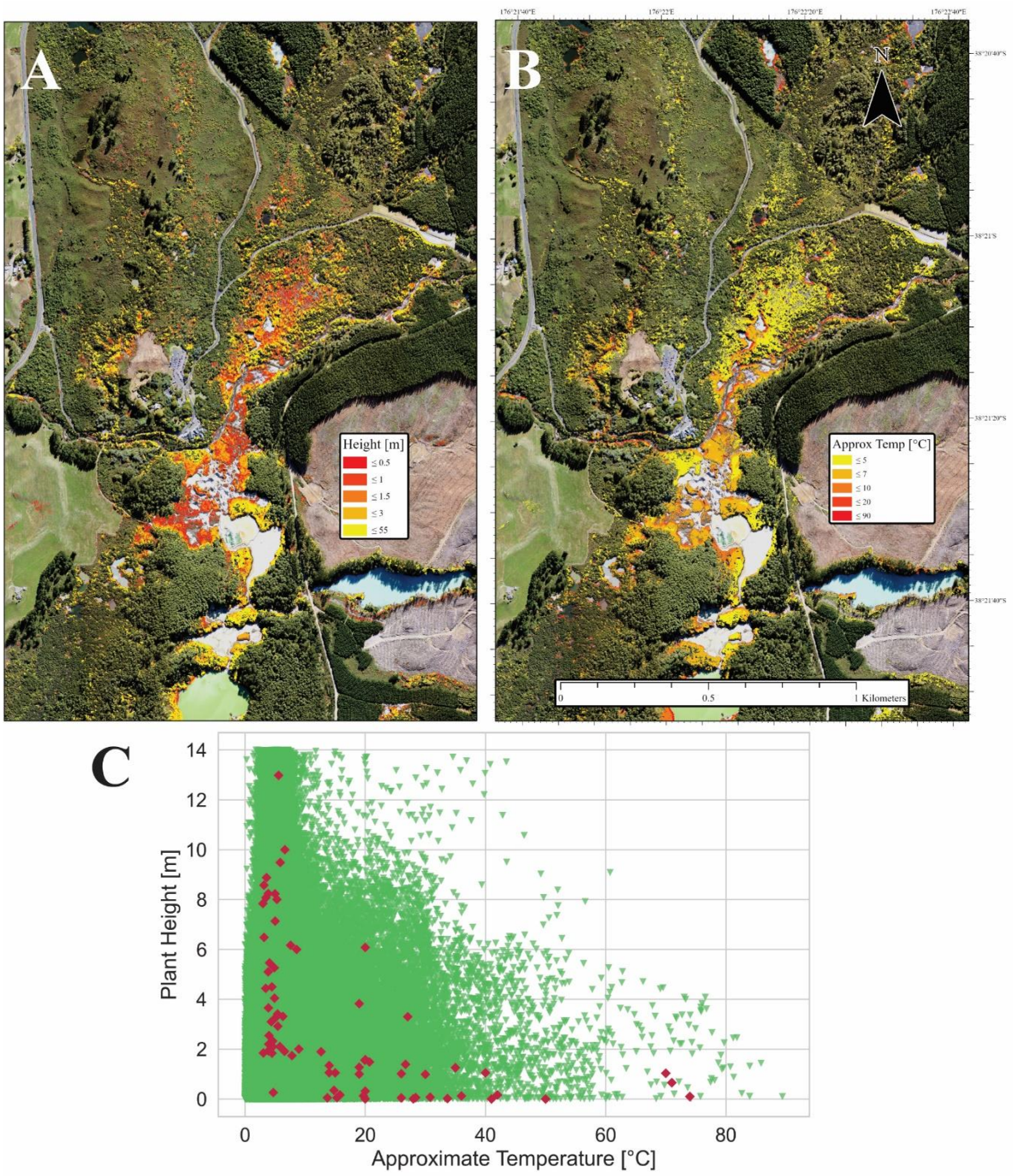

Figure 4.9. (A) Kanuka plant heights from the LiDAR data. (B) Approximate temperatures from airborne-based thermal infrared data. (C) Comparison plot between plant height in meters and approximate temperatures in °C. Red diamonds show the distribution of the plant field samples.

4.7 Discussion

4.7.1 A new tool for elemental zonation using hyperspectral remote sensing

Previous studies have reported changes in the physical and chemical behaviour of plants living in geothermal environments (Burns & Leathwick, 1995; Van Manen & Reeves, 2012; Lattanzi et al., 2020). Such physicochemical changes can become an exploration and monitoring proxy if quantified with hyperspectral imaging. For the first time, this study shows the fingerprinting of physicochemical changes in foliage due to geothermal activity, which can be captured spatially and independently by laboratory, airborne and satellite-based hyperspectral (VNIR/SWIR) remote sensing.

The predicted element zonation maps show strong similarities with the ground samples/field observations (Figures 4.6-4.7 and Figures A2.11-A2.12). The predicted element zones mostly co-occur spatially with physical changes to the canopy structure (e.g. LiDAR-based height) and TIR-based ground temperature (Figure 4.9). These changes in kanuka canopy structure are in line with ground-based studies, documenting kanuka shrub becomes significantly shorter (<0.5 m in height) when ground temperatures are >40°C (Burns & Leathwick, 1995; Smale et al., 2018), and roots start growing horizontally (Van Manen & Reeves, 2012). Spectral changes can therefore be due to a combination of leaf area and chlorophyll content changes, degradation of carotenoids, as well as reduction of plant biomass (Shtangeeva et al., 2011; Sanches et al., 2013; Dong et al., 2019). Nevertheless, high concentrations of Ag, As and Sb can also occur in canopies >1 m in height (Figure 2.10).

The remotely (e.g. airborne and satellite) mapped elemental anomalies alone could still indicate physical variations to the canopy structures associated with the underlying geothermal system (Figures 4.6-4.7). However, our laboratory-based classification models returned similar overall accuracy to the airborne models (0.41-0.47 versus 0.45-0.57, Table 4.3), and very similar spectral band importance regions within the spectrum studied, even though the laboratory-based samples had all been dried and grounded. This highlights that the retrieved foliar element concentration represents a combined effect of thermal and metal-induced stress within an active geothermal area. The marginal but better OA for the air- and spaceborne data (e.g. Table 4.3) can further indicate a small contribution from the canopy structure and neighbouring objects (e.g. exposed ground) due to the increased pixel size.

4.7.2 Remote detection of foliar element concentration in geothermal systems

Regardless of being thermal-, water-, metal- or nutrient-induced, plant stress can often be detected within VNIR by multispectral (Poblete et al., 2020) and hyperspectral remote sensing (Slonecker et al., 2009; Delalieux et al., 2009; Rathod et al., 2018). The assessment of important wavelengths in remotely detected foliar element maps (Figure 4.8) can further yield insights into geothermal systems and changes in shallow hydrological properties. Our study assessed Ag, As, Sb and Ba which are commonly occurring elements in geothermal systems globally (e.g. Yellowstone in U.S.A., Cerro Pabellon in Chile, The Geysers, U.S.A.) (Smith et al., 1987; Macur et al., 2004; Reich et al., 2020). While those elements alone have no unique spectral reflectance within the VNIR and SWIR regions, their presence in plants can be inferred indirectly due to the spectral changes. Our classification models returned important wavelengths for all elements, with unique important wavelengths detected for Ag, Sb and Ba, whereas As shares most of its important wavelengths with the other elements (Table A2.5).

Within the VNIR region, the decrease of chlorophyll-a absorption can cause shifts in the visible and red regions (Sims & Gamon, 2002; Sanches et al., 2013) (Table A2.2), indicating metal and thermal stress (Rathod et al., 2018). In this region, all four elements show an important wavelength at ~452 nm in the laboratory and airborne-based models (Figure 4.8), which coincides with chlorophyll and carotenoid-related absorption (Sanches et al., 2013). At longer wavelengths, Ag, As and Sb for laboratory-based (~642-696 nm) and airborne-based models (~490, ~510, and ~670 nm) returned a series of important wavelengths (Table A2.5), located in a wavelength range that has been associated to the degradation of foliar pigments at 470–510 nm and at 550–750 nm (Sanches et al., 2013) (Figure 4.8). Ba also presents important wavelengths within these two regions at ~480, ~500, and ~670 nm, both in the laboratory and airborne-based models and ~500 and ~690 nm in the laboratory and satellite-based models (Table A2.5). Notably, the four elements present an important wavelength at ~720 nm for the satellite-based model, a wavelength where a shift in the red-edge can signal metal-induced stress (Slonecker et al., 2009). While this region coincides with a minor water vapour absorption feature (Duarte, 1995), this part of the spectrum has also been highlighted in the laboratory-based models (Table A2.5).

Our foliar element classification model highlighted a range of important wavelengths between 800 to 1300 nm, indicative of internal leaf structure damage due to external environmental factors (Roy, 1989; Rathod et al., 2018). For example, Ag has been reported to inhibit water flow across cell membranes leading to leaf damage (Cox et al., 2016; Wang et al., 2018). Similar to Ag, exposure to As can damage cellular membranes, causing electrolyte leakage (Kabata-Pendias, 2010;

Finnegan & Chen, 2012). Both, Ag and As share important wavelengths in the laboratory-based model at ~820-890 and ~1133 nm. Silver presents important wavelengths in the satellite-based model from ~800–910 nm, while As does at ~820 and ~930 nm. Sb can cause growth retardation and inhibition of photosynthesis (Feng et al., 2013), presenting important wavelength regions for the laboratory-based model at ~970-1180 nm, and in the satellite-based model at ~887 nm. These three elements (Ag, As, and Sb) do not present any important wavelengths in the airborne-based model in this region (Table A2.5).

Distinctly, Ba presents important wavelengths in the three scales, sharing wavelengths at ~820 and ~890 nm with Ag, at ~820-890 and ~1180 nm with As and ~1180 nm with Sb at the laboratory-based scale. The airborne-based model has important wavelengths at ~1280 nm and for the satellite-based model there are important wavelengths at ~802-910 nm (Table A2.5). Barium, which can be toxic to plants (>5 mg/kg) (Dunn, 2007; World Health Organization, 2016), can cause stomatal closure and perturbation in the foliar metabolism (Suwa et al., 2008), causing overall plant growth rate reduction (Sleimi et al., 2021). The stomata function regulates gas transfer between plants and the atmosphere for photosynthesis, plants living in geothermal areas have been reported to present lower stomatal conductance and cell membrane damage (Pippucci et al., 2015).

Within the SWIR, the leaf water content can impact spectral reflectance between ~1300-2500 nm, causing 78-83% of the reflectance (Tucker, 1979). Water absorption regions are a valuable indicator of metal-stress, at wavelengths ~1370-1570 nm and ~1825-2170 nm (Curran, 1989b; Rathod et al., 2018) (Figure 4.8). Some of these wavelengths are also sensitive to lignin and protein production, which can be affected by metal uptake-induced stress (Götze et al., 2010; Kokaly & Skidmore, 2015). Our foliar element maps show much less important wavelengths from the SWIR region than the VNIR (Figure 4.8). This can be due to SWIR data having more noise which can degrade model performance, as well as atmospheric processes. Important wavelengths close to indicative regions at laboratory-based scale for Ag and As are located at ~1400, ~1880, and ~2100 nm and several at ~2000 nm for satellite-based models. Ag and Sb share important wavelengths at laboratory-based scale at ~1940, nm, whereas, As and Sb only at ~1980 nm and for satellite-based models at ~ 1400 nm. The presence of important wavelengths in this range throughout the three scales indicates deterioration of the foliar health regarding water content.

The high amount of shared important wavelengths by Ag, As and Sb reflect their similar behaviour in the geothermal environment, congruent with the PCA results (Figure 4.4), as their solubility and toxicities strongly depend on pH and temperature (Ballantyne & Moore, 1988; Wilson et al., 2010). These factors directly affect kanuka's foliar uptake regardless of the possible

mycorrhizal associations which assist kanuka in obtaining nutrients and filtering the uptake of toxic elements (Moyersoen & Beever, 2004), seemingly affecting the plant similarly. In contrast, Ba presents a different behaviour which shows up in its important wavelengths, highlighting its slightly different effects in the foliar internal structure. Furthermore, Ba also has recurrent important wavelengths in the range from ~1280-1400 nm for the three scales (Figure 4.8) (Table A2.5), where leaf internal damage and foliar water content are detected (Rathod et al., 2018).

The classification error metrics resulted in moderate results (0.41 to 0.66), in future studies other pre-processing and post-processing techniques should be tested (e.g. adjusting atmospheric values, pixel unmixing, and elemental data transformations). Furthermore acquiring higher number of samples can allow for different validation methods to be tested (e.g. K-fold cross validation, bootstrapping). Regardless of the moderate error metrics results, the agreement between laboratory, airborne and satellite-based important wavelength areas and their relation to such wavelengths to vital plant processes, as well as their spatial congruency, highlights the feasibility of remote sensing to study the behaviour of plants living in geothermal areas.

4.7.3 Geology and biogeochemistry - relations and processes

Waiotapu Geothermal Field is an ignimbrite-hosted geothermal system with inherent complexity due to permeability and porosity changes influencing groundwater movement and hydrothermal alteration at cm to meter scales. Overall, the northern area is characterised by acid-sulphate alteration, whereas the southern region has near-neutral high-chloride water pools with silica deposits (Giggenbach et al., 1994; Rodriguez-Gomez et al., 2021), these surface features are tightly intermixed in some areas (Figure 2.2).

Both ground samples and foliar maps show elevated Ag, As and Sb concentrations in proximity to Champagne Pool (Figure 4.2), indicating the current location of the deep-seated, chloride-rich and near-neutral pH water discharge. These elements signal deep parental waters (Bundschuh & Maity, 2015), and epithermal ore deposits (Simmons et al., 2016; Smith et al., 1987). Elements like As and Sb, when in soluble state and under certain pH and temperature conditions (Ballantyne & Moore, 1988; Tschan et al., 2009; Wilson et al., 2010) become readily bioavailable and are extremely toxic to plants (Finnegan & Chen, 2012). Mycorrhizal associations can assist plants by filtrating the translocation of toxic elements from the root (e.g. As and Sb) and obtaining nutrients for the plant, in exchange for glucose and energy attached to the roots (Dunn, 2007; Li et al., 2018; Tschan et al., 2009). But as shown by our samples, a considerable and toxic amount of these elements gets translocated to the foliage of kanuka (Table 4.2), affecting the foliage to a degree detectable by hyperspectral remote sensing (VNIR/SWIR).

Further away from the high-chloride, near-neutral pH water pools, Ag, As and Sb decrease in concentration, while other elements, such as Ba become bioavailable and easily uptaken by plants. Foliar enrichment in Ba is a good pathfinder element to identify zones where hot geothermal water is mixing with cold groundwater in the periphery of epithermal systems (Bundschuh & Maity, 2015; Dunn, 2007). Ba solubility increases with decreasing pH, whilst in waters with high sulphate content, Ba reacts to form an insoluble salt (World Health Organization, 2016). We observe this behaviour within our data and classification maps as Ba foliar concentrations increase in the peripheral areas (white arrows in Figures 4.6-4.7) and decrease in areas with neutral-pH fluids with high concentrations of sulphate where Ba is not bioavailable to plants (pink arrow in Figures 4.6-4.7). This is also observable between rock/soil and foliar Ba concentrations (Figures A2.6-A2.7); high rock/soil concentrations of Ba are present north to Champagne Pool, but not bioavailable to plants. The Ba near Champagne Pool may be present as insoluble salts or mineral precipitates (green dot in Figures 4.6-4.7), halting plant bioavailability. Further away, Ba concentrations in rock/soil samples are low, probably due to samples being organic matter rich.

4.7.4 Upscaling

With the spread of airborne imaging and now with the new generation satellites, such as PRISMA and EnMAP, a new avenue for chemical monitoring in Earth's surface can emerge. However, both airborne and satellite hyperspectral have some limitations and challenges, data can be impacted by mixed pixels (e.g., background soil, mixed plant species) (Bhatt & Joshi, 2020; Annam & Singla, 2021), nearby highly reflective surfaces (e.g. large areas of silica sinter deposits) (Lyapustin & Kaufman, 2001; Sun et al., 2021), and canopy structure changes (e.g. canopy height, leaf area) (Almeida et al., 2021; Zhang et al., 2021). In this study, the large pixel size associated with the satellite data resulted in the highest classification accuracies, which is interpreted to be due to spectral mixing and exposure of bare ground (Su, 2016). While these limitations and challenges are inherent of imaging techniques, our workflow returned with highly coherent spatial distributions of element concentrations (Figures 4.6-4.7), matching with independent remote sensing data (TIR and LiDAR), and existing geological/geochemical information.

The current study targeted a New Zealand specific plant species to demonstrate the capability in hyperspectral remote sensing (VNIR/SWIR) to detect slight changes in foliar spectra due to underlying geothermal activity. Similar proxy species in other parts of the world can be studied in geothermal areas, including lichens and shrubs in Italy (*Evernia prunastri*, *Calluna vulgaris*), sagebrush in USA (*Artemisia tridentata*), shrubs in Kenya (*Tarchonanthus camphoratus*) or grasses in Mexico (*Allenrolfea occidentalis* and *Thypa dominguensis*) (Way & Hall, 2001; Nash et al., 2003;

Manzo et al., 2013; Pippucci et al., 2015; González-Acevedo et al., 2018; Lattanzi et al., 2020). These indicator species can provide a global utilisation of hyperspectral remote sensing to track geothermal activity through the foliage.

4.8 Conclusions

The presented study shows the potential of kanuka foliage as a proxy to map geothermal activity in New Zealand with hyperspectral remote sensing (VNIR/SWIR). This study focused on heat- and metal-induced stress on the physicochemical state of foliage, proposing a new mapping approach using hyperspectral remote sensing. Simultaneously, the height and thermal changes were analysed independently with LiDAR and airborne TIR, showing a positive correlation between temperature increase and plant height reduction in many areas (Figure 4.9).

The elements silver (Ag), arsenic (As), barium (Ba), and antimony (Sb) were the focus of this study due to their relevance to understanding and monitoring geothermal areas. Our results confirm that Ag, As and Sb behave similarly in geothermal systems, raising to the surface with deep parental waters and depositing along its pathways at various rates (Bundschuh & Maity, 2015). Soluble forms of these metals can be uptaken by nearby plants and cause stress. High concentrations of Ag, As and Sb in foliage are found near the main focal point where high-chloride near-neutral waters discharge on the surface (i.e. Champagne Pool). Whereas high concentrations of Ba in foliage were found in peripheral areas where cold groundwater mixes with deeper hot fluids (Dunn, 2007) and pH is low (World Health Organization, 2016). To understand the effect of element concentrations in kanuka, we used three spatial scales of remote sensing hyperspectral (VNIR/SWIR) platforms (i.e. laboratory, airborne, and satellite-based). We compared them to elemental concentrations using regression and classification models. Changes in the kanuka foliar spectral response caused by the selected elements in this study were detected in different regions of the electromagnetic spectrum; regions related mainly to chlorophyll absorption, cell structure, and water stress, presenting particular wavelengths for Ba and Sb (Figure 4.8).

The presented methodology proved feasible to map element concentration ranges with airborne and satellite-based, with classification model moderate accuracy results between 0.41 and 0.66 (Table 4.3), congruent spatial map distributions and concordance of results between both dataset results (Figure 4.6-4.7). A similar workflow should be applied and tested for other plant species living in geothermal areas in the future. These results can open new opportunities to explore and monitor geothermal areas with dense plant cover worldwide, with efficient and non-invasive techniques, such as hyperspectral remote sensing.

MASSEY UNIVERSITY
TE KUNENGA KI PŪREHUROA
UNIVERSITY OF NEW ZEALAND

GRADUATE RESEARCH SCHOOL

STATEMENT OF CONTRIBUTION
DOCTORATE WITH PUBLICATIONS/MANUSCRIPTS

We, the candidate and the candidate's Primary Supervisor, certify that all co-authors have consented to their work being included in the thesis and they have accepted the candidate's contribution as indicated below in the *Statement of Originality*.

Name of candidate:	Cecilia Rodriguez-Gomez
Name/title of Primary Supervisor:	Gabor Kereszturi
In which chapter is the manuscript /published work:	Chapter 4

Please select one of the following three options:

(●) The manuscript/published work is published or in press

- Please provide the full reference of the Research Output:

https://doi.org/10.1016/j.geothermics.2023.102716
Published in Geothermics (Elsevier).

( ) The manuscript is currently under review for publication – please indicate:

- The name of the journal:

- The percentage of the manuscript/published work that was contributed by the candidate:

- Describe the contribution that the candidate has made to the manuscript/published work:

( ) It is intended that the manuscript will be published, but it has not yet been submitted to a journal

Candidate's Signature:	Cecilia Rodriguez Gomez — Firmado digitalmente por Cecilia Rodriguez Gomez Fecha: 2023.04.05 16:05:30 -06'00'
Date:	05-abr-2023
Primary Supervisor's Signature:	Gabor Kereszturi — Digitally signed by Gabor Kereszturi Date: 2023.04.06 08:32:58 +12'00'
Date:	6-Apr-2023

This form should appear at the end of each thesis chapter/section/appendix submitted as a manuscript/ publication or collected as an appendix at the end of the thesis.

5 Chapter 5. “Point pattern analysis of thermal anomalies in geothermal fields – and its use for inferring shallow hydrological processes.”

- This chapter has been submitted, reviewed and published in *Geothermics* (Elsevier), under the same title. DOI: 10.1016/j.geothermics.2023.102664

Contributing authors:

- **Cecilia Rodriguez-Gomez** (School of Agriculture and Environment, Massey University, Palmerston North, New Zealand): Conceptualisation, Methodology, Programming, Investigation, Formal analysis, Visualisation, Writing – Original Draft, Writing – Review & Editing.
- **Gabor Kereszturi** (School of Agriculture and Environment, Massey University, Palmerston North, New Zealand): Conceptualisation, Methodology, Investigation, Writing – Review & Editing, Funding acquisition, and Project administration.
- **Melody Whitehead** (School of Agriculture and Environment, Massey University, Palmerston North, New Zealand): Conceptualisation, Methodology, Investigation, Writing – Review & Editing.
- **Robert Reeves** (GNS Science, Wairakei Research Centre, Taupo, New Zealand): Supervision, Investigation, Writing – Review & Editing.
- **Andrew Rae** (GNS Science, Wairakei Research Centre, Taupo, New Zealand): Supervision, Writing – Review & Editing.
- **Reddy Pullanagari** (MAF digital Lab, School of Food and Advanced Technology, Massey University, Palmerston North, New Zealand): Supervision, Writing – Review & Editing.

5.1 Introduction

Magmatic or intrusion-related geothermal systems can develop proximal to active or dormant volcanoes or volcanic fields, typically located near subduction or extensional rift tectonic settings (Pirajno, 2009). However, geothermal systems can occur in any tectonic and crustal setting (even without volcanic activity), where Earth's internal heat can be successfully transported to the near-surface via either conduction or convection (Moeck, 2014). In the case of convective geothermal systems, heat is transported by fluids via the density contrast between uprising hot (i.e., more buoyant) and down-welling cold fluids (Grant, 1982). Hence, convective geothermal systems require adequately permeable media for hot fluids to circulate and develop into a geothermal reservoir (Rowland & Sibson, 2004). If the porosity and permeability of the host rock allows it, the heated fluids can raise to the near-surface forming diverse geothermal surface features such as steaming grounds, fumaroles, hot springs, geysers, mud pools and collapse craters (Lloyd, 1959; Hedenquist & Browne, 1989). Permeability can also be enhanced through the dissolution of primary mineral phases of the host rock via hydrothermal alteration (Heap et al., 2020) or faulting and fracturing (Rowland & Sibson, 2004). Therefore, surface manifestations can provide first-order proxies for the underlying porosity and permeability structures (Mongillo, 1994). In other geothermal system studies modelling of convection cells has shown a tendency to "synchronise" and form patterns directly related to subsurface permeability pathways (McLellan et al., 2010; Patterson et al., 2018).

The underlying permeability and porosity structure hosting convecting hot fluids can be explored via a variety of geophysical techniques (e.g. electrical, magnetic) and interpreted from other types of geophysical techniques, such as remote sensing. Remote sensing techniques including optical (350–2500 nm) and thermal infrared (TIR) (7500–13000 nm) have been widely used (Reath & Ramsey, 2013; Reeves & Rae, 2016; Hoang & Koike, 2018). Optical remote sensing works in regions of the electromagnetic spectrum where stretching and bending-related absorption features can be detected for typically secondary, hydrated clay minerals and sulphates (Chabrillat et al., 2002; Kereszturi et al., 2020; Savitri et al., 2021), or characterising vegetation cover (Chakraborty et al., 2021; Zhu et al., 2021). TIR remote sensing measures the emitted thermal energy by a surface object, providing a comprehensive platform to detect thermal anomalies (Darge et al., 2019), estimate heat output (Jaworowski et al., 2010; Seward et al., 2018) and monitor spatio-temporal changes of the upper parts of the geothermal reservoir (Reeves & Rae, 2016; Heasler & Jaworowski, 2018). Geothermal fields often consist of clusters of smaller thermal anomalies (Figure 5.1), representing discrete point locations where heat and permeability constraints are in constant search for equilibrium within a geothermal system. Furthermore, TIR remote sensing can identify surface thermal anomalies

in a more localised, time-efficient and cost-effective manner than other geophysical methods (e.g. magnetic or electric surveys) (Chan et al., 2018; Cigna, Tapete, & Lu, 2020).

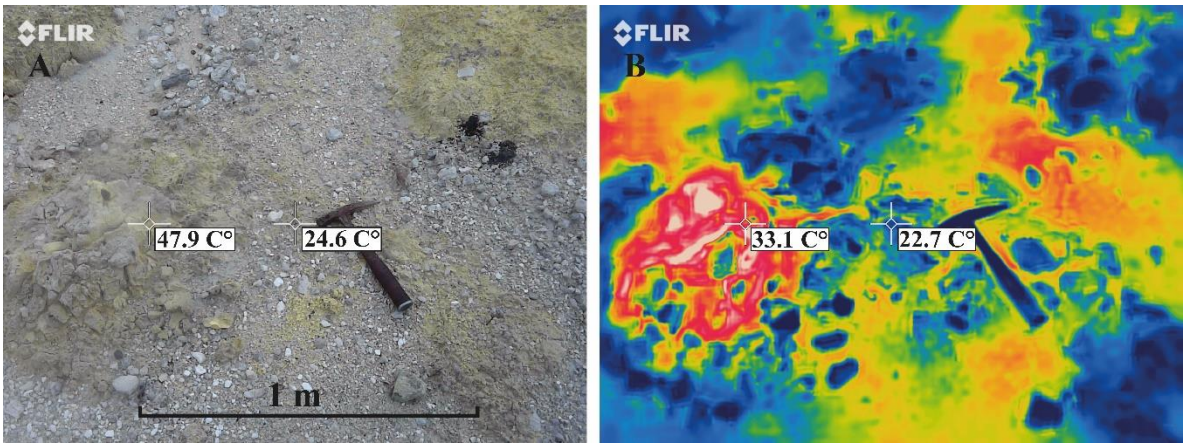

Figure 5.1. (A) Large-scale temperature change within short distances captured by a Handheld FLIR instrument of the same area at the Waiotapu Geothermal Field. (A) RGB image. (B) Thermal Infrared Image.

Point patterns can consist of any mapped object locations (e.g. trees, surface thermal anomalies) within a delineated area (Ben-Said, 2021). Point pattern analyses have been used in volcanology (Connor & Hill, 1995; Runge et al., 2016), geothermal prospecting at a regional scale (Carranza et al., 2008), ecology (Erfanifard et al., 2021), and archaeology (Brandolini & Carrer, 2021). Randomness test-statistics compare observed point locations to a null hypothesis of complete spatial randomness (i.e. described by a homogeneous Poisson process) (Daley & Vere-Jones, 2003). Any departure from this null hypothesis then suggests either clustering or maximum/uniform spacing of these points that are estimated across the whole area (first-order statistics – Clark & Evans, 1954), or over a range of distances (second-order statistics - Ripley, 1979). Application of these test-statistics requires both point locations and the delineated area. The definition of this area is non-trivial, this problem is exasperated in cases where the area cannot be defined directly from geological or geomorphological features (Runge et al., 2015). If the null-hypothesis of complete spatial randomness is rejected by these test-statistics, then probability surfaces can be used to estimate underlying structures from which these points are drawn. Kernel Density Estimates (KDEs), provide empirical approximations of this surface. KDEs have been used for forecasting purposes in seismology (Frankel, 1995) and volcanology (Connor et al., 2019). The dimensions of the kernel bandwidths used to build these surfaces may also be informative as to underlying structures (Cañón-Tapia, 2022).

This study applies point pattern analyses (e.g. Clark-Evans, Ripley's K-test and KDEs) to geothermal areas. We hypothesise that the characteristic distribution of thermal anomalies within a geothermal field extracted from TIR imagery can be linked to underlying shallow hydrology and

geological features (e.g. permeability pathways). Furthermore, we hypothesise previous regional scale point pattern analysis (Carranza et al., 2008) is also applicable at much smaller scales (i.e. within a single geothermal system), since permeability can be controlled by shallow fluid flow, initial host rock porosity and its associated hydrothermal alteration history (Lamur et al., 2017; Liu et al., 2019).

5.2 Geological setting

The Taupo Volcanic Zone (TVZ) is an intra-arc continental rift with an overall NNE-SSW orientation, situated in the central part of the North Island of New Zealand (Wilson & Rowland, 2016). The causes of its extension and notable volcanic productivity are still not completely understood (Seebeck et al., 2014; Bertrand et al., 2022), but approximately four times the erupted magma is believed to be trapped at depth feeding the ~20 geothermal systems (Figure 5.2) with a total thermal energy release of ca. 4.2 GW (Wilson & Rowland, 2016).

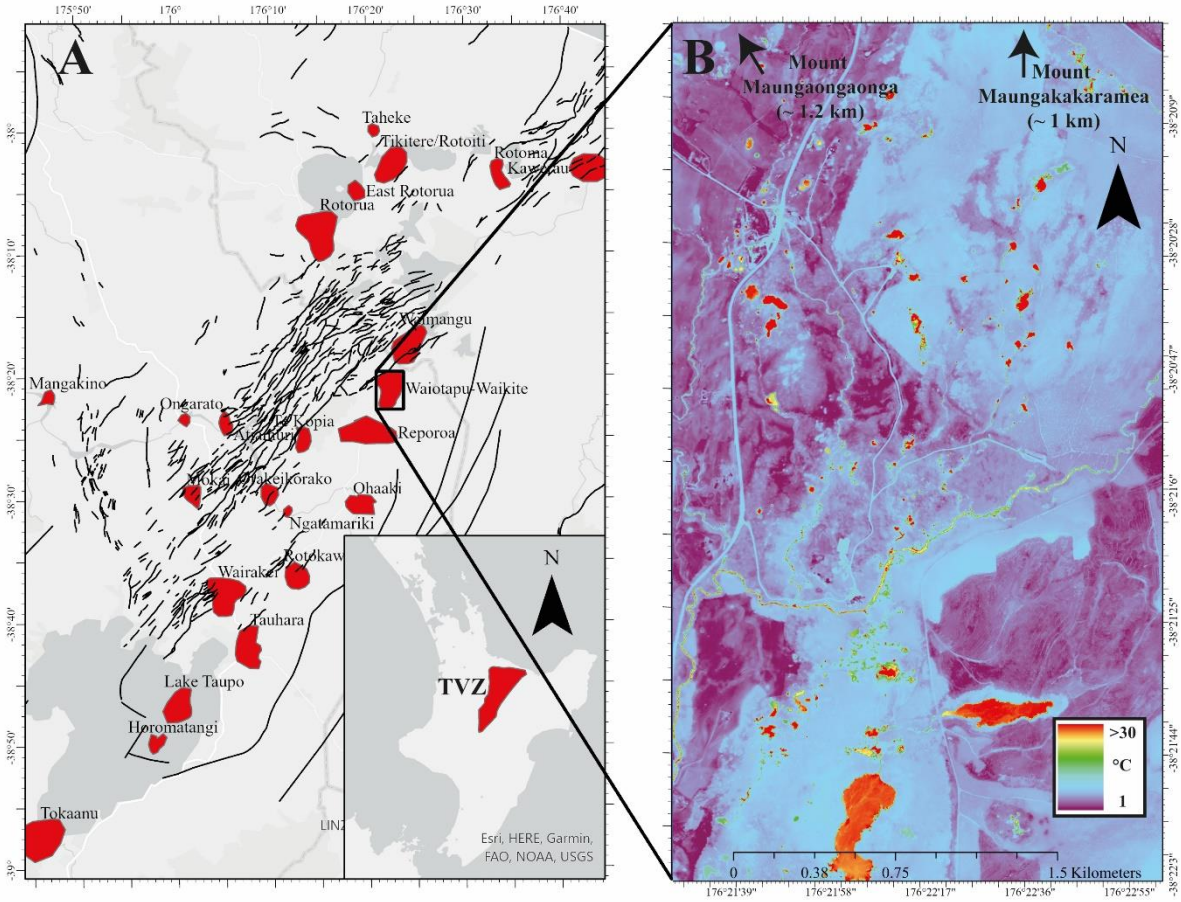

Figure 5.2. (A) Location map of Taupo Volcanic Zone within the Central North Island of New Zealand with red polygons indicating active geothermal areas [modified from (Bibby et al., 1995)]. Black lines are the mapped faults, adopted from QMap Project, GNS Science. (B) Night-time false colour TIR imagery of Waiotapu Geothermal Field.

Waiotapu Geothermal Field is located in the central rhyolitic segment near the west boundary of the TVZ (Rowland et al., 2010) (Figure 5.2) with a heat output of ~500 MW (Kaya et al., 2014). Waiotapu Geothermal Field exhibits a variety of surface features including steaming grounds, fumaroles, acid-sulphate alteration, silica sinter deposits and collapse craters (Hedenquist & Browne, 1989). The driving heat source is located to the south of Maungakakaramea and Maungaongaonga domes (Figure 5.2), flowing mostly to the south in a horizontal manner (Kaya et al., 2014), with a layer of shallow (<50 m), low vertical permeability ($1.17 – 9.90 \times 10^{-15}$ m^2) host rock known as Huka Falls Formation comprised by mudstones acting as a cap rock (Risk et al., 1994). Subsurface lithology is mostly comprised of pyroclastic deposits, including welded ignimbrite and unlithified ash and breccia deposits, with greater horizontal (up to 990×10^{-15} m^2) than vertical (up to 45×10^{-15} m^2) permeability (Kaya et al., 2014). Waiotapu Geothermal Field is classified as a "Protected" geothermal field by Waikato Regional Council, the regional government agency responsible for environmental management. After the first exploration surveys took place in the 1960s, no power production commenced due to the naturally low permeability and reduced permeability caused by hydrothermal mineral precipitates, including quartz, pyrite, calcite, adularia and white micas (Steiner, 1963; Hedenquist & Browne, 1989). Seemingly, normal faulting, imperceptible smaller faults and hydrothermal eruption breccias control the locations of the surface geothermal manifestations (Hedenquist, 1991; Wood, 1994). The closest active known faults, Ngapouri and Paeroa are located 2.5 and 5 km away, with a strike of southwest to northeast (305-55°) and southwest to northeast (310-50°), respectively (Smith et al., 1984; Grindley et al., 1994). There are no documented active faults cross-cutting the geothermal field, however, it is dissected by ring faults from the northern margin of the Reporoa caldera situated in the southern parts (Nairn et al., 1994).

Different hydrothermal alteration/deposition zones at Waiotapu Geothermal Field have been mapped using hyperspectral (VNIR/SWIR) imagery, we have based our lithological zones on Rodriguez-Gomez et al., (2021), as it is the most recent lithological mapping and the only one with hyperspectral remote sensing techniques. The surface lithology can broadly be grouped into three zones; 1) acid-sulphate alteration, occurring mostly along the north of the system, these host mainly rhyolitic rock and have been hydrothermally altered to clays, with mud pools at the surface and overall higher temperatures (i.e. 47°C, Figure A3.1, derived from Chapter 3), 2) "mixed" alteration, on the central-southern area of the field where a combination of chloride-rich water rising through irregularly distributed sulphur-rich waters forms acid alteration causing collapse craters, recrystallization of the ground-mass and veins filled with quartz, pyrite and calcite, 3) silica deposition, from chloride-rich springs at water table level in the central-south area of the field (Hedenquist & Browne, 1989).

5.3 Data and methods

5.3.1 Thermal data

Thermal Infrared (TIR) imagery of Waiotapu Geothermal Field was collected at night (20:30-23:30 UTM +12h) on 13 April 2019, with an airborne FLIR A615. The data processing is detailed in Reeves & Sanders, (2019). The surface brightness temperatures (i.e., radiated heat) were converted to kinetic temperature using ground temperature data from water bodies measured in tandem with the airborne acquisition. The spatial resolution of the TIR image is ~0.7 m and the area used covers ~11 km^2.

5.3.2 Thermal Anomaly Candidates selection

The heat distribution within active geothermal systems is inherently complex. Waiotapu Geothermal Field shows a wide range of temperature anomalies from ambient temperature up to >80 °C and of different sizes (very small cm^2 to a few 100s m^2). Abrupt temperature changes in small areas (10 m^2) present in certain regions are assumed to be related to narrow vertical columns with large vertical permeability, which allows hydrothermal fluid transport (Hedenquist, 1991; Sepúlveda et al., 2012).

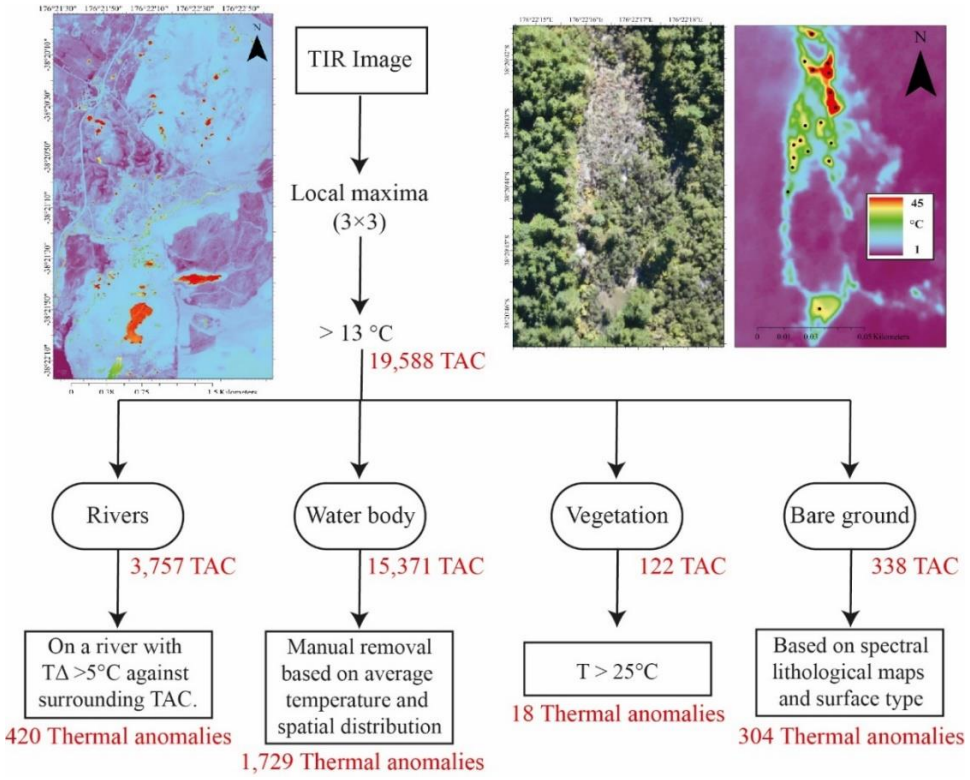

Figure 5.3. Decision flow for thermal anomaly selection from the thermal infrared (TIR) imagery thermal anomaly candidates (TAC), T corresponds to temperature.

Thermal Anomaly Candidates (TAC) from the TIR imagery were extracted following a set of constructed rules specific to this geothermal field (Figure 5.3). First, TAC were extracted using a moving window of 3×3 pixels (i.e. ~2 m^2). This filtering operator returned the locations in which the highest temperature was situated in the middle of the 3×3-pixel matrix. In total, 19,588 TAC were identified (Figure 5.3). Next, only TAC with temperatures above the air temperature at the beginning of the TIR imagery acquisition (i.e. 13°C) were kept. These TAC contain true and false positive thermal anomalies which were carefully filtered and selected based on their location-type (Figure 5.3).

Thermal anomalies on rivers were challenging to select due to water movement and depth as well as their proximity to vegetation that may cause the detection of false thermal anomalies due to sharp temperature contrast. Thus, we kept only those TAC on rivers with an absolute temperature difference of 5°C from their surroundings. Water bodies (e.g. lakes) are also complex and can mask surface manifestations of hot water springs. By visual analysis of temperature histograms, three types of water bodies were assigned (Figure 5.4). Type 1 has temperature variations <5°C and generally lower temperatures <35 °C, a single thermal anomaly in the middle of the water body was assigned with the average temperature value. Type 2 has a seemingly active and minor steaming surface, in which only the hottest TAC with an absolute temperature difference of >5°C with regards to the surrounding area were kept. Finally, type 3 has one or several defined hot water seepages and no visible surface turbulence.

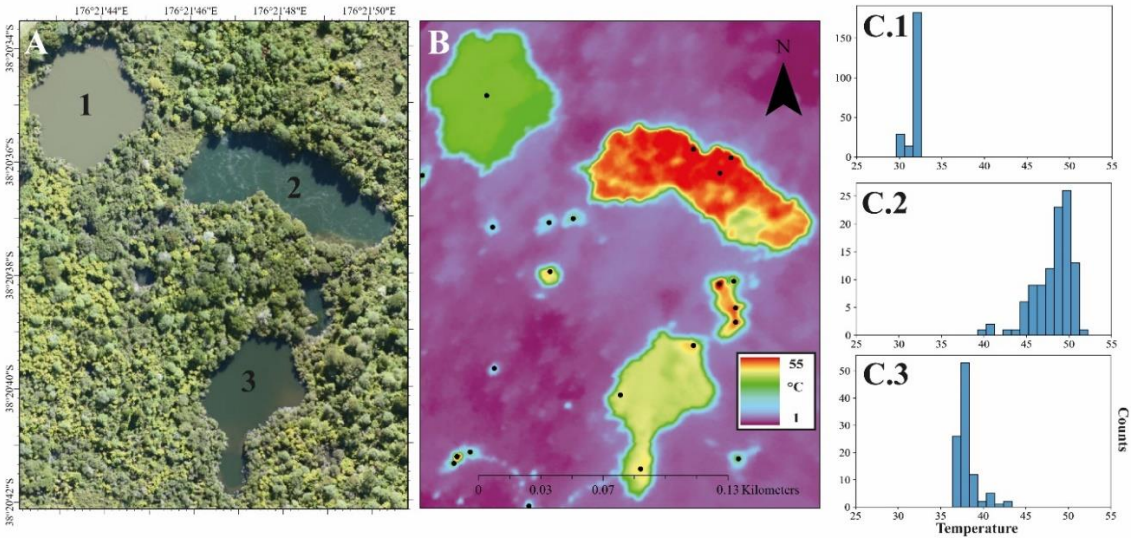

Figure 5.4. Example for the three different lake types and their selected thermal anomalies. (A) RGB orthophoto with the location of three example lake types described in the text. (B) TIR image with the selected thermal anomalies as black dots. (C) Temperature histograms from the entire water body for the three example lakes on A and B. The selection for thermal anomalies in water bodies is explained in the text above.

Vegetation can reduce thermal contrast, masking TAC (e.g. Figure 5.3, top right corner), thus we assigned a larger threshold of >25 °C than for water bodies. This temperature corresponds to the minimum subsurface convection temperature which has been detected on the surface (Seward et al., 2018). Lastly, we kept most of TAC occurring on bare ground, since they have been corroborated using the high resolution RGB imagery and fieldwork.

In total, 2,471 thermal anomalies remained for the point pattern analysis (Figure 5.5B). These were then analysed at different spatial scales using a nested approach, including whole field and sub-field areas (Figure 5.5B). The smaller sub-field areas were selected based on visual clustering, and to cover various areas of the whole geothermal field presenting different lithology.

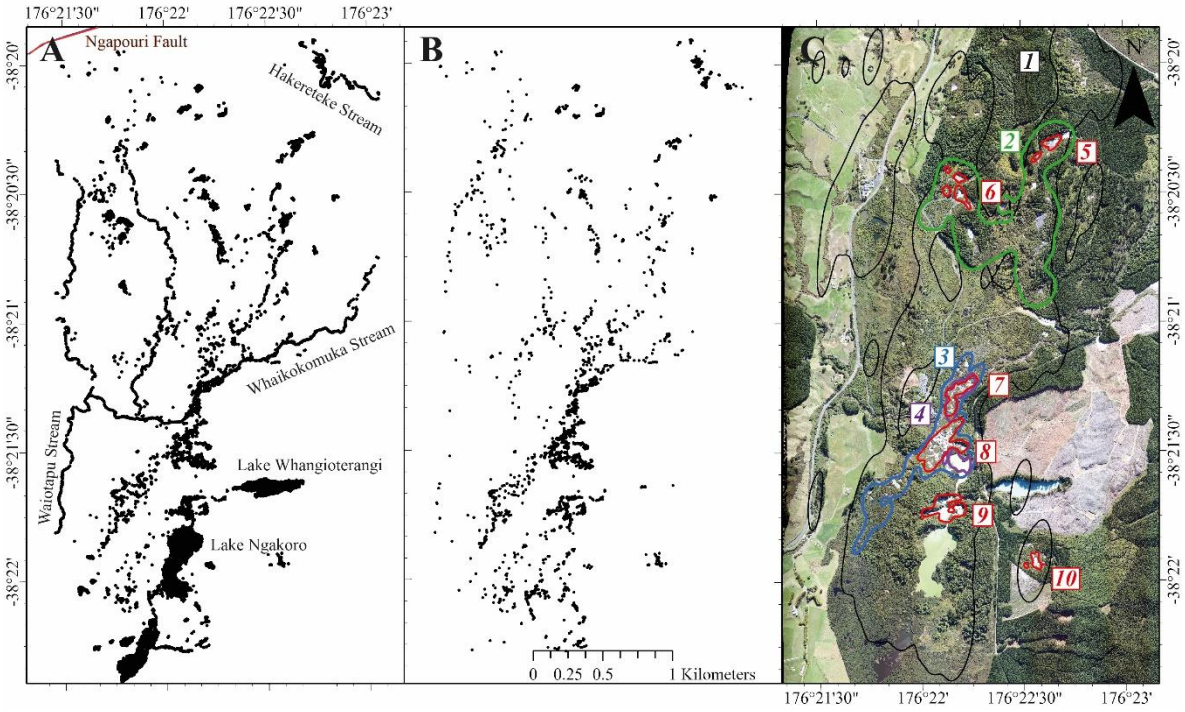

Figure 5.5. (A) Thermal anomaly candidates (TAC) after converting pixels to points (19,588 TAC). (B) Thermal anomalies after carefully filtering TAC (2,471 thermal anomalies). (C) RGB image with overlapping isocontour SAMSE on 99% density contours. (Table 5.1).

5.3.3 Spatial point processes

The spatial thermal regions (i.e. boundary or area) and the corresponding thermal anomaly locations (i.e. points) are required as input for spatial point pattern analyses. Boundary selection is subjective and can substantially influence the results of these statistical analyses (Runge et al., 2015). Ideally, the boundary should represent the true system boundary of the object of study (e.g. geological/geophysical outlines). The spatial boundaries in geothermal systems are commonly

delineated by changes in the lithology, which take place due to the mineral alteration caused by hot fluids and can be detected with electromagnetic and/or resistivity techniques (Bibby et al., 1994; Cherkose & Saibi, 2021; Hacıoğlu et al., 2021). These can encompass deposits and changes in resistivity and magnetic signatures of past and present geothermal activity. Previous resistivity maps have been produced from Waiotapu Geothermal Field with Schlumberger array AB/2 of 500 m which gives a shallow penetration depth (i.e. 300 m) (Bibby et al., 1994) (Figure A3.2). The shape of the 10 Ωm contours resembles the shape of our boundaries for the whole Waiotapu Geothermal Field thermal anomalies (Area ID: 1) (Figure A3.2). However, no boundaries of smaller areas exist from electromagnetic surveys, hence, thermal anomalies from the TIR image were used to estimate a set of potential boundaries. Many boundary options were explored, including rectangular, elliptical, convex hull, and isocontours (Runge et al., 2015; Schmidt et al., 2022). The results from two of these are presented here: (1) buffered convex-hull and (2) isocontours derived from kernel density estimations (KDEs).

(1) The convex-hull is the tightest convex (i.e. all of its interior angles are smaller than 180 °) shape enclosing the observed points (Delmelle, 2009). It is commonly used during spatial point process analysis because the convex hull is unique to a set of points (i.e. no subjectivity during delineation). Here, a spatial buffer was added to expand the area to 120% (Runge et al., 2015), to avoid the exclusion of thermal anomalies placed exactly on the boundary during second-order analyses.

(2) The isocontour boundaries are created by taking a single density level (i.e. an isocontour) from a Kernel Density Estimate (KDE) which is a smoothed surface based on the locations of thermal anomalies (i.e. points). First, a bandwidth for this smoothing kernel is estimated and placed onto each point, the surface is built, and then normalised (1/sum) across the area. This smooth surface is the KDE and provides a generalised observation of a theoretical probability distribution, as an estimate of the underlying natural "point-producing" process. There are multiple methods available to estimate kernel bandwidths and results may vary dramatically based on which estimator is used (Connor et al., 2019).

For this work, four different bandwidth estimators were investigated (Table A3.1), three of which gave similar results, thus, only two are presented here. The two bandwidth estimators applied to each set of thermal anomaly areas are the summed-asymptotic mean squared error (SAMSE) (Duong & Hazelton, 2003), and least-squares cross-validation (LSCV) estimators (Rudemo, 1982; Bowman, 1984). Both were implemented via the *ks* package in R (Duong, 2007). These bandwidth selectors are commonly used in point pattern analysis studies (Bebbington, 2013; Connor et al., 2019;

Schmidt et al., 2022), as they often capture the end members of kernel dimensions, and thus the uncertainty range in any results.

SAMSE bandwidths tend towards rounder kernels as the error is calculated across all points simultaneously (i.e. mean-squared error). The LCSV results are generally more elongated as the error is minimised using leave-one-out rules that force the bandwidth to extend in order to catch the more extreme points (i.e. potential outliers) (Wang et al., 2020). Once a KDE surface is built using these bandwidth estimators, a contour level was then selected as the area boundary. For this work, areas were created using the 99% contour (i.e. 99% of the probability density lies within this region).

The spatial distribution of TAC was first assessed with exploratory test-statistics. Including two first-order randomness tests: Clark-Evans test, which compares the mean distance between neighbouring points with the mean distance between neighbouring random points (Clark & Evans, 1954) and the Hopkins-Skellman test, which compares the distance between each point and its nearest point, with the distance to its nearest random point (Hopkins & Skellam, 1954). These test the null hypothesis of complete spatial randomness, and any statistically significant ($p < 0.05$) deviation provide information as to TAC clustering or spacing (Runge et al., 2015). A second-order randomness test, Ripley's test was also applied. This test compares the number of points within a distance *d* of a point with the number of points expected for a random population (Ripley, 1979). This second order test assesses any departure from randomness at different distances across the area, thus it allows observations of clustering and maximum spacing and random point locations at different scales.

5.4 Results

5.4.1 Spatial orientation

Bandwidth estimators provide kernel dimensions the length of major and minor axes and orientation. This kernel orientation may reflect an underlying structure driving the surface locations of thermal anomalies and can be compared to other geological features in the region. The spatial orientation of TAC in the Waiotapu Geothermal Field was analysed for a variety of spatial scales and different locations (Figure 5.5.C, Table 5.1). These are Area ID 1 – encompassing all available data, three medium sized areas (Area ID: 2, 3 and 4) and 6 smaller areas (Area ID: 5, 6, 7, 8, 9 and 10) that include acid-sulphate alteration, mixed alteration and silica deposition (Table 5.1). Some of these areas were also mapped in April 2019 and November 2021 (Area ID: 2, 3, 6, 8, 9, and 10), providing valuable insights into the lithological and geological controls of Waiotapu Geothermal Field.

Table 5.1. Thermal anomaly density for all areas with a buffered convex-hull and isocontour SAMSE and LSCV at 99% density contour as boundary options.

Area ID	Name	Number of thermal anomalies	Area (km^2)	**Thermal Anomaly Density (km^{-2})**	Number of thermal anomalies	Area (km^2)	**Thermal Anomaly Density (km^{-2})**	Number of thermal anomalies	Area (km^2)	**Thermal Anomaly Density (km^{-2})**	Predominant Lithology
		Buffered Convex-hull			Isocontour (SAMSE)			Isocontour (LSCV)			
1	Waiotapu	2,471	11.4	**216**	2,446	4.8	**514**	2443	3.93	**623**	-
2	Northern mudpools	240	0.99	**242**	238	0.7	**339**	235	0.59	**396**	Acid-sulphate
3	Explosion and collapse craters	952	0.71	**1,333**	952	0.3	**3,213**	909	0.23	**3,912**	Mixed
4	Neutral pH waters	342	0.18	**1,850**	342	0.05	**6,681**	341	0.048	**7,152**	Silica deposition
5	Muddy acid springs	43	0.018	**2,369**	42	0.01	**3,832**	42	0.006	**7,111**	Acid-sulphate
6	Mudpools	59	0.04	**1,352**	58	0.016	**3,524**	56	0.006	**8,820**	Acid-sulphate
7	Old sinter deposition next to river	240	0.044	**5,450**	236	0.024	**9,758**	237	0.02	**12,265**	Mixed (Old Sinter)
8	Collapse craters	381	0.097	**3,920**	376	0.056	**6,696**	376	0.06	**6,696**	Mixed
9	Alum cliffs	202	0.05	**3,804**	199	0.04	**5,564**	12	0.004	**3,416**	Mixed
10	Isolated area east of Lake Ngakoro	35	0.014	**2,485**	34	0.007	**4,901**	33	0.003	**11,196**	Acid-sulphate

The total number of thermal anomalies within the delineated area is similar for the buffered convex-hull (that by definition must contain all points) and isocontour SAMSE (that must contain 99% probability density of KDE) (Table 5.1). However, the area differences between the two, results in notable thermal anomaly density variations (e.g. Area ID 1, 2, 3 and 4, Table 5.1). These may be explained by the large areas in between clusters of thermal anomalies. SAMSE estimates produce higher spatial densities over the mixed alteration areas (3.213 to 9,758 thermal anomalies per km^2, Area ID 3, 7, 8 and 9, Table 5.1), compared to acid-sulphate alteration regions that produce the lowest thermal anomaly densities (339 to 4,901 thermal anomalies per km^2, Area ID 2, 5, 6 and 10, Table 5.1).

Kernel orientations range from N11-74°E for LSCV and N27-78°E for SAMSE areas (Table 5.2). For Area ID; 1, 3, 5, 8, 9, both methods estimated very similar orientations, while other areas (e.g. Area ID; 2, 4, 6, 7, 10) have considerable differences >20°. The LSCV estimator tends to produce more elongated kernels (Major/Minor columns, Table 5.2) as expected, as this estimator is more sensitive to outliers (Wang et al., 2020). The LSCV orientations for acid-sulphate areas (Area ID; 2, 5, 6 and 10) fall closest to the orientation of the whole geothermal field (Area ID; 1). This contrast with the smaller SAMSE derived areas (Area ID; 5 to 10) where orientations fall far from Area ID 1. Mixed alteration areas (Area ID; 3, 7, 8 and 9) present similar orientations for SAMSE and LSCV. Whereas the active silica deposition area (Area ID; 4), has an orientation value of 4.34 for SAMSE and 74 for LSCV.

Table 5.2. Kernel bandwidth estimators. Orientation is measured in degrees clockwise from north.

Area ID	SAMSE Major-axis (m)	SAMSE Minor-axis (m)	SAMSE Major/ Minor	**SAMSE Orientation**	LSCV Major-axis (m)	LSCV Minor-axis (m)	LSCV Major/ Minor	**LSCV Orientation**
1	128.11	38.45	3.33	**11.83**	304.8	0.0009	338667	**22.12**
2	64.41	55.96	3.15	**52.96**	11.08	6	1.85	**11.7**
3	51.49	17.096	3.01	**32.32**	111.4	0.0003	371333	**33.8**
4	40.5	12.23	3.31	**4.34**	31.28	6.78	4.61	**74**
5	29.97	8.24	3.64	**50.76**	9.6	7.2	1.33	**61.4**
6	17.89	11.22	1.59	**-27.72**	12.48	5.64	2.21	**29.2**
7	19.51	8.096	2.41	**35.47**	7.44	4.8	1.55	**55.5**
8	28.15	12.03	2.34	**43.64**	6.84	4.93	1.39	**45.7**
9	20.93	12.46	1.68	**77.93**	41.73	0.019	2196	**71.11**
10	13.26	9.43	1.41	**-27.75**	8.37	5.59	1.50	**22.14**

5.4.2 Spatial pattern analysis

Any departure from complete spatial randomness was assessed using first and second-order statistics for each of the 10 different areas and 3 boundary types, buffered convex-hull and isocontours (SAMSE and LSCV).

For the Clark-Evans test and Hopkins-Skellman tests, the results are interpreted as follows. If R = 1, then the distance metrics for the observed point (here the thermal anomalies) are equivalent to those produced by the homogeneous Poisson process, i.e., R = 1 implies randomness. If R > 1, then the distance metrics are greater for the observed points which suggest maximum or uniform spacing occurs. If R < 1, then the distance metrics are less for the observed points which suggests clustering of points is occurring. A statistical significance level of $p < 0.05$ is taken here, i.e., the R value is not statistically significant if the accompanying p-value is greater than 0.05.

These test statistics were run within the *spatstat* package of R (Baddeley et al., 2015), and presented statistically significant results where $p < 0.05$. All results across all areas, and for all boundary types, suggest thermal anomalies are clustered regardless of the host rock lithology (Figures 5.6 and 5.7, Rc and Rs values, Table A3.1).

Ripley's second-order randomness test compares the number of observed points within a distance *d* of every other observed point to the same statistic calculated for randomly placed points (based on a homogeneous Poisson distribution) (Ripley, 1979). To determine whether the results are statistically significant, the result is plotted alongside a set of Monte Carlo runs (randomly placed points) within the same boundary. These runs provide a significant bound envelope (number of runs = 39, for $p < 0.05$).

Almost all areas suggest clustering at all distances, except for the medium-size acid-sulphate alteration area (Area ID: 2), which presents a clear trend towards separation at ~250 m after clustering at smaller distances with the LSCV boundary (Figure 5.6). Ripley's second-order test results are presented as plots in Figure 5.6 and with detailed results included in Table A3.1.

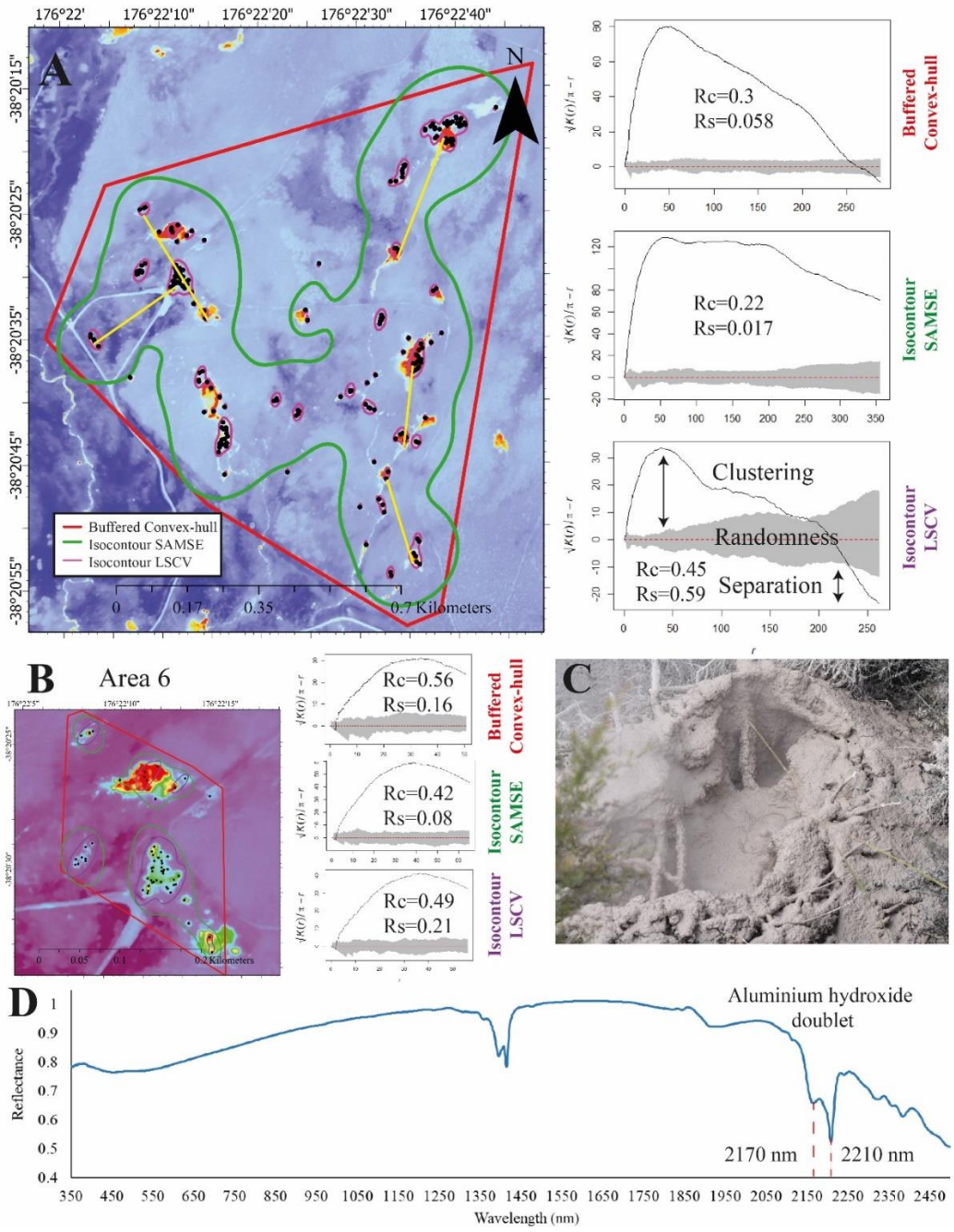

Figure 5.6. (A) TIR image overlaid by three types of boundaries for Area 2, to the right randomness test results for three types of boundaries. The length of the yellow lines is between 220 and 280 m to visualise the documented separation distance. (B) TIR image overlaid by three types of boundaries for Area ID 6, with their randomness test results on the right. Rc, Clark-Evans randomness test results. Rs, Hopkins-Skellman randomness test results, with all p values being significant (i.e. $p < 0.05$). Plot axis $L - r$ against r. (C) Close-up photo of a thermal anomaly associated with a mud pool. The mineralogy of the mud is pure kaolinite, determined using SWIR spectroscopy. Inset shows the characteristic double absorption feature at 2205 nm.

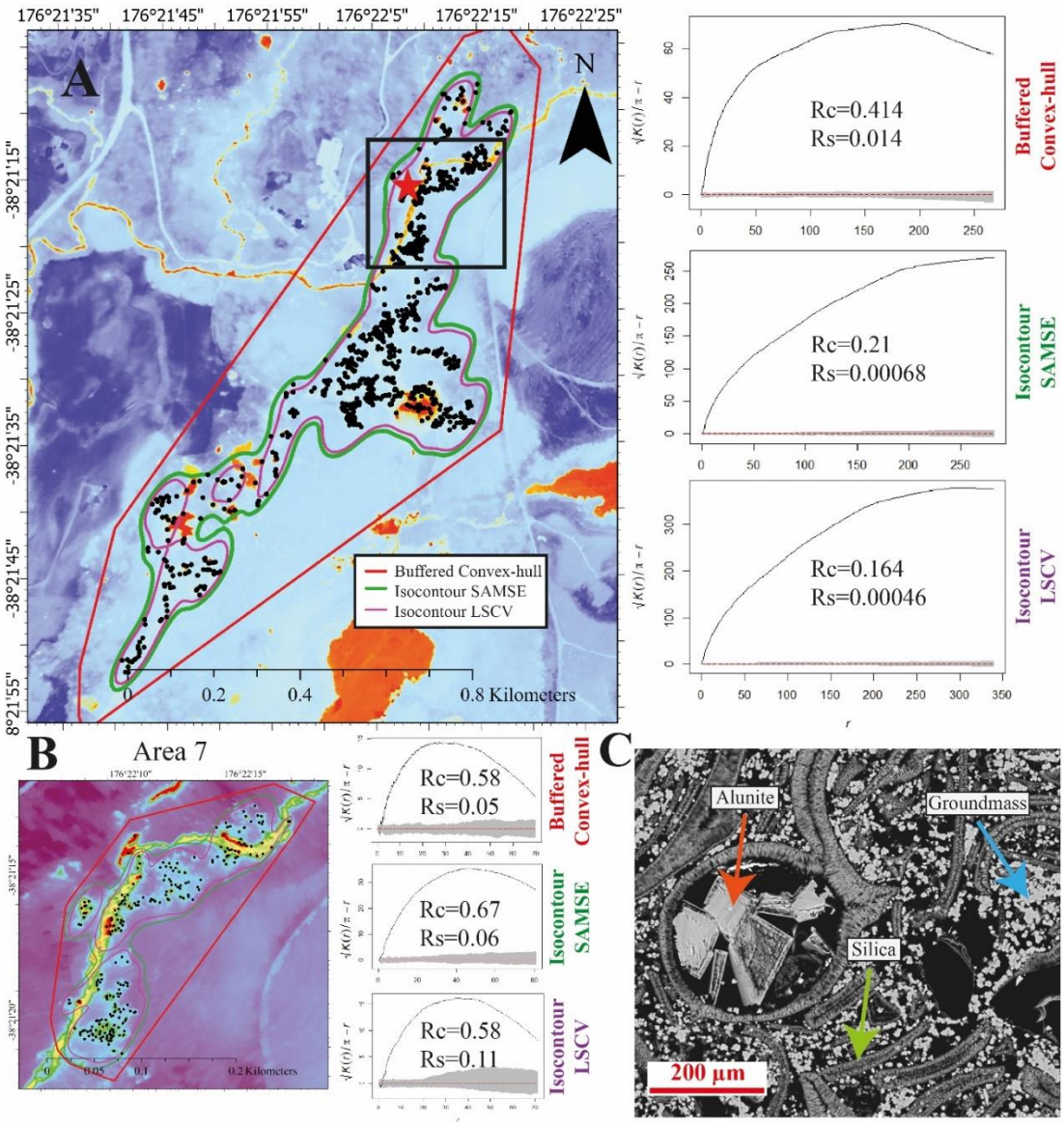

Figure 5.7. (A) TIR image overlaid by three types of boundaries for Area 3, to the right randomness test results for three types of boundaries. Area 6 is marked with a black square. (B) TIR image overlaid by three types of boundaries for Area 6, with their randomness test results on the right. Rc, Clark-Evans randomness test results. Rs, Hopkins-Skellman randomness test results. Plot axis L – r against r. (C) Scanning Electron Microscopy displaying alunite and silica precipitation within initial pore-space and groundmass replacement by amorphous silica. The sample location is indicated by a red star on A.

5.5 Discussion

The methods and subsequent results presented here may provide insight into the shallow geological controls of Waiotapu Geothermal Field and possibly other geothermal systems. Surface thermal anomalies in any hydrothermal system are a clear indication of present activity, therefore, they have the capacity to give information on the actual state of the system and its properties in the

shallow subsurface. However, several limitations have been identified during this work that require further discussion.

5.5.1 Limitations

Three limitations were identified from the results directly related to three assumptions deployed by the methods:

1) Thermal anomalies can be correctly identified as points using the TIR image. Underestimation of thermal anomalies can happen when they are located under thick vegetation or in water bodies, as thermal anomalies lying at the bottom of a water body cannot be directly observed. During our field survey, we rarely observed thermal anomalies under thick vegetation canopy, especially in the northern areas where large thermal anomalies (>1-2 m across) were detected.

2) Areas where these thermal anomalies may occur can be correctly identified. Boundary selection is subjective and can greatly affect the results from point pattern analysis (Runge et al., 2015). Obtaining a boundary from a geophysical survey (e.g. magnetic/electric) can normalise the boundary selection amongst geothermal areas to a similar subsurface process. However, when this is not available for the region(s), like in this study, sensitivity analyses are advised to apply a range of boundaries to estimate result uncertainties.

3) The complex variations of lithology and hydrogeology causing the locations of thermal anomalies define the surface manifestations of a geothermal system and are extremely challenging if not impossible to take into account fully, due to computational limits or data availability. To assess the behaviour of conducting cells and the subsurface constraints controlling it, in this study we used a spatial nested approach to analyse if the subsurface variations causing changes in surface manifestations are observed at different spatial resolutions.

5.5.2 Orientation and potential fault control at Waiotapu Geothermal Field

We interpret the observed pattern of thermal anomalies to be influenced by lithology, tectonic and shallow fluid flow (Mardiati et al., 2020; Weldeyohannes et al., 2022; Zaini et al., 2022). Our proposed thermal anomaly detection methodology (Figure 5.3) can be used to relate shallow hydrogeology and host rock characteristics within the active Waiotapu Geothermal Field. Previous studies have interpreted the elongation and alignment of hot spring and explosion craters at Waiotapu Geothermal Field to be suggestive of fault-controlled fluid movement (Hedenquist & Henley, 1985; Wood, 1994; Rowland & Simmons, 2012), regardless of the lack of documented active crossing faults. Furthermore, fracture patterns have been found to exhibit patterns in other fields (i.e. Yellowstone, U.S.A.) (Dobson et al., 2003) and modelling of cell convection in other studies has also

shown patterns for heating/cooling convection cells (Patterson et al., 2018), possibly following permeable pathways from deep below through the upper crust (McLellan et al., 2010). This was partially observed in this work from the thermal anomalies at Waiotapu Geothermal Field at medium and large scales, which show strong separation at 250 m (Figure 5.6).

The orientation of the thermal anomalies falls within a general NE direction, regardless of the bandwidth estimator method. The LSCV bandwidth estimator provided orientations based on the thermal anomalies that closely resemble the main strike of Paeroa Fault at ~5 km and Ngapouri Fault at ~2.5 km to the northwest with a N40°E-N55°E and N45°E - N60°E, respectively (Smith et al., 1984). Furthermore, this direction also coincides with the overall strike direction of the TVZ, N45°E (Bertrand et al., 2012). Our results further suggest a geographical change in the underlying orientation of the process controlling thermal anomaly locations. For example, acid-sulphate alteration areas (N11°E to N29°E, Table 5.1), closely match the orientation derived from the thermal anomalies across the whole field (N22°E), while the southern parts with mixed alteration are oriented with a NE strike but within a wide range (N33.8E to N71.1E). The measured orientation of the thermal anomalies may therefore suggest fault control. Faulting can influence heat and mass transfer (Rowland & Simmons, 2012), particularly if high-permeability fractures are in place (Graf & Therrien, 2009). The high density of fractures is observed within the mixed alteration lithology thermal anomalies (Area ID 3 and 8, Figure 5.8), which can significantly change local permeability structures (Liu et al., 2019). At Waiotapu Geothermal Field, such areas are also characterised by many scattered collapse pits and phreatic/hydrothermal eruption vents hosted in variously altered rhyolitic ignimbrite (Figure 5.8), which may be influencing the near-surface permeability. The difference in orientation between the northern acid-sulphate and the southern mixed alteration zones can be explained by lithological and alteration variations that can influence heat mobility.

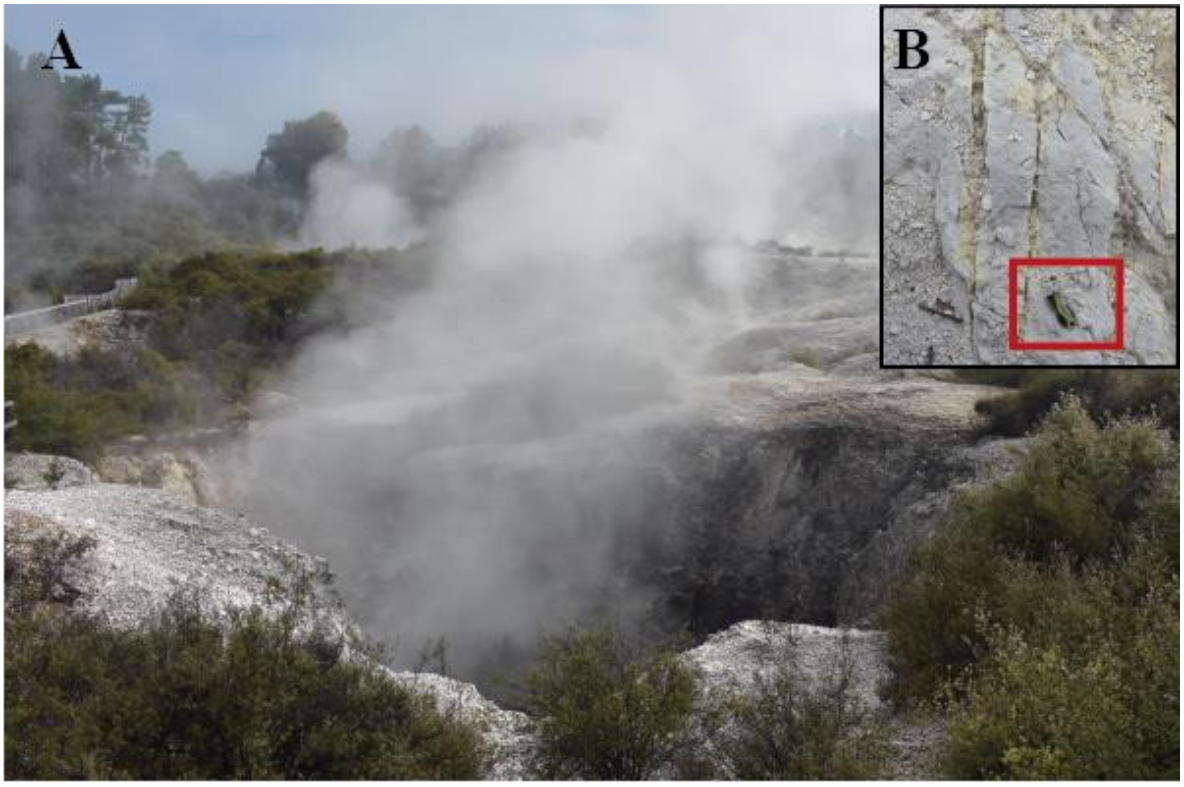

Figure 5.8. Overview field photo of the mixed alteration region, with (A) scattered collapse crater. (B) Close-up photo of highly fractured and altered rhyolitic host rock with fracture-infilling native sulphur precipitation. Multi-tool in red square for scale (~10 cm long).

5.5.3 System subsurface processes - A model for Waiotapu Geothermal Field shallow hydrothermal system

At Waiotapu Geothermal Field, the main heat source is inferred to be located in the northern area (Well 4 in Figure 5.9) based on thermal gradients from drill-holes and water geothermometry (Hedenquist & Browne, 1989; Giggenbach et al., 1994; Kaya et al., 2014). This is concurrent with the higher estimated temperature of the thermal anomalies in the north (>47 °C, derived from Chapter 3), with the acid-sulphate surface features (Figure A3.1). The drill core-based stratigraphy indicates a thicker litho-cap, combined with the higher elevations and deeper water table promoting steam-heated alteration (Fournier, 1989b; Hedenquist & Browne, 1989c; Christiansen et al., 2007; Rodriguez-Gomez et al., 2021b). The litho-cap gradually thins towards the south and the water table comes closer to the surface (Figure 5.9). This hydrological and geological architecture influences heat transport and shallow groundwater circulation, and consequently on the pattern of hydrothermal alteration. The northern areas are characterised by steam-heated (advanced) argillic alteration, which is manifested on the surface as phyllosilicate-rich mud pools (Figures 5.6C and D), while the southern parts are characterised by pervasive silicification and patches of argillic alteration. Microscopically,

the host rock in the southern areas shows dissolution textures (e.g. pore space void) and precipitation of secondary minerals, including alunite, sulphur, baryte, amorphous silica and phyllosilicates (Hedenquist & Browne, 1989; Rodriguez-Gomez et al., 2021). Here, we interpret such alteration (e.g. mineral precipitation and dissolution) processes to influence the porosity and permeability structure of the host rocks at Waiotapu Geothermal Field. This is aligned with observations from alteration of composite volcanoes, such as Whakaari Island (Heap et al., 2017; Kennedy et al., 2020) and Ruapehu (Schaefer et al., 2020, 2021). Permeability can also be increased by explosive and eruptive events that are typical in the south region (Lloyd, 1959; Hedenquist, 1991) by increasing the fracture density (Liu et al., 2019).

Our results on the thermal anomalies and their distribution are consistent with the overall geological and shallow hydrological settings of the Waiotapu Geothermal Field. Consequently, we interpret the mapped thermal anomalies and their spatial distribution to carry currently unutilised information about the hydrothermal and hydrological processes within geothermal fields. Shallow subsurface permeability which allows for fluid movement up to the surface appears to be one of the main factors defining the number and distribution of thermal anomalies. Higher thermal anomaly density within a buffered convex hull (1,333 to 9,758 thermal anomalies/km^2) was found for the southern mixed alteration areas (Area ID: 3, 7, 8 and 9), where also porosities have been reported to be as high as 50% (Gallagher et al., 2020). This can be attributed to mainly two factors: a) frequent hydrothermal explosions developing a highly fractured host rock with almost any orientation (e.g. increasing fracture number and discontinuities of the host rocks); b), the lithology and hydrothermal alteration with pervasive dissolution of the primary mineral phases (i.e. influencing porosity and permeability) (Figure 5.7).

On the other hand, the acid-sulphate alteration areas (Area ID: 2, 5, 6 and 10) exhibit lower thermal anomaly densities within a buffered convex hull (242 to 2,485 thermal anomalies/km^2). This can be attributed to two factors: a) the high clay content reduces conductivity and permeability via clogging of pore-space and fracture (Hedenquist & Browne, 1989); b) a thicker layer of litho-cap rock within this area (i.e. Huka Falls Formation, Figure 5.9) (Wood, 1994). These factors can effectively be controlling the temperature and the distribution of thermal anomalies on the surface, which appear to be separated by >250 m (Figure 5.6). Previous studies have modelled fluid paths within geothermal areas, finding that fractures can be “synchronised” into patterns at a variety of distances up to 250 m (Patterson et al., 2018), controlled by convection cell spacing (McLellan et al., 2010). Our point pattern analyses of thermal anomalies are therefore encouraging for further investigation on the physio-chemical properties of the host rock, and the fluid path controls.

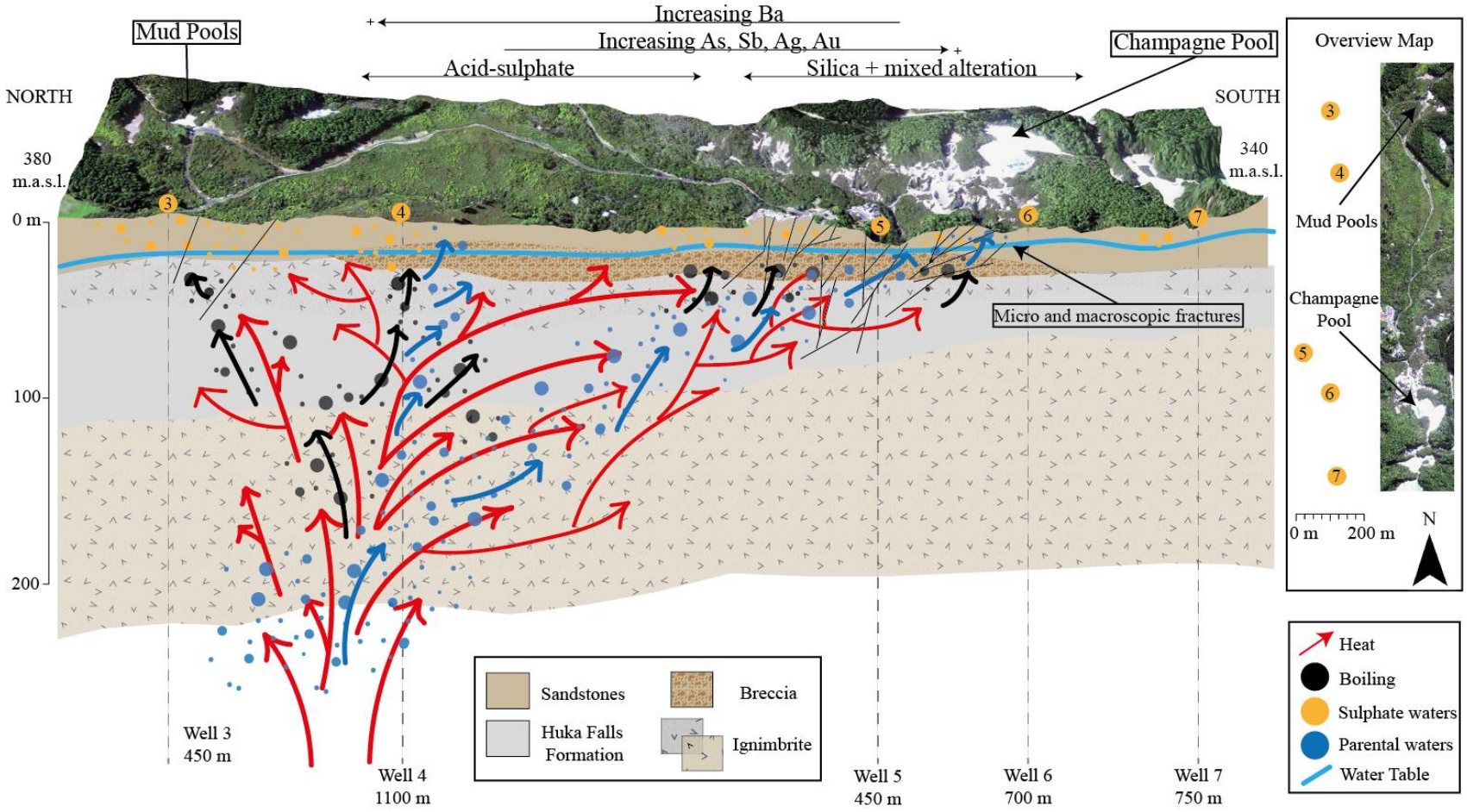

Figure 5.9. A model for the shallow hydrological and geothermal features within the Waiotapu Geothermal Field, vertical exaggeration is × 3, accentuating elevation differences. Inset shows the location of the block diagram relative to the deep borehole (numbered orange circles). Overview map on the left shows well locations as numbered orange circles and thermal anomalies as small black dots. The heat source is located near well 4 and moves horizontally towards the south. Parental high-chloride waters move from depth (~1000 m) towards the southern area with Champagne Pool as the main surface outflow. (Modified from (Grindley, 1963; Hedenquist & Browne, 1989; Kaya et al., 2014; Rodriguez-Gomez et al., 2021)

The mapped and analysed thermal anomaly distributions are not only aligned well with the host-rock properties, such as hydrothermal alteration styles (Lloyd, 1959; Hedenquist & Browne, 1989; Rodriguez-Gomez et al., 2021), but also with soil and plant element anomalies, mapped by laboratory and airborne hyperspectral remote sensing (Rodriguez-Gomez et al., 2022, under revision). For instance, the distribution of arsenic and antimony anomalies in plants vectoring towards the near-neutral, high-chloride water outflows such as the Champagne Pool (Figure 5.9). As the distance from their outflow source increases, arsenic and antimony concentrations decrease while other elements, such as barium, increase. Barium plant concentration is a good fingerprint to locate the mixing of geothermal waters with shallow cold groundwater, signalling to sulphide and carbonate mineralization (Dunn, 2011). With a multidisciplinary approach including hyperspectral (VNIR/SWIR), LiDAR and TIR images complemented with rock/soil and plant samples, a lithological map and an elemental map (i.e. representing elemental enrichment in rock/soil and plants) were created. The findings of these maps complement the interpretations of the present and past studies (Rodriguez-Gomez et al., 2021), locating two broad zones at Waiotapu Geothermal Field, with acid-sulphate alteration in the north, and sulphate-chloride mixed alteration in the southern areas.

5.6 Conclusions

The results from this study present a method to analyse TIR imagery to understand the shallow subsurface hydrological processes of a geothermal system. Point pattern analyses of thermal anomalies can complement exploration efforts and detail geological and hydrological work focused on geothermal systems. The mapped thermal anomalies have been used to estimate underlying structures and orientations, while the first and second-order randomness tests, allowed for the interpretation of clustering and separation of thermal anomalies within geothermal systems.

The kernel-estimator derived orientation data of Waiotapu Geothermal Field, suggest fault control on their distribution that aligns well with the neighbouring active fault lines as well as the broader fault orientation within the TVZ. However, the orientation within Waiotapu Geothermal Field shows a duality: northern areas follow the overall orientation of the regional strike while the southern areas deviate from the overall direction of the system from 12° to 49° (Table 5.2). This contrast, along with differences in thermal anomaly temperature, distribution, host rock lithology and elemental distribution, can be attributed to the differences in hydrology and fluid pathways. Higher temperatures of ~ 47°C and a lower thermal anomaly density are present in the northern area. While the abundance of pathways generates a higher thermal anomaly density in the southern areas, caused by a thinner litho-cap layer than the northern areas and a history of hydrothermal explosions, the abundance of fluid pathways does not present any specific pattern. On the other hand, the medium-sized area of acid-sulphate alteration (Area ID 2) presents separation within clusters at >250 m (Figure 5.6).

There are some limitations to this study, mostly due to the subjective nature of the thermal anomaly selection and user-selected boundaries for the pattern analyses. Furthermore, geophysical studies (e.g. micro-seismic) or mechanical studies are recommended to further interpret some of the results from this study. Such as the separation distance amongst acid-sulphate thermal anomaly clusters. The point pattern analyses from thermal infrared remotely sensed data provide information on the state of the system at a snapshot in time and in combination with other datasets and studies, an interpretation of the hydrogeology behaviour can be constrained.

MASSEY UNIVERSITY
TE KUNENGA KI PŪREHUROA
UNIVERSITY OF NEW ZEALAND

GRADUATE RESEARCH SCHOOL

STATEMENT OF CONTRIBUTION
DOCTORATE WITH PUBLICATIONS/MANUSCRIPTS

We, the candidate and the candidate's Primary Supervisor, certify that all co-authors have consented to their work being included in the thesis and they have accepted the candidate's contribution as indicated below in the *Statement of Originality*.

Name of candidate:	Cecilia Rodriguez-Gomez
Name/title of Primary Supervisor:	Gabor Kereszturi
In which chapter is the manuscript /published work:	Chapter 5

Please select one of the following three options:

(●) The manuscript/published work is published or in press

- Please provide the full reference of the Research Output:

https://doi.org/10.1016/j.geothermics.2023.102664
Published in Geothermics (Elsevier).

( ) The manuscript is currently under review for publication – please indicate:

- The name of the journal:

- The percentage of the manuscript/published work that was contributed by the candidate:

- Describe the contribution that the candidate has made to the manuscript/published work:

( ) It is intended that the manuscript will be published, but it has not yet been submitted to a journal

Candidate's Signature:	Cecilia Rodriguez Gomez — Firmado digitalmente por Cecilia Rodriguez Gomez Fecha: 2023.04.05 16:06:12 -06'00'
Date:	05-abr-2023
Primary Supervisor's Signature:	Gabor Kereszturi — Digitally signed by Gabor Kereszturi Date: 2023.04.06 08:33:19 +12'00'
Date:	6-Apr-2023

This form should appear at the end of each thesis chapter/section/appendix submitted as a manuscript/ publication or collected as an appendix at the end of the thesis.

6 Discussion and conclusions

Our study presents a novel application for exploring and monitoring geothermal areas using laboratory, airborne hyperspectral (VNIR/SWIR) and TIR remote sensing techniques. The integration of such methods with Light Detection and Ranging (LiDAR) data along with rock/soil and plant (bio-) geochemistry has enabled the addition of new concepts to the pre-existing models of the Waiotapu Geothermal Field by synthesising our new findings with existing geological, geophysical and geochemical datasets. Furthermore, the overarching objective of the present research is to develop new methods that can add new capabilities for geothermal prospecting and monitoring using airborne and space-borne platforms. Therefore, the discussion revisits those two core ideas to provide new insights into geothermal systems.

6.1 Geological model for Waiotapu Geothermal Field

Geothermal systems result from complex interactions between upwelling hot water and the host rock (Moeck, 2014; Abubakar et al., 2017). The control factors can include host rock type and its pH buffer capability (Moeck, 2014; Jolie et al., 2021), porosity and permeability (Saepuloh et al., 2018; Niederau et al., 2019), fluid chemistry (Moeck, 2014; Tut Haklidir & Haklidir, 2020), fluid dynamics (Gianelli & Grassi, 2001; Shoedarto et al., 2021; Suherlina et al., 2022), heat source (i.e. thermal regime) (Basantaray & Mandal, 2022; Johnson et al., 2022; Keesari et al., 2022) and stress regime (e.g. tectonic activity, fault zones) (Rowland & Simmons, 2012; Okamoto et al., 2022). In light of such complexity, Waiotapu Geothermal Field is selected since it is representative of an ignimbrite-hosted, convection-related geothermal field in the Taupo Volcanic Zone (TVZ). Its complex temporal evolution has been studied before, including episodes of hydrothermal eruptions (Grindley, 1963; Hedenquist & Henley, 1985; Hedenquist & Browne, 1989; Hedenquist, 1991; Grindley et al., 1994). It has been studied for decades, but since the 1980s when it was categorised as “Protected” by the Waikato Regional Council, only non-invasive exploratory techniques have been allowed that suit well for trialling new remote sensing methods. Waiotapu Geothermal Field also presents a variety of surface features (e.g. fumaroles, near-neutral high-chloride pools, geysers, mud pools, steaming grounds, collapse and hydrothermal eruptions craters) (Lloyd, 1959; Hedenquist & Browne, 1989; Hunt et al., 1994) and is densely covered by vegetation (Given, 1980; Cochrane et al., 1994; Deroin et al., 1995; Mia et al., 2012). Furthermore, the thick plant cover and the underlying active geothermal system provide a natural test-ground for analysing vegetation-geothermal interactions and formulating new tools for monitoring such interactions remotely.

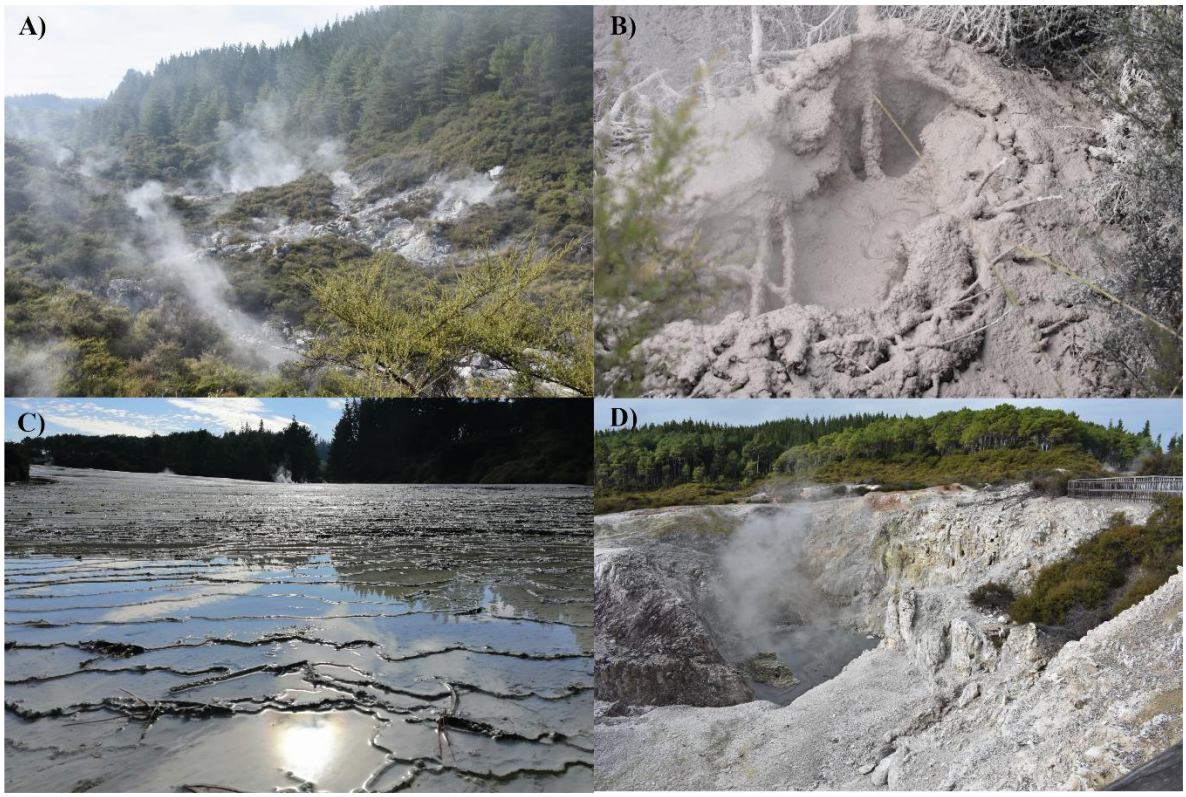

Figure 6.1. A) General view of the steaming grounds of the Waiotapu Geothermal Field. The shrub vegetation is mainly kanuka that tolerate the harsh geothermal environment. B) Close-up photo of a mud pool at Waiotapu Geothermal Field formed by rising H_2S-rich steam. C) Silica sinter terraces forming from outflow from the southern end of Champagne Pool. D) Collapse craters caused by the acid-sulphate alteration present in the 'mixed' areas.

Waiotapu Geothermal Field has <10% of bare surface exposure (including water bodies), while the majority of its surface is covered by *pinus radiata* plantation and native scrub vegetation (Figure 6.1A). Out of the plants living in the area, ~10% is dominated by kanuka shrubs (i.e. *kunzea ericoides* var *microflora*) based on hyperspectral image classification (Chapter 4). The bare ground is characterised by a diverse range of alteration mineral associations and silica deposition that has been mapped by hyperspectral remote sensing and jointly analysed for its thermal signature using airborne TIR surveys and ground surveys. Broadly, Waiotapu Geothermal Field can be subdivided into two end-member zones (Table 6.2): acid-sulphate dominated (northern part), and neutral chloride dominated (southern parts) (Figure 6.2). The two endmembers are marked by a zone where alteration minerals typical for both endmembers are abundant and mingled, which we refer to here as a third zone called simply 'mixed' area (Figure 6.1D).

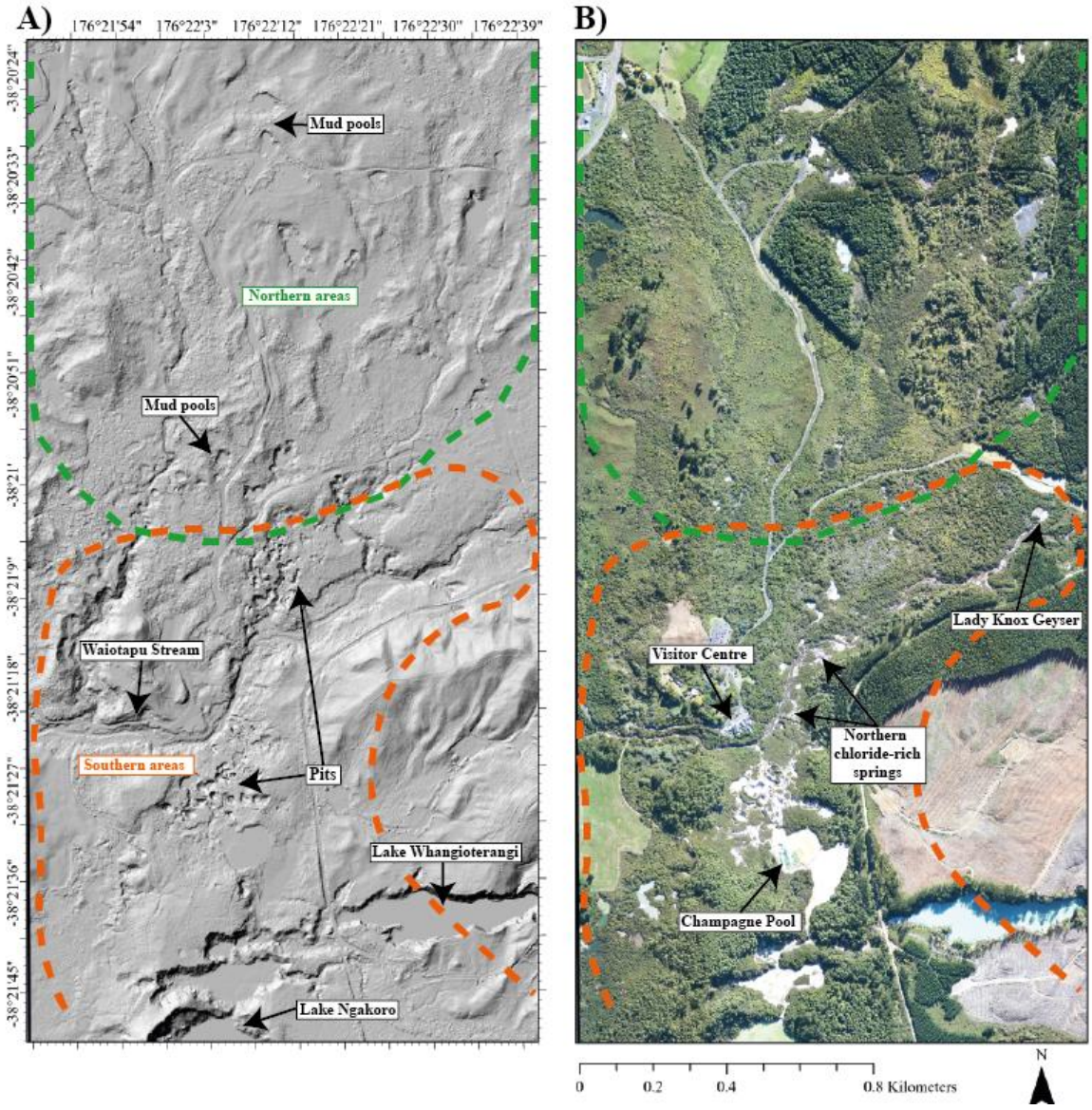

Figure 6.2. A) Hillshade of the Waiotapu Area from LiDAR DEM imagery. B) Orthophoto of the Waiotapu Area. Northern and Southern areas are indicated as green and red dashed lines, respectively. The chloride-rich springs reach the surface at Champagne Pool and Northern chloride-rich springs.

Northern areas: The acid-sulphate alteration is predominant in the northern areas (Figure 6.2), caused by the rising H_2S steam (Hedenquist & Browne, 1989). Mineralogically, this zone is located above the current water table, where rising steam encounters groundwater, characterised by kaolinite, montmorillonite and other phyllosilicates, forming mud pools (Figure 6.1B). Accessory minerals, such as silica polymorphs (e.g. quartz, cristobalite), alunite and jarosite are also present, in vugs and filling in fractures in the host rock (Figure 3.). The alteration minerals found in this research are consistent with mineral forming in advanced argillic alteration in volcanic/epithermal zones (e.g. Berger & Velde, 1992; Heap et al., 2019; Fulignati, 2020), reported previously at Waiotapu Geothermal Field (Hedenquist & Browne, 1989; White & Hedenquist, 1990). The analysed samples represent surface alteration, vertically, the alteration mineralogy changes to adularia (K-feldspar) and illite-dominated zones at 100-

200 m, while albite and chlorite occur at depths 300-400 m under the northern part indicating changes in chemistry and pH with increasing depth (e.g. Wells 3-4 in Steiner, 1963; Hedenquist, 1982, 1991) The occurrence of montmorillonite (smectite group mineral), interlayered illite-smectite and illite are almost solely as a function of temperature from surface to 250 °C (Hedenquist & Browne, 1989; Fulignati, 2020), while, on the other hand, adularia can also indicate permeability structure of the host rock (Browne & Ellis, 1970; Heap et al., 2019). Based on mineralogy, fluid chemistry and temperature, the zone rich in adularia can represent the upwelling hot, near-neutral fluid from depth that is located between Wells 3 and 4 (Figure 6.3). The fluid has high Cl (~1250 mg/kg) and CO_2 (~240 mg/kg) concentrations, enriched in $\delta^{18}O$=−2.50‰, δD=−40‰, and $\delta^{13}C_{CO2}$=−3.45‰ (Giggenbach et al., 1994), indicating a high magmatic signature (Hedenquist & Gulson, 1992; Rowland & Simmons, 2012). The parental fluid is subjected to significant lateral fluid flow towards lower elevations, within the small relief change (<50 m) (Hedenquist, 1991). It is estimated that half of the deep chloride-rich upflow moves laterally at shallow depth (~200 m) towards the south mixing with groundwater (Hedenquist & Browne, 1989; Hedenquist, 1991). Emerging in its least modified form (i.e. un-subjected to fluid/rock interaction) at Champagne Pool, the main focus of near-neutral high-chloride waters (Giggenbach et al., 1994).

Above the lateral fluid flow, upwelling vertical heat and steam condensation zones have formed, driving acid-sulphate alteration within the topmost 100 m. This results in abundant outflows and hot springs dominated by mud pools and other acid-sulphate pools and collapse craters (Figures 6.1B and 6.3B). The distribution of acid-sulphate zones and high-chloride fluids is not only imprinted in the soil/rock mineralogy it is also traceable through the plants living in Waiotapu Geothermal Field. Our study has successfully identified foliar chemistry anomalies by both ground samples and hyperspectral imaging that can be linked to the underlying subsurface alteration processes (Chapter 4). Here, kanuka, a dominant (i.e. >80 % of plant cover in soils with >40 °C (Burns, 1997)) thermotolerant vascular species, endemic to geothermal areas of New Zealand (Smale et al., 2018), was used to map plant foliage as a proxy for subsurface activity in geothermal systems of New Zealand. Based on the foliar element mapping, we have combined bare ground and vegetation cover areas to calculate the total surface abundance of alteration lithologies at the Waiotapu Geothermal Field (Table 6.1).

Table 6.1. Area statistics for alteration styles. Kanuka coverage for each style was obtained by quantifying the kanuka coverage in the northern areas (for acid-sulphate), surrounding silica deposition areas (near-neutral chloride), and areas in the southern region (excluding the silica sinter deposition areas) (Figure 6.2).

Alteration style	Bare ground (km^2)	Kanuka coverage (km^2)
Acid-Sulphate	0.36	0.13
Near-neutral chloride	0.073	0.054
“Mixed”	0.031	0.15

Kanuka has been previously reported to uptake high quantities of toxic elements (e.g. Ag, Au, As, Sb) in Waiotapu Geothermal Field (Dunn & Christie, 2019). The effects of such elements on plants [e.g. apples (*braeburn* and *rewena)*, *Pteris* fern, Sunflower (*Helianthus annus* L.)] have only been analysed in pot experiments, in which they confirmed spectral changes detectable with in-situ hyperspectral remote sensing (Delalieux et al., 2009; Slonecker et al., 2009; Rathod et al., 2018). Our study has applied hyperspectral image classification to map, for the first time, foliar element concentration in kanuka, offering a new sampling media for geothermal exploration on the ground and remotely. Besides spectral changes in the NIR and SWIR regions, kanuka also exhibits visible physical changes that can be correlated to soil temperature variations, becoming shorter as the soil temperature increases (Muukkonen, 2005; Smale et al., 2018). We have confirmed such qualitative relationships through joint analysis of LiDAR and TIR imagery, in which we also observe tall kanuka canopy (>1 m) can grow even in close vicinity to thermal anomalies in the northern areas (Table 4.9). The surface heat flux in the north is much more point-like, defined by sharp boundaries between thermal anomalies and soil/rock with lower temperatures. This can allow for kanuka's roots to grow deeper and develop a taller canopy next to the thermal areas (Figure 6.3).

The spectral changes caused by damage or stress to the plant can be correlated to the environmental conditions, which in this case include alteration trends, shallow ground temperatures and (fluid/soil) pH. One great advantage of plants is their capacity to uptake elements deeper and broader than what a rock/soil sample may represent (i.e. rock/soil samples are a punctual representation) (Dunn, 2011; Rincheval, 2019). The hyperspectral-derived foliar elemental maps show two main geochemical trends. In the north, kanuka is enriched with Ba, indicating hot geothermal water and cold groundwater mixing (Dunn, 2011; Bundschuh & Maity, 2015), while the lower sulphate concentrations in soil can make Ba bioavailable to plants (World Health Organization, 2016). This is in strong contrast with the upflow regions in the south, in which high concentrations of Ba are not bioavailable to plants due to high sulphate (SO^{-}_{4}) (>2,000 mg/kg) concentrations in the soil where kanuka is living (Figure A2.6). Furthermore, closer to Champagne Pool's outflow, kanuka has instead been mapped to be enriched with silver, arsenic and antimony (Figures 4.6 and 4.7, Chapter 4), elements which are natural by-products from hydrothermal mass and heat transfer (Simmons, et al., 2016). Their concentrations are constrained via redox state, pH and H_2S availability to form aqueous metal complexes (Seward, et al., 2014) and are limited by magmatic intrusions, deep country rock and related fluids (Simmons, et al., 2016). A positive correlation between Ag and Sb has been found amongst these elements coming from parental waters (Simmons, et al., 2016), confirmed by our investigation.

Overall surface temperatures derived from the TIR imagery in this area can be greater than 47 °C (Figure A3.1, derived from Chapter 3), which along with the mineralogy described in wells (Steiner,

1963; Hedenquist & Browne, 1989) and the surface manifestations (i.e. fumaroles and mud pools) places the deep subsurface heat source in the northern region of the system (Figure 6.3) (Giggenbach et al., 1994; Kaya et al., 2014). The heat output has been studied at Waiotapu Geothermal Field using aerial thermal infrared mapping (Mongillo, 1994) combined with ground surveying techniques (ground probes and calorimeters) (Reeves & Sanders, 2019) and the heat flux has been estimated to be ~500 MW by geochemical methods (Benseman et al., 1963; Bibby, Glover, et al., 1995) and numerical models (Kaya et al., 2015). Our study has used point pattern analysis on TIR imagery to reveal the structural controls on the distribution of heat anomalies. The point patterns and the spacing between thermal anomalies altogether suggest lower permeability, possibly caused by a thicker litho-cap (Wood, 1994) and precipitation of clay minerals (Hedenquist & Browne, 1989). Lower permeability was deduced from TIR-derived thermal anomalies low density (i.e. thermal anomalies/m^2) (Table 5.1) and spacing of ~250 m between thermal anomalies clusters (Figure 5.6). Thermal anomalies in the north follow an orientation (Table 5.1) similar to that of the whole system (~ N22E°) (Hedenquist & Henley, 1985; Cochrane et al., 1994), which is interpreted as some structural control over permeability within the system (Hedenquist, 1991; Wood, 1994; Rowland & Simmons, 2012).

Southern areas: In contrast with the north, the southern areas are characterised by near-neutral high-chloride fluids surfacing from various springs (e.g. Champagne Pool and nearby northern areas) (Figure 6.2) that precipitate silica sinter (Hedenquist, 1991; Giggenbach et al., 1994; Hamilton et al., 2022). Champagne Pool itself was formed from a hydrothermal eruption ~900 years ago (Lloyd, 1959; Hedenquist & Henley, 1985; Gallagher et al., 2020). As the fluids cool down they deposit silica sinter towards the south forming terraces (Figure 6.1C) (Hedenquist, 1991). The surface deposits surrounding the areas of silica deposition are comprised of lacustrine sediments and rhyolite with the mineralogy containing secondary minerals of quartz, pyrite and adularia (Hedenquist, 1982; Hedenquist & Browne, 1989) found in Wells 5 and 6 (Figure 6.3) from surface to ~400 m. Outflow from Champagne Pool is composed of high concentrations of Cl (~1800 mg/kg), SO^{-}_{4} (~122 mg/kg), As (~3.9 mg/kg), and Sb (~3.9 mg/kg) (Hedenquist & Browne, 1989; Giggenbach et al., 1994).

The rock/soil samples collected from the vicinity of Champagne Pool's outflow (< 400 m) are enriched with Ag (0.01-6.9 mg/kg), As (0.7-12,000 mg/kg), Au (0-001-3.3 mg/kg), S (100-120,000 mg/kg), and Sb (0.02-392 mg/kg) caused by the high concentrations of these elements contained in the outflowing waters (Giggenbach et al., 1994; Pope & Brown, 2014). Following a similar trend (Figure 4.4) kanuka presents high concentrations of Ag (0.003-0.15 mg/kg), As (0.019-6.21 mg/kg), and Sb (0.04-2.87 mg/kg). These elements are common in geothermal systems, typically outflowing from near-neutral high-chloride springs which are linked to deep parental waters (i.e. with the least rock/water interaction) (Hedenquist, 1991; Bundschuh & Maity, 2015). These elements behave similarly, as has also been shown in other studies (with Ag and Sb presenting positive correlations; Simmons et al., 2016) and decrease in concentration with increasing distance away from Champagne Pool (Figure 3.8). Lady

Knox Geyser, another silica deposition area, does not present enrichment of Ag, As, Au, S and Sb in the nearby rock/soil or plant samples, possibly due to the lower flux outflow compared to Champagne Pool (Figure 5.5). However, outflow areas have been indicated by our foliar element maps around the northern Waiotapu areas (Figure 6.3, 4.6 and 4.7), which are in close agreement with ground-based spring water geochemistry, indicating near-neutral high-chloride outflows (Hamilton et al., 2022). The foliar elemental maps derived from hyperspectral and elemental concentration data, clearly exhibit enrichment of Ag, As, and Sb in the southern area, which pinpoints the capability of kanuka to work as a proxy for geothermal activity (Figures 4.6 and 4.7). Moreover, the areas nearby silica sinter deposition exhibit various kanuka heights depending on the outflow temperatures. For example, south of Champagne Pool where silica sinter terraces are located, kanuka is about 1-2 m tall, while kanuka closer to the main outflow of Champagne Pool has a shorter height <1 m. Champagne Pool has the highest Cl concentrations of the various near-neutral high-chloride springs, suggesting dilution of the "parental" fluids in an uneven form as they rise to the surface (Hedenquist & Browne, 1989). The "parental" fluids get intermixed with shallow waters which provokes different types of alteration, pH and fluid chemistry (Hedenquist & Browne, 1989; Pope & Brown, 2014).

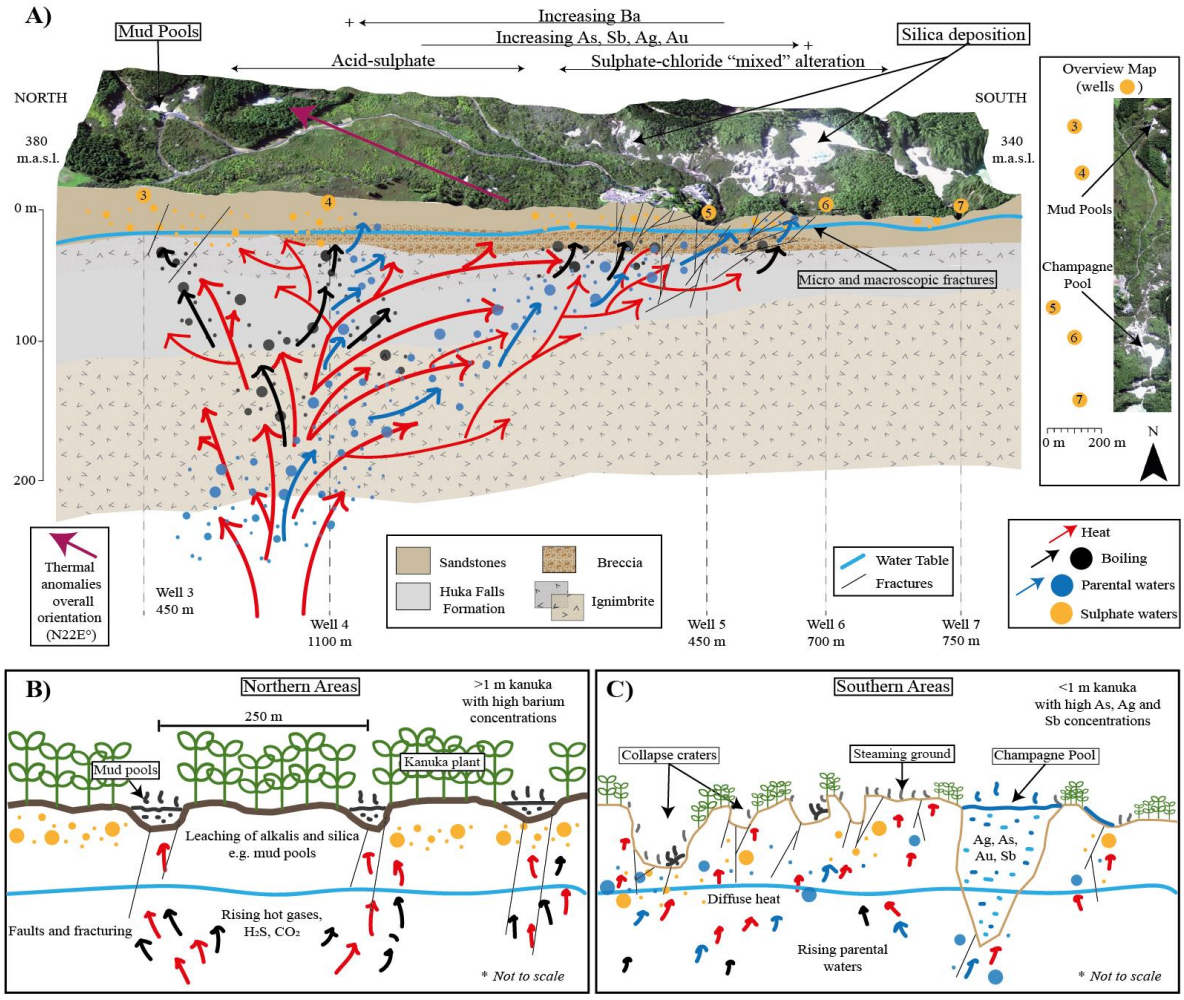

*Figure 6.3. (A) Cross-section diagram of Waiotapu Geothermal Field with representation of upflows, heat, element enrichment, lithology and thermal anomalies overall orientation. (B) Representation of processes taking place in the northern areas. (C) Representation of processes taking place in the southern areas. *B and C are not to scale. Based and modified from (Steiner, 1963; Hedenquist & Browne, 1989)*

The southern areas ('mixed' areas): The central/southern area of the system (Figure 6.2 and 6.3C) exhibits a mix of deposits that has been altered by acid-sulphate rich water and near-neutral chloride-rich waters with some areas of local silica sinter deposits/formation (Figure 6.1C) (Lloyd, 1959; Hedenquist, 1991). The combination of a thinning litho-cap towards the south (Wood, 1994) and evidence of hydrothermal eruptions (Hedenquist & Browne, 1989; Kaya et al., 2015; Simpson & Bignall, 2016) can altogether increase the host rock permeability. The uprising chloride-rich fluids are diluted by discontinuous H_2S and CO_2-rich steam-heated waters, indicated by the measured wide range of chloride concentration (200-1,800 mg/kg) (Lloyd, 1959)at hot springs as well as acid-sulphate features (Figure 6.3) (Hedenquist & Browne, 1989; Giggenbach et al., 1994).

The higher permeability and changes in fluid flow are the result of acid-sulphate alteration destabilising the shallow geology which has also caused the formation of extensive collapse craters (Lloyd, 1959; Hedenquist & Henley, 1985) (Figure 6.1D and 6.2A), as well as a change from adularia

stability to white mica due to the change of pH (Hedenquist & Browne, 1989). Mineralogically, our rock/soil samples indicate extensive silicification and weak acid-sulphate mineral associations occurring together, whereas these associations are not present elsewhere (Figures 3.4) (Giggenbach et al., 1994; Pope & Brown, 2014). The alteration mineralogy includes Fe-oxides like goethite and hematite (Figure 3.3); and Ti and Ba-rich minerals (e.g. baryte), occupying vug/voids which are reported for the first time in Waiotapu Geothermal Field (Figure 3.6). There is a high concentration of barium in the soil/rock samples (Figure A2.7), but the acidity and high concentrations of sulphur and sulphates can react with barium forming insoluble barium sulphate and salts (Llugany et al., 2000; Monteiro et al., 2011), which can decrease barium bioavailability (World Health Organization, 2016). This has been captured by the foliar maps (Figures 4.6 and 4.7), which in the nearby areas of Champagne Pool present low concentrations of barium in plants, regardless of high concentrations in the rock/soil samples.

Kanuka living in this area is stunted (<1 m tall), as the plant develops shallow roots due to the diffuse heat output which enables them to survive (Boothroyd, 2009), but not to grow tall. This behaviour has been previously observed in other geothermal areas of New Zealand (e.g. Karapiti, Waimangu and Tokaanu) (Burns, 1997; Muukkonen, 2005; Mia et al., 2012). In our investigation we can observe that it is the style of heat output (i.e. “diffuse”) which provokes the short height of kanuka, affecting the root system. Such “diffuse” heat output is a consequence of the high permeability in the shallow subsurface (<200 m) which can also be observed in the TIR-derived thermal anomaly pattern (Table 5.1). Even though the eruption craters present a preferred orientation (N80°E) (Lloyd, 1959; Hedenquist & Browne, 1989)), the thermal anomalies observed in our analysis present no preferred orientation, possibly due to the inclusion of all thermal anomalies (Table 5.1). Overall, this area has lower surface temperatures (<47 °C) than in the north (Figure A3.1 and Table 6.2) and are in part caused by the dilution of fluids (Giggenbach et al., 1994) by cooler groundwater, but also due to the higher amount of permeable pathways which enables the “diffuse” heat output.

Table 6.2. North/South areas differentiating characteristics.

Characteristic	**North (acid-sulphate alteration)**	**South (sulphate-chloride "mixed" alteration)**
Mineralisation	Kaolinite, alunite, jarosite and pyrite	Silica polymorphs, phyllosilicate minerals, baryte and iron oxides
pH	Acidic	Neutral to acidic
Average temperature at thermal anomalies	>47 °C	<47 °C
Fluid type	Steam-heated acid-sulphate waters	Sulphate-chloride waters
Thermal anomaly clustering	250 m	At all distances
Thermal anomaly orientation	N22°E	Majority within a NE orientation
Subsurface permeability	Limited to significant faults and fractures	Micro-fracturing and rock permeability
Rock/soil element enrichment	-	Ag, Au, Sb
Kanuka foliar element enrichment	Ba	Ag, Au, Sb
Kanuka height	>1 m	<1 m
Rock/Soil Ag	<0.10 (mg/kg)	0.10-6.94 (mg/kg)
Rock/Soil As	<700 (mg/kg)	500-12000 (mg/kg)
Rock/Soil Sb	<30 (mg/kg)	30-392 (mg/kg)
Rock/Soil Ba	<700 (mg/kg)	700-1020 (mg/kg)
Plant Ag	<0.015 (mg/kg)	0.006–0.15 (mg/kg)
Plant As	<1.20 (mg/kg)	1.20–6.50 (mg/kg)
Plant Sb	<0.25 (mg/kg)	0.25-2.86 (mg/kg)
Plant Ba	5-33.65 (mg/kg)	<5 (mg/kg)

In synthesis, Waiotapu Geothermal Field is a remarkable natural laboratory for observing interactions among host rock and uprising geothermal fluids and how these are being imprinted into the distribution of the thermal anomalies, soil/rock and plant systems. The given 'Protected' status has allowed such systems to evolve and manifest naturally, giving new avenues of information not only to understand the geothermal system but to design new exploration and monitoring tools in the future.

6.2 Implications for geothermal exploration

6.2.1 New Zealand context

Exploration of geothermal areas in New Zealand has been active since the 1950s, with Wairakei becoming the first power plant in 1958, starting with a generation of 11.2 MWe (Lund et al., 2022). During the last couple of decades low carbon emitting energy production has gained renewed interest

due to New Zealand's goal to become carbon neutral by 2050 (i.e. cutting greenhouse gas emissions to as close to zero as possible) (New Zealand Institute of Economic Research, 2018; Timperley, 2020; Wang et al., 2022). Geothermal energy represents ~18% of the electricity supply in New Zealand with 1,064 MWe of installed capacity (Lund et al., 2022). However, the geothermal energy production potential in New Zealand is estimated to be ~2,500 MWe on top of the existing installed capacity (Kelly, 2011), indicating potential growth in the future. Only 9 out of 29 high temperature geothermal fields in New Zealand are presently utilised for power generation (Simpson & Bignall, 2016). Waiotapu Geothermal Field along with another 6 geothermal fields (Waimangu, Orakei Korako, Te Kopia, Horomatangi, Tongariro and Ruapehu), have a 'Protected' status and therefore they will not be exploited for their energy potential.

Most of the geothermal systems in the TVZ share many commonalities. For example, they are rhyolite-hosted, have liquid-dominated reservoirs with near-neutral high-chloride waters and present distributed surface thermal anomalies and features (Simpson & Bignall, 2016). Furthermore, most of the geothermal systems in New Zealand also share similar mineralogy/alteration styles and permeability structures. Likewise, Waiotapu Geothermal Field can be considered as a representative geothermal field. Such commonalities can facilitate the adaptation of new methods for exploration and monitoring. The understanding of most of these systems in New Zealand have come from geophysical (i.e. magnetic, resistivity, seismicity and gravity) (Soengkono, 2001; Hurst et al., 2016; Bertrand et al., 2022), and geochemical surveys (Bignall et al., 1996; Pope & Brown, 2014; Bégué et al., 2017). Alternative techniques include vegetation studies and calorimetry measurements. Calorimetry techniques involve a water-based calorimeter which measures surface heat flux and relates it to boiling point measured at diverse depths to calculate heat loss (Bromley & Hochstein, 2005). This technique has been linked to plant category maps (derived remotely), finding relationships between plant categories and heat flux (Seward et al., 2018).

The plant cover amongst geothermal systems of the TVZ presents the same plant communities (e.g. kanuka shrub, fernland, lichenfield, mossfield) (Burns, 1997; Beadel et al., 2018). Kanuka shrub (i.e. *kunzea ericoides* var. *microflora*) is the dominant species in soils >40 °C, across geothermal areas of the TVZ (Burns, 1997). Kanuka's height inversely correlates to the soil temperature (i.e. shorter heights as the soil becomes hotter) (Burns, 1997; Van Manen & Reeves, 2012). This has been quantitatively confirmed by our LiDAR-derived height maps (Chapter 4), however, kanuka can grow tall (>1 m) in areas where surface manifestations can have high temperatures (>47°C) as long as the heat output is point-like and constrained, like in the northern areas (Figure 6.3). Whereas in the southern region kanuka is shorter, not solely due to temperature, but because of the heat output being very "diffuse" (Chapter 5). Furthermore, the change of kanuka canopy structure has mostly been associated with the surface heat output, such relationships have been studied in association with calorimeters (Bromley & Hochstein, 2005) with the addition of subsurface temperature measurements to calculate

the heat-flux in geothermal areas (Seward et al., 2018). However, the effects of kanuka's capacity to uptake toxic elements have not been used as a tool for exploration and monitoring geothermal systems, until now.

Besides the physical changes to the canopy structure and plant height, this study has also shown the potential to use kanuka plants for measuring foliar element concentration that can be linked to underlying geological processes (Chapter 4). This can be adopted into the geothermal exploration methods in New Zealand for both monitoring and improving the geological understanding of geothermal areas. The uptake of toxic elements Ag, As and Sb by kanuka previously reported (Dunn & Christie, 2019), which our research has been able to detect via airborne and satellite hyperspectral imaging. Combining the hyperspectral imagery with ground-based samples, the developed foliar element maps correspond well with underlying geology (e.g. known from drill cores, water chemistry and geological/geophysical mapping), and, these foliar element maps follow the same trend as rock/soil samples (Figure 4.4). On the contrary, barium, a non-essential/toxic element to plants (Monteiro et al., 2011; Sleimi et al., 2021), show the opposite trend that Ag, As and Sb (Figure 4.4). In this case, Ba in plants does not correlate positively with Ba concentrations of rock/soil samples (Figures A2.6 and A2.7). This is due to changes in the form of Ba and the environment that affects its bioavailability (Llugany et al., 2000; World Health Organization, 2016). However, sampling a variety of soil horizons in future surveys is recommended as this can elucidate mobility and bioavailability processes which can vary between different geothermal areas. Other plant species living in the vicinity of geothermal areas should also be sampled and analysed to further understand the translocation processes for each species (Further recommendations are given in Chapter 6.2.3).

The point pattern analysis derived from TIR imagery is a technique with the potential to be applied to other geothermal areas. TIR imagery is time and cost-effective (Harvey & Luketina, 2014; Abubakar et al., 2019), providing a snapshot of the system's present state (Zaini et al., 2022). TIR imagery has been used to assess heat-output in geothermal systems of New Zealand (Mongillo, 1994; Mia et al., 2012; Harvey et al., 2016; Reeves & Sanders, 2019), likewise point pattern analysis can be used in the exploration phases as well as with repeat surveys for monitoring purposes. The latter can assist in the understanding of spatio-temporal associations within the system, particularly in the shallow subsurface (<200 m) (Chapter 5), using historic TIR imagery (Reeves et al., 2015; Ramsey & Flynn, 2020). Previous airborne TIR data (from previous years employed for heat-output calculations) as well as satellite and drone-derived TIR, can be used to detect thermal anomaly changes which can be associated with subsurface changes within the system. Satellite data have the advantage of being freely available but only to a certain spatial resolution per pixel (e.g. ~100 m with Landsat 8 and 9) (Costanzini et al., 2021), which does not provide enough details for point pattern analysis of single geothermal fields. On the other hand, drone-derived TIR imagery can provide high spatial resolution (cm per pixel) in

relatively smaller areas (Marwan et al., 2021) and high temporal frequency which can be employed to monitor the hazards from geothermal areas (e.g. Hipaua (Hegan et al., 2001)).

Table 6.3. Cost and benefit comparison table for different techniques employed in geothermal areas. For a geothermal area like Waiotapu Geothermal Field (18 km^2) the total cost of ground surveys would add up to ~$200,000 NZD. While airborne surveys (TIR and hyperspectral) would add up to ~$50,000 NZD.

Technique	Cost (NZD)	Pros	Cons
Reconnaissance ground mapping	~400 $/km^2	Detailed and inclusive contextually	Accessibility, time
Geochemistry (water)	~$50 per sample. (50-5,000 samples)	Simple and fast	Accessibility, limited sampling
Ground magneto-telluric	~$54,000 per station (station every 200 m^2–1 km^2)	Detailed and direct detection	Accessibility, time consuming
Airborne magnetic	~200 $/km^2	Surface coverage and accessibility	Lower resolution
Airborne TIR	~800 $/km^2	Surface coverage and accessibility	Tandem ground survey for calibration.
Airborne hyperspectral	~400 $/km^2	Surface coverage, accessibility and detail	Complex processing and large computational demands (data storage and processing power)
Satellite hyperspectral	Free	Surface coverage and cost	Spatial resolution and time-frequency. Complex processing and large computational demands (data storage and processing power)

6.2.2 International context

The methods presented and workflows have the potential to be not only used throughout New Zealand but also in other geothermal systems internationally. Countries located in temperate climates with tropical climates such as México, Dominica, Indonesia and Costa Rica have geothermal systems densely covered by vegetation (Figure 6.4), and therefore exploration methods can aid in such contexts. Plant species that are thermotolerant and prevail in the harsh environment of geothermal areas have already been identified, including shrubs in Italy (*Evernia prunastri*, *Calluna vulgaris*), sagebrush in the U.S.A. (*Artemisia tridentata*), shrubs in Kenya (*Tarchonanthus camphoratus*) or grasses in Mexico (*Allenrolfea occidentalis* and *Thypa dominguensis*) (Way & Hall, 2001; Nash et al., 2003; Manzo et al., 2013; Pippucci et al., 2015; González-Acevedo et al., 2018; Lattanzi et al., 2020). Species like these can therefore become a primary target for geothermal exploration efforts with hyperspectral imaging, opening up new avenues for the development and use of technology for understanding and exploring geothermal resources.

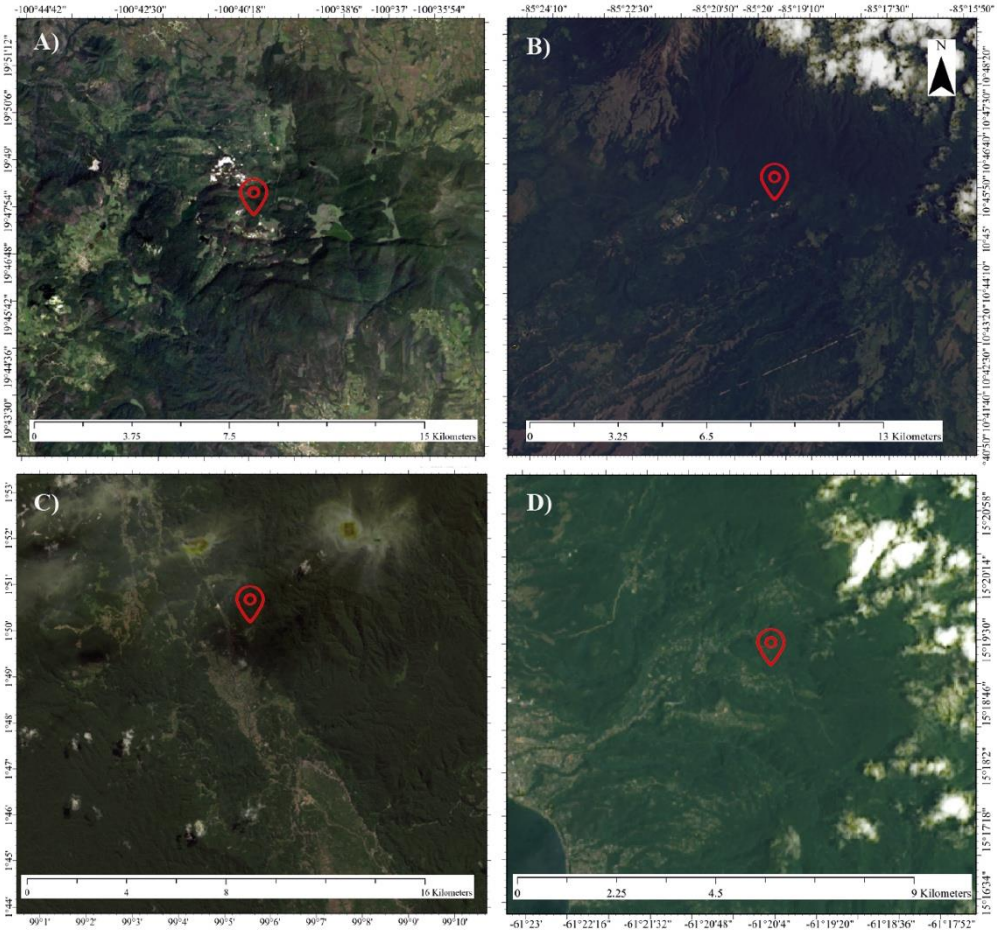

Figure 6.4. Landsat 8 images from densely vegetated geothermal areas. A) Los Azufres, México. B) Las Pailas, Costa Rica. C) Sarulla, Indonesia. D) Wotton Waven Laudat, Dominica.

Geothermal systems of New Zealand are comparable geologically with other systems hosted by volcanic rocks around the world which also have surface thermal manifestations and liquid-dominated reservoirs (Moeck, 2014; Santilano et al., 2015, McCleskey et al., 2022). Similarities within systems can allow for the techniques employed in New Zealand to be used in other countries. The volcano-derived geothermal areas share systematic conditions that generate similar surface manifestations with comparable fluid chemistry, soil pH, and temperatures. These conditions in combination with other environmental constraints particular to the region (e.g. water availability, air temperature, organic matter) will directly influence the plant species growing in the area and their chemical uptake capabilities (Zhou et al., 2015; Ubeynarayana et al., 2021). Fluid chemistry controls the media where nutrients and non-essential elements are transported and uptaken by plants under preferential conditions (Finlay et al., 2020). One of the main conditions for plant uptake is soil pH, which has also an impact on substance availability and biological processes (Neina, 2019). In geothermal, areas soil pH values can range from highly acidic to basic, with predominant strong acidic soils (e.g. pH of 3-4 in geothermal areas of TVZ) (Smale et al., 2018). Correlations between plant species, soil pH and soil temperature have been found in countries like New Zealand and Italy (Pippucci et al., 2015; Smale et al., 2018). Due

to the relevance of these parameters (i.e. fluid chemistry, soil pH and temperature), they must be taken into account when observing the element uptake by plants living in geothermal areas. Acquiring these either from previous studies or preferably in-situ measurements in the field while sampling the plant material is highly recommended (Further recommendations in Section 6.2.3)

New generations of hyperspectral satellites (e.g. PRISMA, EnMAP, SBG (Qian, 2021) (Table 6.4)) can be an attractive vehicle to expand some of the novel retrieval methods for generating foliar element concentration maps to other geothermal areas globally. Given the distribution of indicator and (hyper-)accumulator plant species, our approach should be tested for feasibility in other geothermal areas. In this study, freely available PRISMA satellite imagery gave good results (Overall accuracy of 0.57–0.66) for the elemental zonation maps (Chapter 4). Satellite imagery can be particularly relevant in countries where the financial budget does not allow for the acquisition of airborne surveys and vegetation cover is dense (e.g. Caribbean and Central America) (Table 6.3).

The potential applications for element mapping from different remote sensing platforms are wide. The uptake of non-essential elements is in some cases human induced (e.g. remediation purposes) (Neina, 2019; Sridhar et al., 2022), but concerns regarding their mobility and the possible effect on the food chain is an emerging concern which requires urgent attention (Pullagurala et al., 2018; Abedi & Mojiri, 2020).

Table 6.4. Spectral and spatial specifications of current and planned hyperspectral satellites.

Satellite	Band number	Bandwidth (nm)	Spatial resolution (m^2)	Reference
PRISMA (PRecursore IperSpettrale della Missione Applicativa)	230	≤12	~30	(Cogliati et al., 2021)
EnMAP (Environmental Mapping and Analysis Program)	242	6.5-10	~30	(Guanter et al., 2015)
SBG (Surface Biology and Geology)	210	4-12	~30	(Stavros et al., 2023)

6.2.3 Recommended surveying and processing guidelines

From this investigation, we provide a summary of recommendations that can improve geothermal exploration efforts.

- Field and ground sampling considerations:
    - Both soil/rock and plant samples should be collected covering a diverse range of locations (e.g. temperature, type of lithology, elevation, closeness to surface features)

as well as background values that are located outside of the geothermal field. To analyse for elemental concentrations, soil pH and spectral responses.

- Measurements of soil pH and nearby fluids if no previous study has been presented.
- Ground temperature measurements to calibrate the airborne TIR imagery. If possible water bodies can provide the most accurate results (Reeves & Sanders, 2019).
- Even though the number of ground samples should be at least a 100 for the best performance of some of the methods (Rattenbury et al., 2018; Santaga et al., 2021), the number will be a function of the size of the field and available surface features and accessibility.
- When airborne data are used for mapping, it is always a good practice to develop prediction models using ground-based spectroscopy (e.g. using an ASD-type spectroradiometer). This can provide guidance and additional proof for quantifying rock/soil/plant interpretation over a highly dynamic geothermal setting.

- Data processing and mapping considerations:
  - Geo-rectification and atmospheric corrections are critical, due to the complex distortions inherent in remotely sensed imagery (Kruse, 2004; Jia et al., 2020; Sun et al., 2021). Novel geo-rectification approaches can be tested (e.g. Optical flow estimation and deep learning based methods), to improve accuracy (Feng et al., 2021). Atmospheric corrections usually follow a standardised process which does not use in-situ (i.e., ground, aircraft) measurements (Jia et al., 2020). However, in-flight calibrations and in-situ measurements (e.g. water vapour and aerosol optical thickness) (Rodger, 2011; Zhang et al., 2015) could help to improve accuracy in subsequent applications (Jia et al., 2020).
  - Post-processing method can further be explored, in particular un-mixing techniques (Heylen et al., 2014; Annam & Singla, 2021; Pattathal et al., 2022). The higher overall accuracy values from airborne and spaceborne models in comparison to laboratory models could be a consequence of the mixed spectral information contained in each pixel (e.g. bare ground exposure). The “real-world” situations include a variety of materials in each pixel (Sahoo et al., 2021), which can be positively influencing the model’s accuracy in this study. Therefore, un-mixing techniques should be explored to understand how much is plant information and how much the surrounding materials (Wei et al., 2020; Sun et al., 2021).
  - Validation should be based on a combination of cross-validation or training/validation split methods (Pawluszek-Filipiak & Borkowski, 2020; An et al., 2021), as well as using existing geological information (e.g. water chemistry, geological maps and independent observation) (Rossel et al., 2008; Deon et al., 2019; Thompson et al., 2019).

6.2.4 Challenges and opportunities of hyperspectral imaging in geothermal exploration

Convectional geothermal systems follow an overall structure (i.e. heat source, deep parental waters and enough permeability to allow convection) which forms similar surface manifestations, but each system has its particularities. In other words, these particularities can create the necessity to develop and fine-tune hyperspectral-based mapping methods case-by-case. This geological uniqueness can also be complemented by plant species and their various metal uptake capabilities which can make remote sensing-based mapping geothermal systems intrinsically challenging.

Due to the uniqueness of the study areas and the complexity of the acquired data, there is a necessity to test various methods. In this investigation, we detailed some of the limitations and challenges to roll out hyperspectral and TIR-based exploration techniques (Chapters 3 to 5), which here are broadly revisited.

Intrinsic limitations by the data: Narrow bandwidth hyperspectral data are superior in resolving fine-scale reflection and absorption features, capable of discriminating minerals (van Ruitenbeek et al., 2006) and plant processes (Wang et al., 2018). Data from air- and spaceborne platforms must undergo pre-processing techniques (e.g. geo-rectification, atmospheric correction), which are standardised and rely on parameters usually not measured during the data acquisition (Sun et al., 2021). Furthermore, this type of data presents lower signal-to noise ratio, band saturation and spectral mixing than laboratory-based data. Regardless, in this investigation, better overall accuracies were achieved from air- and spaceborne models than laboratory-based models (Table 4.3), possibly due to the additional information provided by canopy structure (i.e. plant shape and biomass) (Croft et al., 2014; Almeida et al., 2021; Zeng et al., 2022) and the degree of mixed pixels (i.e. plant and bare ground exposure).

Due to conventional methods and the appearance of new sophisticated processing algorithms for de-noising, data transformation, un-mixing, regression, and classification we are not limited by the options. Designing new and optimal workflows that are appropriate for handling the complexity of the hyperspectral data and are capable of detecting processes important for geothermal exploration is critical. Based on this research, we recommend considering the limitation of the data and designing workflows accordingly to optimize the outputs.

In this investigation, the SWIR region from the airborne-based data was noisier than the VNIR, but simple smoothing techniques (i.e. Savitzky-Golay filter (Savitzky & Golay, 1964)) are effectively overcoming such limitations to improve the mapping results (Pan et al., 2015; Hou et al., 2018). De-noising techniques can also be employed to improve spectral data (Rasti et al., 2018, 2021), while de-noising can take away some information it can also maximise the regression and classification performance (Rasti et al., 2018; Pattathal et al., 2022). In Chapter 3,

an inherent data limitation was presented; the acquired hyperspectral range (i.e. VNIR and SWIR) is incapable of identifying minerals such as quartz or silica-polymorphs due to their lack of characteristic absorption features (except for opal, which has absorption features in the SWIR). However, Support Vector Machine (SVM) algorithm was capable of overcoming this by incorporating light intensity, differentiating silica sinter deposition from other lithologies (e.g. pumice). Even though it worked for Waiotapu Geothermal Field, we caution against broader use of this approach without robust ground data or remote sensing data capturing other parts of the electromagnetic spectrum (e.g. TIR infrared hyperspectral data) (Vaughan et al., 2005; Qudsi & Noor, 2022) confirm such relations. In future geothermal exploration and monitoring hyperspectral surveys where only VNIR and SWIR regions are available, surface classification with SVM can present an advantage.

Elemental concentrations cannot be directly predicted with VNIR/SWIR hyperspectral data due to the lack of absorption features of such elements (Chapter 4). However, their presence can be inferred using physical and chemical features of the plant that tend to co-vary with such elements (i.e. the pathfinder approach). To analyse the causality of spectral changes, mean decrease accuracy and mean decrease Gini values were extracted, ranked and added to compute a single total variable score of importance, following Hong et al. (2016). Relevant wavelengths within the VNIR and SWIR regions found by our models were successfully correlated to specific physio-chemical effects within the plant (Figure 4.8). Most of the important wavelengths are in the visible range for all datasets (i.e. laboratory, airborne and spaceborne), and >1000 nm for the laboratory-based dataset (Figure 4.8). The found important wavelengths have also been previously documented in pot experiments to show chlorophyll and carotenoid absorption, red-edge shift, metal-induced stress, water content, and degradation of foliar pigments (Delalieux et al., 2009; Slonecker et al., 2009; Rathod et al., 2018). Ag, Ba and Sb presented unique important wavelengths, whereas As shares most of its important wavelengths with the other elements (Table A2.5). This has resulted in a decrease in the classification's overall accuracy for As in comparison to the other elements (Table 3.4). Laboratory-based models present very similar important wavelengths regardless of all plant samples being dried and grounded. This strengthens the argument that it is not only the plant's physical variations (e.g. canopy structure, leaf area index, biomass) (Ryu et al., 2020; Neinavaz et al., 2021; Xie et al., 2021) which can reflect the underlying geothermal activity but chemistry and cellular structure variations as well.

Model performance is directly impacted by the input data. The elemental concentration training data were skewed for all elements (i.e. Ag, As, Ba and Sb) even though the random forest algorithm can handle non-normal data distribution (Pullanagari et al., 2016). An improvement in the models was observed when Log-Ratio (LR) transformation was applied to the chemical data. LR converts the data into compositional data which allows for traditional statistical methods to

be used. For regression models, performance is low, and no significant improvement was observed between raw data (e.g. mg/kg) and LR transformed data. The foliar elemental maps for Ag, As, Ba and Sb (Chapter 4) were developed using Kernel Partial Least Squares (KPLS) regression and Random Forest classification models. For small sample populations like this study (77 samples), outliers can contain relevant information about the system. The 77 ground samples acquired in this study were potentially just enough to produce prediction models using leave one out cross-validation (LOOCV), but the quantity does not allow for band selection methods, such as Successive Projection Algorithm (SPA) (Cao et al., 2018; Liu et al., 2022) and sCARS-SPA (stable Competitive Adaptive Reweighting Sampling-SPA) (Wei et al., 2020; Annam & Singla, 2021). Future studies should be targeting adding new sampling locations and also expanding this methodology to other geothermal areas. This can allow the application of other validation methods (e.g. K-fold cross validation, bootstraping) (Stehman & Foody, 2019; An et al., 2021), as well as stratifying samples into other types of categories (e.g. temperature, type of lithology, elevation, closeness to surface features) to analyse particular traits of their behaviour.

In this research, a standard deviation method was employed to classify elemental values (Figure 4.3), dividing the element concentration values into three classes (low, medium and high). This is an apparent relative approach that maps any departures from the mean (e.g. Chapter 4), however, in the future, similar methods should be trialled using element construction sampled outside of geothermal areas to maximise the range of element concentrations. It is also self-evident that such levels can differ for each element in a case-by-case scenario. Random Forest classification algorithm was selected due to its capacity to deal with big datasets (Xia et al., 2014) with high co-linearity (Belgiu & Drăgu, 2016), while the KPLS regression algorithm was chosen for its capacity to solve non-linear problems and previous application to plant datasets (Pullanagari et al., 2016). Even though both models (i.e. classification and regression) present spatially congruent results, accuracy values are significantly better for classification than regression models (Table 4.3 and A2.4). Furthermore, successful upscaling of the methodology from airborne data (AisaFENIX) to spaceborne data (PRISMA) resulted in slightly higher overall accuracies (OA) for spaceborne (i.e. airborne OA of 0.45 to 0.57, spaceborne OA of 0.57 to 0.66), possibly due to the higher proportion of mixed pixels (e.g. exposed bare ground). Thus, this should be investigated in the future via un-mixing methods (Bhatt & Joshi, 2020; Annam & Singla, 2021; Pattathal et al., 2022).

The detected spectral responses and foliar maps are qualitative representations of the environmental generalities and do not represent exact element quantities in the plant foliage. A great deal of research is still pending to fully understand the spectral responses that a complex environment such as geothermal areas cause to plants. Since a wide range of parameters can control the element uptake the individual effect of those parameters are yet to be understood on a

species-by-species level (Lichtenthaler, 1996; Zweifel et al., 2009; Lausch et al., 2018; Ryu et al., 2020; Zhu et al., 2021; Húdoková et al., 2022; Li et al., 2022; Zeng et al., 2022). This can certainly add complication to generalising the proposed methods due to the uniqueness of each plant's response when under stress. Therefore, besides understanding how element uptake and storage affect plants (Dunn, 2011; Dunn & Christie, 2019; Húdoková et al., 2022), knowledge about the geological setting can maximise the efficiency of the method. Previous knowledge on the possible environmental factors controlling plant-uptake (e.g. temperature, soil pH, fluid chemistry) (Pippucci et al., 2015; Crowther et al., 2019; Morfopoulos et al., 2022; Uchimiya et al., 2020; Zeng et al., 2022), can assist on an assertive interpretation of results (spatial trends and important wavelengths).

Even though our classification models perform moderately, by error metrics (e.g. R^2), spatially our foliar element predictions are consistent with independent LiDAR and TIR datasets, field data and existing geological, geophysical and geochemical datasets available for Waiotapu Geothermal Field. However, there have been studies where the opposite trend is observed, high accuracy figures (e.g. R^2, OA) which are spatially unrepresentative, due to mislabelling of small geological features (caused by over-smoothing before an SVM classification) (Lorenz et al., 2021). Therefore, error metrics must be taken with caution and validated independently with other datasets.

TIR imagery can be used to detect thermal anomalies, however, the spatial organization has barely been analysed through point pattern analysis. Our study has found two main user-bias when point pattern analysis is applied to the thermal image and geothermal settings: the selection of thermal anomalies and boundaries for pattern analysis. The selection of thermal anomalies is complex; it requires manual on-screen assessment and includes several assumptions. Only distinguishable thermal anomalies from the TIR imagery were selected, this means that in bare soil the selection is straightforward, but areas with vegetation cover can mask some thermal anomalies out. The arbitrarily chosen temperature threshold of 25 °C was assumed to be indicative of a thermal anomaly, a temperature that corresponds to convection effects on the surface (Seward et al., 2018). In water bodies where no clear hot water outflow was detected, a single point in the middle of the water body was digitised. These assumptions can cause underestimation of thermal anomalies, regardless, it does not conflict with the general interpretations due to the two clear styles of thermal anomalies' heat output: point-like and diffuse (Chapter 5). In northern areas (Figure 6.2), point-like heat output allows plants to grow tall (>1 m), possibly masking small thermal anomalies. However, diffuse thermal anomalies (present in the "mixed" area) were not observed in the northern areas, reducing the possibility of small thermal anomalies being masked by vegetation.

For the point pattern analyses, a boundary must be selected by the user, increasing subjectivity. In this case, we selected the boundaries which seemed more naturally occurring, but the variation of boundaries greatly changes the results (more details in Chapter 5). The spatial pattern analysis has been used previously for volcanic studies (Runge et al., 2015, 2016; Schmidt et al., 2022), and even though deep magmatic heat and active faults are relevant for the permeability control on volcanic events (Cassidy et al., 2018; Lin et al., 2018). For geothermal systems, the shallow subsurface (<300 m) plays an important role in surface manifestation and thermal anomaly patterns, which can also be linked to plant density and height (Chapter 5). The similar deep geological constraints throughout the geothermal systems of the TVZ, would allow for the shallow subsurface permeability parameters to be compared through the thermal anomaly point pattern analysis.

In terms of the inferred information combined from TIR and LiDAR datasets, in general, the results strengthen the inverse correlation between height and soil temperature and enlighten the relevance of element uptake and their effects on plants. In general, areas of high Ag, As and Sb concentration overlap with high temperatures and short plant heights (<1 m). However, there are areas where vegetation is >1 m and presents high element concentrations, exposing the complexity of bioaccumulation processes, and requiring further studies.

Other challenges may arise as the method advances, but the opportunities are far-reaching. With applications in soil remediation, agriculture and environmental sciences, the scope is considerable. Furthermore, the methods and workflows can evolve accordingly to the site and there is space for improvement due to the always improving techniques and computational power.

6.3 Future work and new directions

a) Due to the complexity of geothermal environments, a deeper understanding of how fluid chemistry, soil pH and temperature affect plants is required. Controlled experiments with the species of interest (e.g. indicator species or metal accumulators) should be carried out to understand each parameter individually and as a group. Experimentally testing a range of temperatures, soil and fluid pH values, and element concentrations on soil and fluid, along with a combination of these. These methods have been applied to plants which are used for remediation in mining sites, to understand their tolerance to be exposed to toxic elements, their uptake capabilities and how they reflect these in their spectral reflectance (Craw et al., 2007; Lassalle et al., 2019; Sridhar et al., 2022). Studies have also been performed to understand the effects of drought on plants and how this can be detected through remote sensing techniques (Bendig et al., 2012; Khaleghi et al., 2019; Khayatnezhad & Gholamin, 2020). Studies in salinity and air temperature also exist (Buitrago et al., 2016; Zhu et al., 2021; Morfopoulos et al., 2022), but specific studies to understand the environmental effect of geothermal areas on plants do not exist.

b) Biophysical traits of plants living in geothermal areas can influence their spectral signature (Xie et al., 2019; Pascucci et al., 2020; Neinavaz et al., 2021; Xie et al., 2021; Almeida et al., 2021; Mngadi et al., 2022). Therefore, field measurements of biophysical variables (e.g. canopy structure, leaf area index, chlorophyll and nitrogen content, fraction of photosynthetically active radiation), can further enrich data as the one presented in this investigation. Allowing for the interpretation to be segmented to the different possible traits the spectral sensor is retrieving from the plant.

c) Integrating VNIR/SWIR with broadband single-band or narrowband hyperspectral data should also be part of future efforts in New Zealand. Narrowband TIR has already been proven to be a promising tool for detecting (alteration) minerals (e.g. quartz and its polymorphs and feldspars) (Vaughan et al., 2012; Notesco et al., 2016; Hecker et al., 2019; Nyahucho, 2020; Laukamp et al., 2021). On the other hand, studies involving remote sensing techniques of plants living in geothermal areas are not vast. Technological advances, including airborne Hyperspectral Thermal Emission Spectrometer (HyTES) and satellite ECOSTRESS, have increased the interest and allowed for more studies to take place (Chang et al., 2021; Neinavaz et al., 2021; Rosas-Chavoya et al., 2021). The insights available by analysing TIR imagery (e.g. water stress and biophysical parameters) are relevant for geothermal studies.

d) Exploring point pattern analysis application in geothermal areas requires further investigation at different spatial scales. It has been carried out at regional scales before (e.g. Carranza et al., 2008), and in this investigation, it was presented for a single geothermal system (Chapter 5). Furthermore, with a standardised methodology, a comparison can be carried out between densely vegetated and non-vegetated geothermal areas, to corroborate if the patterns relating thermal anomalies and shallow subsurface permeability found in this investigation (Chapter 5) persist in other geothermal areas of New Zealand and the world. If such interpretations are validated, then the application of point pattern analysis derived from thermal infrared imagery can become common practice for exploration and monitoring efforts in geothermal areas.

e) Other pre and post-processing techniques should be carried out on different datasets going through the presented methodologies to improve model performance. It is not a one-size-fits-all, and therefore, different techniques must be tested. Some pre-processing techniques include Centred Log-Ratio (CLR), Minimum Noise Fraction (MNF), spectral derivatives, multiplicative scatter correction (MSC) or Orthogonal Total Variation Component Analysis (OTVCA) (Rasti et al., 2016; Li et al., 2021; Lorenz et al., 2021; Sonobe et al., 2021) can be applied. While post-processing can include pixel un-mixing, smoothing and subspace clustering techniques (Sahoo et al., 2021; Pattathal et al., 2022). These can benefit model's performance and provide more accurate results as well as diminishing computational requirements.

f) Analysis of gas emissions from volcanoes has previously been analysed with remote sensing techniques, prediction of volcanic unrest (Queißer et al., 2019), and effects of degassing on vegetation

(Tortini et al., 2017). Degassing has been measured remotely (Sun et al., 2022) and with ground techniques (Jentsch et al., 2020) for geothermal applications to locate geological structures (e.g. faults) and assess permeability. Remote sensing detection techniques could therefore complement and give further detail to our models on the shallow hydrology of geothermal areas, in particular for "blind" geothermal systems (i.e. systems which do not present surface manifestations) or geothermal systems heavily covered by vegetation (Kratt et al., 2009; Sun et al., 2022).

6.4 Conclusions

Our research demonstrates a novel exploration and monitoring tool for geothermal areas using airborne and satellite-based remote sensing. Waiotapu Geothermal Field is a great natural laboratory to develop new methods that are non-invasive and fast to track changes within a geothermal system. The methodology which included hyperspectral, thermal infrared (TIR) and LiDAR data complemented by rock/soil and plant (kanuka) samples, has been carried out to look at plant relations and reaction to the subsurface activity, surface alteration mapping and thermal anomaly patterns analysis. Our results have been tested promising on the research level, but it needs further research to exploit the technology in the commercial sector (e.g. geothermal exploration).

This research has integrated its results into a detailed conceptual model for the Waiotapu Geothermal Field. Waiotapu Geothermal Field can be subdivided into spatial zones that are characterised by an array of physical and chemical properties. The northern parts are characterised by acid-sulphate alteration driven by H_2S-rich steam condensation, removing alkalis and silica from the host rock to develop kaolinite and other phyllosilicates (Chapter 3 and Figure 6.1B) (Hedenquist & Browne, 1989; White & Hedenquist, 1990). While these areas in the north were flagged to be different compared to the southern areas due to how plants interact with geothermal processes (Chapter 4). Furthermore, TIR-based point pattern analysis has been conducted to reveal the heat output, which reflects a more constricted permeability in shallow subsurface (Chapter 5). Possibly due to a thicker litho-cap (Wood, 1994) and precipitation of clay minerals (Hedenquist & Browne, 1989). Structural control suggested previously at Waiotapu Geothermal Field (Hedenquist, 1991; Wood, 1994; Rowland & Simmons, 2012) is inferred from TIR-imagery derived thermal anomaly patterns, which follow the system's orientation (~ N22E°) and nearby active faults (i.e. Paeroa and Ngapouri Faults ~ N40E° and ~ N60E°, respectively) (Hedenquist & Henley, 1985; Cochrane et al., 1994; Wood, 1994). From the TIR-derived thermal anomaly pattern analysis, a ~250 m spacing has been attributed to the possible "synchronisation" of convection cells (Chapter 5), a behaviour found in three-dimensional numerical simulations (Patterson et al., 2018). The point-like heat output allows plants to develop deeper roots and grow tall (>1 m) in close vicinity to the thermal anomaly (Chapter 5). The kanuka plants living in the northern areas are enriched with barium (Chapter 4), an element associated with hot water mixing with

shallow colder waters (Dunn, 2011). Such high concentrations were detected with models derived from hyperspectral data and elemental concentrations in soil and plant samples (Chapter 5).

The "mixed" areas in the south result from the combination of rising high-chloride "parental" fluids which encounter a shallow discontinuous sulphur-rich water body (Lloyd, 1959; Hedenquist & Browne, 1989). Resulting in intermittent weakly to pervasive acid-sulphate alteration (e.g. Fe-oxides with extensive silicification) and areas of silica sinter deposition areas. (Lloyd, 1959; Hedenquist, 1991; Giggenbach et al., 1994) (Chapter 3). These were identified in the lithology mapping from the hyperspectral imagery and corroborated with rock/soil samples (Chapter 3). The evolution of the system has changed the hydrogeology, alteration, as well as heat output style, which is diffuse and with overall lower temperatures (<47°C) than the north (Chapter 5). The higher permeability possibly initiated by lowering of the water table and hydrothermal eruptions in combination with acid-sulphate alteration has provoked collapse craters (Lloyd, 1959; Hedenquist & Henley, 1985) (Figure 6.1D). The higher permeability is also inferred from the TIR-derived point pattern analysis where thermal anomalies do not follow a particular direction and the point density is much higher with no detected spacing between clusters (Chapter 5). The diffuse heat output directly affects the growth of kanuka shrubs in the area; they are shorter (<1 m) because their roots cannot grow any deeper due to the near surface heat (Chapters 4 and 5). Plants present high concentrations of Ag, As, and Sb uptaken from the near-neutral chloride-rich outflow of Champagne Pool and other silica sinter deposition areas (Figure 6.3), which decrease as distance increases from Champagne Pool. The foliar Ag, As, and Sb broadly follow the same trend as rock/soil samples, indicating the potential of kanuka shrub to work as a proxy for subsurface activity (Chapter 4) that can be detected remotely (Figures 4.6 and 4.7).

Evaluating the objectives of this research, we can recapitulate the following.

To characterise surface alteration and deposition types in geothermal systems using hyperspectral remote sensing and ground exploration techniques. We employed supervised image classification methods on the hyperspectral imagery to delineate surface hydrothermal alteration at Waiotapu Geothermal Field. Our results show acid-sulphate and acid-sulphate with chloride alteration zones, which are in good agreement with previous studies (Lloyd, 1959; Hedenquist & Henley, 1985; Hedenquist & Browne, 1989; Hedenquist, 1991), while we have described barite occurrence at Waiotapu Geothermal Field for the first time (Chapter 3).

To develop a new remote sensing approach for chemical fingerprinting of geothermal activity using plant cover. We combined ground sampling of plants and laboratory, airborne and satellite-based hyperspectral data to develop a new zoning method for detecting foliar element concentrations. The mapped element anomalies/zones agree with independent geological/geophysical and geochemical data, while it is also supported by LiDAR-based height estimates of the plants (Chapter 4). These present

relevant findings which prove the potential of plants to act as a proxy for subsurface activity in geothermal areas (Chapters 4 and 5).

To quantify thermal manifestations and their preferred spatial occurrence using thermal infrared remote sensing. We applied thermal remote sensing for detecting thermal anomalies and combined it with point pattern analysis. Our results indicate that the thermal anomalies change from random to clustering in relation to their heat output "style" and subsurface permeability (Chapter 5). The orientation of northern thermal anomalies follows the overall system's orientation (~N22E), which consequently follows the nearby active fault's strike, in concordance with previous studies. Whereas southern areas present a range of orientations, predominantly with a NE orientation. Indicating to some degree of fault-controlled permeability.

Future studies should further examine and test the plant-environment relationship in geothermal areas, and how this is reflected in its spectral signature (Sections 6.2.3 and 6.2.4). The new methods and workflows can open a window for time and cost-effective techniques to be applied for the exploration and monitoring of geothermal areas with dense plant cover.

7 Appendices

7.1 Appendix 1 (A1)

Table A1.7.1. ICPMS data table for field soil and rock samples. Values in mg/kg.

mg/kg	Ag	Al	As	Au	Ba	Bi	Ce	Cr	Cs	Cu	Fe	Ga	Hf	K	La	Li	Mn	Mo
WAIs_01	0.039	4200	16.8	0.0012	52.3	0.2	7.9	12	2.14	11.04	6400	3.1	0.07	500	4.1	0.4	32	0.62
WAIs_02	0.05	3200	8.9	0.0005	95.8	0.22	3.1	3	2.5	1.33	18000	12.7	0.59	700	1.4	0.3	52	0.81
WAIs_03	0.039	1000	34.3	0.0013	164	0.3	10.5	2.8	1.91	3.37	7100	2.4	0.06	300	5.4	0.2	25	0.57
WAIs_04	0.084	600	12.2	0.0012	14.7	0.24	3.4	3	1.14	2.26	8300	2.7	0.2	200	1.7	0.4	29	0.43
WAIs_05	0.05	600	2.6	0.0003	20.9	0.09	3.2	2.1	0.9	1.52	3800	1.1	0.01	200	1.7	0.3	32	0.17
WAIs_06	0.017	1200	11.2	0.0006	137.2	0.21	10.8	0.8	0.09	0.46	2400	2	0.05	500	7.1	0.1	6	0.16
WAIs_07	0.008	6100	15.7	0.0001	163.3	0.67	10.2	5.4	0.71	1.99	25400	17.1	1.43	400	5.4	0.7	78	0.98
WAIs_08	0.01	31600	1.1	0.0001	489.9	0.73	86.8	3.2	0.08	0.64	16800	11.3	1.91	100	43	1	207	0.12
WAIs_09A	0.016	76800	4.9	0.0001	143.6	0.76	3.7	2.5	0.4	3.18	17700	17.2	3.64	50	1.5	0.8	83	0.09
WAIs_09B	0.015	8700	11.4	0.0001	487.2	0.42	0.4	1.2	0.06	0.24	40500	12.1	3.17	50	0.25	0.05	10	0.38
WAIs_10	0.025	700	2.5	0.0001	77	0.12	1.4	3.2	0.09	1.27	2600	2	0.27	50	0.5	0.1	11	0.25
WAIs_11	0.061	1900	27.9	0.0014	31.1	0.31	13.3	4.4	1.24	5.89	12800	4.9	0.46	200	6.3	0.4	35	0.53
WAIs_12	0.03	11300	5.4	0.0001	48.8	0.2	7.7	2.1	1.35	3.06	7700	4.8	0.18	200	4	1.5	57	0.34
WAIs_13	0.03	2800	41.4	0.0007	58	0.18	13.3	37.7	1.64	31.37	5700	1.6	0.38	200	4.7	1.8	83	0.52
WAIs_14	0.033	9300	7.5	0.0001	34.8	0.21	5.9	6.5	0.63	6.88	7200	5.3	0.28	400	2.7	0.8	35	0.45
WAIs_15	0.012	2900	32.1	0.0001	55.4	0.1	14.7	10.1	1.42	9.55	6900	1.5	0.32	100	6.6	1.5	89	0.7
WAIs_16	0.038	2000	2	0.0026	10.2	0.72	0.6	2	0.08	8.82	300	1.2	2.24	100	0.25	0.2	1	0.4
WAIs_17	0.073	1100	20.8	0.0001	11.9	0.34	2	2.9	0.79	1.18	16000	11.6	0.94	200	0.9	0.3	42	0.86
WAIs_18	0.056	29000	9.9	0.0006	51.1	0.27	8	4.3	4.25	3.01	17300	12.4	0.56	300	2.8	1.3	117	1.06
WAIs_19	0.107	1300	18.5	0.0012	17	0.42	3.6	3.1	0.7	3.19	14200	7.7	0.38	100	2	0.3	39	0.89
WAIs_20	0.916	300	157.2	0.6454	203.6	0.16	1	0.25	6.4	0.65	100	0.2	0.04	300	0.7	0.2	6	0.1
WAIs_21	0.073	50	4.5	0.036	957.8	0.21	0.6	0.9	0.06	0.05	50	0.05	0.08	50	0.25	0.5	0.5	0.15
WAIs_22	0.131	100	5.9	0.0327	605.4	0.58	0.7	0.25	0.05	0.36	50	0.05	0.13	50	1.7	0.05	0.5	0.49
WAIs_23	0.041	50	12	0.032	618.6	0.58	0.8	0.25	1.06	0.25	300	0.05	0.21	100	2	0.05	0.5	0.36
WAIs_24	0.32	1900	30.6	0.0464	238.7	0.26	3.7	2.3	0.7	4.29	3700	1.2	0.08	700	2.1	0.5	8	0.45
WAIs_25	0.061	1500	19.4	0.0033	290.8	0.24	6.8	2.1	6.27	2.55	5900	1.3	0.01	600	3.1	0.2	11	0.51
WAIs_26	0.551	1900	4.6	0.015	251	0.24	6.2	3.7	1	7.73	3700	1.1	0.01	400	3.1	0.2	10	0.29
WAIs_28	0.023	50	1.1	0.0033	314.2	0.15	0.8	0.25	0.02	0.55	50	0.05	0.09	50	1.1	0.05	0.5	0.14
WAIs_29	0.049	200	0.7	0.0041	632.1	0.2	1.7	0.25	0.06	1.15	50	0.05	0.16	50	2.1	0.05	0.5	0.14
WAIs_30	4.157	300	626.6	1.8959	15	0.02	0.4	0.8	7.73	2.35	300	1	0.01	300	0.25	7.1	3	0.07

WAIs_31A	0.026	300	31.4	0.0086	219.3	0.22	6.9	0.25	14.32	0.67	600	0.1	0.03	500	5	0.05	4	0.18
WAIs_31B	0.669	400	>10000.0	0.8354	151.4	0.39	1.7	0.5	3.35	1.88	200	0.05	0.13	200	1.2	0.9	2	0.26
WAIs_32	0.087	4700	40.8	0.0127	182.5	0.36	13.6	3.3	2.48	4.21	23600	4.5	0.05	2200	7.1	0.9	22	1.18
WAIs_33	0.151	500	5.5	0.0031	302.5	0.13	1.8	0.25	0.87	1.11	500	0.2	0.01	200	1.3	0.2	2	0.32
WAIs_34	0.105	4600	36.2	0.012	130.8	0.21	16.6	5.2	2.1	7.22	20500	2.7	0.01	1100	8.5	1	44	0.72
WAIs_35	6.251	200	423.4	3.2831	3.9	0.01	0.8	4.2	11.01	10.66	300	1.5	0.01	500	0.25	11.1	1	0.31
WAIs_36	6.942	300	1472.6	3.2621	4.3	0.01	0.9	2.4	11.39	3.11	300	1.7	0.01	300	0.25	3.2	2	0.29
WAIs_37	0.131	2000	24.4	0.0066	200.9	0.42	3.1	3.4	2.82	1.63	25100	18.6	1.48	700	1.7	0.6	60	1.11
WAIs_38	0.158	11900	112.7	0.0044	378.9	0.42	2.7	6.1	1.29	3.5	36400	39.1	1.75	400	1.7	0.6	31	0.79
WAIs_39	0.059	200	10.2	0.0101	589.3	0.45	0.6	0.25	0.22	0.45	200	0.2	0.31	50	0.6	0.1	1	0.1
WAIs_40	0.022	200	2.5	0.0141	734.6	0.54	1.1	0.25	0.06	1.87	200	0.1	0.86	50	2	0.05	0.5	0.12
WAIs_41	0.028	600	4.4	0.002	374.1	0.09	1.1	0.8	0.75	0.94	800	0.6	0.02	100	1.1	0.05	1	0.08
WAIs_42	0.026	1200	17	0.0041	251.9	0.2	3.5	0.9	1.95	1.85	1700	1.2	0.03	400	1.9	0.2	5	0.34
WAIs_43	0.056	3100	102.9	0.0066	312.4	0.29	8.4	5.6	3.38	6.45	12700	4.1	0.05	1800	5.3	0.5	19	0.49
WAIs_44	0.098	12200	499.2	0.0283	203	0.31	14.5	4.2	7.14	1.35	47700	15	0.05	9800	9.2	0.9	10	0.84
WAIs_45	0.149	4100	102.5	0.0123	362.2	0.32	7.2	0.8	7.56	0.81	5900	3.3	0.01	800	4	1.1	15	0.68
WAIs_46	0.025	50	6.1	0.0179	1018.3	0.41	1.6	0.25	0.19	0.15	200	0.1	0.09	50	4.9	0.05	0.5	0.15
WAIs_47	0.109	100	3.9	0.0135	516.8	0.1	0.9	2.1	0.07	0.25	100	0.05	0.1	50	0.25	0.4	0.5	0.08
WAIs_48	0.09	1300	7.4	0.0203	485.9	0.36	3.1	1.9	10.38	1.21	2100	1.1	0.11	500	3	0.1	11	0.38
WAIs_49	0.08	3500	113.5	0.017	396	0.46	8.1	1	2.8	0.75	12000	3	0.08	1200	4.5	0.8	11	0.91
WAIs_50	4.807	700	2781.7	2.2365	26.1	0.06	1.7	3	39.21	5.83	200	1.6	0.01	400	0.8	2.1	4	0.28
WAIs_51	0.097	5600	510.5	0.0339	201	0.39	10.8	2.4	17.7	1.73	36600	7.8	0.06	5300	8.3	0.4	5	1
WAIs_52	0.025	50	2.9	0.0104	4.2	0.01	0.05	0.25	0.12	0.04	100	0.05	0.01	50	0.25	0.3	0.5	0.03
WAIs_53	0.035	3900	10.3	0.002	18.2	0.32	4.6	5.2	1.54	12.82	17100	11.7	0.59	100	2.1	0.7	61	0.88
WAIs_54	0.083	9500	10	0.0013	26	0.42	8.9	4.5	3.91	7.45	13700	10.3	0.48	200	3.5	0.9	41	0.8
WAIs_55	0.052	2000	1054.2	0.0555	71.9	0.14	16.4	1.5	61.54	1.97	1600	51.2	0.07	600	7.9	6.2	4	1.29
WAIs_56	0.098	2600	6.9	0.0013	35.2	0.23	5.2	3.1	1.81	1.69	11900	6.5	0.13	100	2.6	0.4	61	0.65
WAIs_57	0.153	2800	5.9	0.0016	25.7	0.24	5	6.3	0.31	9.76	9600	4.5	0.1	100	2.8	0.2	38	0.6
WAIs_58	0.031	1000	4.7	0.0009	17.8	0.2	5.9	2.7	2.18	1.56	7500	4.3	0.11	200	3	0.4	28	0.53
WAIs_59	0.018	500	73.8	0.001	11.8	0.11	2.5	1.7	35.09	0.96	3100	1.9	0.03	200	1.1	2	29	1.91
WAIs_60	0.053	2200	4.5	0.0007	131.3	0.37	4.1	1.4	5.5	1.68	7700	6.9	0.85	600	2.5	0.5	22	0.34
WAIs_61	0.044	6400	12.3	0.0008	27.9	0.29	7	3.5	4.14	3.35	13600	9.7	0.25	200	2.6	0.7	71	0.68
WAIs_62	0.071	1000	8	0.0005	17.4	0.4	3.2	1.5	5.61	2.78	6200	1.5	0.06	200	1.6	0.4	61	0.53
WAIs_63	0.009	17600	83.4	0.0006	63.3	0.28	7.3	9.9	2.31	11.35	12800	10.3	0.46	300	2.3	0.5	58	0.8
WAIs_64	0.019	17800	2.9	0.001	82.5	0.15	8.3	1.6	1.1	2.43	7200	4.9	0.35	500	3.4	1.6	62	0.34
WAIs_65A	0.026	10400	22.8	0.0006	55.7	0.19	7.8	2.4	2.9	2.73	7600	5.1	0.2	300	3.5	6	44	0.5
WAIs_65B	0.014	700	197.4	0.0021	60.8	0.12	2.6	1	15.03	2.43	800	1.4	0.04	200	1.2	2.7	5	0.61
WAIs_66	0.032	21800	5.6	0.0001	186	0.33	4.6	2	1.83	3.87	11900	9.4	0.67	600	2.4	0.9	45	0.4
WAIs_67	0.019	5500	5.3	0.0001	37.1	0.21	6.2	3.4	1.2	2.25	8700	4.9	0.27	300	2.7	0.4	176	0.59
WAIs_68	0.04	4000	5.6	0.0008	31.3	0.22	5.3	2.3	1.01	4.46	7900	4.5	0.09	200	2.3	0.8	76	0.41
WAIs_69	0.156	200	8	0.0565	265.3	0.27	0.6	1.1	0.5	1.58	900	0.3	0.05	50	0.25	0.05	2	0.15

WAIs_70	0.029	50	21.2	0.0208	895.8	0.36	0.3	0.25	0.09	0.23	2000	0.3	0.73	50	0.8	0.05	0.5	0.2
WAIs_71	0.049	4100	126.5	0.0151	220.9	0.44	8.9	1.2	3.51	1.02	8700	4	0.1	1400	4.7	1.4	8	0.99
WAIs_72	0.013	1600	23.7	0.0001	408.5	0.43	1.3	1	0.52	0.62	10500	7.4	3.64	300	0.9	0.2	9	0.3
WAIs_73	0.082	1200	46.2	0.0011	266.6	0.27	2.6	3.4	2.99	1.7	26900	19.1	0.63	900	1.4	0.6	59	0.86
WAIs_74	0.017	2300	330.1	0.0015	128.9	0.11	4.3	0.9	16.96	0.72	3000	1.7	0.05	400	2.1	2.4	17	0.31
WAIs_76	0.012	5300	3.2	0.0001	53	0.12	6.3	1.6	1.57	2.41	6700	2	0.03	500	2.6	1.6	70	0.18

mg/kg	Na	Nb	Ni	P	Pb	Rb	S	Sb	Sc	Se	Sn	Sr	Th	Ti	V	Y	Zn	Zr
WAIs_01	90	1.15	0.7	430	13.99	6.5	1500	1	0.7	0.3	1.3	4.5	0.2	290	9	1.43	13.7	4
WAIs_02	180	3.17	0.4	200	9.95	5.8	2000	0.78	1.2	0.4	1.2	2.4	2.3	880	10	0.68	6.1	37.7
WAIs_03	60	0.97	0.3	230	11.09	3.9	500	2	0.7	0.4	0.9	2.3	0.5	350	13	1.27	6.1	2.8
WAIs_04	90	1.9	0.5	370	4.39	2.8	100	0.76	0.7	0.9	1.3	0.7	1	720	14	0.52	7.1	9.8
WAIs_05	80	0.28	0.3	80	2.59	2.6	100	0.13	0.7	0.4	0.5	1	0.3	500	11	0.51	7.9	0.7
WAIs_06	30	0.33	0.05	220	9.19	0.3	900	0.43	0.5	0.3	0.5	30	1.3	220	5	0.43	1.7	3
WAIs_07	50	3.65	1.1	400	26.33	1.2	1300	1.21	2.9	2.7	6.4	6.1	8.4	2290	26	0.82	15.5	94.6
WAIs_08	20	0.01	0.05	110	29.04	0.8	600	0.08	14.3	2.5	5.7	7.8	16	580	2	47.04	24.5	80.9
WAIs_09A	5	0.08	0.7	140	10.2	0.7	700	0.02	3.8	0.1	2.8	0.5	16.3	1900	8	0.7	10.6	151.5
WAIs_09B	5	0.18	0.05	180	5.34	0.2	400	0.23	0.7	0.05	2.4	1.4	3.9	880	25	0.12	2.3	125.6
WAIs_10	5	0.28	0.1	180	4.27	0.6	100	0.97	1.2	2.6	3.3	0.9	0.8	260	4	0.18	3.9	17.5
WAIs_11	50	1.7	0.6	150	9.04	3.2	300	0.93	2.4	0.8	1	1.3	3.1	700	16	2.03	6.5	24.4
WAIs_12	160	1.27	0.7	340	6.1	5.1	500	0.35	1.4	0.2	0.9	2.7	0.6	590	11	2.94	12.4	9.2
WAIs_13	70	0.47	1.2	160	4.42	2	300	1.66	2.6	0.05	0.7	4.4	2	350	8	8.08	17.4	10.8
WAIs_14	240	1.94	0.4	230	5.06	3.9	1000	0.26	1.5	0.2	1	2.9	1.3	570	10	1.81	8.6	16.7
WAIs_15	60	0.68	0.7	80	4.5	1.3	300	1.75	2.5	0.2	1.5	2	3.2	380	6	8.43	23.5	11.9
WAIs_16	60	0.12	0.2	5	0.61	0.6	9800	5.93	0.6	0.05	1.5	1.2	4.1	70	0.5	0.33	0.5	76.8
WAIs_17	60	3.91	0.4	240	8.81	1.5	400	0.89	1.1	0.05	2.2	0.5	4.9	1500	17	0.43	10.2	45.7
WAIs_18	170	3.37	0.6	430	9.11	10.3	1300	0.73	5.5	0.7	1.3	2.1	3	1240	16	2	12.5	39.6
WAIs_19	60	2.86	0.4	570	7.15	1.3	300	1.32	0.9	0.1	2.1	0.8	3.2	1310	24	0.66	7.5	19
WAIs_20	50	0.04	0.1	10	7.5	3.4	1300	99.08	0.3	0.6	0.6	3.8	0.2	20	0.5	0.24	1.1	1.3
WAIs_21	5	0.01	0.2	20	5.72	0.2	500	7.04	0.05	0.05	4	3.4	0.05	30	0.5	0.03	0.8	1.5
WAIs_22	50	0.18	0.2	20	15	0.3	5700	21.59	0.3	1.6	2.1	23	0.2	80	0.5	0.08	0.5	3.4
WAIs_23	10	0.01	0.05	5	18.44	0.7	400	17.41	0.2	0.05	1.9	15.6	0.2	40	1	0.08	0.7	4
WAIs_24	60	0.23	0.2	120	12.12	5.2	3200	21.73	0.5	1.1	1	8.6	0.8	50	3	0.72	2	2.5
WAIs_25	50	0.23	0.3	320	11.15	7	1100	5.04	0.7	0.5	0.7	8.2	0.5	70	6	0.72	1.6	0.7
WAIs_26	40	0.2	0.6	100	11.27	2.2	1300	5.82	0.6	0.6	0.7	6.2	0.3	100	4	0.9	2.6	0.7
WAIs_28	60	0.1	0.1	5	7.29	0.2	3800	0.24	0.8	0.05	0.7	8.5	0.2	130	0.5	0.03	0.4	2.6
WAIs_29	60	0.33	0.05	5	17.61	0.4	5600	0.46	0.3	0.05	1.2	11.5	0.7	70	0.5	0.06	0.4	4.7
WAIs_30	990	0.01	0.5	10	0.93	4.1	33100	78.66	0.2	2.8	0.05	1.5	0.2	10	0.5	0.09	0.9	0.7
WAIs_31A	80	0.01	1.8	20	10.61	6.7	500	1.18	0.4	0.05	0.4	10.2	0.7	70	0.5	0.43	0.5	2.5
WAIs_31B	20	0.32	0.4	10	1.86	2.1	31700	391.87	1.7	0.6	4	5.2	0.6	40	0.5	0.17	0.3	5.6
WAIs_32	1060	0.35	0.4	120	26.94	13.6	8300	0.73	1.9	0.05	1.2	40	3.7	140	19	2.35	7	3

WAIs_33	80	0.17	0.2	40	6.53	1.4	1500	0.36	0.3	0.05	0.7	6.1	0.05	90	0.5	0.18	0.7	0.4
WAIs_34	150	0.22	2	250	14.53	7.9	2100	1.4	1.7	0.05	0.6	13.2	1.8	50	17	1.58	16	0.5
WAIs_35	1620	0.01	0.05	60	0.65	7.5	1800	84.28	0.9	0.7	0.05	1.5	0.5	10	0.5	0.1	0.4	0.3
WAIs_36	500	0.01	0.1	60	0.88	5.1	14600	159.26	1.5	2	0.05	1.5	0.6	10	0.5	0.16	1.1	0.5
WAIs_37	350	4.5	0.5	560	17.89	4	3100	2.2	1.1	0.3	2.2	9.6	6.8	1770	14	0.46	7.7	85.4
WAIs_38	330	2.92	0.5	510	19.33	3.2	2800	0.4	2.2	0.05	2.4	18.7	19.1	1880	14	0.33	9.8	113.3
WAIs_39	20	0.08	0.05	30	6.13	0.4	400	2.63	0.2	0.05	1	2.4	0.4	110	2	0.09	0.6	11.1
WAIs_40	20	0.04	0.05	20	18.6	0.3	500	4.48	0.3	0.2	1.2	11	0.4	60	0.5	0.07	2.7	20.4
WAIs_41	30	0.07	0.1	50	5.05	1.4	400	0.67	0.4	0.05	0.4	4.3	0.2	60	3	0.19	1.2	1
WAIs_42	50	0.15	0.3	70	8.91	4.2	700	3.8	0.4	0.2	0.8	4.3	0.4	40	3	1.23	1.7	1.4
WAIs_43	410	0.09	1.4	130	15.16	9.9	4900	6.13	0.7	0.8	1.2	28.1	1.8	100	13	1.17	7.3	2.2
WAIs_44	1440	0.07	0.05	120	21.89	77.9	24700	8.47	1.3	5.1	1.4	95.4	4.2	20	9	1.49	1.4	3.3
WAIs_45	130	0.09	0.1	60	16.76	8.8	1900	8.36	0.7	0.6	0.8	14	2.5	20	5	1.24	1.8	1.3
WAIs_46	5	0.04	0.05	10	14.33	0.3	300	10.89	0.3	0.3	1.6	34.5	0.2	50	0.5	0.05	0.5	2.2
WAIs_47	20	0.09	0.05	20	5.67	0.3	400	1.31	1.2	2.7	3.9	3.2	0.05	50	0.5	0.05	0.3	2.4
WAIs_48	70	0.1	0.4	60	19.92	2.4	1400	14.71	0.4	1.4	1.4	16.8	0.8	120	5	0.36	2.3	3.6
WAIs_49	670	0.16	0.1	180	30	12.5	4400	7.54	0.6	1.4	1.1	50.5	1.6	20	5	1.59	1.2	3.4
WAIs_50	340	0.01	0.05	20	3.53	11.8	8100	223.3	0.5	2.1	0.2	2.7	0.8	20	0.5	0.3	1.5	0.9
WAIs_51	1110	0.05	0.05	80	25.38	43.2	16500	9.8	0.7	1.8	1.3	27.2	2.9	10	5	0.72	1	2.4
WAIs_52	30	0.09	0.05	5	0.21	0.3	120000	0.87	0.1	4.8	0.05	0.025	0.05	20	0.5	0.02	2.2	0.5
WAIs_53	80	3.22	0.7	250	9.9	2.3	300	0.88	1.7	0.7	1.7	0.9	3.7	1530	25	1.02	14.2	31.7
WAIs_54	60	3.06	1.3	260	12.08	3.2	500	1.6	3.6	0.3	1.7	1.7	2.2	1240	20	1.96	9.9	25.5
WAIs_55	1140	0.12	0.05	30	4.31	22.9	800	30.47	1	0.2	0.4	11.6	3.5	60	3	4.6	0.9	3.7
WAIs_56	150	1.68	0.6	180	6.89	3.9	400	0.41	1	0.3	0.9	1.1	0.6	850	17	1.24	12.6	9.2
WAIs_57	40	1.09	0.4	270	18.41	1.1	200	0.4	0.9	0.5	0.8	1.2	0.5	750	18	0.94	7.4	4.5
WAIs_58	100	1.44	0.3	230	7.06	4.3	600	0.2	0.6	0.5	1	0.9	0.2	620	10	0.95	6.7	5.6
WAIs_59	390	0.34	0.1	30	1.78	6	300	10.33	1.1	0.05	0.6	2.5	0.2	510	8	0.58	7.5	1.1
WAIs_60	90	1.25	0.2	250	18.65	9.7	1000	0.4	1	0.2	2	7.8	1.7	970	7	0.5	5.4	44.5
WAIs_61	90	2.4	0.6	280	10.49	6.6	400	0.61	1.8	0.2	1.6	0.9	1.3	1100	21	1.52	12.6	15.6
WAIs_62	120	1.6	0.4	130	3.1	2.1	300	0.49	0.7	0.2	2.2	0.6	0.3	950	12	0.77	13.7	2.4
WAIs_63	90	2.8	0.5	300	11.14	10.4	800	0.52	2.6	0.7	1.3	1.2	2.4	940	22	1.62	9.2	23.3
WAIs_64	160	1.16	0.6	210	5.66	9.1	1200	0.14	2.7	0.2	0.8	3.4	1.7	630	7	2.52	11.7	19.9
WAIs_65A	850	1.42	0.5	240	6.59	6.1	1600	3.36	1.6	0.4	0.9	1.8	0.5	550	9	2.28	6.5	11
WAIs_65B	460	0.45	0.2	30	2.74	3.4	2400	53.56	1.5	0.1	0.6	2.2	0.5	230	2	0.57	1.5	2.1
WAIs_66	150	0.98	0.6	610	16.24	6.7	1900	0.17	3.8	0.05	1.5	5.5	4.9	930	8	0.68	10.1	47.4
WAIs_67	90	1.7	0.5	290	5.31	5.4	300	0.25	2.1	0.4	0.8	1.9	1.4	740	12	1.52	8	15.7
WAIs_68	90	0.99	0.4	200	4.68	4	200	0.14	1.1	0.5	0.7	1.4	0.4	560	11	1.28	7.4	5.6
WAIs_69	20	0.12	0.2	40	6.1	0.7	200	8.81	0.2	0.3	1.1	1.5	0.2	100	2	0.21	0.5	1.4
WAIs_70	5	0.02	0.05	5	5.12	0.1	400	3.88	0.2	0.9	1	8.4	0.3	70	3	0.03	0.5	15.5
WAIs_71	160	0.14	0.05	60	27.22	11.4	3000	8.24	0.7	1.1	1	12	3.1	20	5	1.48	1.3	4.5
WAIs_72	40	0.12	0.2	100	25.4	1.3	900	1.36	0.5	1.2	2.3	2.8	3.1	730	5	0.18	2.8	154.2

WAIs_73	430	2.18	0.5	730	18.22	9.4	3700	1.42	1.2	0.6	1.4	13.6	5.1	1290	17	0.59	9.2	43.8
WAIs_74	180	0.25	0.05	60	4.01	5.8	600	29.67	1	0.2	0.3	7.3	0.8	300	6	1.13	3.5	2.5
WAIs_76	80	0.74	0.6	170	4.53	12	300	0.16	0.8	0.05	0.4	1.5	0.5	540	13	1.85	11.9	2.1

741

Table A1.2. Field soil and rock samples, coordinate, wavelength absorptions and mineral classification.

Samples	Coordinates		Composition	wvl absorptions (μm)	Minerals (Mayor)	Minerals (Minor)
WAIs_01	5754625.02	444762.8976	Bulk soil sample	0.521, 1.43, 1.92 (ls), 2.2, 2.26 (flat?)	Phyllosilicate	
WAIs_01B	5754625.02	444762.8976	Bulk soil sample	0.412, 1.4 (ls), 1.91, 2.2	Perthite	Phyllosilicate
WAIs_02	5754585.184	444811.6649	Bulk soil sample	0.4, 0.474, 1.4, 1.91, 2.21 (br)	Perthite	
WAIs_03	5754581.281	444841.3126	Bulk soil sample	0.52 (br), 1.4, 1.91, 2.2	Phyllosilicate	Fe Oxides
WAIs_04	5754610.536	444835.433	Bulk soil sample	0.46, 1.4 (ls), 1.91, 2.2, 2.31	Phyllosilicate	Fe Oxides
WAIs_05	5754629.988	444824.0282	Bulk soil sample	0.46, 1.4, 1.91, 2.2	Phyllosilicate	Fe Oxides
WAIs_06	5754659.776	444831.2516	Rock	0.39, 0.48, 1.47 (db-rs), 1.76, 1.92, 2.0, 2.17 (db-ls), 2.32 (sy), 2.39, 2.42	Alunite	Schwertmannite
WAIs_07	5754693.127	444840.1983	Rock	0.500, 1.41 (ls), 1.91, 2.20, 2.31, 2.35, 2.38	Phyllosilicate	
WAIs_08	5754686.99	444851.4247	Rock	0.43, 0.48, 0.93 (br), 1.41 (rs), 1.91, 2.20	Kaolinite	Goethite
WAIs_08B	5754686.99	444851.4247	Rock	0.43, 0.48, 0.93 (br), 1.41 (rs), 1.91, 2.20 (sy), 2.31, 2.35, 2.38, 2.44	Kaolinite	Goethite
WAIs_09	5754715.577	444845.2875	Rock	0.53 (br), 0.878, 1.41 (ls), 1.91, 2.2 (ls)	Fe oxides	Phyllosilicates (smectite)
WAIs_09B	5754715.577	444845.2875	Rock	0.53 (br), 1.41 (ls), 1.91, 2.2 (db-ls)	minor Fe Oxides	Phyllosilicates (smectite)
WAIs_10	5754703.018	444826.2375	Rock	0.50 (br), 1.43, 1.91, 2.2	Phyllosilicate	
WAIs_11	5754876.719	444929.4694	Bulk soil sample	0.50 (br), 1.41 (ls), 1.91, 2.2	Phyllosilicate	Schwertmannite
WAIs_12	5756030.599	444954.8906	Bulk soil sample	0.50 (br), 1.41 (ls), 1.91, 2.2	Phyllosilicate	Schwertmannite
WAIs_13	5756055.728	444929.7247	Rock	0.50 (br), 1.41 (db-rs), 1.91, 2.2 (db-rs), 2.32, 2.35, 2.38, 2.44	Kaolinite	
WAIs_13B	5756055.728	444929.7247	Rock	0.50 (br), 1.41 (db-rs), 1.91, 2.2 (db-rs), 2.31, 2.35, 2.38, 2.45	Kaolinite	
WAIs_14	5756123.614	444942.3706	Bulk soil sample	0.48 (br), 1.42, 1.91, 2.2, 2.26 (br)	Phyllosilicate	
WAIs_15	5756098.025	444932.5823	Rock	0.46 (br), 1.41 (rs), 1.91 (ls), 2.2 (rs), 2.32, 2.38	Kaolinite	
WAIs_16	5755229.51	444820.4523	Rock	0.46 (br), 1.41 (db-rs), 1.91, 2.2 (db-rs), 2.32, 2.39, 2.44	Kaolinite	
WAIs_16B	5755229.51	444820.4523	Rock	0.46 (br), 1.41, 1.91, 2.2 (sy)	Phyllosilicate	
WAIs_17	5755181.478	444709.2788	Bulk soil sample	0.46 (br), 1.41, 1.91, 2.2	Phyllosilicate	Schwertmannite
WAIs_18	5755162.345	444700.0199	Bulk soil sample	0.4, 0.47, 1.41 (br), 1.91, 2.2	Phyllosilicate	Schwertmannite

WAIs_19	5755175.561	444818.3947	Bulk soil sample	0.46 (br), 1.41, 1.91, 2.2	Phyllosilicate	Fe Oxides
WAIs_20	5754163.45	444818.3947	Bulk soil sample	0.45, 1.41 (db-ls), 1.91, 2.2	Phyllosilicate	Fe Oxides
WAIs_21	5754163.45	444818.3947	Rock	0.45, 0.52, 1.42, 1.91, 2.2	Phyllosilicate	
WAIs_22	5754231.624	444833.75	Rock	0.39, 0.45 (br), 1.41, 1.91, 2.3	Phyllosilicate	Sulphur
WAIs_22B	5754231.624	444833.75	Rock	0.39, 1.42, 1.93, 2.2 (br)	Sulphur	Phyllosilicate
WAIs_23	5754240.579	444852.0301	Rock	0.50, 1.4 (db-ls), 1.9, 2.2 (br)	Phyllosilicate	
WAIs_24	5754111.31	444885.4165	Bulk soil sample	0.50, 1.4 (db-ls), 1.9, 2.2 (ls)	Phyllosilicate	Fe Oxides
WAIs_25	5754074.99	444864.0838	Bulk soil sample	0.51, 1.41, 1.9, 2.2	Phyllosilicate	Fe Oxides
WAIs_26	5754078.424	444928.1913	Bulk soil sample	0.51, 1.41, 1.9, 2.2 (flat?)	Fe Oxides	
WAIs_27			Rock	0.39 (db), 1.41 (rs), 1.9, 2.26	Opal	Montmorillonite
WAIs_28	5754049.685	444912.0491	Rock	0.39, 1.41 (db-ls), 1.9, 2.2 (br)	Sulphur	Phyllosilicate
WAIs_29	5753949.163	444914.0462	Rock	0.39, 0.56, 1.41, 1.9, 2.2 (br)	Sulphur	Phyllosilicate
WAIs_29B	5753949.163	444914.0462	Rock	0.52 (br), 1.41 (db-ls), 1.9, 2.2 (br)	Phyllosilicate	Fe Oxides
WAIs_30	5753924.288	444943.8346	Rock	0.39, 1.41 (db-ls), 1.9, 2.2 (br)	Phyllosilicate	
WAIs_31	5753904.17	445003.9078		0.417, 0.54, 0.67 (db-rs), 1.2, 1.45, 1.71, 1.91, 2.1 (br), 2.3	-Vegetation-	Sulphur
WAIs_31B	5753904.17	445003.9078		0.417, 0.67, 1.41, 1.91, 2.2 (br)	-Vegetation-	Sulphur
WAIs_32	5753893.4	444970.4312	Bulk soil sample	0.37,0.43, 1.41 (db-ls), 1.91, 2.2	Montmorillonite	
WAIs_33	5753798.187	444921.1058	Bulk soil sample	0.47, 1.41 (ls), 1.91, 2.2 (br)	Phyllosilicate	Fe Oxides
WAIs_34	5753711.97	444889.019	Bulk soil sample	0.38, 0.48, 1.41 (db-ls), 1.91, 2.2, 2.31, 2.35	Goethite	Phyllosilicates
WAIs_35	5754024.175	444978.8877	Bulk soil sample	0.417, 0.51, 0.45, 0.67 (db-rs), 1.41 (br), 1.91, 2.2 (br)	-Vegetation-	Sulphur
WAIs_36	5754035.121	444973.0465	Rock	0.417, 0.54, 0.67 (db-rs), 1.41 (db-ls), 1.91 (ls), 2.2 (br)	-Vegetation-	Sulphur
WAIs_37	5754422.909	444805.2608	Bulk soil sample	0.39, 0.47, 0.94 (br), 1.41 (db-ls), 1.91, 2.2 (br)	Fe oxides	Phyllosilicates
WAIs_38	5754416.612	444841.8269	Bulk soil sample	0.4, 0.47, 0.94 (br), 1.41, 1.91, 2.2 (ls)	Fe oxides	Phyllosilicates
WAIs_39	5754357.941	444878.7509	Bulk soil sample	0.52, 1.41 (db-ls), 1.91, 2.2 (br)	Fe oxides	Phyllosilicates
WAIs_39B	5754357.941	444878.7509	Bulk soil sample	0.52, 1.41 (db-ls), 1.91, 2.2 (br)	Phyllosilicate	Fe Oxides
WAIs_40	5754341.659	444866.8044	Bulk soil sample	0.52, 1.41 (db-ls), 1.91, 2.2 (br)	Phyllosilicate	Fe Oxides

WAIs_41	5754353.348	444904.82	Bulk soil sample	0.52, 1.41 (db-ls), 1.91, 2.2 (br), 2.31, 2.35	Fe oxides	Phyllosilicates
WAIs_42	5754317.965	444890.7322	Bulk soil sample	0.52, 1.41 (db-ls), 1.91, 2.2 (br), 2.31	Phyllosilicate	Fe Oxides
WAIs_43	5754291.911	444894.1431	Bulk soil sample	0.38, 0.43, 1.41 (db-ls), 1.9, 2.2 (db-rs), 2.26, 2.31	Phyllosilicate	Jarosite
WAIs_44	5754276.592	444925.7898	Bulk soil sample	0.38, 0.43, 0.93 (br), 1.41 (db-ls), 1.9, 2.2 (db-rs), 2.26	Kaolinite Group	Jarosite
WAIs_45	5754288.263	444944.8451	Bulk soil sample	0.50, 1.41 (db-ls), 1.9, 2.2 (db-rs), 2.31	Kaolinite Group	Jarosite
WAIs_46	5754272.062	444944.8683	Bulk soil sample	0.50, 1.41 (db-ls), 1.9, 2.2	Phyllosilicate	Phyllosilicates
WAIs_47	5754279.877	444968.1438	Bulk soil sample	0.50, 1.41 (br), 1.9, 2.2	Phyllosilicate	Phyllosilicates
WAIs_48	5754259.781	444966.5334	Bulk soil sample	0.50, 1.42 (db), 1.9, 2.2 (rs), 2.32	Kaolinite Group	Jarosite
WAIs_49	5754231.235	444929.8565	Bulk soil sample	0.38, 0.43, 1.41 (db-ls), 1.9, 2.2 (db-rs), 2.31	Kaolinite Group	Jarosite
WAIs_50	5754170.676	444982.7812	Rock	0.41, 0.67, 1.41 (db-ls), 1.9, 2.2	Fe oxide	
WAIs_51	5754208.901	444941.8044	Rock	0.38, 0.43, 0.93, 1.41 (db-ls), 1.9, 2.2 (db-rs), 2.26, 2.32	Kaolinite Group	Jarosite
WAIs_52	5754202.472	444812.8853	Bulk soil sample	0.5 (br), 1.41 (db-ls), 1.91, 2.2 (br)	Phyllosilicate	
WAIs_52B	5754202.472	444812.8853	Bulk soil sample	0.39, 1.41 (br), 1.92, 2.2 (br)	Sulphur	Phyllosilicates
WAIs_53	5755078.801	444947.8385	Bulk soil sample	0.41, 1.41, 1.92, 2.2 (br)	Fe oxide	
WAIs_54	5755068.344	444976.3966	Bulk soil sample	0.48, 1.41, 1.92, 2.2	Fe oxide	
WAIs_55	5755122.201	444917.133	Bulk soil sample	0.45, 1.41 (db-ls), 1.92, 2.2 (db-rs)	Kaolinite Group	Jarosite
WAIs_56	5755154.34	444976.0723	Bulk soil sample	0.47, 1.41 (ls), 1.92, 2.2 (br)	Fe oxide	
WAIs_57	5755161.61	445082.2812	Bulk soil sample	0.47, 1.41 (ls), 1.92, 2.2 (br)	Fe oxide	
WAIs_58	5755191.067	445138.7056	Bulk soil sample	0.47, 1.41 (ls), 1.92, 2.2 (br)	Fe oxide	
WAIs_59	5755232.862	445198.2797	Bulk soil sample	0.45, 1.41 (ls), 1.91, 2.2 (br)	Fe oxide	
WAIs_60	5755188.408	445220.9519	Bulk soil sample	0.38, 0.43, 0.48, 1.41 (ls), 1.91, 2.2 (br)	Fe oxide	
WAIs_61	5755166.192	445266.717	Bulk soil sample	0.47, 1.41 (ls), 1.91, 2.2 (br)	Fe oxide	
WAIs_61B	5755166.192	445266.717	Bulk soil sample	0.52, 1.41 (ls), 1.91, 2.2 (flat?)	Fe oxide	
WAIs_62	5755183.002	445241.9607	Bulk soil sample	0.49, 1.41 (ls), 1.91, 2.2 (br)	Fe oxide	
WAIs_63	5755183.849	445285.0352	Bulk soil sample	0.39, 0.48, 1.41 (ls), 1.91, 2.2 (ls)	Fe oxide	

WAIs_64	5755217.332	445379.0957	Bulk soil sample	0.38, 0.48, 1.41 (db-ls), 1.91, 2.2 (br)	Fe oxide	
WAIs_65	5755297.397	445338.6187	Bulk soil sample	0.41, 1.41 (ls), 1.91, 2.2	Fe oxide	
WAIs_65B	5755297.397	445338.6187	Bulk soil sample	0.45, 1.41, 1.91, 2.2, 2.38	Fe oxide	Phyllosilicates
WAIs_66	5755208.565	445510.3185	Bulk soil sample	0.38, 0.48, 1.41 (db-ls), 1.91, 2.2 (db-ls)	Fe oxide	Phyllosilicates
WAIs_67	5755105.957	445515.3806	Bulk soil sample	0.39, 0.48, 1.41 (db-ls), 1.91, 2.2	Fe oxide	
WAIs_68	5755109.645	445601.6027	Bulk soil sample	0.41, 1.41 (db-ls), 1.91, 2.2	Fe oxide	
WAIs_69	5754244.458	444802.6374	Bulk soil sample	0.53, 1.41 (db-ls), 1.91, 2.2 (ls)	Fe oxide	
WAIs_70	5754283.696	444812.4169	Bulk soil sample	0.54, 0.89, 1.41 (db-ls), 1.91, 2.2	Fe oxide	
WAIs_71	5754300.634	444790.4574	Bulk soil sample	0.38, 0.50, 1.41 (db-ls), 1.92, 2.2 (db-rs), 2.31, 2.35, 2.38	Kaolinite Group	Jarosite
WAIs_72	5754316.081	444761.3434	Bulk soil sample	0.38, 0.51, 0.91, 1.41 (db-ls), 1.92, 2.2 (ls)	Fe oxide	
WAIs_73	5754368.815	444765.0889	Bulk soil sample	0.39, 0.48, 0.95, 1.41 (db-ls), 1.91, 2.2	Fe oxide	
WAIs_74	5754434.986	444721.5595	Bulk soil sample	0.42, 0.54, 0.61, 0.67, 1.2, 1.45, 1.7, 1.92, 2.13, 2.3 (db)	-Vegetation-	Sulphur
Abbreviations				Abbreviations		
rs - asymmetric, right skewed absorption feature						
ls - asymmetric, left skewed absorption feature						
sy - symmetric absorption feature						
db - double absorption feature						
br - broad absorption feature						

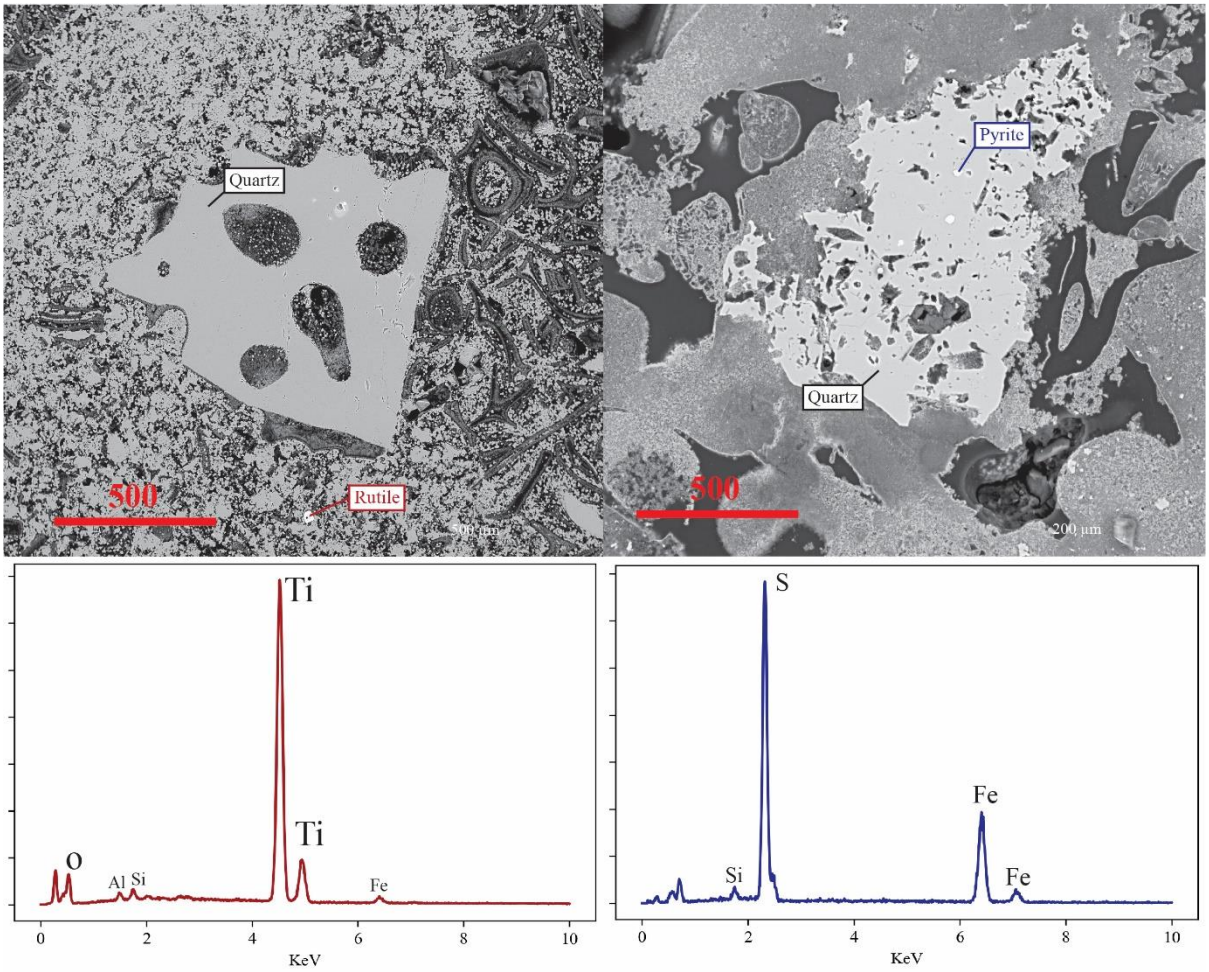

Figure A1.7.1. Field sample, WAIs_06 showing a quartz crystal in a groundmass of voids filled by silica rich mineralisation and small a rutile crystal. The right column is from sample WAIs_22 where a pyrite is visible inside a mass of quartz polymorph.

Table A1.3. Spectral average signature extracted from image of the selected classes for image classification algorithms. Wavelengths in µm.

Class	Training Points	Testing Points	Spectral Signature
Dry Silica	242	250	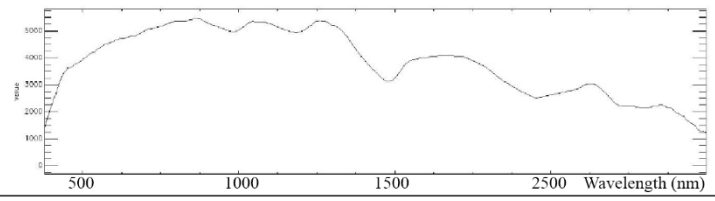
Wet Silica	334	145	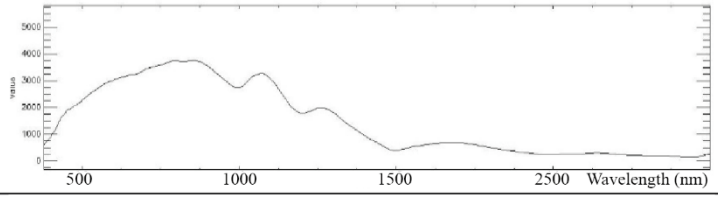
Green Water	359	87	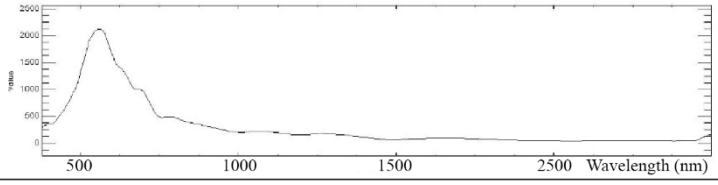
River Water	219	100	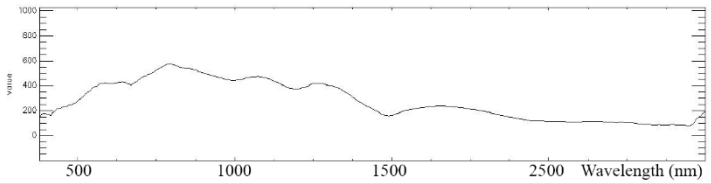
Other Water	316	134	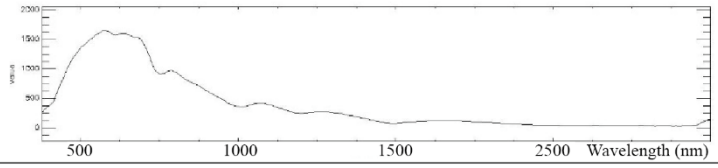
Champagne Pool Outflow	246	122	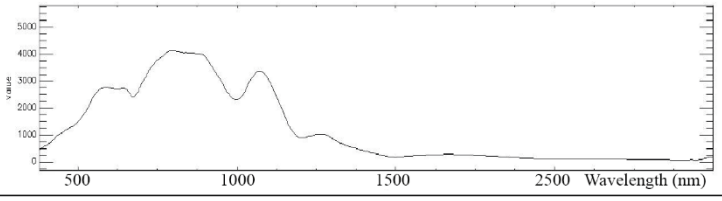
Ignimbrite Dominated	314	94	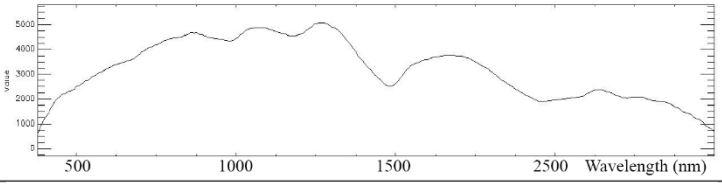
Kaolinite Dry	204	22	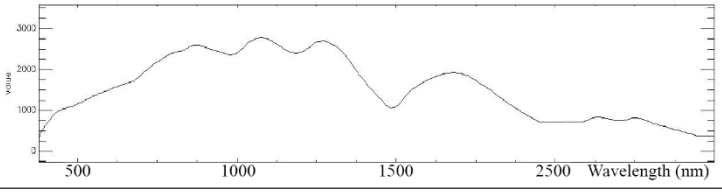

7.2 Appendix 2 (A2)

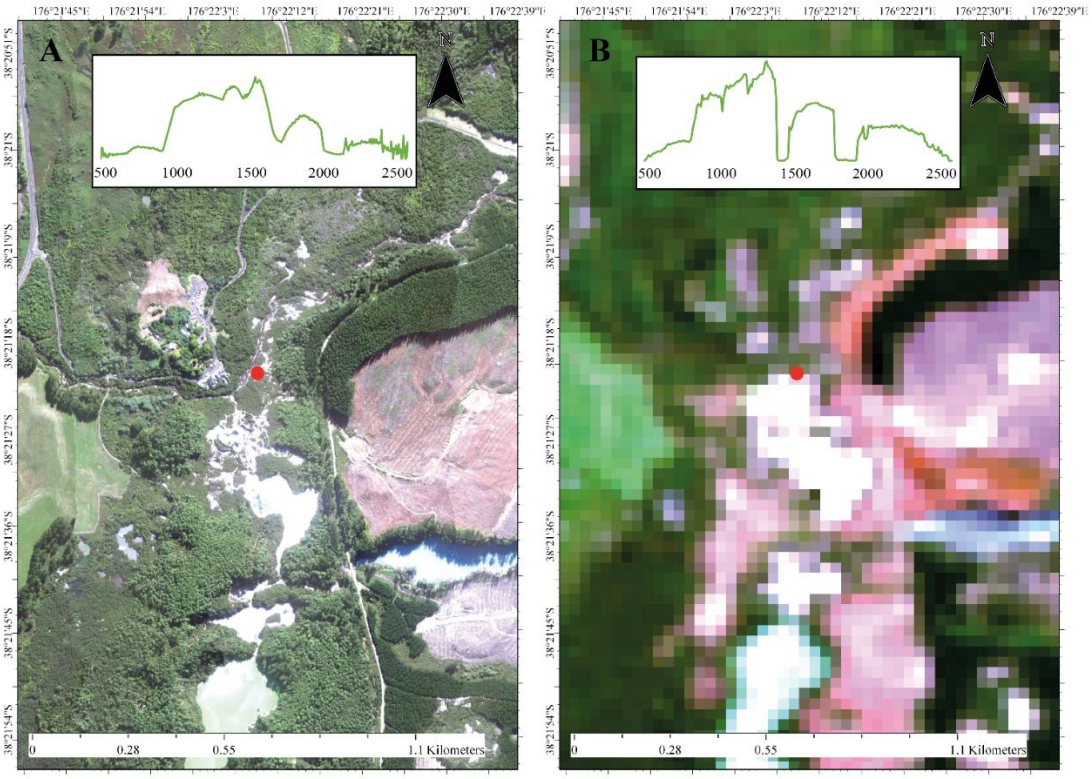

Figure A7.2. Visual comparison of spectral and spatial differences between a) airborne image and b) satellite image. For more sensor details please refer to Table 1. A) Hyperspectral (VNIR/SWIR) image from AisaFenix airborne platform with a spectral signature from vegetation in green, red dot is the location of the spectral signature. B) Hyperspectral (VNIR/SWIR) image from PRISMA satellite platform with a spectral signature from vegetation in green. This is a visual aid to understand the great difference in spatial and spectral resolution within hyperspectral (VNIR/SWIR) datasets.

Table A2.1 Confusion matrix by sample count for Random Forest supervised classification on the airborne-based hyperspectral image for all surfaces.

	Reference Class											
Map class	**Buildings**	**Water**	**Roads**	**Rock/ Soil**	**Bare Soil**	**Black berry**	**Grass**	**Mixed Bush**	**Pine**	**Fern**	**Kanuka**	**Sum**
Buildings	157	4	8	25	0	0	0	0	0	0	0	194
Water	1	512	0	3	0	0	0	0	0	0	0	516
Roads	37	11	1448	20	12	0	7	0	0	0	0	1535
Rock/Soil	23	22	27	2082	0	0	0	0	0	0	23	2177
Bare Soil	6	0	20	116	3578	0	10	1	0	5	13	3749
Blackberry	0	0	17	1	1	1239	0	2	1	8	3	1272
Grass	3	0	35	3	7	0	1628	1	0	12	0	1689
Mixed Bush	0	0	16	17	1	10	5	4180	79	129	22	4459
Pine	0	0	0	0	0	1	0	237	2227	53	0	2518
Fern	0	0	8	0	2	6	24	43	3	1336	0	1422
Kanuka	1	0	8	37	2	4	0	86	0	36	951	1125

Sum	228	549	1587	2304	3603	1260	1674	4550	2310	1579	1012	20656

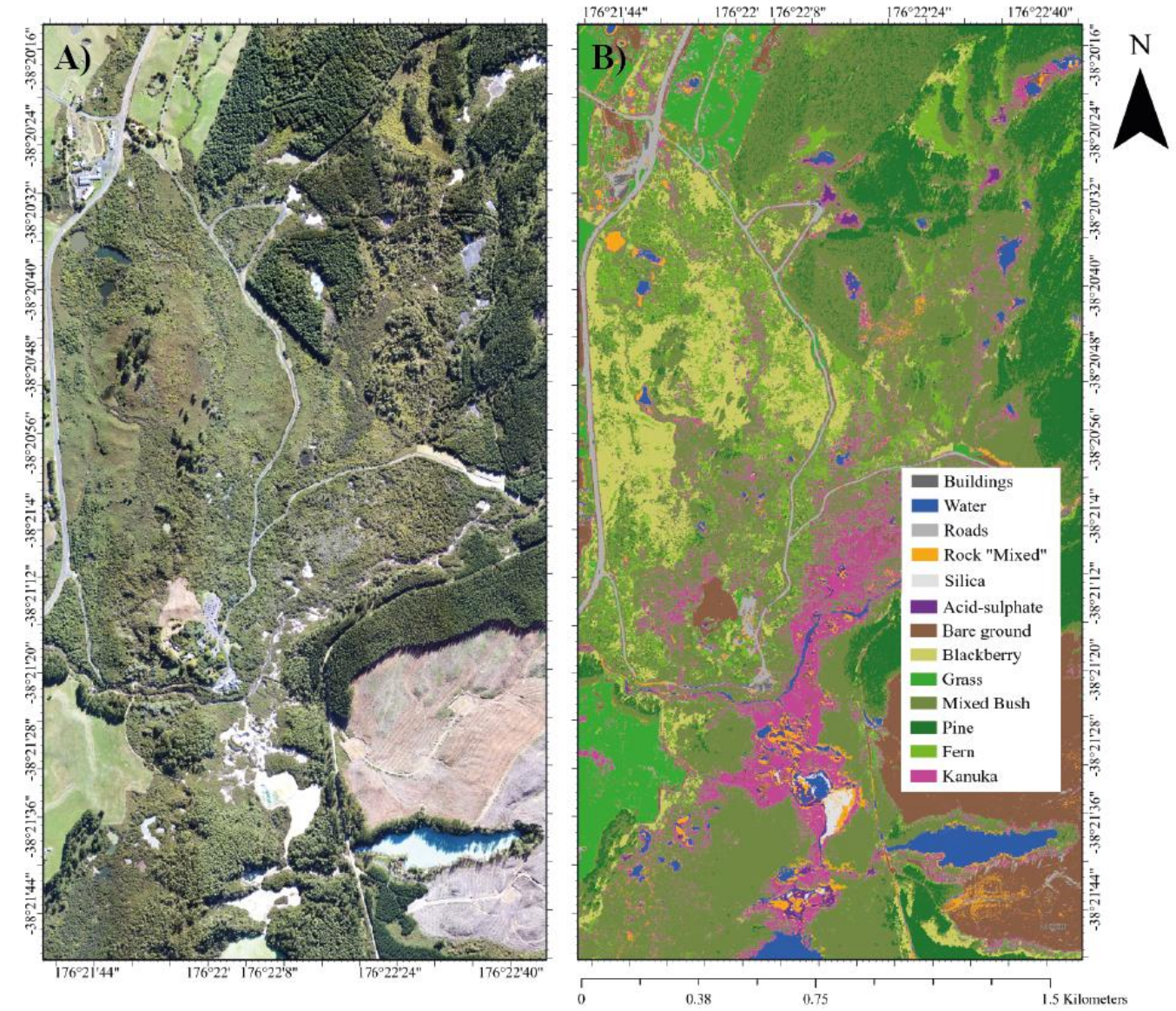

Figure A7.3. Land surface classification. A) RGB photo from Waiotapu Geothermal Field taken by the hyperspectral sensor (VNIR/SWIR) AisaFenix. B) Land surface classification from random forest algorithm (Table S1).

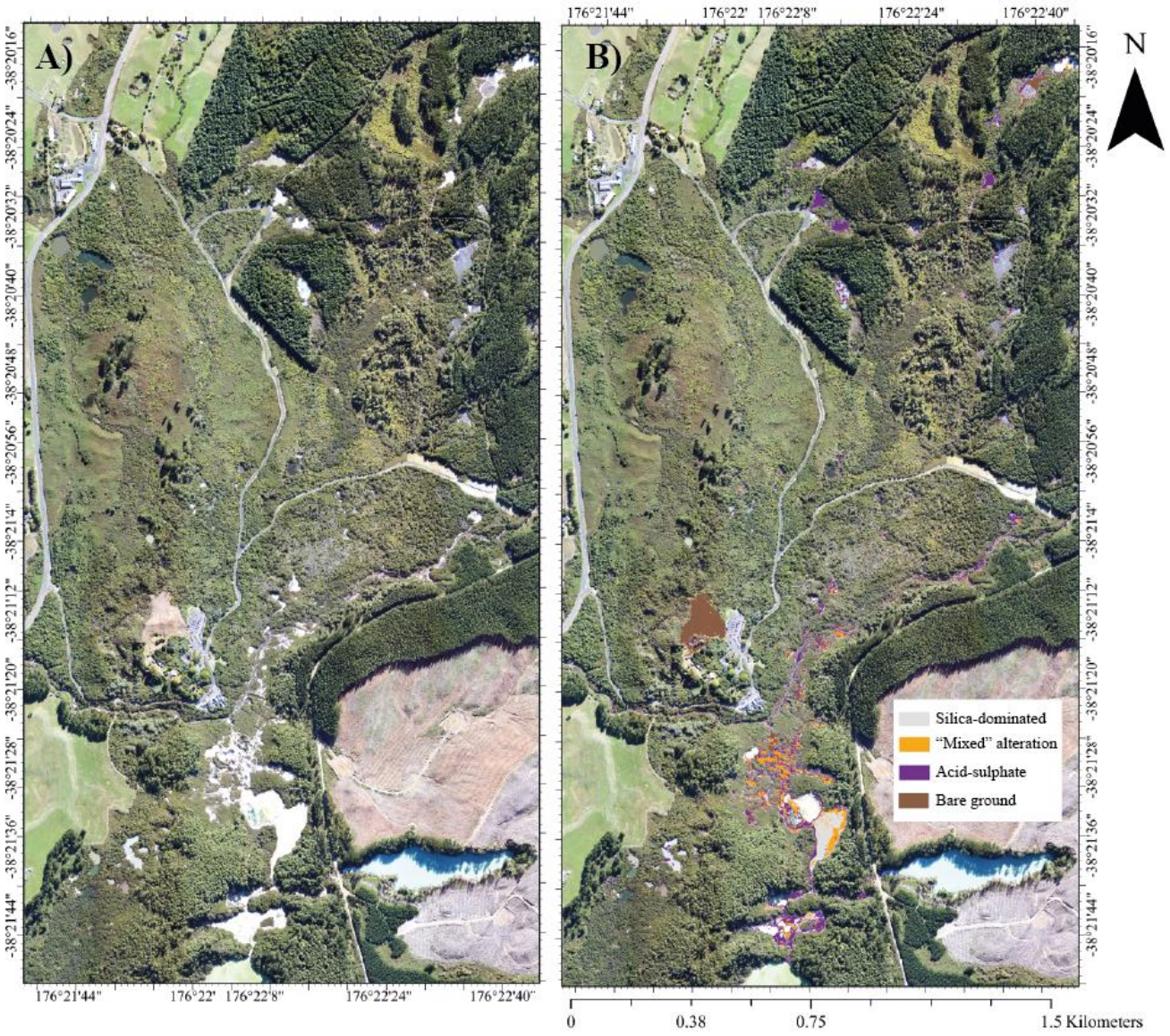

Figure A7.4. Lithological map of Waiotapu Geothermal Field. A) RGB photo of the area. B) Classification overlapping the RGB photo. The classification map for lithology which includes silica-dominated, "mixed" alteration and acid-sulphate areas as presented in Rodriguez-Gomez et al., (2021).

Table A2.3. Element concentration for all elements presented in parts per million (ppm).

ppm	Ag	Al	As	Au	B	Ba	Be	Bi	Ca	Cd	Ce	Co	Cr	Cs	Cu	Fe	Ga	Ge
WAI-01	0.00355349	150.944848	0.1415108	0.00089938	20.5347887	10.1133048	0.00314468	0.00157234	3066.06722	0.01006299	0.13522143	0.03144684	0.34277059	0.42296004	4.47614368	78.6171082	0.05660432	0.01257874
WAI-02	0.00120169	46.429035	0.05462239	0.00021303	21.8762689	3.18448558	0	0.00054622	2681.95955	0.00327734	0.03004232	0.01911784	0.10651367	0.35613801	4.59101223	40.9667956	0.02458008	0.00819336
WAI-03	0.0018623	98.9345016	0.20077884	0.00027934	41.4069988	4.9787333	0	0.00116394	2243.48532	0.00378279	0.05819677	0.01745903	0.13094272	0.76674239	4.90598734	81.4754719	0.0378279	0.00872952
WAI-04	0.00131782	70.0966289	0.05046957	0.00013739	30.6462461	12.3482221	0.00280387	0	3866.53005	0.00560773	0.04205798	0.02803865	0.10935074	0.39113919	7.13078986	64.4888985	0.02523479	0.0084116
WAI-05	0.00783233	51.3595166	0.07061934	0.00010272	24.2994713	10.1820242	0	0.00064199	5277.19033	0.00866692	0.03530967	0.01925982	0.16370846	0.21314199	3.62116692	38.5196375	0.02888973	0.00641994
WAI-06	0.00083755	47.8598613	0.05982483	0.00010529	19.8618425	4.30020854	0	0.0007179	3852.71884	0.01148637	0.02632292	0.01914395	0.11007768	0.25844325	2.86680569	33.5019029	0.03110891	0.00717898
WAI-07	0.00101066	77.7429467	0.06025078	5.25E-05	32.1661442	3.66169279	0.00194357	0.00058307	1214.73354	0.0013605	0.02915361	0.01554859	0.10689655	0.83534796	2.99018809	56.3636364	0.02332288	0.00388715
WAI-08	0.00272101	261.833414	0.08727781	0.0004903	25.9779819	8.05009398	0.00256699	0.0020536	3070.12513	0.00256699	0.11808174	0.01796896	0.20792654	0.75623651	3.04599538	84.7108104	0.08214382	0.00770098
WAI-09	0.00888594	88.8594305	0.06165756	3.45E-05	11.2434382	1.88236916	0.00181346	0.0023575	2281.32987	0.00253884	0.04352299	0.01450766	0.17771886	0.39986744	3.37683971	54.403733	0.03264224	0.00362692
WAI-10	0.00072162	48.709085	0.07396565	3.25E-05	17.7156746	2.31097548	0	0.00108242	2213.55731	0.00180404	0.03247272	0.02525656	0.17138382	0.21810846	2.44826294	34.2767635	0.01984444	0.00541212
WAI-11	0.00059951	37.1124163	0.05995083	6.28E-05	31.0031417	6.60030051	0.0057096	0.00057096	4290.76629	0.0042822	0.03996722	0.01712881	0.08278924	0.24950963	3.16397623	34.2576151	0.03140281	0.0085644
WAI-12	0.00317527	420.42912	0.14406313	0.00011466	19.316219	10.3519646	0.01176026	0.0044101	2648.99746	0.01470032	0.39984867	0.07350159	0.59389288	0.38426634	5.36679241	123.482679	0.11172242	0.01176026
WAI-13	0.00375369	471.394154	0.64889442	0.00060525	51.504176	10.9671887	0.00581968	0.00407378	3864.26812	0.00407378	0.34627101	0.0931149	0.37536942	12.8117365	5.29940144	119.303459	0.13385266	0.01163936
WAI-14	0.00190832	633.705692	0.17642943	0.00025564	25.8883178	3.70501794	0.0144024	0.00324054	4601.56747	0.01764294	0.6805135	0.07561261	0.36726125	0.17570931	4.27643324	108.018016	0.16922823	0.018003
WAI-15	0.00443247	937.516005	0.70792025	0.0010268	76.5319188	7.50331687	0	0.00446436	2790.22621	0.00733431	0.70154259	0.12436437	0.36033778	8.09580148	5.41495214	89.2872386	0.23278459	0.01913298
WAI-16	0.0023085	60.7500608	0.15552016	0.00025758	20.6064206	11.1634312	0	0.000729	2707.02271	0.004131	0.03402003	0.01944002	0.0947701	0.47628048	2.88587089	38.8800389	0.02430002	0.00729001
WAI-17	0.00179789	81.4667592	0.05618397	4.49E-05	18.5968947	8.59614769	0	0.00252828	3918.83204	0.00365196	0.05899317	0.02528279	0.14326913	0.46155133	3.79073258	39.3287803	0.02809199	0.0056184
WAI-18	0.00110265	94.8794292	0.07436496	8.98E-05	20.9504037	10.9726778	0.00256431	0.00076929	3000.24141	0.00384646	0.05897911	0.02564309	0.08462219	0.41234087	3.14999705	35.9003246	0.03333602	0.00512862
WAI-19	0.00197465	449.781565	0.13712853	3.57E-05	19.9933391	8.50196861	0	0.00246831	3414.5003	0.00274257	0.27974219	0.0466237	0.26328677	0.68399709	3.92928078	57.5939809	0.11518796	0.00822771
WAI-20	0.02211113	78.2496994	0.85627528	0.0023229	53.6569367	1.61194381	0	0.00067071	1312.35924	0.00111785	0.06036405	0.02682847	0.17438504	2.95403794	2.94330655	55.8926424	0.02235706	0.00894282
WAI-21	0.1485834	197.891322	1.6359016	0.00292549	35.0597459	1.4017302	0.00329819	0.00395783	2638.55096	0.00131928	0.2341714	0.04617464	0.57058665	3.26553663	5.96081644	138.523925	0.09234928	0.01319276
WAI-22	0.03402242	137.825269	1.30678773	0.00392547	61.2556749	2.16181486	0	0.00229709	829.503931	0.00178662	0.14803455	0.02807552	0.2960691	2.10489813	5.01377699	112.302071	0.04338944	0.01020928
WAI-23	0.01021159	100.507746	1.58400208	0.00262727	48.2437183	0.8342143	0.00201016	0.00281422	1005.07746	0.00160812	0.06030465	0.03216248	0.22915766	4.04845202	4.63260305	102.517901	0.04221325	0.01005078
WAI-24	0.11721744	166.635189	2.96298195	0.02679181	48.6366457	1.69499231	0.00260368	0.00520735	2174.06848	0.00494698	0.27859321	0.06769555	0.30723363	2.67163074	2.68621132	127.580066	0.05988452	0.0104147
WAI-25	0.01333919	168.495021	0.49425206	0.00187591	67.3980082	1.2159724	0.00280825	0.0011233	1707.41621	0.00814393	0.20781053	0.03650725	0.24150953	9.72918331	3.38955816	112.330014	0.06178151	0.00842475
WAI-26	0.01015086	169.568184	0.90591222	0.0018699	55.7484442	1.19394585	0.01161426	0.00209057	1844.34436	0.00325199	0.35075063	0.10452833	0.26712796	5.38994541	1.7277372	104.528333	0.06039415	0.00696856
WAI-27	0.00295255	66.2816297	0.29726307	0.00022496	48.2048216	0.85764412	0.00200853	0.00100427	1904.09045	0.00160683	0.05222189	0.01606827	0.12653766	4.75962357	3.32512842	54.2304243	0.01606827	0.01004267
WAI-28	0.02828424	101.101123	0.45736222	0.00012999	57.7720703	1.52614552	0.00240717	0.00096287	2980.07596	0.00192574	0.29608186	0.06017924	0.14443018	2.44399929	4.11674144	52.9577311	0.03129321	0.00481434
WAI-29	0.00605734	152.05671	0.45118467	4.99E-05	37.4159217	2.69215159	0	0.00174491	2639.8042	0.00199419	0.15953491	0.0299128	0.40382274	0.29538886	4.89298552	77.2747217	0.04486919	0.0074782
WAI-30	0.00972822	177.887373	0.65595969	2.22E-05	66.7077649	2.60160283	0	0.0011118	2562.68997	0.00222359	0.26683106	0.03613337	0.31964137	3.44767965	6.67828111	83.3847061	0.03613337	0.01389745
WAI-31	0.0048449	170.99634	6.20574217	9.62E-05	65.2992273	1.66365189	0.00356242	0.00142497	2654.00569	0.00178121	0.14249695	0.0605612	1.53540464	0.70607239	4.01770151	131.809679	0.05699878	0.0142497
WAI-32	0.0114241	166.107058	0.2711952	0.00012543	42.6454446	6.33240783	0	0.00237296	3810.2925	0.00779686	0.23390586	0.04406922	0.38645315	0.44679409	5.15914961	91.5283786	0.06101892	0.01016982
WAI-33	0.02246525	42.3872679	0.27388696	0.00011086	31.7904509	5.30492961	0	0.00195634	3159.48174	0.00195634	0.04890839	0.0163028	0.25432361	1.03979229	4.67172904	42.3872679	0.02608447	0.01304224
WAI-34	0.0042241	363.008664	0.56431347	0.00035971	50.8542137	3.34957994	0.01320032	0.0042901	3349.57994	0.0039601	0.47191126	0.08250197	1.07582568	0.56959359	5.34315752	217.805198	0.14190339	0.01320032
WAI-35	0.00428986	49.0788504	0.30537951	0.00048534	43.6256448	0.48715303	0	0.00090887	1056.10415	0.00236306	0.03817244	0.01817735	0.10361091	1.30349791	2.86438713	49.0788504	0.02363056	0.00727094
WAI-36	0.00343826	58.0205594	0.39754828	0.00037391	51.5738306	0.42763301	0	0.00085956	1171.15574	0.00171913	0.04297819	0.0214891	0.0902542	3.03189657	3.84547374	120.338938	0.01934019	0.00859564
WAI-37	0.0020801	273.012587	0.26651229	0.00010401	41.6019179	7.52734703	0.00975045	0.00260012	3211.14804	0.00390018	0.27951289	0.04875225	0.48427233	1.18175448	7.47436959	117.005394	0.08775405	0.00975045

WAI-38	0.00378695	284.021411	0.29754624	6.76E-05	33.7782606	5.31863904	0.01352483	0.00304309	3780.18973	0.00879114	0.35840797	0.07100535	0.89601993	1.4894218	4.67722402	185.9664	0.10143622	0.01014362
WAI-39	0.00326253	195.141941	0.57018036	4.27E-05	29.6981641	1.33855175	0	0.00182946	4567.54105	0.003354	0.18599466	0.05183458	0.47260939	1.09462432	4.04340199	97.5709703	0.07317823	0.01219637
WAI-40	0.00389092	53.9496864	0.66864914	0.00012261	16.3810866	1.44192798	0	0.0009809	1646.28286	0.00179832	0.04087098	0.01961807	0.13242196	1.33321119	3.74688746	35.9664576	0.02452259	0.00490452
WAI-41	0.00196087	105.396664	0.19608682	7.11E-05	34.315193	5.12767027	0	0.00147065	2267.25382	0.00196087	0.07353256	0.02205977	0.17157597	1.04342698	6.54684861	63.7282156	0.02696194	0.00980434
WAI-42	0.00570894	178.404239	0.68090951	9.81E-05	46.325634	3.731622	0.00594681	0.0014867	3157.75503	0.00178404	0.18137764	0.03568085	0.41924996	0.86109779	5.93075158	118.936159	0.05649468	0.00892021
WAI-43	0.00694906	165.040215	1.64461126	0.00022295	45.4005362	2.43506702	0.00579089	0.00347453	3274.74531	0.00405362	0.58198391	0.07817694	0.63699732	6.1435496	9.7252118	104.235925	0.06080429	0.01158177
WAI-44	0.00634469	307.001297	0.78066044	9.36E-05	58.1255788	4.2775514	0.00584764	0.00263144	2610.97293	0.00204668	0.38009684	0.04093351	0.80989866	3.41180774	5.61139894	187.1246	0.10233377	0.01169529
WAI-45	0.02126491	143.834294	1.26066528	9.02E-05	37.6507416	2.57491589	0.00282028	0.0019742	2882.32644	0.00141014	0.14947485	0.0282028	0.42022176	1.7167046	4.73553261	93.069249	0.04794477	0.00846084
WAI-46	0.00402398	91.9056574	0.43220498	4.22E-05	41.6307789	2.25293058	0	0.00149036	2454.12945	0.00149036	0.1018414	0.02980724	0.28565272	0.82367341	4.82107272	59.6144805	0.03477511	0.01241968
WAI-47	0.00124469	166.970338	0.24590177	0.00017911	30.8743335	4.59623804	0.01517912	0.00242866	3642.9892	0.00394657	0.42805123	0.06678814	0.47966025	0.30054661	5.84851558	94.1105544	0.06678814	0.0121433
WAI-48	0.00265447	154.844075	0.52259875	0.00019909	50.3519751	2.55492724	0.01106029	0.00193555	2914.38669	0.00276507	0.2848025	0.04700624	0.26544699	0.94399584	4.52697713	110.602911	0.05806653	0.01106029
WAI-49	0.0043846	192.922569	0.54076781	0.00054954	70.1536613	1.15753541	0.00584614	0.00321538	2797.37725	0.00584614	0.41507583	0.04092297	0.55830622	9.43391361	3.78391311	116.922769	0.05553832	0.01169228
WAI-50	0.0029408	97.127348	0.90382393	0.00029138	64.7515653	0.81209255	0.00539596	0.00134899	2652.1162	0.00269798	0.16997286	0.04586569	0.18346277	7.69950071	3.4110585	137.597076	0.0296778	0.01618789
WAI-51	0.00707007	147.032355	0.80711378	0.00082276	75.0803514	2.17420184	0.0062567	0.00187701	4342.14699	0.00437969	0.37540176	0.05943861	0.29406471	8.06300407	6.81729591	78.2086994	0.03754018	0.01251339
WAI-52	0.01831173	107.30443	1.31331291	0.00079779	55.9849199	2.82490575	0.00233271	0.00209943	2628.95853	0.00186616	0.11196984	0.01632894	0.25893025	16.4042813	2.71130302	69.9811499	0.03965599	0.00933082
WAI-53	0.00096857	41.5101878	0.01937142	0.0002878	23.4394194	6.03004661	0.00553469	0.0008302	2374.38274	0.00525796	0.04151019	0.01937142	0.06364896	0.26289786	4.37794114	27.6734585	0.02213877	0.00830204
WAI-54	0.0011367	197.569351	0.10825718	9.20E-05	31.6110961	4.84450873	0	0.00135322	2617.11729	0.00405964	0.12720219	0.02977072	0.14344076	1.0858195	5.1890372	48.7157303	0.07578003	0.00811929
WAI-55	0.00389756	118.318771	1.17854776	0.00012528	55.6794215	5.90897861	0.00231998	0.00139199	2241.09672	0.00347996	0.09743899	0.02783971	0.31319675	13.763257	4.58914432	60.3193733	0.04407954	0.00695993
WAI-56	0.00068468	44.8581512	0.02833146	0.00010152	20.186168	7.01439827	0	0.00070829	1900.56904	0.00377753	0.03069242	0.0212486	0.09207726	0.48659289	4.04549695	33.0533746	0.01652669	0.00472191
WAI-57	0.00045583	28.7889577	0.01919264	5.28E-05	13.8186997	8.85260448	0	0.00047982	2281.5249	0.00479816	0.01919264	0.02638988	0.07437147	0.40544449	3.53432437	26.3898779	0.01679356	0.00479816
WAI-58	0.00053318	59.2420809	0.0710905	7.70E-05	22.0972962	4.04919623	0.0029621	0.00088863	2873.24092	0.01481052	0.05331787	0.01777262	0.12440837	0.29354451	2.96476994	44.4315606	0.03258314	0.00592421
WAI-59	0.00139047	53.9162598	0.47105785	6.24E-05	68.1047492	4.47504956	0	0.00056754	2116.92262	0.00482409	0.03405238	0.05107856	0.10499482	18.8979328	5.08770854	70.9424471	0.03121468	0.00851309
WAI-60	0.00037992	48.8464771	0.18453114	4.61E-05	32.5100442	7.97011684	0	0.00081411	2431.46908	0.00542739	0.04341909	0.02170955	0.11668881	5.66402039	4.09333478	51.5601703	0.02985063	0.00814108
WAI-61	0.0016473	38.7599777	0.40697977	8.40E-05	59.6580657	14.2410618	0.00968999	0.001292	3042.65825	0.01001299	0.07105996	0.03229998	0.12273993	3.27005012	5.01651012	32.2999814	0.04198998	0.01937999
WAI-62	0.00074657	49.7715913	0.13272424	5.53E-05	34.7848122	3.47571613	0	0.00082953	1764.1264	0.0030416	0.03594615	0.03871124	0.09677809	2.5209311	4.33427608	96.7780943	0.03041597	0.00829527
WAI-63	0.0014605	38.434222	0.2075448	0.00024598	22.4712085	14.6050044	0	0.00128114	3246.41062	0.00614948	0.03074738	0.01281141	0.11530267	2.30759069	2.66707878	33.3096591	0.0281851	0.01024913
WAI-64	0.00119974	79.9828982	0.05998717	7.43E-05	44.3048126	12.6173022	0	0.00114261	4270.51546	0.0091409	0.06855677	0.02570879	0.19995725	0.12625872	6.14954226	48.5610454	0.03142185	0.01142613
WAI-65	0.00083329	178.912933	0.81858794	4.41E-05	58.8206902	4.2350897	0.00245086	0.00098035	2691.04658	0.0053919	0.11273966	0.02205776	0.20587242	2.79471804	4.39194487	66.1732765	0.05636983	0.00980345
WAI-66	0.00157464	475.480106	0.11732626	3.40E-05	17.1975597	6.87284881	0.00308753	0.00308753	3099.88329	0.00586631	0.27479045	0.05866313	1.65491777	0.36463767	4.61647958	166.726791	0.13585146	0.0092626
WAI-67	0.00103796	62.7601447	0.04586318	0.00014	11.6106268	10.7102601	0.0048277	0.00096554	2558.68282	0.00386216	0.10138177	0.02172467	0.2100051	0.10283008	4.48203988	48.2770344	0.02172467	0.0048277
WAI-68	0.00092445	137.176471	0.16103325	4.47E-05	32.6241432	7.01389258	0.0029821	0.00119284	3703.76471	0.00984092	0.11630179	0.03876726	0.35785166	0.38677801	4.15435959	86.4808184	0.04771356	0.00894629
WAI-69	0.00585434	87.3781291	1.23421607	0.00030364	52.4268775	1.78032938	0	0.00109223	2354.84058	0.00218445	0.05898024	0.01966008	0.22281423	3.65764849	3.51107167	65.5335968	0.02621344	0.00655336
WAI-70	0.00391983	222.032583	0.72914404	0.00027686	65.7874321	3.05637445	0.00822343	0.00274114	3426.42876	0.00465994	0.31523145	0.07126972	0.63594518	1.06246703	2.76224981	139.798293	0.08771658	0.00548229
WAI-71	0.00404113	340.860801	0.69226369	0.00014056	42.6954508	4.79313539	0.01054209	0.00316263	4677.17243	0.00281122	0.6325252	0.08433669	1.19476982	1.48010896	3.57341596	210.841733	0.1335331	0.00351403
WAI-72	0.00366776	315.935567	0.43214175	0.00023968	66.9638144	2.85068299	0.00726289	0.00290516	4840.71392	0.0065366	0.54108505	0.07626031	0.59192526	2.58885593	3.69099897	185.203608	0.11620619	0.01089433
WAI-73	0.00231785	110.853607	0.13352821	8.82E-05	60.465604	5.46709836	0	0.0012597	2927.543	0.00226746	0.09573721	0.0176358	0.24690122	1.06948537	3.89826788	65.5044044	0.0302328	0.0075582
WAI-74	0.00126153	50.4613201	0.0841022	9.81E-05	36.0518098	2.41653655	0	0.00084102	3476.22427	0.00280341	0.03644429	0.01682044	0.15699077	0.45443222	4.02625266	42.0511001	0.01962385	0.01121363
WAI75	0.00774913	202.151212	0.11792154	0.00034113	16.5090157	33.6455424	<0.1	0.00800182	8528.25426	0.03958795	0.26532347	0.14319044	0.85071968	0.35502807	7.82072502	134.767475	0.05474929	0.05
WAI76	0.00779259	88.114053	0.05507128	6.33E-05	22.0009776	31.1125214	0.00275356	0.00220285	3554.85132	0.00798534	0.09637475	0.05782485	0.20101018	0.57604562	4.47206354	52.3177189	0.02202851	0.05
WAI77	0.00595404	147.405722	0.18497973	0.00027169	21.2726689	14.6105084	0.00578062	0.00289031	2494.33605	0.00578062	0.22544405	0.06358678	0.38730131	0.82431592	6.34220346	83.8189401	0.04335462	0.00289031

ppm	Hf	In	K	La	Li	Mg	Mn	Mo	Na	Nb	Ni	P	Pb	Pd	Pt	Rb	Re	S
WAI-01	0	0	3773.6212	0.06289369	0.25786412	1078.62673	208.712699	0.06981199	1886.8106	0.00440256	0.80818387	858.498822	0.26729817	0	9.43E-05	37.7519354	0	1047.17988
WAI-02	0	0	3277.34365	0.01638672	0.21575846	1136.1458	151.631766	0.05079883	1281.98759	0.00109245	0.31954101	805.680314	0.15376204	0	0	30.1706794	0	808.411433
WAI-03	0	0	3491.80594	0.03491806	0.24151658	733.279247	162.456271	0.02589756	1745.90297	0.00232787	0.67217264	972.17697	0.18157391	0	0	33.3205582	0	1847.74731
WAI-04	0	0	3364.63819	0.01962706	0.3140329	796.297704	168.680528	0.02719749	843.402638	0.00112155	0.91406004	1022.28924	0.19206476	0	0	18.6120569	0	476.657076
WAI-05	0	0	3851.96375	0.01925982	0.105929	1380.28701	204.731873	0.04782855	839.4071	0.00128399	0.85385196	935.385196	0.15472054	0	6.42E-05	13.4465634	0	523.225076
WAI-06	0	0	2871.59168	0.01435796	0.19383244	890.193421	235.709817	0.0342198	1435.79584	0.0016751	0.64371514	753.074918	0.1373578	0	0	11.6419113	0	839.940566
WAI-07	0.00058307	0	2332.2884	0.01554859	0.29931035	553.918495	70.5517241	0.01496552	1166.1442	0.0013605	0.72495298	764.601881	0.11505956	0	0	14.4290909	0	544.200627
WAI-08	0	0	3080.39311	0.05390688	0.55960475	515.965845	136.795124	0.07367274	1540.19655	0.00462059	0.80860319	873.034746	0.19355137	0	0	17.9176199	0	682.820472
WAI-09	0	0	2176.14932	0.02357495	0.11968821	738.077311	164.625696	0.01142478	682.041466	0.00326422	0.32279548	571.783234	0.1695583	0	0	12.5201124	0	729.010022
WAI-10	0	0	2164.84822	0.0180404	0.18220806	1253.80793	89.1195852	0.00613374	1082.42411	0.00198444	0.5520363	571.700335	0.16128119	0	0	9.10138274	0	690.947391
WAI-11	0	0	3425.76151	0.01998361	0.20554569	927.810408	342.576151	0.0516719	767.370578	0.0014274	0.33401175	986.333834	0.20040705	0	0	28.1140828	0	411.091381
WAI-12	0	0	3528.07653	0.21462466	1.00844187	893.779387	179.696698	0.19228017	1764.03826	0.00705615	0.74089607	740.308058	0.30635465	0	0	22.2239421	8.82E-05	635.053775
WAI-13	0	0	3491.80855	0.17459043	2.85164365	1420.00214	164.69697	0.19641423	1745.90427	0.00814755	1.94668326	842.398811	0.31542671	0	0	20.7617116	0.00311353	529.590963
WAI-14	0	0	4320.72063	0.35285885	0.46447747	1213.40238	432.072063	0.06049009	1427.99817	0.00756126	0.64450749	692.755541	0.26248378	0	0.00010802	19.0795822	0.00097216	1033.37235
WAI-15	0	0.00063777	3826.59594	0.37947076	28.559161	1093.76867	173.631791	0.35268459	1913.29797	0.01084202	1.58165966	659.131151	0.28571916	0	9.57E-05	34.7901348	0.00060588	1055.50271
WAI-16	0	0	2916.00292	0.01944002	0.2988903	913.680914	186.794287	0.11518212	1156.92416	0.002187	0.56862057	738.963739	0.12854713	0	0	18.2128682	0	366.930367
WAI-17	0.00084276	0	3371.03831	0.03090119	0.51689254	1101.20585	279.65572	0.07444376	1273.97156	0.00309012	0.55622132	930.687493	0.17445123	0	0	22.024117	0	474.754562
WAI-18	0	0	3077.17068	0.03077171	0.5487621	884.68657	137.80596	0.18104021	1538.58534	0.00282074	0.61286983	918.279016	0.18155307	0	0	22.6941337	2.56E-05	415.418041
WAI-19	0	0	3291.08462	0.16181166	0.46349442	1519.38407	191.266868	0.06993555	963.190766	0.00740494	0.76517718	791.780109	0.24271749	0	0	24.1071949	0	614.335796
WAI-20	0	0	2682.84684	0.03129988	0.37783426	742.254291	51.7342298	0.04471411	1341.42342	0.00178857	0.43596261	385.659233	0.14755658	0	0	29.3883514	0	1088.78867
WAI-21	0	0	3957.82644	0.10224385	0.31332793	933.387402	43.766964	0.041887	1001.00027	0.00824547	0.82124899	437.010003	0.42480671	0	0	29.8815896	0	2275.7502
WAI-22	0	0	3062.78375	0.06891263	0.58448123	400.714207	22.5369837	0.0311383	1531.39187	0.00612557	0.26799358	556.405714	0.24119422	0	0	37.3965895	0	2141.3963
WAI-23	0	0	2412.18591	0.03417263	0.13267023	942.762661	22.4132274	0.05085692	803.65994	0.01387007	1.26840776	659.732847	0.23438407	0	0	24.8254134	0	1089.50397
WAI-24	0	0	3124.40979	0.13018374	1.60646737	1179.4647	169.082643	0.02395381	1562.20489	0.00624882	1.08833608	729.289318	0.18798532	0	0	29.4397512	0.0004947	1780.91358
WAI-25	0	0	3369.90041	0.10952176	0.74137809	963.229867	184.165057	0.02387013	1684.95021	0.00393155	2.02194025	710.206511	0.17354987	0	0	47.9256003	0	1791.66372
WAI-26	0.00046457	0	2787.42221	0.17421389	2.75257943	1263.6314	149.707801	0.13100884	1393.7111	0.00975598	1.31937985	851.78977	0.2696831	0	0	23.611789	0.00018583	1135.87455
WAI-27	0	0	2410.24108	0.02611095	6.03564537	1088.62555	45.7343245	0.01707254	1205.12054	0.00220939	0.77328568	598.744055	0.18096893	0	0	26.6773517	4.02E-05	747.174734
WAI-28	0	0	2888.60351	0.12517282	4.02719473	1533.36703	288.860351	0.02046094	1444.30176	0.00216645	1.72834777	610.217492	0.14418946	0	0	17.8900844	0.00012036	1624.83948
WAI-29	0	0	2991.27955	0.07228926	0.438721	974.658586	64.5867109	0.03564608	1495.63977	0.00498547	1.45824878	626.423792	0.17698404	0	0	13.086848	0.00211882	1784.7968
WAI-30	0.00083385	0	3335.38824	0.1139591	10.3925139	983.939532	134.249377	0.06754161	1667.69412	0.00250154	2.11797154	792.988555	0.20734997	0	0	28.51479	0.00011118	1745.51985
WAI-31	0	0	4274.9085	0.08549817	2.67181781	694.672631	91.2336722	0.04916145	2137.45425	0.00391867	3.07793412	726.378203	0.17099634	0	0	16.5510207	0.00042749	1734.90037
WAI-32	0.00237296	0	4067.92794	0.1016982	0.38645315	1284.78724	406.792794	0.02406857	2033.96397	0.0054239	1.34580616	846.129011	0.32882418	0	0	28.5771938	0.0003051	1840.73739
WAI-33	0	0	3912.67088	0.02608447	0.26736584	824.921445	143.595021	0.01369435	298.667211	0.00326056	0.37496429	653.416038	0.21291451	0	0	38.1778862	0	2852.98919
WAI-34	0	0	3960.09451	0.22110528	0.61051457	1478.43529	396.009451	0.01056025	1980.04726	0.00957023	2.13845104	853.07036	0.32142767	0	0	23.9618719	0.00151804	1488.33552
WAI-35	0	0	2181.28224	0.02181282	2.19037092	672.562024	49.8422992	0.00690739	1090.64112	0.00309015	0.35809383	696.919676	0.22867109	0	5.45E-05	25.2737902	0	799.803488

WAI-36	0.00107446	0	2578.69153	0.0214891	3.9819295	569.461046	27.6134885	0.01848062	1289.34577	0.00279358	0.63392833	1037.92334	0.18674025	0	0	35.802983	0.00010745	1207.6872
WAI-37	0	0	3900.17981	0.13000599	0.55577562	877.540457	215.744946	0.02242603	1950.0899	0.00845039	1.99234185	874.940337	0.27951289	0	0	35.35513	6.50E-05	1599.07372
WAI-38	0	0	4057.44873	0.16906036	0.93997562	855.44544	304.815836	0.02299221	2028.72436	0.00946738	1.76160899	993.736817	0.21605915	0	0.00013525	17.5822778	0.0002705	1531.68689
WAI-39	0	0	3658.91139	0.07012914	1.0214461	1021.4461	183.189497	0.01737983	1829.45569	0.00487855	2.70454533	692.753889	0.23478015	0	6.10E-05	14.7576093	0	1259.27534
WAI-40	0	0	1961.80678	0.01961807	0.15040519	632.682686	60.1947713	0.01193433	980.90339	0.00228878	0.964555	635.952364	0.17411035	0	0	18.6289902	3.27E-05	1020.13953
WAI-41	0	0	2941.30226	0.03431519	0.17892922	977.983	34.0455736	0.00710815	1470.65113	0.0029413	0.71081471	651.253341	0.20368518	0	7.35E-05	23.3343312	0	1348.09687
WAI-42	0.00059468	0	3568.08478	0.08920212	0.19624466	1308.29775	85.5745666	0.02765266	1784.04239	0.00564947	2.3133083	547.106333	0.21557179	0	0	20.4986471	0	1787.01579
WAI-43	0.00086863	0	3474.53083	0.23453083	1.38691689	1245.04021	195.036997	0.04632708	1737.26542	0.00868633	3.43978552	1138.19839	0.15287936	0	5.79E-05	21.4928686	0.00964182	2003.64611
WAI-44	0	0	3508.58625	0.18420078	0.36840156	1464.83476	36.1676766	0.02836107	663.999947	0.00847908	1.86247453	565.174768	0.31489562	0	0	21.4813193	0	1584.71146
WAI-45	0	0	3384.33633	0.06486645	0.55277493	1037.86314	87.9927445	0.02087007	1692.16816	0.00535853	0.87710717	607.206343	0.19657354	0	0	21.4059273	5.64E-05	2346.47319
WAI-46	0	0	2980.72402	0.04967873	0.17635951	774.988246	83.9322207	0.01018414	411.836703	0.00546466	1.06064097	597.635167	0.14083921	0	0	20.5421564	2.48E-05	1905.17944
WAI-47	0	0	3642.9892	0.18822111	1.99757241	1493.62557	278.202942	0.05798425	1821.4946	0.0103218	2.26168913	933.819565	0.20340023	0	0	19.5841028	0.00021251	1867.03197
WAI-48	0.00082952	0	3318.08732	0.12995842	0.73550936	1625.86279	216.173389	0.03622245	1659.04366	0.00829522	1.80559252	954.779626	0.1786237	0	0	17.137921	5.53E-05	1335.53015
WAI-49	0	0	3507.68307	0.17830722	0.97630512	1379.68867	207.099454	0.02396917	1753.84153	0.00496922	3.77368237	609.167626	0.19029181	0	0	33.6942189	0.00017538	2206.91726
WAI-50	0.00107919	0	3237.57827	0.07554349	1.0576089	1303.12525	108.917529	0.08795421	1618.78913	0.00350738	1.58371537	870.099159	0.19533389	0	0	36.3660979	0	1748.29226
WAI-51	0	0	3754.01757	0.18144418	2.0083994	1689.30791	195.584315	0.03847868	1436.85023	0.00437969	3.6257553	830.263553	0.18989072	0	6.26E-05	34.4243411	3.13E-05	1489.09364
WAI-52	0	0	2799.24599	0.05365222	0.59483977	356.903864	40.3324694	0.05271913	657.589538	0.00419887	0.32424599	403.557964	0.16235627	0	0	40.3184731	0	1590.90481
WAI-53	0	0	3320.81502	0.02213877	0.31824477	725.044613	212.504488	0.07610201	1660.40751	0.00166041	0.52026102	1212.09748	0.20782767	0	0	26.228904	0	547.934479
WAI-54	0	0	3247.71535	0.07036717	0.27876223	622.478776	209.342319	0.02977072	1623.85768	0.00893122	0.84981885	1020.59455	0.21191343	0	0	25.1589683	0	849.81885
WAI-55	0	0	2783.97108	0.05103947	18.2164507	505.754745	91.9406448	0.59321784	1391.98554	0.00208798	0.57535402	492.76288	0.23269358	0	0	31.1804761	0.0001392	832.871347
WAI-56	0	0	2833.14639	0.01888764	0.42733291	639.818893	102.111318	0.19619539	1416.5732	0.00141657	0.54065877	771.5602	0.16455859	0	0	27.9253796	0	583.155965
WAI-57	0	0	2878.89577	0	0.33347209	798.893575	160.594402	0.14922276	1439.44788	0.00095963	0.59976995	896.296215	0.13146957	0	0	19.9819357	0	398.247248
WAI-58	0	0	3554.52485	0.02665894	0.34360407	559.837664	200.030886	0.01777262	1189.58098	0.00207347	0.33767986	807.765772	0.15254836	0	0	23.4480156	0	779.033363
WAI-59	0	0	3405.23746	0.01702619	21.1607131	675.372097	77.9799379	1.20460275	1702.61873	0.00141885	0.69807368	737.80145	0.17508596	0	0	68.1047492	0	621.455837
WAI-60	0	0	3256.43181	0.02170955	3.73946919	732.697156	208.9001	0.34002575	1091.17602	0.00162822	0.44504568	748.165207	0.22279421	0	0	35.3729905	2.71E-05	610.580964
WAI-61	0	0	3875.99777	0.03552998	12.9619826	597.549657	209.17468	0.63469464	1245.16428	0.002261	0.61046965	1588.51309	0.27713384	0	0	34.74832	0	645.999629
WAI-62	0	0	3318.10609	0.01935562	0.48112538	550.252593	90.4736927	0.03373408	1659.05305	0.00165905	0.44241415	752.104047	0.22341914	0	5.53E-05	28.3145053	0	940.130059
WAI-63	0	0	3074.73776	0.01793597	0.80968094	1445.12675	217.102109	0.07020651	1108.18674	0.00102491	0.36640625	856.314467	0.25315341	0	5.12E-05	27.2165538	0	543.203671
WAI-64	0.00057131	0	3427.8385	0.03427839	0.48846699	936.942522	342.78385	0.09940732	830.965182	0.00314219	0.41419715	1231.45098	0.29536542	0	0	22.8665393	0	571.306416
WAI-65	0	0	2941.03451	0.05882069	10.8671225	813.686215	130.581932	0.12572923	1470.51726	0.00367629	0.4460569	900.446733	0.35831604	0	7.35E-05	32.7631245	0	615.166385
WAI-66	0	0	3705.03979	0.14202653	0.70395756	886.122016	106.14939	0.07132202	1476.45836	0.01543767	1.30911406	859.260478	0.37575279	0	0	21.1496021	0	938.61008
WAI-67	0	0	2896.62207	0.05310474	0.29207606	868.986619	169.597222	0.04296656	1085.50912	0.00217247	0.42966561	789.812283	0.31307657	0	7.24E-05	23.2574613	0	576.910561
WAI-68	0.00059642	0	3578.51662	0.05964194	0.73061381	1136.17903	238.567775	0.12793197	1216.69565	0.00477136	0.48906394	1087.57084	0.27107263	0	0	28.2881739	2.98E-05	846.915601
WAI-69	0	0.00043689	2621.34387	0.02839789	3.59997892	674.996047	32.3080632	0.01419895	1310.67194	0.00262134	0.62693808	492.594203	0.22936759	0	0	20.3044928	0	1155.57576
WAI-70	0	0	3289.37161	0.13705715	0.62223946	1323.97207	264.821826	0.02604086	1644.6858	0.00740109	1.97088182	749.976726	0.34976985	0	8.22E-05	12.9628653	0	1175.95035
WAI-71	0	0.00070281	3239.93462	0.28815037	1.58482702	1243.96622	339.736312	0.03197766	1440.40044	0.00843367	2.93070008	874.290384	0.3162626	0	0	16.6986652	7.03E-05	1521.5745
WAI-72	0	0	4357.73196	0.25056959	15.499	1133.01031	304.56915	0.01960979	1603.28222	0.00762603	2.13165722	582.120361	0.30504124	0	7.26E-05	25.7832474	0.00098049	1815.72165
WAI-73	0	0	3023.2802	0.0453492	0.36783242	581.981439	149.198878	0.0403104	1110.29965	0.00277134	1.68547871	828.882655	0.29854892	0	0	29.7012086	0	891.867659
WAI-74	0	0	3364.08801	0.01962385	0.1261533	1054.08091	129.068843	0.04681689	883.633783	0.00252307	0.75131299	768.413769	0.18866927	0	0	27.2715401	0	939.141235
WAI75	<0.02	<0.02	120000	0.17267083	0.5896077	1575.09486	112.825645	0.27332529	921.893757	0.00968641	1.04444793	1279.02756	0.52643545	#¡VALOR!	0.00033692	14.4538117	8.42E-05	656.991439
WAI76	<0.02	<0.02	120000	0.06057841	0.37448473	842.590631	>10000	0.18421344	1000.64521	0.00302892	0.81230143	1016.89124	0.22138656	#¡VALOR!	8.26E-05	25.7595927	2.75E-05	539.698574
WAI77	<0.02	<0.02	120000	0.13295418	0.68500306	867.092484	207.842068	0.1725514	1193.69732	0.00664771	1.49139907	1344.86044	0.27342316	#¡VALOR!	0.00017342	34.6952606	0.00020232	540.487648

ppm	Sb	Sc	Se	Sn	Sr	Ta	Te	Th	Ti	Tl	U	V	W	Y	Zn	Zr
WAI-01	0.01478002	0.08490648	0.00943405	0.01572342	8.88373323	0	0	0.01572342	7.92460451	0.01069193	0.00943405	0.12578737	0.00943405	0.06037794	14.0158581	0.00628937
WAI-02	0.01065137	0.10378255	0	0.00819336	7.76184221	0	0.00109245	0.00273112	4.47903632	0.00655469	0.00546224	0.05462239	0.00546224	0.01556738	10.9845635	0
WAI-03	0.02007788	0.08438531	0	0.00872952	9.16017091	0	0	0.00581968	5.70328303	0.01484018	0.00581968	0.08729515	0.00872952	0.03317216	10.8013197	0.01454919
WAI-04	0.01065469	0.09533142	0	0.04205798	19.0410483	0	0	0	4.90676402	0.00560773	0.00280387	0.08411596	0.01121546	0.02271131	10.4163591	0.0084116
WAI-05	0.01508686	0.09950906	0	0	14.0018882	0	0	0	5.23225076	0.00770393	0	0.09629909	0.00320997	0.01797583	9.42126133	0.00320997
WAI-06	0.01292216	0.11486367	0	0	6.54722903	0	0	0.00239299	4.69026641	0.00406809	0.00239299	0.09571972	0.00478599	0.01387936	11.9290704	0.00717898
WAI-07	0.00894044	0.02526646	0	0.00388715	7.5877116	0	0	0.00388715	4.60626959	0.00932915	0.00194357	0.05830721	0.00583072	0.01613166	8.94821317	0.00971787
WAI-08	0.01540197	0.09754578	0.00770098	0.02053595	13.5871006	0	0.0007701	0.03080393	10.6016863	0.01873906	0.00770098	0.10267977	0.00770098	0.06058106	9.8726599	0
WAI-09	0.01885996	0.06347102	0	0.00725383	5.51835198	0	0	0.00725383	4.7875285	0.00453364	0.00181346	0.10880747	0.01088075	0.01922265	6.69165916	0.00362692
WAI-10	0.01497353	0.05772929	0.00360808	0.00360808	5.78014476	0	0	0.00360808	3.95084801	0.01407151	0.00180404	0.07216161	0.00541212	0.01569515	10.5355947	0.00541212
WAI-11	0.01141921	0.09706324	0	0	8.33031007	0	0.00085644	0	5.30993034	0.04824614	0.0028548	0.14274006	0.0028548	0.02398033	7.9477667	0.0057096
WAI-12	0.03733881	0.11466249	0	0.0323407	19.7836891	0	0	0.04704102	15.3765335	0.0091142	0.01764038	0.26460574	0.05586121	0.18404799	19.8836513	0.00882019
WAI-13	0.02851644	0.13094282	0	0.02618856	8.81390674	0	0	0.05528697	15.0729736	0.12745101	0.01745904	0.23278724	0.05528697	0.11290181	11.1534185	0.00872952
WAI-14	0.03240541	0.12602102	0.018003	0.0216036	25.5138553	0	0	0.05760961	14.9064862	0.00576096	0.0252042	0.32405405	0.09001501	0.31073183	14.1503601	0.0036006
WAI-15	0.0487891	0.11798671	0	0.02551064	7.57347113	0	0	0.09885373	19.7707457	0.02869947	0.02232181	0.318883	0.16581916	0.25159868	12.6787879	0.01594415
WAI-16	0.00656101	0.0972001	0	0.00243	5.61573562	0	0	0.00486001	4.37400437	0.01409401	0.00243	0.07290007	0.00972001	0.01628102	8.37378837	0.00972001
WAI-17	0.00674208	0.09270355	0	0.0056184	13.5178636	0	0	0.0084276	5.73076513	0.05168925	0.0056184	0.11236794	0.01123679	0.02219267	8.34612902	0.01685519
WAI-18	0.02436094	0.07692927	0.00769293	0.00769293	7.52624661	0	0	0.01025724	5.89791046	0.00718007	0.00256431	0.07692927	0.01538585	0.01974518	8.92635927	0
WAI-19	0.04634944	0.09873254	0	0.01645542	9.28634378	0	0	0.05210884	10.696025	0.00685643	0.01097028	0.19197994	0.10421768	0.05896527	10.3477186	0.00548514
WAI-20	0.31702307	0.02906417	0.02235706	0.00670712	2.37208374	0	0	0.00670712	4.31491199	0.0858511	0.00223571	0.06707117	0.02459276	0.02325134	6.34493277	0.00670712
WAI-21	1.08873209	0.09894566	0.09894566	0.02308732	33.5128954	0	0.00098946	0.00329819	13.6545012	0.01022439	0.00659638	0.23087321	0.06596377	0.09037037	5.04622871	0.00989457
WAI-22	0.56533883	0.04594176	0.10719743	0.01020928	46.2965286	0	0	0.02041856	8.52474809	0.03522201	0.00510464	0.12761599	0.0382848	0.06329753	7.73608128	0.01020928
WAI-23	0.54736519	0.0402031	0.13669054	0.01005078	4.40022914	0	0	0.01608124	10.211587	0.23257493	0.00804062	0.1206093	0.12663976	0.03155943	7.29485223	0.00603047
WAI-24	2.86820819	0.05467717	0.0729029	0.01562205	4.92615277	0	0	0.01822572	8.9045679	0.01484095	0.00520735	0.20829399	0.01301837	0.12315382	11.6488412	0.01822572
WAI-25	0.36423007	0.04774026	0.01404125	0.00842475	4.87793084	0	0	0.01404125	7.52611092	0.0056165	0.0056165	0.16849502	0.011233	0.07104873	10.4691573	0.0056165
WAI-26	0.16190277	0.06503985	0.00929141	0.00929141	3.68404302	0	0	0.02322852	11.2658314	0.0078977	0.00696856	0.23228518	0.01625996	0.11985916	8.11372148	0.01858282
WAI-27	0.0556364	0.05623896	0.00803414	0.0060256	3.40044846	0	0	0.0060256	4.43886065	0.0090384	0.00401707	0.06025603	0.03012801	0.01847852	9.65301552	0.00401707
WAI-28	0.06090139	0.07462226	0.00240717	0	7.70775704	0	0	0.00481434	4.81433919	0.00312932	0.00481434	0.12035848	0.00962868	0.01782071	8.98837127	0.00481434
WAI-29	0.04711265	0.08724565	0.01246367	0.0074782	10.6115642	0	0	0.01246367	7.10428893	0.00448692	0.00498547	0.12463665	0.00498547	0.05309521	9.43250151	0.0149564
WAI-30	0.03001849	0.07782573	0.00555898	0.00555898	5.63402664	0	0.00083385	0.00833847	5.78133962	0.00444718	0.00555898	0.13897451	0.02223592	0.09366882	14.5673082	0.01667694
WAI-31	0.18132737	0.06412363	0	0.01068727	1.92727125	0	0	0.0142497	7.37421716	0.00427491	0.00712485	0.14249695	0.02493697	0.04132412	6.32686458	0.0142497
WAI-32	0.02881449	0.17966682	0	0.00677988	18.1632983	0	0.00067799	0.01355976	7.83076128	0.00440692	0.0169497	0.1355976	0.00677988	0.08576548	14.2106283	0.02033964
WAI-33	0.03782249	0.09129565	0.00978168	0.03586615	5.99616813	0	0	0.00652112	4.79302183	0	0	0	0	0.02151969	6.99063865	0.02282391
WAI-34	0.03630087	0.1551037	0	0.02310055	6.99286689	0	0	0.0462011	17.6554214	0.02409058	0.01650039	0.46201103	0.00660016	0.13299317	14.4015437	0.01320032
WAI-35	0.06562024	0.0363547	0.00363547	0.00545321	1.25969049	0	0	0.00545321	4.74428887	0.00072709	0	0.0363547	0.00545321	0.01690494	8.04711373	0.01090641
WAI-36	0.08402237	0.05802056	0	0.00644673	1.19909156	0	0.00042978	0.00429782	5.73758865	0.00214891	0.00429782	0.06446729	0.01719128	0.02578692	7.45671634	0.0214891
WAI-37	0.06402795	0.14625674	0	0.02275105	10.6832425	0	0	0.0260012	11.5705334	0.02275105	0.00975045	0.19500899	0.0130006	0.09815453	15.4317114	0.0130006
WAI-38	0.13288145	0.1859664	0	0.02704966	16.3346123	0	0	0.03719328	13.7277015	0.01521543	0.01014362	0.30430865	0.01014362	0.10853675	16.2264137	0.02704966
WAI-39	0.09269242	0.13111099	0.00609819	0.01524546	23.0328472	0	0	0.00609819	8.14107783	0.00945219	0.00609819	0.15245464	0.01829456	0.08385005	12.022573	0.00609819
WAI-40	0.08141498	0.05558453	0.01144387	0.00326968	7.95839617	0	0.00049045	0.00490452	4.28327813	0.01356916	0.00163484	0.06539356	0.01798323	0.01487704	6.43472624	0.00163484
WAI-41	0.05073746	0.0490217	0	0.00735326	9.67933551	0	0	0.00735326	5.29434406	0.11299503	0.00490217	0.07353256	0.01225543	0.03210922	9.12784133	0
WAI-42	0.04519574	0.11001595	0.00892021	0.00892021	6.29172283	0	0	0.02081383	8.23632903	0.36186327	0.00594681	0.17840424	0.00892021	0.0588734	9.71411081	0.02081383
WAI-43	0.2362681	0.12739946	0.02316354	0.02316354	9.32621984	0	0.00086863	0.01737265	10.4235925	0.13840215	0.00579089	0.20268097	0.06080429	0.19746917	18.4671314	0.04053619
WAI-44	0.07280317	0.09648612	0.213439	0.01754293	29.4399624	0	0	0.03508586	12.8063398	0.08362131	0.01169529	0.38009684	0.00877147	0.10028709	15.8529622	0.0263144
WAI-45	0.05358533	0.08460841	0.03948392	0.0141014	18.4559141	0	0	0.01128112	7.98139317	0.02453644	0.0141014	0.16921682	0.00846084	0.05414938	7.06480208	0.00846084
WAI-46	0.05390143	0.09935747	0.01738756	0.00993575	7.80701301	0	0	0.00745181	6.68178969	0.26429086	0.00496787	0.09935747	0.00745181	0.0352719	7.64804106	0.01738756
WAI-47	0.03248332	0.1001822	0.00607165	0.01517912	10.2459071	0	0	0.02125077	12.2950886	0.01851853	0.00910747	0.18214946	0.00910747	0.13387985	13.5185258	0.0121433
WAI-48	0.02875676	0.11060291	0.03318087	0.01382536	7.31361746	0	0	0.01659044	10.3413721	0.02599168	0.00553015	0.19355509	0.00829522	0.10037214	10.8390852	0.01106029
WAI-49	0.07366134	0.08476901	0.26892237	0.01461535	7.86597928	0	0	0.02046149	7.97997898	0.00350768	0.01461535	0.20461485	0.00584614	0.12715351	16.5504179	0.02046149
WAI-50	0.09092199	0.08363744	0.00809395	0.00809395	4.40310644	0	0	0.00809395	6.23233816	0.01348991	0.00269798	0.08093946	0.0890334	0.05288045	9.89889555	0.02158386
WAI-51	0.11606171	0.10949218	0.00938504	0.01564174	13.8398114	0	0	0.01251339	7.78958646	0.03065781	0.0062567	0.12513392	0.02189844	0.11887722	10.8303407	0.01564174
WAI-52	0.48520264	0.07464656	0.01399623	0.01166353	13.2241046	0	0	0.01166353	5.83176249	0.02239397	0.00466541	0.1399623	0.0466541	0.03778982	7.44366164	0.01166353
WAI-53	0.00774857	0.0664163	0	0.00830204	9.5418085	0	0	0	6.22652817	0.00774857	0.00276735	0	0.00830204	0.0215853	9.79363697	0.04151019
WAI-54	0.04952766	0.08119288	0.00811929	0.01082572	8.17341697	0	0	0.01894501	9.93259612	0.00460093	0.00541286	0.10825718	0.19486292	0.03031201	12.8771914	0.00541286
WAI-55	0.02273576	0.06031937	0	0.01159988	9.66269961	0	0	0.01391986	6.12473637	0.00139199	0.00695993	0.1159988	0.22503766	0.04477554	6.61425128	0.00463995
WAI-56	0.00590239	0.05430197	0	0.00708287	9.46979181	0	0	0.00472191	4.60386288	0.00401362	0.00236096	0	0.00708287	0.01652669	12.5484776	0.00472191
WAI-57	0.00407844	0.059977	0.00719724	0.00479816	10.551153	0	0	0	4.84614121	0.00167936	0	0	0.00239908	0.00935641	8.18086214	0.0119954
WAI-58	0.01303326	0.06516629	0.01184842	0.00592421	7.67184947	0	0.00059242	0.00592421	5.2725452	0.00088863	0	0	0.0029621	0.02428925	9.54093712	0.01481052
WAI-59	0.01305341	0.07378015	0	0.01418849	6.34793017	0	0.00056754	0.0028377	4.73895547	0.02582305	0	0	0.14756029	0.01872881	8.47052819	0.00851309
WAI-60	0.01275436	0.08412449	0.00542739	0.00814108	8.78965218	0	0	0.00271369	4.36904601	0.0070556	0.00271369	0	0.01628216	0.02469461	11.3812292	0.00814108
WAI-61	0.02260999	0.11627993	0.00968999	0	13.5853722	0	0.000646	0.00323	8.62409504	0.01356599	0.00323	0	0.03552998	0.04328198	12.196473	0.01614999
WAI-62	0.01382544	0.08295265	0	0.00553018	6.22144892	0	0.00082953	0.00553018	4.59004676	0.00801876	0	0	0.00829527	0.02018515	8.5634788	0.00829527
WAI-63	0.01024913	0.09992898	0	0	14.0079928	0	0.00076868	0.00256228	4.43274694	0.0017936	0	0	0.00512456	0.01511746	10.4387347	0.00512456
WAI-64	0.0134257	0.12854394	0	0.01713919	21.7953398	0	0	0.0085696	7.25559148	0.00885525	0.00285653	0.1428266	0.00285653	0.04541886	15.6595089	0.01713919
WAI-65	0.25636018	0.07352586	0	0.00735259	6.31832247	0	0	0.01715604	6.76437937	0.02107741	0.00735259	0.14705173	0.16420776	0.05686	10.7029148	0.00490172

WAI-66	0.01204138	0.12658886	0	0.0555756	7.11367639	0	0	0.05248806	14.1100265	0.00617507	0.01543767	0.27787798	0.0092626	0.13060265	11.0101432	0.02161273
WAI-67	0.0082071	0.11586488	0.0048277	0.00965541	19.1466719	0	0	0.0048277	5.09322713	0.03524224	0.00241385	0.1448311	0.00241385	0.08665728	15.1203672	0.01931081
WAI-68	0.01073555	0.11630179	0	0.01789258	12.7275908	0	0	0.01192839	8.5884399	0.01759437	0.00596419	0.2087468	0.00596419	0.06202762	12.6798772	0.00596419
WAI-69	0.11009644	0.0699025	0.02184453	0.00873781	18.0697971	0	0	0.00655336	4.74026351	0.03779104	0.00436891	0.13106719	0.01092227	0.02446588	10.8501792	0.00655336
WAI-70	0.12307732	0.10964572	0.05208172	0.02192914	15.9918283	0	0	0.02741143	10.7178692	0.03481252	0.00822343	0.35634859	0.01370572	0.09456943	11.0934057	0.01644686
WAI-71	0.08222828	0.16515936	0.02108417	0.0245982	16.8146282	0	0.00105421	0.04568238	14.7940616	0.03549169	0.01054209	0.49196404	0.00702806	0.17851267	12.3131572	0.01405612
WAI-72	0.04285103	0.15615206	0.01089433	0.01452577	10.8471211	0	0	0.03994588	14.2352577	0.00435773	0.01089433	0.47208763	0.02905155	0.17576186	7.36819845	0.01452577
WAI-73	0.03250026	0.07810141	0	0.0100776	12.7280097	0	0.00075582	0.0100776	6.29850042	0.10127989	0.0025194	0.12597001	0.0075582	0.03980652	12.8590185	0.0075582
WAI-74	0.01261533	0.12054649	0	0.00560681	6.59080908	0	0	0.00560681	4.87792761	0.01429737	0	0.14017033	0.00280341	0.01541874	8.69336409	0.00841022
WAI75	0.12381762	0.08422967	0.05	0.07580671	25.5763398	<0.05	<0.02	0.03369187	12.5081062	0.03411302	0.00842297	0.33691869	0.02105742	0.11623695	36.5051397	0.01263445
WAI76	0.0170721	0.03579633	0.05	0.01652139	16.8352912	<0.05	<0.02	0.01101426	5.45205703	0.01762281	<0.1	0.05507128	0.00826069	0.04846273	24.4461426	0.01652139
WAI77	0.04537784	0.06358678	0.05	0.04624493	9.30101205	<0.05	<0.02	0.01734185	9.27788958	0.02370053	0.00578062	0.08670925	0.01734185	0.11301105	17.8303118	0.02023216

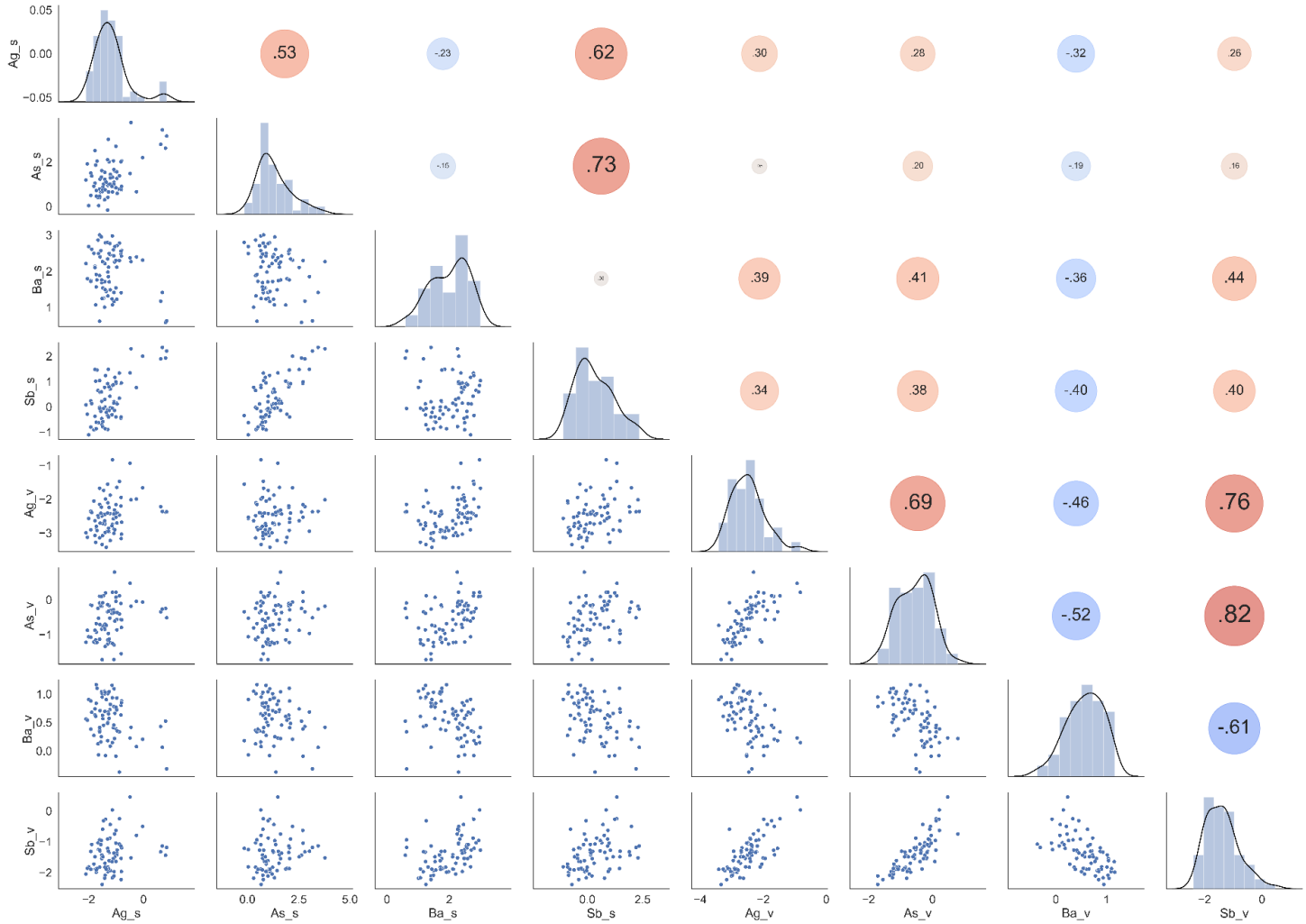

Figure A7.5. Chemical concentration relationships between rock/soil and foliage field samples. Rock/soil is represented with elementX_s and foliage with elementX_v, with elementX varying by element, values on the top right half represent correlations with red for positive and blue for negative correlations. Values on the left bottom half visually represent the correlations as scatterplots. Finally, the middle values across the diagonal are histograms per element for each type of sample (i.e. elementX_s for rock/soil and elementX_v for foliar chemical concentrations).

Table A7.2. Confusion matrices for prediction models of elemental concentrations, with a classification of 3 classes (high, medium and low) using one standard deviation as a measure to create the class ranges (Chapter 3.4 of article). Categorised on the type of platform (Satellite-based, Airborne-based and Laboratory-based) and shown as percentages.

Satellite-based	Class Error		
	High	Medium	Low
Ag	0.54	0.59	0.32
As	0.23	0.73	0.38
Ba	0.31	0.62	0.24
Sb	0.36	0.69	0.39
Airborne-based	Class Error		
	High	Medium	Low
Ag	0.75	0.71	0.36
As	0.23	0.75	0.47
Ba	0.36	0.66	0.56
Sb	0.5	0.75	0.52
Laboratory-based	Class Error		
	High	Medium	Low
Ag	0.63	0.62	0.68
As	0.44	0.73	0.85
Ba	0.68	0.62	0.48
Sb	0.36	0.5	0.78

Table A7.3. Statistical measures of accuracy for laboratory and airborne-based classifications with class ranges from one standard deviation.

Element	***Silver, Ag***	***Arsenic, As***	***Barium, Ba***	***Antimony, Sb***
Data set	Accuracy	Accuracy	Accuracy	Accuracy
Laboratory-based	0.72	0.67	0.66	0.78
Airborne-based	0.71	0.62	0.67	0.75
Satellite-based	0.58	0.64	0.68	0.74

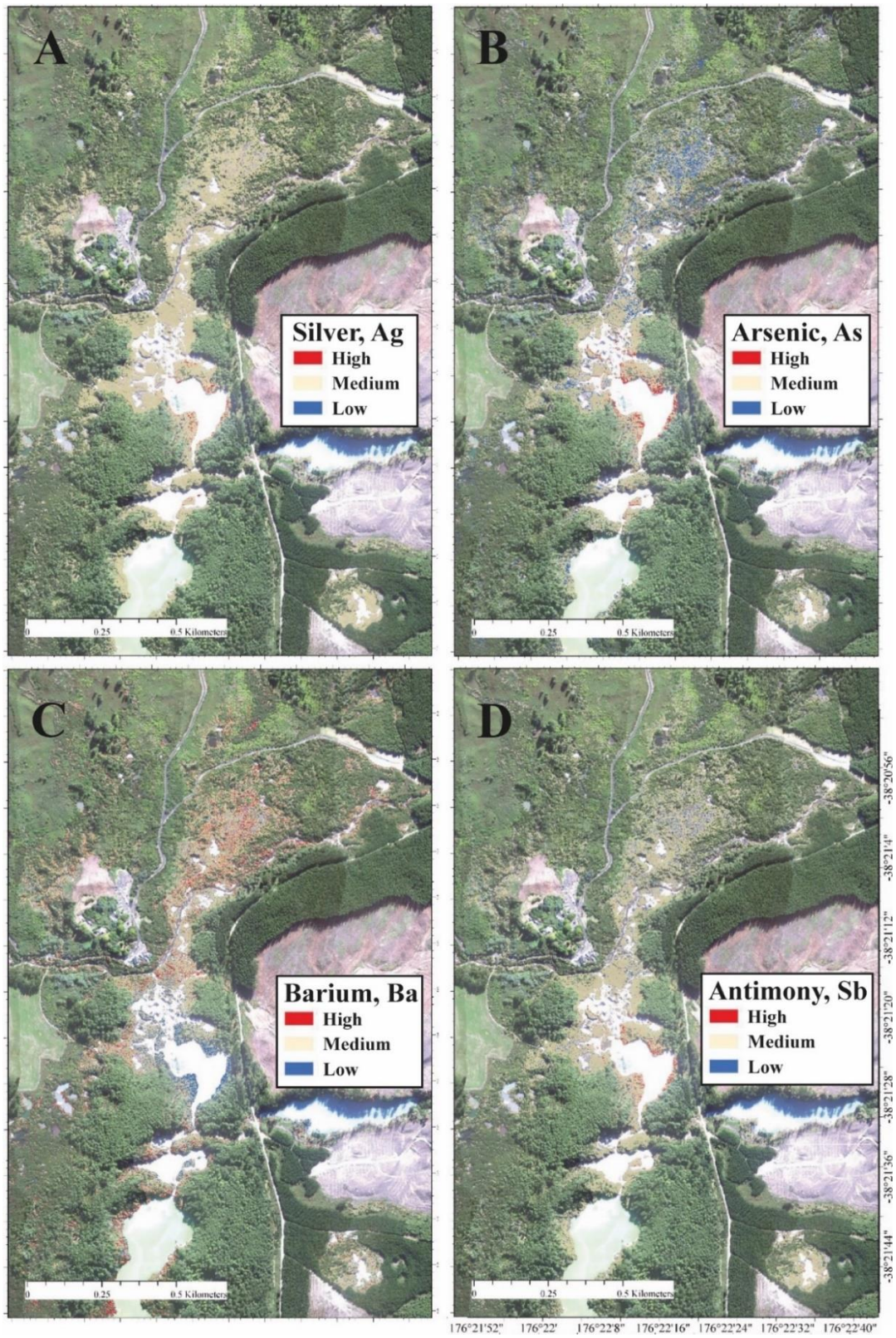

Figure A7.6. Chemical concentration predictions with one standard deviation for airborne-based dataset. A) Silver, B) Arsenic, C) Barium and D) Antimony. Hyperspectral (VNIR/SWIR) image acquired with AisaFENIX used as background.

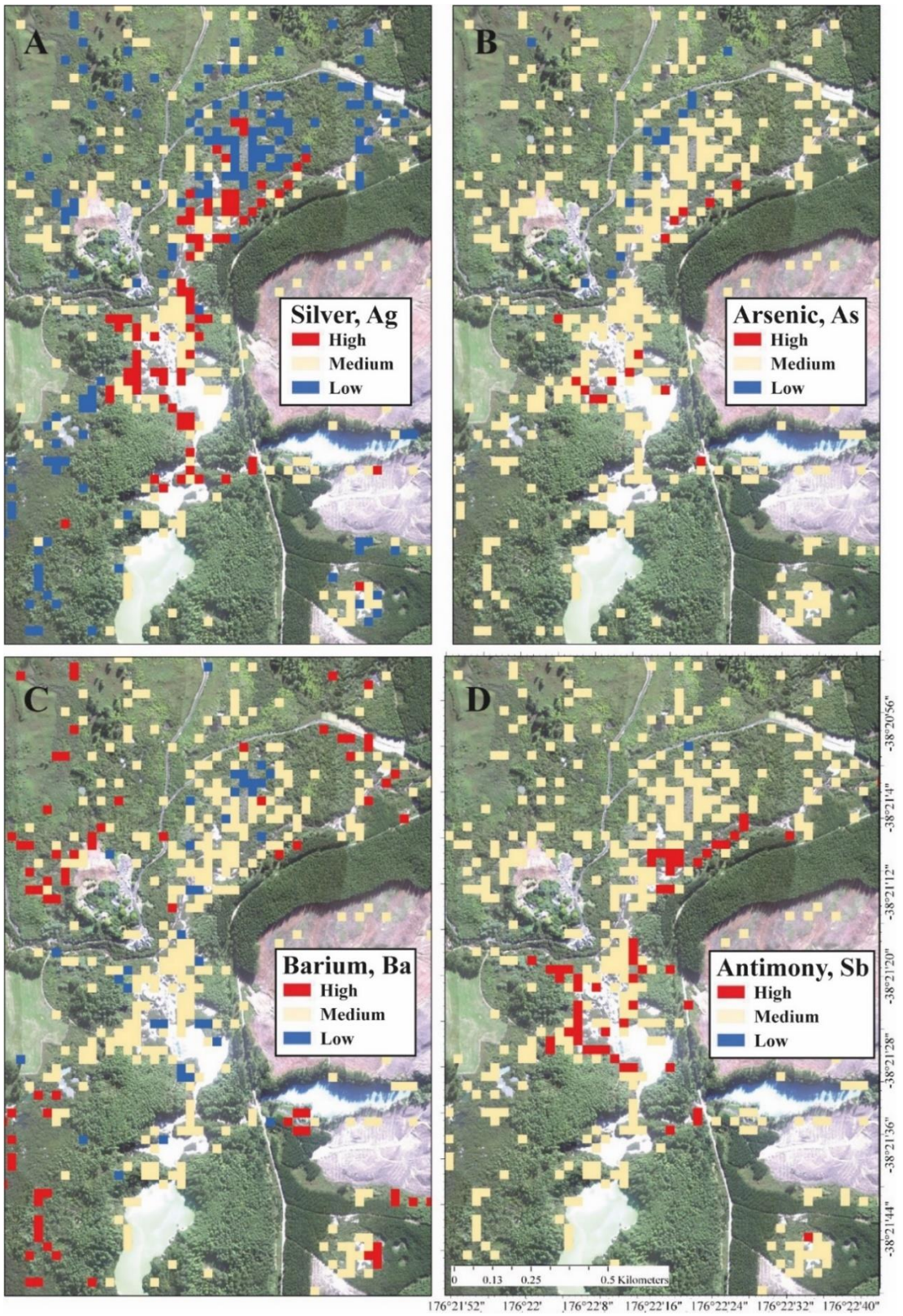

Figure A7.7. Chemical concentration predictions with one standard deviation for satellite-based dataset. A) Silver, B) Arsenic, C) Barium and D) Antimony. Hyperspectral (VNIR/SWIR) image acquired with AisaFENIX used as background.

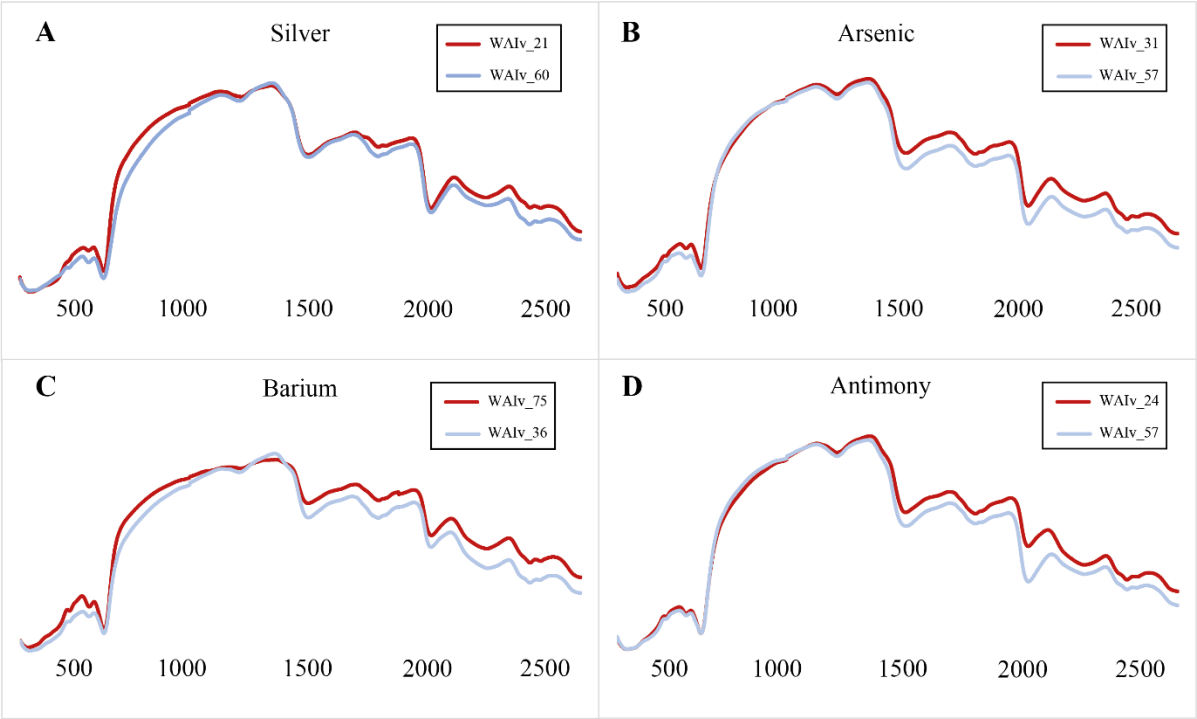

Figure A7.8. Spectral signatures from laboratory hyperspectral (VNIR/SWIR) ASD equipment from kanuka plant samples WAIv_XX (number of sample). Red coloured lines correspond to the sample with the highest concentration per element, blue coloured lines correspond to the spectral signature of the sample with the lowest concentration for each element. Differences are already visible with the naked eye.

Table A7.4. Regression model accuracy results after LOOCV. Models for laboratory, airborne and satellite-based data, maps for airborne and satellite-based imagery.

Element	***Silver, Ag***			***Arsenic, As***			***Barium, Ba***			***Antimony, Sb***		
Measure	RMSE	R^2	MAE	RMSE	R^2	MAE	RMSE	R^2	MAE	RMSE	R^2	MAE
Laboratory-based	0.46	0.26	0.33	0.52	0.12	0.42	0.32	0.08	0.25	0.53	0.02	0.4
Airborne-based	0.45	0.22	0.36	0.48	0.17	0.38	0.31	0.22	0.25	0.49	0.23	0.39
Satellite-based	0.49	0.16	0.38	0.50	0.16	0.41	0.29	0.29	0.23	0.53	0.14	0.41

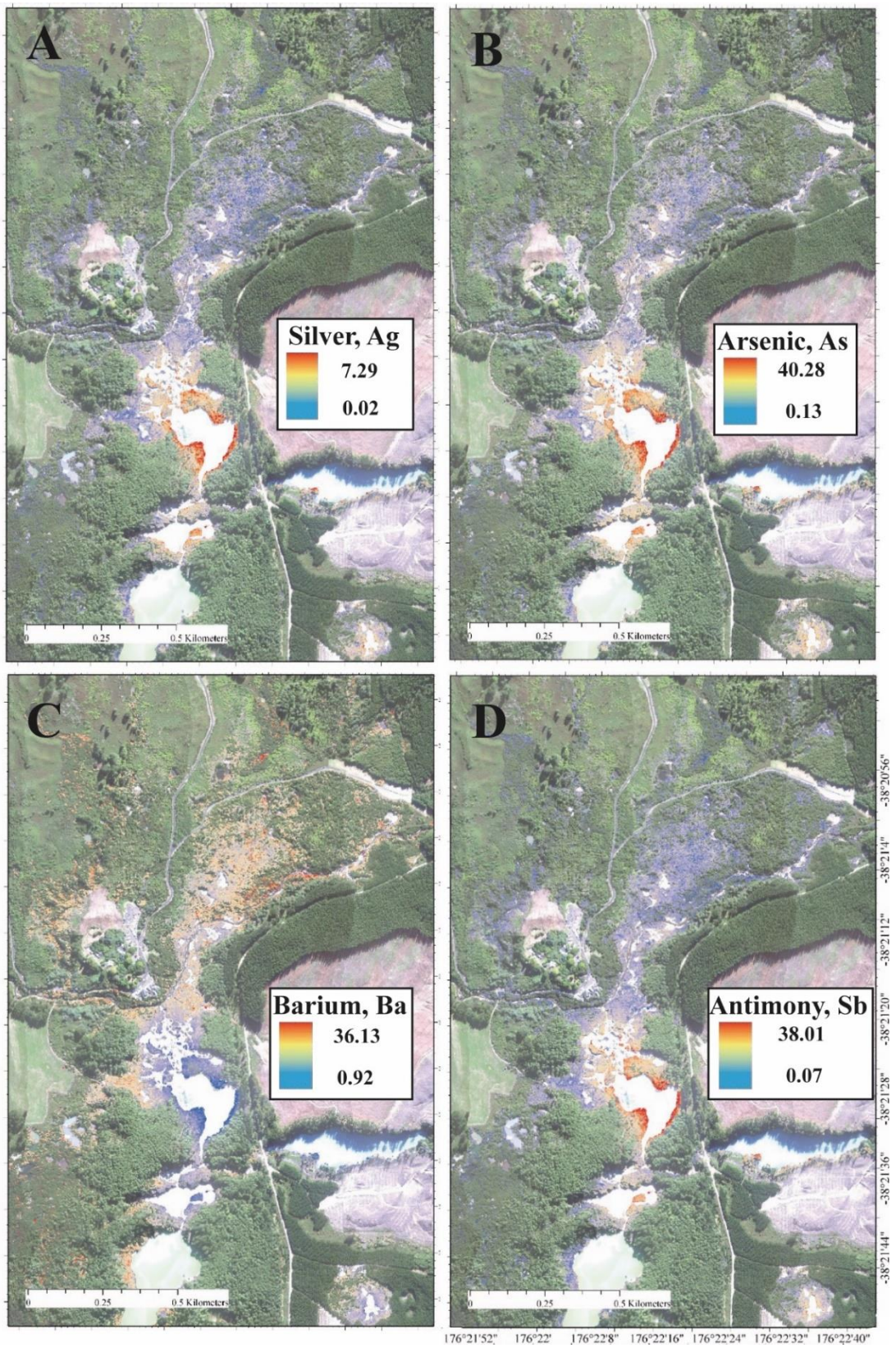

Figure 7.9. KPLS regression models applied to predict approximate [mg/kg] values across the whole airborne-based image of Waiotapu Geothermal Field. (A) Silver, (B) Arsenic, (C) Barium, (D) Antimony.

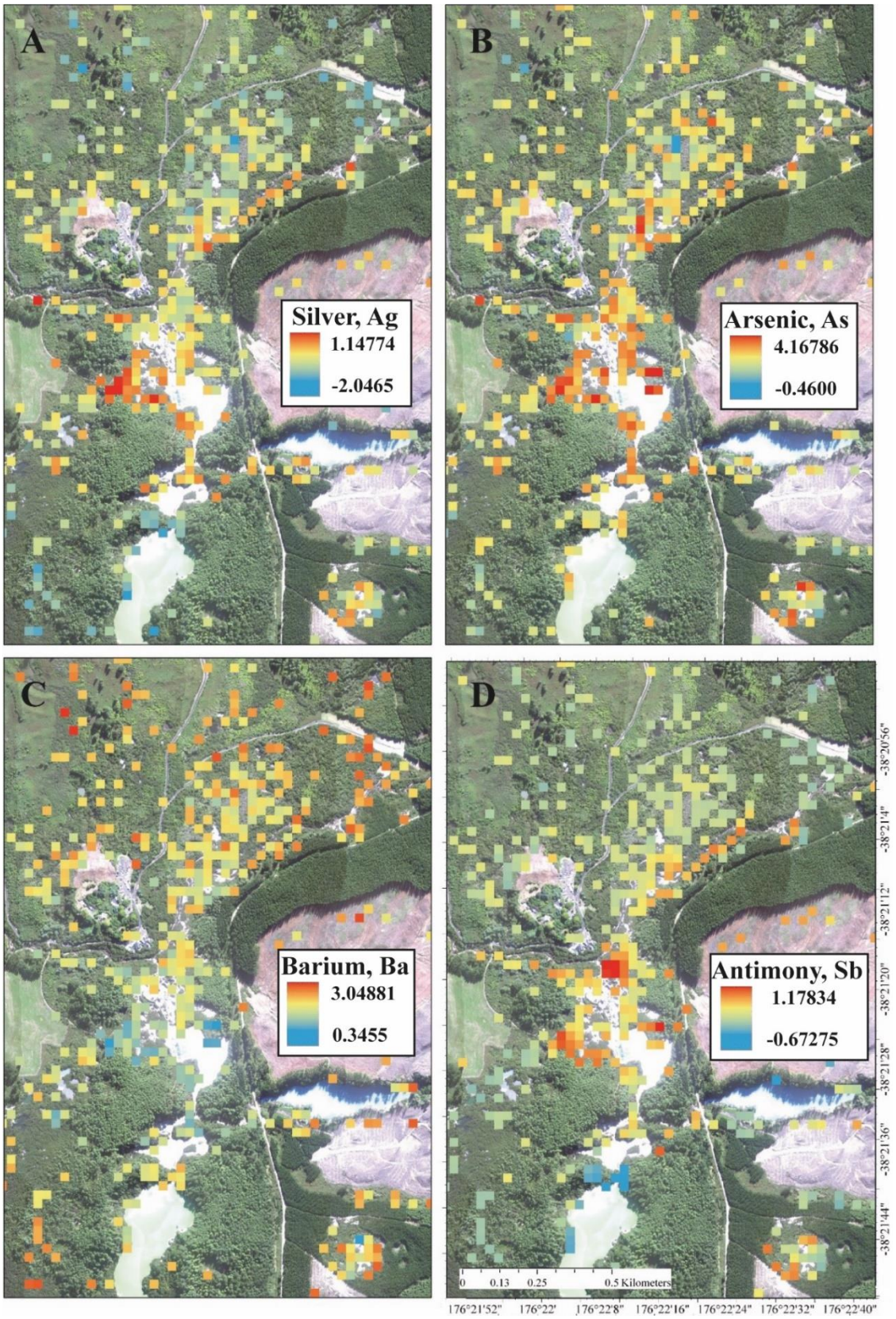

Figure A7.10. KPLS regression models applied to predict approximate [mg/kg] values across the satellite-based image of Waiotapu Geothermal Field. (A) Silver, (B) Arsenic, (C) Barium, (D) Antimony.

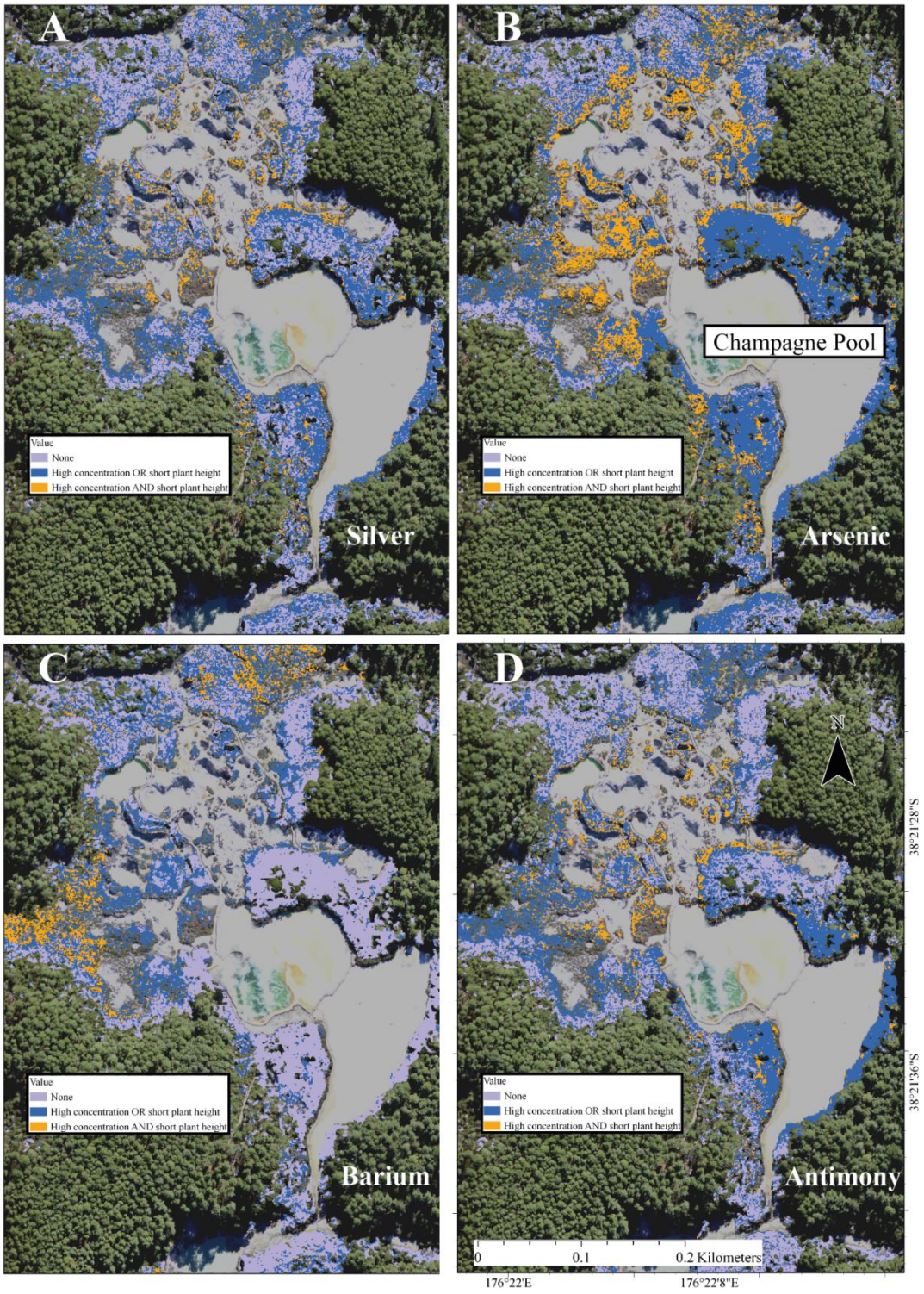

Figure A7.11. Spatial comparison between elemental distribution maps and LiDAR-derived plant height. Both images were converted into Boolean (1-0) images. For the elemental distribution maps: high concentrations were represented with values of 1, medium and low as zeroes. For plant heights, "short" plants, below 1 m are represented with 1, the rest with zero. These two were added up so we have three categories, high concentrations along with "short" plants (value=2), high concentrations OR "short" plant heights (value=1) or none (value=0). A) Silver, B) Arsenic, C) Barium and D) Antimony.

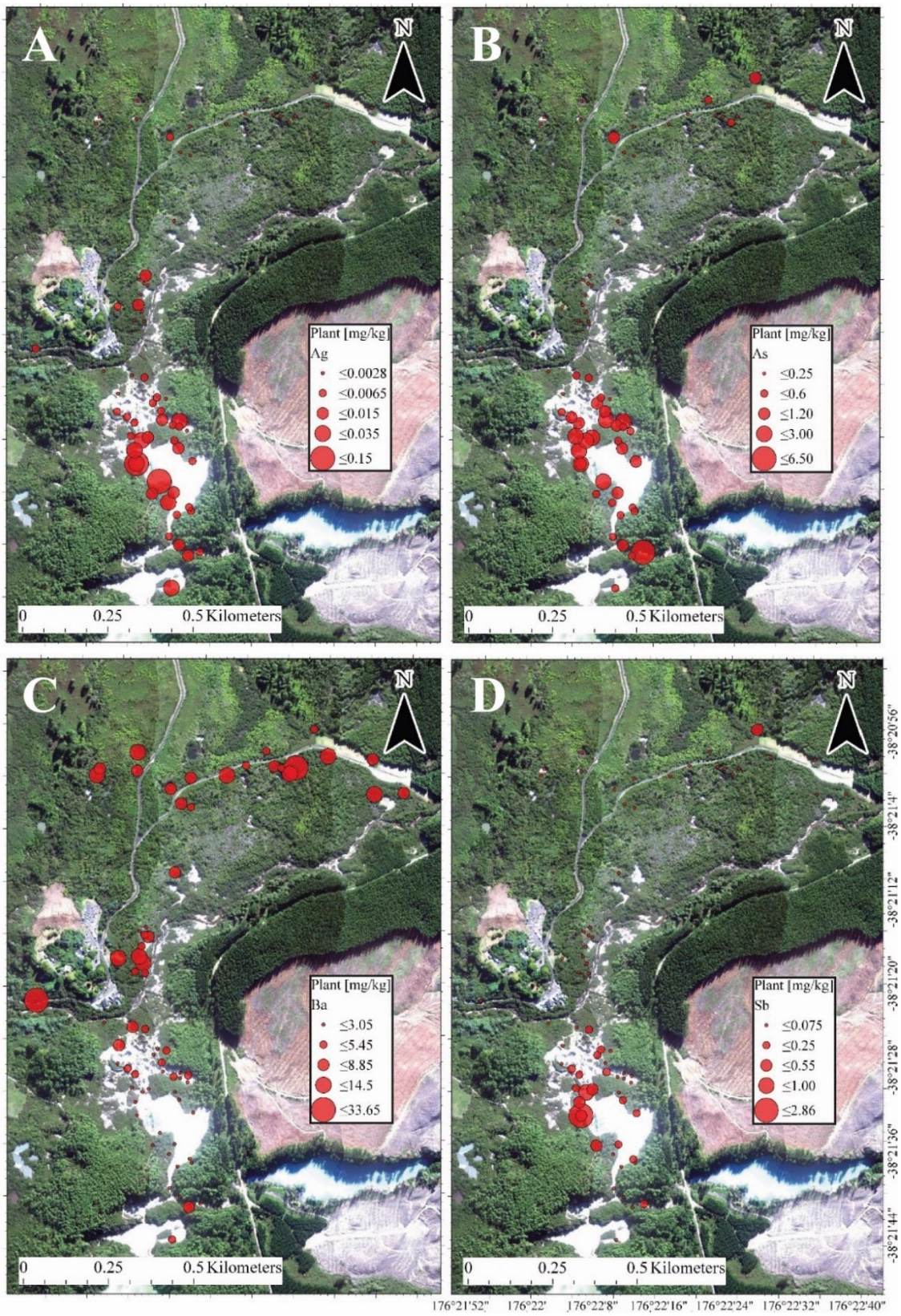

Figure A7.12. Foliar chemical concentration (mg/kg) spatial distribution on Waiotapu Geothermal Field from field samples. A) Silver, B) Arsenic, C) Barium and D) Antimony.

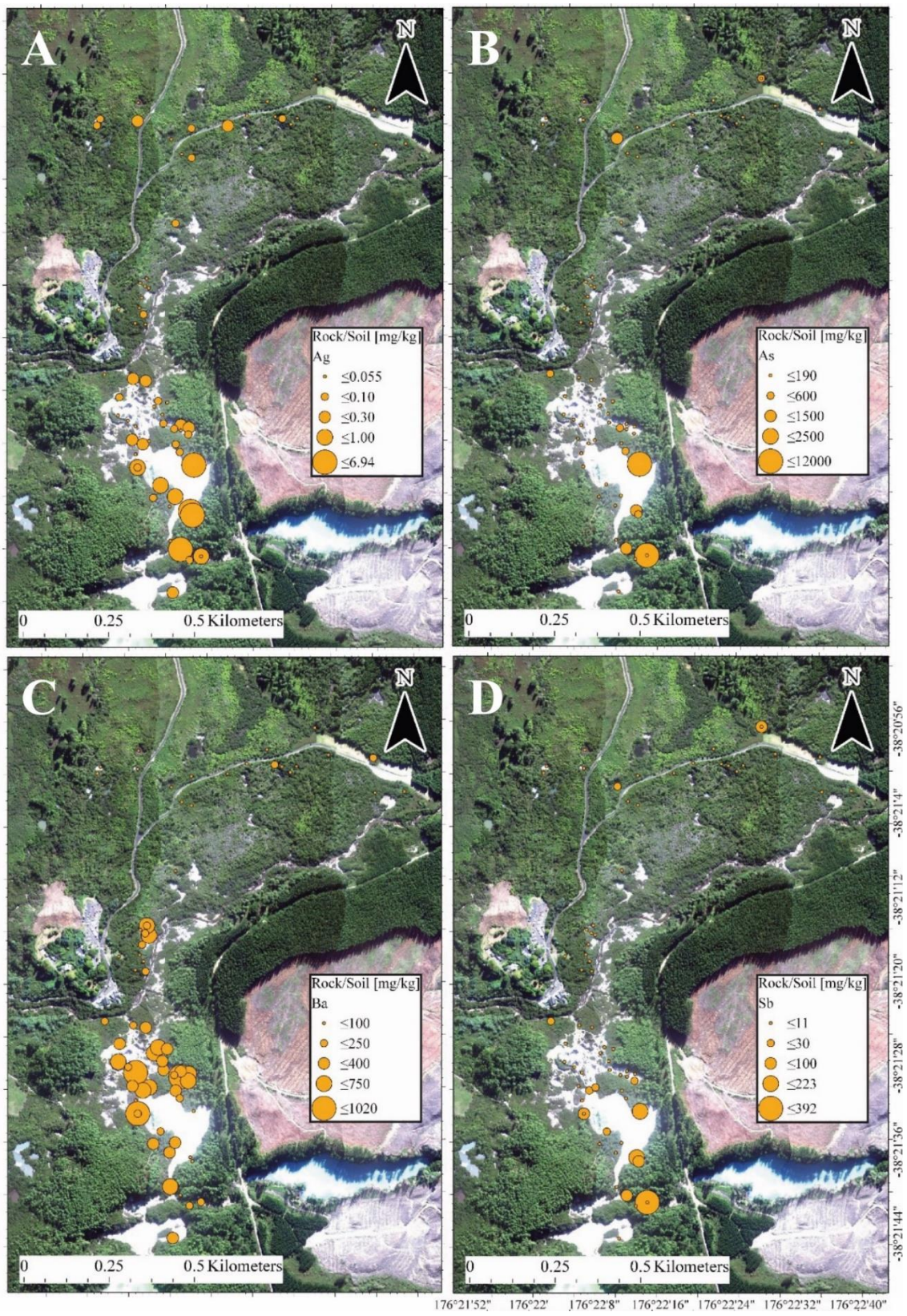

Figure A7.13. Rock/soil chemical concentration (mg/kg) spatial distribution on Waiotapu Geothermal Field from field samples. A) Silver, B) Arsenic, C) Barium and D) Antimony.

Table A2.5. Important wavelengths for laboratory, airborne and spaceborne models (units in nm).

Laboratory-Based				Airborne-Based				Spaceborne-Based			
Silver	Arsenic	Barium	Antimony	Silver	Arsenic	Barium	Antimony	Silver	Arsenic	Barium	Antimony
350	355	350	384	384.44	377.73	381.09	384.44	411.3164	411.3164	434.3084	426.9674
351	357	360	388	387.8	384.44	384.44	411.35	426.9674	419.3725	463.731	456.3773
352	366	366	399	394.52	391.16	387.8	418.09	449.0336	426.9674	470.9489	470.9489
354	371	369	402	401.25	394.52	394.52	421.46	463.731	500.1372	485.4096	500.1372
357	372	374	403	404.61	397.88	401.25	424.84	470.9489	650.7905	492.6999	530.6671
360	374	375	405	407.98	401.25	404.61	428.21	507.6631	660.2636	515.1758	538.4871
366	375	377	407	411.35	404.61	407.98	431.59	515.1758	669.8167	530.6671	554.5646
375	380	385	412	414.72	411.35	414.72	438.35	522.9162	679.4728	538.4871	562.7366
384	383	386	413	418.09	414.72	418.09	441.73	530.6671	719.1722	546.48	587.8235
389	386	388	416	421.46	418.09	421.46	451.88	562.7366	729.2445	587.8235	605.3912
394	390	391	419	424.84	421.46	424.84	458.66	669.8167	812.5399	679.4728	614.1723
417	391	394	422	428.21	424.84	428.21	465.44	719.1722	823.1458	708.9966	641.3333
418	397	398	424	448.5	431.59	431.59	475.62	760.0969	929.3855	719.1722	650.7905
423	403	399	428	451.88	434.97	434.97	482.41	770.5285	1360.8427	729.2445	689.4208
428	409	401	429	455.27	438.35	438.35	485.81	780.9124	1383.0083	887.2659	699.0959
430	410	412	430	462.05	441.73	441.73	489.21	801.9366	1394.5247	1349.599	719.1722
436	411	413	432	465.44	445.11	445.11	492.61	812.5399	1405.3883	1383.0083	739.4175
438	412	415	433	468.83	448.5	448.5	496.01	833.7513	1831.7412	1405.3883	749.7307
443	413	416	434	472.22	451.88	451.88	499.41	844.4271	1850.2787	1416.3103	780.9124
452	415	417	436	479.01	455.27	455.27	502.82	887.2659	1931.9916	1878.4633	791.3616
455	416	418	437	485.81	458.66	458.66	509.63	908.644	1949.639	1886.8109	801.9366
457	417	419	438	496.01	462.05	462.05	519.85	1383.0083	2483.5906	1914.0479	855.1821
460	422	421	440	499.41	465.44	468.83	526.67	2414.1565	2490.0281	1923.0891	908.644
462	423	423	441	509.63	468.83	472.22	533.5				
466	424	424	444	513.04	472.22	475.62	536.91				
471	425	425	445	516.44	475.62	479.01	547.16				
472	426	426	446	523.26	479.01	482.41	560.84				
475	436	428	447	533.5	482.41	485.81	588.23				
479	444	429	449	540.33	485.81	489.21	595.09				
482	449	430	450	550.58	489.21	492.61	598.51				
491	452	433	451	557.42	492.61	496.01	601.94				
492	453	434	452	564.26	496.01	499.41	605.37				
494	462	435	455	567.68	499.41	502.82	608.8				
495	464	436	456	571.1	502.82	506.22	612.24				
506	471	437	458	577.95	506.22	509.63	622.53				
507	478	438	459	581.38	540.33	513.04	625.97				
509	488	439	463	591.66	547.16	526.67	629.4				

514	498	440	465	598.51	646.58	533.5	636.27				
517	513	441	472	608.8	660.33	536.91	653.46				
594	515	442	486	650.02	670.65	543.75	656.89				
606	560	443	529	653.46	674.09	547.16	660.33				
608	580	444	582	656.89	680.97	550.58	667.21				
609	593	445	591	670.65	684.41	560.84	670.65				
610	608	446	598	674.09	698.18	564.26	674.09				
611	612	448	602	677.53	1663.54	577.95	680.97				
612	634	449	619	680.97	2008.59	595.09	1405.96				
615	642	450	621	684.41	2014.13	629.4	1568.49				
616	644	451	627	691.29	2025.21	646.58	1607.65				
627	664	454	631	698.18	2257.08	660.33	1635.6				
632	665	456	642	701.62	2284.58	663.77	1674.72				
633	666	459	647	1669.13	2290.07	667.21	1680.3				
634	685	460	650	2003.04	2344.98	674.09	1691.47				
635	693	461	651	2008.59	2383.35	677.53	1697.05				
639	695	462	652	2014.13	2394.3	687.85	1713.8				
640	702	463	654	2025.21	2399.78	1248.67	1719.38				
641	707	465	656	2086.09	2405.25	1265.54	1736.11				
642	713	467	657	2301.06	2410.73	1271.16	1769.57				
643	720	470	659	2394.3	2438.08	1276.78	1780.72				
644	723	472	662	2416.2	2443.54	1282.4	1786.29				
646	726	473	663	2459.94	2449.01	1288.02	1803				
647	727	475	664	2465.4	2454.47	2019.67	2157.9				
648	729	476	666	2476.32	2459.94	2091.62	2179.97				
650	731	478	667	2481.78	2465.4	2454.47	2202.02				
651	734	479	668	2487.24	2470.86	2459.94	2235.07				
652	735	480	671	2492.7	2476.32	2481.78	2268.08				
656	736	484	673	2498.15	2498.15	2487.24	2323.03				
658	743	485	674								
660	746	488	676								
661	747	490	677								
664	750	492	678								
665	755	494	679								
671	760	496	681								
676	761	497	682								
680	764	500	683								
682	765	501	684								
683	767	503	685								
684	768	505	686								
685	769	509	687								

686	770	533	688								
687	772	607	689								
689	774	611	690								
690	775	653	691								
691	776	654	694								
692	777	655	700								
694	778	670	701								
695	782	675	705								
697	792	677	709								
698	825	678	780								
699	828	679	788								
700	839	684	1098								
701	842	689	1335								
702	843	690	1354								
703	845	699	1900								
704	854	702	1904								
706	869	707	1927								
707	874	748	1940								
708	876	776	1941								
709	879	788	1942								
710	885	793	1947								
711	886	796	1953								
712	887	804	1954								
715	888	808	1961								
716	889	809	1964								
721	890	810	1967								
737	893	813	1968								
747	894	814	1973								
754	896	818	1974								
771	902	819	1975								
772	903	820	1977								
779	908	821	1978								
788	910	824	1979								
794	915	825	1981								
809	920	826	1982								
823	922	828	1985								
827	926	829	1989								
829	927	830	1993								
849	929	832	2005								
856	930	843	2007								
861	962	845	2008								

864	969	846	2009								
885	970	879	2011								
936	973	890	2012								
947	1006	891	2013								
953	1092	919	2014								
1125	1126	971	2016								
1133	1177	973	2017								
1140	1265	1165	2018								
1174	1283	1169	2019								
1179	1299	1170	2020								
1180	1308	1174	2021								
1182	1309	1177	2022								
1184	1310	1182	2023								
1187	1347	1183	2026								
1188	1355	1186	2027								
1190	1373	1189	2028								
1194	1389	1200	2030								
1195	1396	1206	2033								
1203	1402	1212	2036								
1281	1405	1258	2043								
1310	1419	1319	2045								
1344	1542	1916	2426								
1345	1885	1942	2446								
1359	1893	1946	2450								
1369	1916	1957	2457								
1402	1933	1958	2459								
1408	1935	2016	2465								
1896	1984	2025	2469								
1928	2014	2028	2475								
1947	2290	2471	2478								

7.3 Appendix 3 (A3)

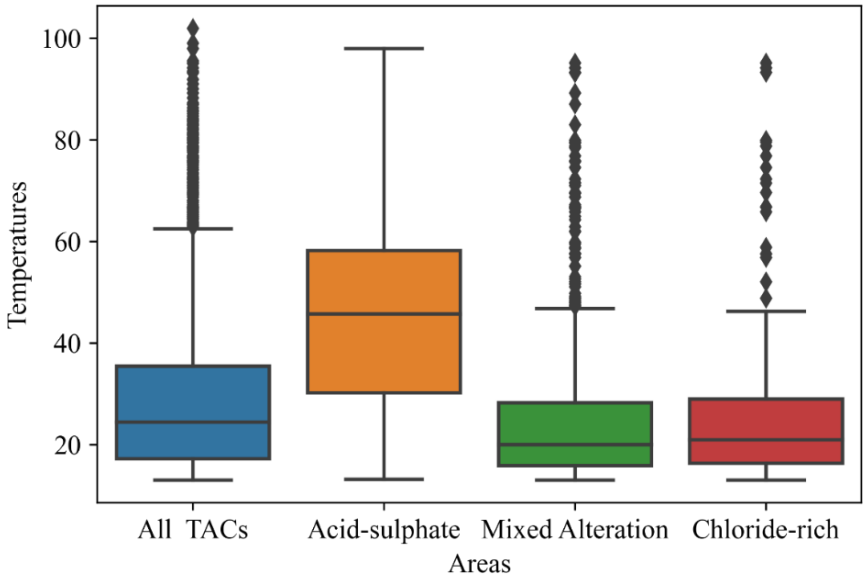

Figure A3.1. Boxplots representing the temperature ranges for Areas 1, 2, 3 and 4 (i.e all TAC and medium areas).

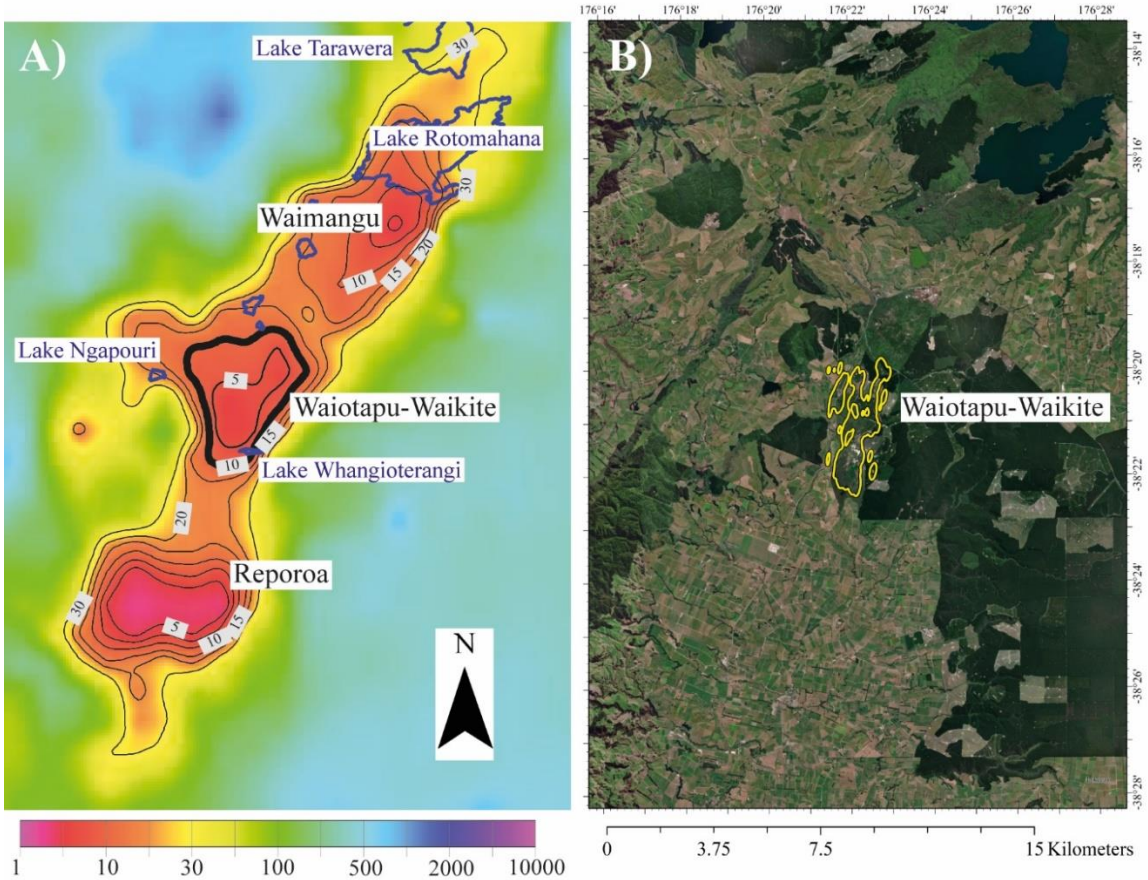

Figure A3.2. A) Resistivity boundary map delineated with a Schlumberger array AB/500 by (Bibby et al., 1994). 10

Table A3.1. Randomness test results for all areas with the boundary shapes on the right. Red for buffered convex hull, green for isocontour KDE (SAMSE) and pink for isocontour KDE (LSCV).

Area ID	Boundary	Randomness Test	Results	Shape
1	Buffered convex hull	Clark-Evans	0.26	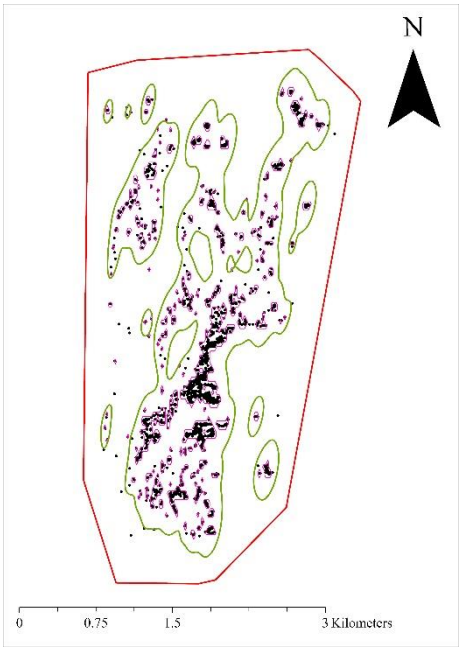
		Hopkins Skellman	0.011	
		Ripley's K	clustered	
	KDE (SAMSE)	Clark-Evans	0.18	
		Hopkins Skellman	0.004	
		Ripley's K	clustered	
	KDE (LSCV)	Clark-Evans	0.14	
		Hopkins Skellman	0.0014	
		Ripley's K	clustered	
2	Buffered convex hull	Clark-Evans	0.30	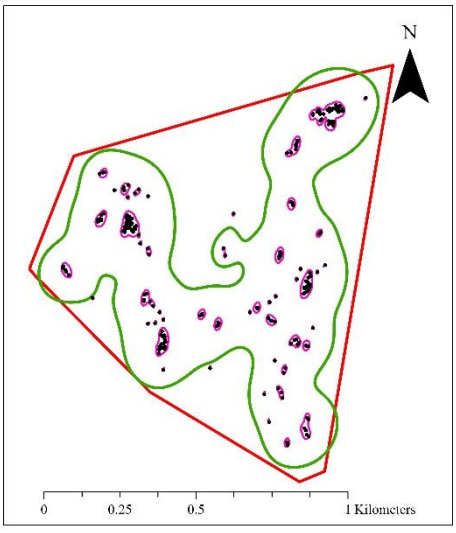
		Hopkins Skellman	0.058	
		Ripley's K	Separation	
	KDE (SAMSE)	Clark-Evans	0.215	
		Hopkins Skellman	0.018	
		Ripley's K	Clustering	
	KDE (LSCV)	Clark-Evans	0.45	
		Hopkins Skellman	0.59	
		Ripley's K	Separation	

3	Buffered convex hull	Clark-Evans	0.413	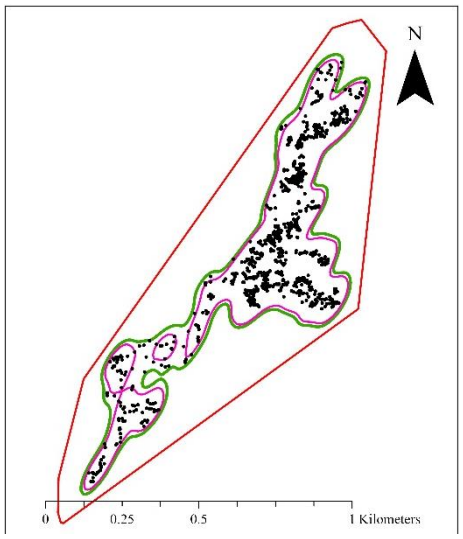
		Hopkins Skellman	0.014	
		Ripley's K	Clustering	
	KDE (SAMSE)	Clark-Evans	0.213	
		Hopkins Skellman	0.0006	
		Ripley's K	Clustering	
	KDE (LSCV)	Clark-Evans	0.164	
		Hopkins Skellman	0.00046	
		Ripley's K	Clustering	
4	Buffered convex hull	Clark-Evans	0.38	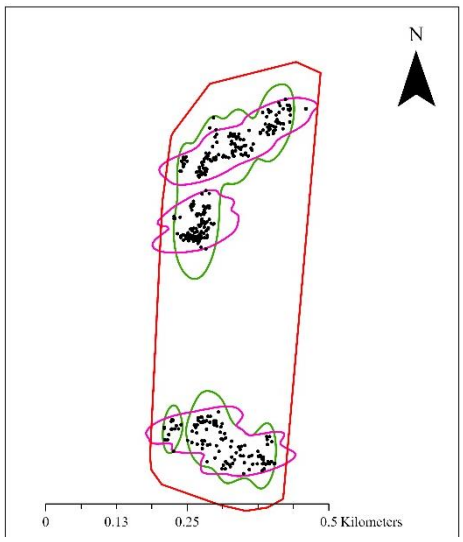
		Hopkins Skellman	0.0047	
		Ripley's K	Clustering	
	KDE (SAMSE)	Clark-Evans	0.31	
		Hopkins Skellman	0.005	
		Ripley's K	Clustering	
	KDE (LSCV)	Clark-Evans	0.368	
		Hopkins Skellman	0.0108	
		Ripley's K	Clustering	
5	Buffered convex hull	Clark-Evans	0.57	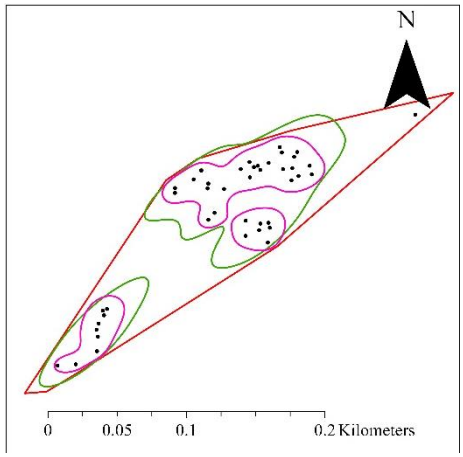
		Hopkins Skellman	0.393	
		Ripley's K	Clustering	
	KDE (SAMSE)	Clark-Evans	0.295	
		Hopkins Skellman	0.1006	
		Ripley's K	Clustering	
	KDE (LSCV)	Clark-Evans	0.453	
		Hopkins Skellman	0.362	
		Ripley's K	Clustering	

6	Buffered convex hull	Clark-Evans	0.56	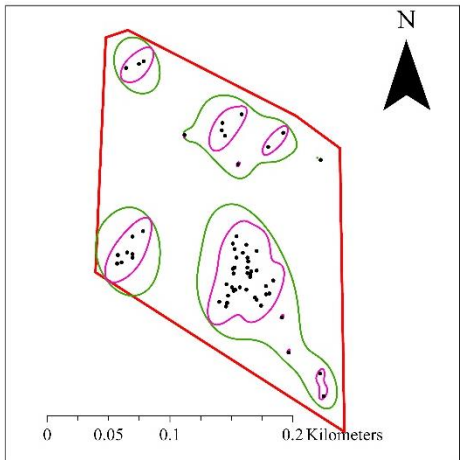
		Hopkins Skellman	0.16	
		Ripley's K	Clustering	
	KDE (SAMSE)	Clark-Evans	0.416	
		Hopkins Skellman	0.088	
		Ripley's K	Clustering	
	KDE (LSCV)	Clark-Evans	0.487	
		Hopkins Skellman	0.1995	
		Ripley's K	Clustering	
7	Buffered convex hull	Clark-Evans	0.582	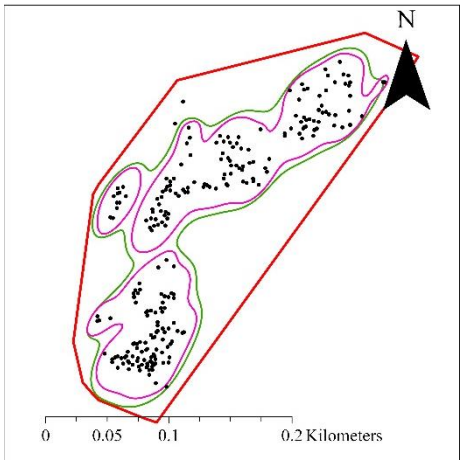
		Hopkins Skellman	0.051	
		Ripley's K	Clustering	
	KDE (SAMSE)	Clark-Evans	0.669	
		Hopkins Skellman	0.060	
		Ripley's K	Clustering	
	KDE (LSCV)	Clark-Evans	0.5798	
		Hopkins Skellman	0.0956	
		Ripley's K	Clustering	
8	Buffered convex hull	Clark-Evans	0.5	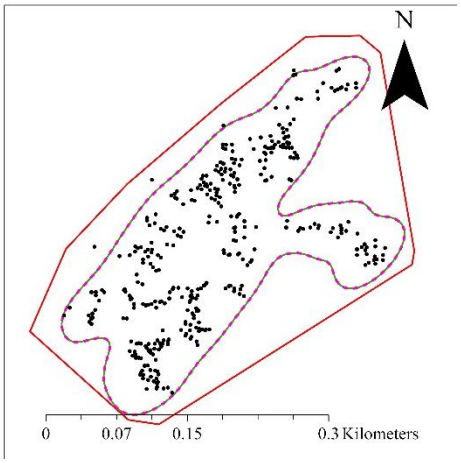
		Hopkins Skellman	0.04	
		Ripley's K	Clustering	
	KDE (SAMSE)	Clark-Evans	0.3523	
		Hopkins Skellman	0.011	
		Ripley's K	Clustering	
	KDE (LSCV)	Clark-Evans	0.552	
		Hopkins Skellman	0.158	
		Ripley's K	Clustering	

9	Buffered convex hull	Clark-Evans	0.57	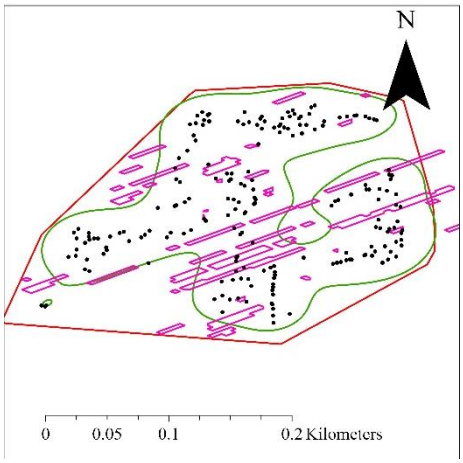
		Hopkins Skellman	0.096	
		Ripley's K		
	KDE (SAMSE)	Clark-Evans	0.392	
		Hopkins Skellman	0.021	
		Ripley's K	Clustering	
	KDE (LSCV)	Clark-Evans	0.73	
		Hopkins Skellman	0.105	
		Ripley's K	Clustering	
10	Buffered convex hull	Clark-Evans	0.49	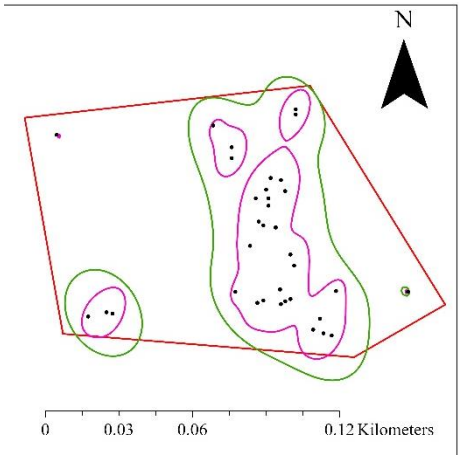
		Hopkins Skellman	0.4	
		Ripley's K		
	KDE (SAMSE)	Clark-Evans	0.327	
		Hopkins Skellman	0.21	
		Ripley's K	Clustering	
	KDE (LSCV)	Clark-Evans	0.39	
		Hopkins Skellman	0.64	
		Ripley's K	Clustering	

8 References

Abdi, H. (2003). Partial least-squares regression. In *The SAGE encyclopedia of social science research methods*.

Abedi, T., & Mojiri, A. (2020). Cadmium Uptake by Wheat (Triticum aestivum L.): An Overview. *Plants*, *9*(4), 500. https://doi.org/10.3390/plants9040500

Abera, M. G. (2018). *Characterization of Rock Samples Using SWIR-LWIR Hyperspectral Imaging Techniques—An Example of The High Sulfidation Epithermal System of Rodalquilar, Southeast Spain*.

Abubakar, A. J., Hashim, M., & Pour, A. B. (2019). Remote sensing satellite imagery for prospecting geothermal systems in an aseismic geologic setting: Yankari Park, Nigeria. *International Journal of Applied Earth Observation and Geoinformation*, *80*(April), 157–172. https://doi.org/10.1016/j.jag.2019.04.005

Abubakar, A. J., Hashim, M., Pour, A. B., & Shehu, K. (2017). A review of geothermal mapping techniques using remotely sensed data. *Science World Journal*, *12*(4), 72–82.

Abuzied, S. M., Kaiser, M. F., Shendi, E. A. H., & Abdel-Fattah, M. I. (2020). Multi-criteria decision support for geothermal resources exploration based on remote sensing, GIS and geophysical techniques along the Gulf of Suez coastal area, Egypt. *Geothermics*, *88*(May), 101893. https://doi.org/10.1016/j.geothermics.2020.101893

Achmad, R., & Salam, R. (2022). Geothermal Potential in a Small Volcanic Island. *IOP Conference Series: Earth and Environmental Science*, *1031*(1), 012028. https://doi.org/10.1088/1755-1315/1031/1/012028

Acquarelli, J., Marchiori, E., Buydens, L., Tran, T., & Laarhoven, T. (2018). Spectral-Spatial Classification of Hyperspectral Images: Three Tricks and a New Learning Setting. *Remote Sensing*, *10*(7), 1156. https://doi.org/10.3390/rs10071156

Adler-Golden, S. M., Matthew, M. W., Bernstein, R. Y., Levine, A., Berk, A., Richtsmeier, S. C., Acharya, P. K., Anderson, G. P., Felde, G., Gardner, J., Hoke, M., Jeong, L. S., Pukall, B., Mello, J., Ratkowski, A., & Burke, H. H. (1999). Atmospheric Correction for Short-wave Spectral Imagery Based on MODTRAN4. *SPIE Proceedings on Imaging Spectrometry V*, 3753:61-69.

Aguilera, F., Layana, S., Rodríguez-Díaz, A., González, C., Cortés, J., & Inostroza, M. (2016). Hydrothermal alteration, fumarolic deposits and fluids from Lastarria Volcanic Complex: A multidisciplinary study. *Andean Geology*, *43*(2), 166–196. https://doi.org/10.5027/andgeoV43n2-a02

Ahmed, A. A., Assadi, M., Kalantar, A., Sliwa, T., & Sapińska-Śliwa, A. (2022). A Critical Review on the Use of Shallow Geothermal Energy Systems for Heating and Cooling Purposes. *Energies*, *15*(12), 4281. https://doi.org/10.3390/en15124281

Aitchison, J. (1986). *The Statistical Analysis of Compositional Data*. Chapman and Hall Ltd.

Aitchison, J. (2008). The single principle of compositional data analysis, continuing fallacies, confusions and misunderstandings and some suggested remedies. *CoDaWork 2008*, 1–28.

Allis, R. G. (1979). *Heat Flow And Temperature Investigations In Thermal Ground.*

Allis, R. G. (1981). Changes in heat flow associated with exploitation of Wairakei geothermal field, New Zealand. *New Zealand Journal of Geology and Geophysics*, *24*(1), 1–19. https://doi.org/10.1080/00288306.1981.10422694

Almeida, D. R. A. de, Broadbent, E. N., Ferreira, M. P., Meli, P., Zambrano, A. M. A., Gorgens, E. B., Resende, A. F., de Almeida, C. T., do Amaral, C. H., Corte, A. P. D., Silva, C. A., Romanelli, J. P., Prata, G. A., de Almeida Papa, D., Stark, S. C., Valbuena, R., Nelson, B. W., Guillemot, J., Féret, J. B., … Brancalion, P. H. S. (2021). Monitoring restored tropical forest diversity and structure through UAV-borne hyperspectral and lidar fusion. *Remote Sensing of Environment*, *264*(July). https://doi.org/10.1016/j.rse.2021.112582

An, C., Park, Y. W., Ahn, S. S., Han, K., Kim, H., & Lee, S.-K. (2021). Radiomics machine learning study with a small sample size: Single random training-test set split may lead to unreliable results. *PLOS ONE, 16*(8), e0256152. https://doi.org/10.1371/journal.pone.0256152

Annam, S., & Singla, A. (2021). Spectral unmixing of heavy metal content in agricultural soil using hyperspectral remote sensing data. *2021 Sixth International Conference on Image Information Processing (ICIIP)*, 433–438. https://doi.org/10.1109/ICIIP53038.2021.9702646

Asadzadeh, S., & de Souza Filho, C. R. (2016). A review on spectral processing methods for geological remote sensing. *International Journal of Applied Earth Observation and Geoinformation*, *47*, 69–90. https://doi.org/10.1016/j.jag.2015.12.004

Aslett, Z., Taranik, J. V., & Riley, D. N. (2018). Mapping rock forming minerals at Boundary Canyon, Death Valey National Park, California, using aerial SEBASS thermal infrared hyperspectral image data. *International Journal of Applied Earth Observation and Geoinformation*, *64*(July 2017), 326–339. https://doi.org/10.1016/j.jag.2017.08.001

Baddeley, A., Rubak, E., & Turner, R. (2015). *Spatial Point Patterns: Methodology and Applications with R*.

Bakker, W. H., Feringa, W., Gieske, A. S. M., Gorte, B. G. H., Grabmaier, K. A., Hecker, C. A., Horn, J. A., Huurneman, G. C., Janssen, L. L. F., Kerle, N., Meer, F. D. V. D., Parodi, G. N., Pohl, C., Reeves, C. V., Ruitenbeek, F. J. V., Schetselaar, E. M., Tempfli, K., Weir, M. J. C., Westinga, E., & Woldai, T. (2009). *Principles of Remote Sensing*. ITC Educational Textbook Series.

Ballantyne, J. M., & Moore, J. N. (1988). Arsenic geochemistry in geothermal systems. *Geochimica et Cosmochimica Acta*, *52*(2), 475–483. https://doi.org/10.1016/0016-7037(88)90102-0

Bannister, S. C., Bourguignon, S., Sherbum, S., & Bertrand, E. A. (2013). Seismic imaging of the central Taupo Volcanic Zone using double-difference tomography. *Proceedings of the 35th New Zealand Geothermal Workshop*.

Barbier, E. (2002). Geothermal energy technology and current status: An overview. *Renewable and Sustainable Energy Reviews*, *6*(1–2), 3–65. https://doi.org/10.1016/S1364-0321(02)00002-3

Barker, S. J., Wilson, C. J. N., Illsley-Kemp, F., Leonard, G. S., Mestel, E. R. H., Mauriohooho, K., & Charlier, B. L. A. (2020). Taupō: An overview of New Zealand's youngest supervolcano. *New Zealand Journal of Geology and Geophysics*. https://doi.org/10.1080/00288306.2020.1792515

Basantaray, A. K., & Mandal, A. (2022). Interpretation of gravity–magnetic anomalies to delineate subsurface configuration beneath east geothermal province along the Mahanadi rift basin: A case study of non-volcanic hot springs. *Geothermal Energy*, *10*(1), 6. https://doi.org/10.1186/s40517-022-00216-4

Bateson, L., Vellico, M., Beaubien, S. E., Pearce, J. M., Annunziatellis, A., Ciotoli, G., Coren, F., Lombardi, S., & Marsh, S. (2008). The application of remote-sensing techniques to monitor CO2-storage sites for surface leakage: Method development and testing at Latera (Italy) where naturally produced CO2 is leaking to the atmosphere. *International Journal of Greenhouse Gas Control*, *2*(3), 388–400. https://doi.org/10.1016/j.ijggc.2007.12.005

Beadel, S., Shaw, W., Bawden, R., Bycroft, C., Wilcox, F., McQueen, J., & Lloyd, K. (2018). Sustainable management of geothermal vegetation in the Waikato Region, New Zealand, including application of ecological indicators and new monitoring technology trials. *Geothermics*, *73*(October 2017), 91–99. https://doi.org/10.1016/j.geothermics.2017.11.001

Beadel, S., Shaw, W., Bawden, R., Bycroft, C., Wilcox, F., McQueen, J., & Lloyd, K. (2018c). Sustainable management of geothermal vegetation in the Waikato Region, New Zealand, including application of ecological indicators and new monitoring technology trials. *Geothermics*, *73*(October 2017), 91–99. https://doi.org/10.1016/j.geothermics.2017.11.001

Bebbington, M. S. (2013). Assessing spatio-temporal eruption forecasts in a monogenetic volcanic field. *Journal of Volcanology and Geothermal Research*, *252*, 14–28. https://doi.org/10.1016/j.jvolgeores.2012.11.010

Bech, J., Poschenrieder, C., Llugany, M., Barceló, J., Tume, P., Tobias, F. J., Barranzuela, J. L., & Vásquez, E. R. (1997). Arsenic and heavy metal contamination of soil and vegetation around a copper mine in Northern Peru. *Science of The Total Environment*, *203*(1), 83–91. https://doi.org/10.1016/S0048-9697(97)00136-8

Bedell, R. L., Rivard, B., Browning, D., & Coolbaugh, M. (2017). Spectral Geology and Remote Sensing Paper 81 Thermal Infrared Sensing for Exploration and Mining-An Update on Relevant Systems for Remote Acquisition to Drill Core Scanning. *Proceedings of Exploration*, *17*, 881–897.

Bégué, F., Deering, C. D., Gravley, D. M., Chambefort, I., & Kennedy, B. M. (2017). From source to surface: Tracking magmatic boron and chlorine input into the geothermal systems of the Taupo Volcanic Zone, New Zealand. *Journal of Volcanology and Geothermal Research*, *346*, 141–150. https://doi.org/10.1016/j.jvolgeores.2017.03.008

Belgiu, M., & Drăgu, L. (2016). Random forest in remote sensing: A review of applications and future directions. *ISPRS Journal of Photogrammetry and Remote Sensing*, *114*, 24–31. https://doi.org/10.1016/j.isprsjprs.2016.01.011

Bendig, J., Bolten, a., & Bareth, G. (2012). Introducing a Low-Cost Mini-Uav for Thermal- and Multispectral-Imaging. *ISPRS - International Archives of the Photogrammetry, Remote Sensing and Spatial Information Sciences*, *XXXIX-B1*(September), 345–349. https://doi.org/10.5194/isprsarchives-XXXIX-B1-345-2012

Bennett, J. P., & Wetmore, C. M. (1999). Geothermal elements in lichens of Yellowstone National Park, USA. *Environmental and Experimental Botany*, *42*(3), 191–200. https://doi.org/10.1016/S0098-8472(99)00036-2

Ben-Said, M. (2021). Spatial point-pattern analysis as a powerful tool in identifying pattern-process relationships in plant ecology: An updated review. *Ecological Processes*, *10*(1), 56. https://doi.org/10.1186/s13717-021-00314-4

Benseman, R. F., Fisher, R. G., & Dickinson, D. J. (1963). Survey of Surface Heat Output at Waiotapu. *DSIR Bulletin*, *155*, 50–58.

Berger, G., & Velde, B. (1992). Chemical parameters controlling the propylitic and argillic alteration process. *European Journal of Mineralogy*, *4*(6), 1439–1455. https://doi.org/10.1127/ejm/4/6/1439

Berni, J. A. J., Zarco-Tejada, P. J., Suárez, L., Fereres, E., Suarez, L., & Fereres, E. (2009). Thermal and narrowband multispectral remote sensing for vegetation monitoring from an unmanned aerial vehicle. *IEEE Transactions on Geoscience and Remote Sensing*, *47*(3), 722–738. https://doi.org/10.1109/TGRS.2008.2010457

Berrar, D. (2019). Cross-Validation. In *Encyclopedia of Bioinformatics and Computational Biology* (Vols. 1–3, pp. 542–545). Elsevier. https://doi.org/10.1016/B978-0-12-809633-8.20349-X

Bertrand, E. A., Caldwell, T. G., Hill, G. J., Wallin, E. L., Bennie, S. L., Cozens, N., Onacha, S. A., Ryan, G. A., Walter, C., Zaino, A., & Wameyo, P. (2012). Magnetotelluric imaging of upper-crustal convection plumes beneath the Taupo Volcanic Zone, New Zealand. *Geophysical Research Letters*, *39*(2), n/a-n/a. https://doi.org/10.1029/2011GL050177

Bertrand, E. A., Kannberg, P., Caldwell, T. G., Heise, W., Constable, S., Scott, B., Bannister, S., Kilgour, G., Bennie, S. L., Hart, R., & Palmer, N. (2022). Inferring the magmatic roots of volcano-geothermal systems in the Rotorua Caldera and Okataina Volcanic Centre from magnetotelluric models. *Journal of Volcanology and Geothermal Research*, *431*, 107645. https://doi.org/10.1016/j.jvolgeores.2022.107645

Bhatt, J. S., & Joshi, M. V. (2020). Deep Learning in Hyperspectral Unmixing: A Review. *IGARSS 2020 - 2020 IEEE International Geoscience and Remote Sensing Symposium*, 2189–2192. https://doi.org/10.1109/IGARSS39084.2020.9324546

Bhuiyan, C., Saha, A. K., Bandyopadhyay, N., & Kogan, F. N. (2017). Analyzing the impact of thermal stress on vegetation health and agricultural drought–a case study from Gujarat, India.

GIScience and Remote Sensing, *54*(5), 678–699. https://doi.org/10.1080/15481603.2017.1309737

Bibby, H. M., Bennie, S. L., Stagpoole, V. M., & Caldwell, T. G. (1994). Resistivity Structure of the Waimangu, Waiotapu, Waikite and Reporoa Geothermal Areas, New-Zealand. *Geothermics*, *23*(5–6), 445–471. https://doi.org/10.1016/0375-6505(94)90013-2

Bibby, H. M., Caldwell, T. G., Davey, F. J., & Webb, T. H. (1995). Geophysical evidence on the structure of the Taupo Volcanic Zone and its hydrothermal circulation. *Journal of Volcanology and Geothermal Research*, *68*(1–3), 29–58. https://doi.org/10.1016/0377-0273(95)00007-H

Bibby, H. M., Caldwell, T. G., & Risk, G. F. (1998). Electrical resistivity image of the upper crust within the Taupo Volcanic Zone, New Zealand. *Journal of Geophysical Research: Solid Earth*, *103*(B5), 9665–9680. https://doi.org/10.1029/98JB00031

Bibby, H. M., Glover, R. B., & Whiteford, P. C. (1995). The Heat Output of the Waimangu, Waiotapu-Waikite and Reporoa Geothermal Systems (NZ): Do Chloride Fluxes Provide An Accurate Measure? *Geothermal Workshop*.

Bignall, G., Browne, P. R. L., & Kyle, P. R. (1996). Geochemical characterisation of hydrothermally altered ignimbrites in active geothermal fields from the central Taupo Volcanic zone, New Zealand. *Journal of Volcanology and Geothermal Research*, *73*(1–2), 79–97. https://doi.org/10.1016/0377-0273(96)00015-7

Birkle, P., Bundschuh, J., & Sracek, O. (2010). Mechanisms of arsenic enrichment in geothermal and petroleum reservoirs fluids in Mexico. *Water Research*, *44*(19), 5605–5617. https://doi.org/10.1016/j.watres.2010.05.046

Bishop, J. L., & Murad, E. (2005). The visible and infrared spectral properties of jarosite and alunite. *American Mineralogist*, *90*(7), 1100–1107. https://doi.org/10.2138/am.2005.1700

Bjornsson, G., Grimsson, G., Sigurdsson, A., & Laenen, V. S. (2019). Thermal Mapping of Icelandic Geothermal Surface Manifestations with a Drone. *Proceedings of 44th Workshop on Geothermal Reservoir Engineering*, *2018*, 1–8.

Blagus, R., & Lusa, L. (2015). Joint use of over-and under-sampling techniques and cross-validation for the development and assessment of prediction models. *BMC Bioinformatics*, *16*(1), 1–11. https://doi.org/10.1186/s12859-015-0784-9

Blanchard, G., & Krämer, N. (2010). Kernel Partial Least Squares is universally consistent. *Journal of Machine Learning Research*, *9*, 57–64.

Blasco, M., Gimeno, M. J., & Auqué, L. F. (2018). Low temperature geothermal systems in carbonate-evaporitic rocks: Mineral equilibria assumptions and geothermometrical calculations. Insights from the Arnedillo thermal waters (Spain). *Science of the Total Environment*, *615*, 526–539. https://doi.org/10.1016/j.scitotenv.2017.09.269

Bobos, I., & Williams, L. B. (2017). Boron, lithium and nitrogen isotope geochemistry of NH4-illite clays in the fossil hydrothermal system of Harghita Bãi, East Carpathians, Romania. *Chemical Geology*, *473*(September), 22–39. https://doi.org/10.1016/j.chemgeo.2017.10.005

Boothroyd, I. K. G. (2009). Ecological characteristics and management of geothermal systems of the Taupo Volcanic Zone, New Zealand. *Geothermics*, *38*(1), 200–209. https://doi.org/10.1016/j.geothermics.2008.12.010

Borengasser, M., Hungate, W. S., Watkins, R., Weng, Q., & Navulur, K. (2013). Hyperspectral Remote Sensing. In *Airborne Measurements for Environmental Research: Methods and Instruments*. https://doi.org/10.1002/9783527653218.ch8

Borovička, J., Řanda, Z., & Jelínek, E. (2006). Antimony content of macrofungi from clean and polluted areas. *Chemosphere*, *64*(11), 1837–1844. https://doi.org/10.1016/j.chemosphere.2006.01.060

Bowman, A. W. (1984). An Alternative Method of Cross-Validation for the Smoothing of Density Estimates. *Scandinavian Journal of Statistics*, *71*(2), 353–360.

Brandolini, F., & Carrer, F. (2021). Terra, Silva et Paludes. Assessing the Role of Alluvial Geomorphology for Late-Holocene Settlement Strategies (Po Plain–N Italy) Through Point Pattern Analysis. *Environmental Archaeology*, *26*(5), 511–525. https://doi.org/10.1080/14614103.2020.1740866

Brock, T. D. (1978). *Thermophilic Microorganisms and Life at High Temperatures*. Springer New York. https://doi.org/10.1007/978-1-4612-6284-8

Brogi, A., Lazzarotto, A., Liotta, D., & Ranalli, G. (2003). Extensional shear zones as imaged by reflection seismic lines: The Lardello geothermal field (central Italy). *Tectonophysics*, *363*(1–2), 127–139. https://doi.org/10.1016/S0040-1951(02)00668-6

Bromley, C. J., & Hochstein, M. P. (2005). *Heat Discharge of Steaming Ground at Karapiti (Wairakei), New Zealand*. *April*, 24–29.

Bromley, C. J., Van Manen, S. M., & Graham, D. (2010). Monitoring surface geothermal features using time series of aerial and ground-based photographs. *American Geophysical Union, Fall Meeting 2010*.

Bromley, C. J., van Manen, S. M., & Mannington, W. (2011). Heat Flux From Steaming Ground: Reducing Uncertainties. *Thirty-Sixth Workshop on Geothermal Reservoir Engineering.*

Brook, A., & Dor, E. B. (2011). Supervised vicarious calibration (SVC) of hyperspectral remote-sensing data. *Remote Sensing of Environment*, *115*(6), 1543–1555. https://doi.org/10.1016/j.rse.2011.02.013

Browne, P. R. L. (1978). Hydrothermal Alteration in Active Geothermal Fields. *Annual Review of Earth and Planetary Sciences*, *6*(Steiner 1963), 229–250.

Browne, P. R. L., & Ellis, A. J. (1970). The Ohaki-Broadlands hydrothermal area, New Zealand; mineralogy and related geochemistry. *American Journal of Science*, *269*(2), 97–131. https://doi.org/10.2475/ajs.269.2.97

Bruzzone, L., Chi, M., & Marconcini, M. (2005). A novel transductive SVM for semisupervised classification of remote sensing images. *Image and Signal Processing for Remote Sensing XI*, *5982*(11), 59820G. https://doi.org/10.1117/12.628862

Buitrago, M. F., Groen, T. A., Hecker, C. A., & Skidmore, A. K. (2016). Changes in thermal infrared spectra of plants caused by temperature and water stress. *ISPRS Journal of Photogrammetry and Remote Sensing*, *111*, 22–31. https://doi.org/10.1016/j.isprsjprs.2015.11.003

Bundschuh, J., & Maity, J. P. (2015). Geothermal arsenic: Occurrence, mobility and environmental implications. *Renewable and Sustainable Energy Reviews*, *42*, 1214–1222. https://doi.org/10.1016/j.rser.2014.10.092

Burgos, M. I. M. (1999). Geochemical interpretation of thermal fluid discharge from wells and springs in Berlin geothermal field, El Salvador. *The United Nations University Reports*, *7*(7), 165–191.

Burns, B. (1997). Vegetation change along a geothermal stress gradient at the Te Kopia steamfield. *Journal of the Royal Society of New Zealand*, *27*(2), 279–293. https://doi.org/10.1080/03014223.1997.9517539

Burns, B., & Leathwick, J. (1995). *Geothermal Vegetation Dynamics*.

Burns, B. R., & Leathwick, J. R. (1995). Geothermal Vegetation Dynamics. In *Wellington, N.Z.: Department of Conservation.* Department of Conservation.

Burns, B. R., Ward, J., & Downs, T. M. (2013). Trampling impacts on thermotolerant vegetation of geothermal areas in new zealand. *Environmental Management*, *52*(6), 1463–1473. https://doi.org/10.1007/s00267-013-0187-5

Calin, M. A., Calin, A. C., & Nicolae, D. N. (2021). Application of airborne and spaceborne hyperspectral imaging techniques for atmospheric research: Past, present, and future. *Applied Spectroscopy Reviews*, *56*(4), 289–323. https://doi.org/10.1080/05704928.2020.1774381

Calvin, W., Coolbaugh, M., & Kratt, C. (2005). Application of remote sensing technology to geothermal exploration. *Geological Society of Nevada Symposium 2005: Window to the World, May*, 1083–1089. https://doi.org/10.1002/nav.3800300412

Calvin, W. M., Littlefield, E. F., & Kratt, C. (2015). Remote sensing of geothermal-related minerals for resource exploration in Nevada. *Geothermics*, *53*, 517–526. https://doi.org/10.1016/j.geothermics.2014.09.002

Calvin, W. M., & Pace, E. L. (2016). Mapping alteration in geothermal drill core using a field portable spectroradiometer. *Geothermics*, *61*, 12–23. https://doi.org/10.1016/j.geothermics.2016.01.005

Canet, C., Trillaud, F., Prol-Ledesma, R. M., González-Hernández, G., Peláez, B., Hernández-Cruz, B., & Sánchez-Córdova, M. M. (2015). Thermal history of the Acoculco geothermal system, eastern Mexico: Insights from numerical modeling and radiocarbon dating. *Journal of Volcanology and Geothermal Research*, *305*, 56–62. https://doi.org/10.1016/j.jvolgeores.2015.09.019

Cañón-Tapia, E. (2022). Kernel Analyses of Volcanic Vent Distribution: How Accurate and Complete are the Objective Bandwidth Selectors? *Frontiers in Earth Science*, *10*(April), 1–21. https://doi.org/10.3389/feart.2022.779095

Cao, J., Liu, K., Liu, L., Zhu, Y., Li, J., & He, Z. (2018). Identifying mangrove species using field close-range snapshot hyperspectral imaging and machine-learning techniques. *Remote Sensing*, *10*(12). https://doi.org/10.3390/rs10122047

Cao, X., Yao, J., Xu, Z., & Meng, D. (2020). Hyperspectral Image Classification With Convolutional Neural Network and Active Learning. *IEEE Transactions on Geoscience and Remote Sensing*, *58*(7), 4604–4616. https://doi.org/10.1109/TGRS.2020.2964627

Capezzuoli, E., Gandin, A., & Pedley, M. (2014). Decoding tufa and travertine (fresh water carbonates) in the sedimentary record: The state of the art. *Sedimentology*, *61*(1), 1–21. https://doi.org/10.1111/sed.12075

Carbajal-Martínez, D., Peiffer, L., Hinojosa-Corona, A., Trasviña-Castro, A., Arregui-Ojeda, S. M., Carranza-Chávez, F. J., Flores-Luna, C., Méndez-Alonzo, R., Inguaggiato, C., & Casallas-Moreno, K. L. (2021). UAV-based thermal imaging and heat output estimation of a coastal geothermal resource: La Jolla beach, Baja California, Mexico. *Renewable Energy*, *168*, 1364–1376. https://doi.org/10.1016/j.renene.2020.12.113

Card, D. H., Peterson, D. L., Matson, P. A., & Aber, J. D. (1988). Prediction of leaf chemistry by the use of visible and near infrared reflectance spectroscopy. *Remote Sensing of Environment*, *26*(2), 123–147. https://doi.org/10.1016/0034-4257(88)90092-2

Carmon, N., Berk, A., Bohn, N., Brodrick, P. G., Kalashnikova, O., Nguyen, H., Thompson, D. R., & Turmon, M. (2022). Unified Topographic and Atmospheric Correction for Remote Imaging Spectroscopy. *Frontiers in Remote Sensing*, *3*, 916155. https://doi.org/10.3389/frsen.2022.916155

Carranza, E. J. M., Wibowo, H., Barritt, S. D., & Sumintadireja, P. (2008). Spatial data analysis and integration for regional-scale geothermal potential mapping, West Java, Indonesia. *Geothermics*, *37*(3), 267–299. https://doi.org/10.1016/j.geothermics.2008.03.003

Carter, G. A. (1993). Responses of Leaf Spectral Reflectance to Plant Stress. *American Journal of Botany*, *80*(3), 239–243.

Cassidy, M., Manga, M., Cashman, K., & Bachmann, O. (2018). Controls on explosive-effusive volcanic eruption styles. *Nature Communications*, *9*(1), 2839. https://doi.org/10.1038/s41467-018-05293-3

Cavallaro, G., Dalla Mura, M., Benediktsson, J. A., & Bruzzone, L. (2015). Extended Self-Dual Attribute Profiles for the Classification of Hyperspectral Images. *IEEE Geoscience and Remote Sensing Letters*, *12*(8), 1690–1694. https://doi.org/10.1109/LGRS.2015.2419629

Chabrillat, S., Goetz, A. F. H., Krosley, L., & Olsen, H. W. (2002). Use of hyperspectral images in the identification and mapping of expansive clay soils and the role of spatial resolution.

Remote Sensing of Environment, *82*(2–3), 431–445. https://doi.org/10.1016/S0034-4257(02)00060-3

Chai, T., & Draxler, R. R. (2014). Root mean square error (RMSE) or mean absolute error (MAE)? – Arguments against avoiding RMSE in the literature. *Geoscientific Model Development*, *7*(3), 1247–1250. https://doi.org/10.5194/gmd-7-1247-2014

Chakraborty, R., Kereszturi, G., Pullanagari, R., Durance, P., Ashraf, S., & Anderson, C. (2021). Mineral prospecting from biogeochemical and geological information using hyperspectral remote sensing—Feasibility and challenges. *Journal of Geochemical Exploration*, *232*(March 2021), 15. https://doi.org/10.1016/j.gexplo.2021.106900

Chambefort, I. (2021). Sulfur in New Zealand geothermal systems: Insights from stable isotope and trace element analyses of anhydrite from Rotokawa and Ngatamariki geothermal fields, Taupo Volcanic Zone. *New Zealand Journal of Geology and Geophysics*, *64*(2–3), 372–388. https://doi.org/10.1080/00288306.2020.1851265

Champagne, C., Pattey, E., Bannari, A., & Stratchan, I. B. (2001). Mapping Crop Water Status: Issues of Scale in the Detection of Crop Water Stress Using Hyperspectral Indices. *Proceedings of the 8th International Symposium on Physical Measurements and Signatures in Remote Sensing*, *January*, 79–84.

Chan, H. P., Chang, C. P., & Dao, P. D. (2018). Geothermal Anomaly Mapping Using Landsat ETM+ Data in Ilan Plain, Northeastern Taiwan. *Pure and Applied Geophysics*, *175*(1), 303–323. https://doi.org/10.1007/s00024-017-1690-z

Chang, Y., Xiao, J., Li, X., Middel, A., Zhang, Y., Gu, Z., Wu, Y., & He, S. (2021). Exploring diurnal thermal variations in urban local climate zones with ECOSTRESS land surface temperature data. *Remote Sensing of Environment*, *263*, 112544. https://doi.org/10.1016/j.rse.2021.112544

Chenaker, H., Houha, B., & Vincent, V. (2018). Hydrogeochemistry and geothermometry of thermal water from north-eastern Algeria. *Geothermics*, *75*(May), 137–145. https://doi.org/10.1016/j.geothermics.2018.04.009

Cherkose, B. A., & Saibi, H. (2021). Investigation of the Ayrobera geothermal field using 3D magnetotelluric data inversion, Afar depression, NE Ethiopia. *Geothermics*, *94*(February), 102114. https://doi.org/10.1016/j.geothermics.2021.102114

Chicco, D., Warrens, M. J., & Jurman, G. (2021). The coefficient of determination R-squared is more informative than SMAPE, MAE, MAPE, MSE and RMSE in regression analysis evaluation. *PeerJ Computer Science*, *7*, e623. https://doi.org/10.7717/peerj-cs.623

Christiansen, R., Lowenstern, J. B., Smith, R. B., Heasler, H., Morgan, L., Nathenson, M., Mastin, L. G., Muffler, P., & Robinson, J. E. (2007). *Preliminary Assessment of Volcanic and Hydrothermal Hazards in Yellowstone National Park and Vicinity* (Open-File Report).

Chu, H., Zhang, C., Wang, M., Gouda, M., Wei, X., He, Y., & Liu, Y. (2022). Hyperspectral imaging with shallow convolutional neural networks (SCNN) predicts the early herbicide stress in wheat cultivars. *Journal of Hazardous Materials*, *421*(March 2021), 126706. https://doi.org/10.1016/j.jhazmat.2021.126706

Cigna, F., Tapete, D., Garduño-Monroy, V. H., Muñiz-Jauregui, J. A., García-Hernández, O. H., & Jiménez-Haro, A. (2019). Wide-Area InSAR Survey of Surface Deformation in Urban Areas and Geothermal Fields in the Eastern Trans-Mexican Volcanic Belt, Mexico. *Remote Sensing*, *11*(20), 2341. https://doi.org/10.3390/rs11202341

Cigna, F., Tapete, D., & Lu, Z. (2020). Remote sensing of volcanic processes and risk. *Remote Sensing*, *12*(16), 1–17. https://doi.org/10.3390/RS12162567

Cigna, F., Tapete, D., Muñiz-Jauregui, J. A., Garduño-Monroy, V. H., García, O., & Jiménez-Haro, A. (2020). Wide-area observations of surface deformation in Mexican urban areas and geothermal fields using ENVISAT InSAR. *IOP Conference Series: Earth and Environmental Science*, *509*(1), 10–12. https://doi.org/10.1088/1755-1315/509/1/012007

Cisternas, I., Velásquez, I., Caro, A., & Rodríguez, A. (2020). Systematic literature review of implementations of precision agriculture. *Computers and Electronics in Agriculture*, *176*, 105626. https://doi.org/10.1016/j.compag.2020.105626

Clark, P. J., & Evans, F. C. (1954). Distance to Nearest Neighbor as a Measure of Spatial Relationships in Populations. *Ecology*, *35*(4), 445–453. https://doi.org/10.2307/1931034

Clark, R. N. (1999a). Chapter 1: Spectroscopy of rocks and minerals, and principles of spectroscopy. In *Manual of Remote Sensing* (Vol. 3, pp. 3–58). https://doi.org/10.1111/j.1945-5100.2004.tb00079.x

Clark, R. N. (1999b). Chapter 1: Spectroscopy of Rocks and Minerals, and Principles of Spectroscopy. In *Manual of Remote Sensing* (Vol. 3, pp. 3–58). https://doi.org/10.1111/j.1945-5100.2004.tb00079.x

Clark, R. N., King, T. V. V., Klejwa, M., Swayze, G. A., & Vergo, N. (1990). High spectral resolution reflectance spectroscopy of minerals. *Journal of Geophysical Research*, *95*(B8), 12653. https://doi.org/10.1029/JB095iB08p12653

Clark, R. N., & Roush, T. L. (1984). Reflectance spectroscopy: Quantitative analysis techniques for remote sensing applications. *Journal of Geophysical Research*, *89*(B7), 6329–6340. https://doi.org/10.1029/JB089iB07p06329

Clark, R. N., Swayze, G. A., Livo, K. E., Kokaly, R. F., Sutley, S. J., Dalton, J. B., McDougal, R. R., & Gent, C. A. (2003). Imaging spectroscopy: Earth and planetary remote sensing with the USGS Tetracorder and expert systems. *Journal of Geophysical Research: Planets*, *108*(E12). https://doi.org/10.1029/2002JE001847

Cochrane, G. R., Mongillo, M. A., Browne, P. R. L., & Deroin, J. P. (1994). *SATELLITE STUDIES OF THE WAIMANGU AND WAIOTAPU GEOTHERMAL AREAS , TVZ*. 181–186.

Cogliati, S., Sarti, F., Chiarantini, L., Cosi, M., Lorusso, R., Lopinto, E., Miglietta, F., Genesio, L., Guanter, L., Damm, A., Pérez-López, S., Scheffler, D., Tagliabue, G., Panigada, C., Rascher, U., Dowling, T. P. F., Giardino, C., & Colombo, R. (2021). The PRISMA imaging

spectroscopy mission: Overview and first performance analysis. *Remote Sensing of Environment*, *262*(April), 112499. https://doi.org/10.1016/j.rse.2021.112499

Cohen, D. R., Hoffman, E. L., & Nichol, I. (1987). Biogeochemistry: A geochemical method for gold exploration in the Canadian Shield. *Journal of Geochemical Exploration*, *29*(1–3), 49–73. https://doi.org/10.1016/0375-6742(87)90070-7

Cohen, D. R., Zissimos, A. M., Schifano, J. A., & Rutherford, N. F. (2021). Biogeochemical response of Pinus brutia and Olea europaea to lithological variations and Cu mineralisation in Cyprus. *Science of The Total Environment*, *759*, 143434. https://doi.org/10.1016/j.scitotenv.2020.143434

Cole, J. W. (1990). Structural control and origin of volcanism in the Taupo volcanic zone, New Zealand. *Bulletin of Volcanology*, *52*(6), 445–459. https://doi.org/10.1007/BF00268925

Connor, B., & Hill, E. (1995). Three nonhomogeneous Poisson models for the probability of basaltic volcanism: Application to the Yucca Mountain region, Nevada. *Journal of Geophysical Research*, *100*.

Connor, C. B., Connor, L., Germa, A., Richardson, J., Bebbington, M., Gallant, E., & Saballos, A. (2019). How to use kernel density estimation as a diagnostic and forecasting tool for distributed volcanic vents. *Statistics in Volcanology*, *4*, 1–25. https://doi.org/10.5038/2163-338x.4.3

Coolbaugh, M. F., Kratt, C., Fallacaro, A., Calvin, W. M., & Taranik, J. V. (2007). Detection of geothermal anomalies using Advanced Spaceborne Thermal Emission and Reflection Radiometer (ASTER) thermal infrared images at Bradys Hot Springs, Nevada, USA. *Remote Sensing of Environment*, *106*(3), 350–359. https://doi.org/10.1016/j.rse.2006.09.001

Coppo, P., Taiti, A., Pettinato, L., Francois, M., Taccola, M., & Drusch, M. (2017). Fluorescence imaging spectrometer (FLORIS) for ESA FLEX mission. *Remote Sensing*, *9*(7), 1–18. https://doi.org/10.3390/rs9070649

Costanzini, S., Ferrari, C., Despini, F., & Muscio, A. (2021). Standard Test Methods for Rating of Solar Reflectance of Built-Up Surfaces and Potential Use of Satellite Remote Sensors. *Energies*, *14*(20), 6626. https://doi.org/10.3390/en14206626

Cox, A., Venkatachalam, P., Sahi, S., & Sharma, N. (2016). Silver and titanium dioxide nanoparticle toxicity in plants: A review of current research. *Plant Physiology and Biochemistry*, *107*, 147–163. https://doi.org/10.1016/j.plaphy.2016.05.022

Craw, D., Rufaut, C., Haffert, L., & Paterson, L. (2007). Plant colonization and arsenic uptake on high arsenic mine wastes, New Zealand. *Water, Air, and Soil Pollution*, *179*(1–4), 351–364. https://doi.org/10.1007/s11270-006-9238-3

Croft, H., Chen, J. M., & Zhang, Y. (2014). The applicability of empirical vegetation indices for determining leaf chlorophyll content over different leaf and canopy structures. *Ecological Complexity*, *17*, 119–130. https://doi.org/10.1016/j.ecocom.2013.11.005

Crósta, A. P., Sabine, C., & Taranik, J. V. (1998). Hydrothermal alteration mapping at Bodie, California, using AVIRIS hyperspectral data. *Remote Sensing of Environment*, *65*(3), 309–319. https://doi.org/10.1016/S0034-4257(98)00040-6

Crowther, T. W., van den Hoogen, J., Wan, J., Mayes, M. A., Keiser, A. D., Mo, L., Averill, C., & Maynard, D. S. (2019). The global soil community and its influence on biogeochemistry. *Science*, *365*(6455), eaav0550. https://doi.org/10.1126/science.aav0550

Curran, P. J. (1989). Remote Sensing of Foliar Chemistry. *Remote Sensing of Environment*, *30*(3), 271–278. https://doi.org/10.1016/0034-4257(89)90069-2

Daley, D. J., & Vere-Jones, D. (2003). *An Introduction to the Theory of Point Processes. Volume I: Elementary Theory and Methods.* (2nd ed.). Springer.

Dalponte, M., Ørka, H. O., Gobakken, T., Gianelle, D., & Næsset, E. (2013). Tree species classification in boreal forests with hyperspectral data. *IEEE Transactions on Geoscience and Remote Sensing*, *51*(5), 2632–2645. https://doi.org/10.1109/TGRS.2012.2216272

Darge, Y. M., Hailu, B. T., Muluneh, A. A., & Kidane, T. (2019). Detection of geothermal anomalies using Landsat 8 TIRS data in Tulu Moye geothermal prospect, Main Ethiopian Rift. *International Journal of Applied Earth Observation and Geoinformation*, *74*(June 2018), 16–26. https://doi.org/10.1016/j.jag.2018.08.027

Das, S., & Thakur, N. (2021). The Microbial Diversity of Hot Springs Located in Himalayan Geothermal Belts (HGB). In A. Pandey & A. Sharma (Eds.), *Extreme Environments* (1st ed., pp. 18–43). CRC Press. https://doi.org/10.1201/9780429343452-2

Davy, B. W., & Caldwell, T. G. (1998). Gravity, magnetic and seismic surveys of the caldera complex, Lake Taupo, North Island, New Zealand. *Journal of Volcanology and Geothermal Research*, *81*(1–2), 69–89. https://doi.org/10.1016/S0377-0273(97)00074-7

de Lange, P. (2014). A revision of the New Zealand Kunzea ericoides (Myrtaceae) complex. *PhytoKeys*, *40*, 1–185. https://doi.org/10.3897/phytokeys.40.7973

Debba, P., Van Ruitenbeek, F. J. A., Van Der Meer, F. D., Carranza, E. J. M., & Stein, A. (2005). Optimal field sampling for targeting minerals using hyperspectral data. *Remote Sensing of Environment*, *99*(4), 373–386. https://doi.org/10.1016/j.rse.2005.05.005

Delalieux, S., Somers, B., Verstraeten, W. W., van Aardt, J. A. N., Keulemans, W., & Coppin, P. (2009). Hyperspectral indices to diagnose leaf biotic stress of apple plants, considering leaf phenology. *International Journal of Remote Sensing*, *30*(8), 1887–1912. https://doi.org/10.1080/01431160802541556

Delmelle, E. (2009). Point Pattern Analysis. *International Encyclopedia of Human Geography*, 204–211. https://doi.org/10.1016/B978-008044910-4.00494-6

Deon, F., Lievens, C., Barnhoorn, A., Welink, C., Imaro, T., Ryannugroho, R., Reyhanitash, E., Bruhn, D., van der Meer, F., Hutami, R., Sibarani, B., Hecker, C., Appelt, O., Wilke, F., Daud, Y., & den Hartog, T. (2019). Geothermal exploration in Indonesia based on Mineralogy and Hydrothermal Alteration. *IOP Conference Series: Earth and Environmental Science*, *254*, 012002. https://doi.org/10.1088/1755-1315/254/1/012002

Deroin, J. P., Cochrane, G. R., Mongillo, M. A., & Browne, P. R. (1995). Methods of remote sensing in geothermal regions: The geodynamic setting of the Taupo Volcanic Zone (North Island, New Zealand). *International Journal of Remote Sensing*, *16*(9), 1663–1677. https://doi.org/10.1080/01431169508954503

Dhawale, R., & Paul, S. K. (2018). A comparative analysis of drought indices on vegetation through remote sensing for Latur region of India. *International Archives of the Photogrammetry, Remote Sensing and Spatial Information Sciences - ISPRS Archives*, *42*(5), 403–407. https://doi.org/10.5194/isprs-archives-XLII-5-403-2018

Dill, H. G. (2001). The geology of aluminum phosphate and sulphates of the alunite group minerals: A review. *Earth Science Reviews*, *53*(1–2), 35–93. https://doi.org/10.1016/S0012-8252(00)00035-0

Dobson, P. F., Kneafsey, T. J., Hulen, J., & Simmons, A. (2003). Porosity, permeability, and fluid flow in the Yellowstone geothermal system, Wyoming. *Journal of Volcanology and Geothermal Research*, *123*(3–4), 313–324. https://doi.org/10.1016/S0377-0273(03)00039-8

Dong, T., Liu, J., Shang, J., Qian, B., Ma, B., Kovacs, J. M., Walters, D., Jiao, X., Geng, X., & Shi, Y. (2019). Assessment of red-edge vegetation indices for crop leaf area index estimation. *Remote Sensing of Environment*, *222*(May 2018), 133–143. https://doi.org/10.1016/j.rse.2018.12.032

Drake, N. A., Mackin, S., & Settle, J. J. (1999). Mapping vegetation, soils, and geology in semiarid shrublands using spectral matching and mixture modeling of SWIR AVIRIS imagery. *Remote Sensing of Environment*, *68*(1), 12–25. https://doi.org/10.1016/S0034-4257(98)00097-2

Duarte, F. J. (1995). *Tunable Laser Applications*.

Dunn, C. E. (2007). *Biogeochemistry in Mineral Exploration* (M. Hale, Ed.). Elsevier.

Dunn, C. E. (2011). *Biogeochemistry in Mineral Exploration*. Elsevier.

Dunn, C. E., & Christie, A. B. (2019). Tree Ferns and Tea Tree in Biogeochemical Exploration for Epithermal Au and Ag in New Zealand. *The Geological Society*.

Dunn, C. E., & Christie, A. B. (2020). Tree ferns and tea trees in biogeochemical exploration for epithermal Au and Ag in New Zealand. *Geochemistry: Exploration, Environment, Analysis*, *20*(3), 299–314. https://doi.org/10.1144/geochem2019-047

Duong, T. (2007). Ks: Kernel density estimation and kernel discriminant analysis for multivariate data in R. *Journal of Statistical Software*, *21*(7), 1–16. https://doi.org/10.18637/jss.v021.i07

Duong, T., & Hazelton, M. L. (2003). Plug-in bandwidth matrices for bivariate kernel density estimation. *Journal of Nonparametric Statistics*, *15*(1), 17–30. https://doi.org/10.1080/10485250306039

Eberhart-Phillips, D., Reyners, M., Chadwick, M., & Stuart, G. (2008). Three-dimensional attenuation structure of the Hikurangi subduction zone in the central North Island, New Zealand. *Geophysical Journal International*, *174*(1), 418–434. https://doi.org/10.1111/j.1365-246X.2008.03816.x

Efron, B., & Tibshirani, R. (1993). *An Introduction to the Bootstrap*. Chapman & Hall.

Eisele, A., Chabrillat, S., Hecker, C., Hewson, R., Lau, I. C., Rogass, C., Segl, K., Cudahy, T. J., Udelhoven, T., Hostert, P., & Kaufmann, H. (2015). Advantages using the thermal infrared (TIR) to detect and quantify semi-arid soil properties. *Remote Sensing of Environment*, *163*, 296–311. https://doi.org/10.1016/j.rse.2015.04.001

Eismann, M. T. (2012). *Hyperspectral Remote Sensing*.

Ekanayake, E. M. M. B., Ekanayake, E. M. H. E. B., Rathnayake, A. R. M. A. N., Vithana, S. S. P., Herath, H. M. V. R., Godaliyadda, G. M. R. I., & Ekanayake, M. P. B. (2018). A Semi-Supervised Algorithm to Map Major Vegetation Zones Using Satellite Hyperspectral Data. *2018 9th Workshop on Hyperspectral Image and Signal Processing: Evolution in Remote Sensing (WHISPERS)*, 1–5. https://doi.org/10.1109/WHISPERS.2018.8747025

El Alem, A., Lhissou, R., Chokmani, K., & Oubennaceur, K. (2021). Remote Retrieval of Suspended Particulate Matter in Inland Waters: Image-Based or Physical Atmospheric Correction Models? *Water*, *13*(16), 2149. https://doi.org/10.3390/w13162149

El Bouazouli, A., Baidder, L., Pasquier, P., & Rhouzlane, S. (2019). Remote sensing contribution to the identification of potential geothermal deposits: A case study of the Moroccan Sahara. *Materials Today: Proceedings*, *13*, 784–794. https://doi.org/10.1016/j.matpr.2019.04.041

Elarab, M., Ticlavilca, A. M., Torres-Rua, A. F., Maslova, I., & McKee, M. (2015). Estimating chlorophyll with thermal and broadband multispectral high resolution imagery from an unmanned aerial system using relevance vector machines for precision agriculture. *International Journal of Applied Earth Observation and Geoinformation*, *43*, 32–42. https://doi.org/10.1016/j.jag.2015.03.017

Ellis, A. J., & Mahon, W. A. J. (1967). Natural hydrothermal systems and experimental hot water/rock interactions (Part II). *Geochimica et Cosmochimica Acta*, *31*(4), 519–538. https://doi.org/10.1016/0016-7037(67)90032-4

ENVI. (2009). ENVI Atmospheric Correction Module: QUAC and FLAASH user's guide. In *Module Version*. http://scholar.google.com/scholar?hl=en&btnG=Search&q=intitle:ENVI+Atmospheric+Correction+Module:+QUAC+and+FLAASH+user's+guide#0

Erfanifard, Y., Kraszewski, B., & Stereńczak, K. (2021). Integration of remote sensing in spatial ecology: Assessing the interspecific interactions of two plant species in a semi-arid woodland using unmanned aerial vehicle (UAV) photogrammetric data. *Oecologia*, *196*(1), 115–130. https://doi.org/10.1007/s00442-021-04928-5

Fagbohun, B., Hecker, C., van Ruitenbeek, F., Riley, D., & Dilles, J. (2015). Exploring the complementarity of SWIR and TIR airborne hyperspectral mineral mapping (Abstract). *Remote Sensing: Understanding the Earth for a Safer World. The International Geoscience and Remote Sensing Symposium (IGARSS)*, 5–8.

Fahselt, D. (1995). Growth form and reproductive character of lichens near active fumaroles in Japan. *Symbiosis*, *18*(3), 211–231.

Falorni, G., Morgan, J., & Eneva, M. (2011). Advanced InSAR techniques for geothermal exploration and production. *Transactions - Geothermal Resources Council*, *35 2*, 1661–1666.

Farooq, M. A., Islam, F., Ali, B., Najeeb, U., Mao, B., Gill, R. A., Yan, G., Siddique, K. H. M., & Zhou, W. (2016). Arsenic toxicity in plants: Cellular and molecular mechanisms of its transport and metabolism. *Environmental and Experimental Botany*, *132*, 42–52. https://doi.org/10.1016/j.envexpbot.2016.08.004

Feng, J., Rogge, D., & Rivard, B. (2018). Comparison of lithological mapping results from airborne hyperspectral VNIR-SWIR, LWIR and combined data. *International Journal of Applied Earth Observation and Geoinformation*, *64*, 340–353. https://doi.org/10.1016/j.jag.2017.03.003

Feng, R., Shen, H., Bai, J., & Li, X. (2021). Advances and Opportunities in Remote Sensing Image Geometric Registration: A systematic review of state-of-the-art approaches and future research directions. *IEEE Geoscience and Remote Sensing Magazine*, *9*(4), 120–142. https://doi.org/10.1109/MGRS.2021.3081763

Feng, R., Wei, C., Tu, S., Ding, Y., Wang, R., & Guo, J. (2013). The uptake and detoxification of antimony by plants: A review. *Environmental and Experimental Botany*, *96*, 28–34. https://doi.org/10.1016/j.envexpbot.2013.08.006

Féret, J. B., François, C., Gitelson, A., Asner, G. P., Barry, K. M., Panigada, C., Richardson, A. D., & Jacquemoud, S. (2011). Optimizing spectral indices and chemometric analysis of leaf chemical properties using radiative transfer modeling. *Remote Sensing of Environment*, *115*(10), 2742–2750. https://doi.org/10.1016/j.rse.2011.06.016

Filella, M., Belzile, N., & Lett, M.-C. (2007). Antimony in the environment: A review focused on natural waters. III. Microbiota relevant interactions. *Earth-Science Reviews*, *80*(3–4), 195–217. https://doi.org/10.1016/j.earscirev.2006.09.003

Finlay, R. D., Mahmood, S., Rosenstock, N., Bolou-Bi, E. B., Köhler, S. J., Fahad, Z., Rosling, A., Wallander, H., Belyazid, S., Bishop, K., & Lian, B. (2020). Reviews and syntheses: Biological weathering and its consequences at different spatial levels – from nanoscale to global scale. *Biogeosciences*, *17*(6), 1507–1533. https://doi.org/10.5194/bg-17-1507-2020

Finnegan, P. M., & Chen, W. (2012). Arsenic toxicity: The effects on plant metabolism. *Frontiers in Physiology*, *3 JUN*(June), 1–18. https://doi.org/10.3389/fphys.2012.00182

Flores-Armenta, M., & Gutiérrez-Negrín, L. C. A. (2011). *GEOTHERMAL ACTIVITY AND DEVELOPMENT IN MEXICO*. 12.

Foody, G. M. (2008). Harshness in image classification accuracy assessment. *International Journal of Remote Sensing*, *29*(11), 3137–3158. https://doi.org/10.1080/01431160701442120

Foody, G. M. (2009). Classification accuracy comparison: Hypothesis tests and the use of confidence intervals in evaluations of difference, equivalence and non-inferiority. *Remote Sensing of Environment*, *113*(8), 1658–1663. https://doi.org/10.1016/j.rse.2009.03.014

Foody, G. M. (2020). Explaining the unsuitability of the kappa coefficient in the assessment and comparison of the accuracy of thematic maps obtained by image classification. *Remote Sensing of Environment*, *239*(January), 111630. https://doi.org/10.1016/j.rse.2019.111630

Fournier, R. O. (1989). Geochemistry and Dynamics of the Yellowstone National Park Hydrothermal System. *Annual Review of Earth and Planetary Sciences*, *17*(1), 13–53. https://doi.org/10.1146/annurev.ea.17.050189.000305

Fourty, Th., Baret, F., Jacquemoud, S., Schmuck, G., & Verdebout, J. (1996). Leaf optical properties with explicit description of its biochemical composition: Direct and inverse problems. *Remote Sensing of Environment*, *56*(2), 104–117. https://doi.org/10.1016/0034-4257(95)00234-0

Fox, J. (2002). *Bootstrapping Regression Models*.

Frankel, A. (1995). Mapping seismic hazard in the central and eastern United States. *Seismological Research Letters*, *66*(4), 8–21. https://doi.org/10.1785/gssrl.66.4.8

Freski, Y. R., Hecker, C., van der Meijde, M., & Setianto, A. (2021). The effects of alteration degree, moisture and temperature on laser return intensity for mapping geothermal manifestations. *Geothermics*, *97*, 102250. https://doi.org/10.1016/j.geothermics.2021.102250

Fulignati, P. (2020). Clay Minerals in Hydrothermal Systems. *Minerals*, *10*(10), 919. https://doi.org/10.3390/min10100919

Gallagher, A., Montanaro, C., Cronin, S. J., Scott, B., Dingwell, D. B., & Scheu, B. (2020). Hydrothermal eruption dynamics reflecting vertical variations in host rock geology and geothermal alteration , Champagne Pool , Wai-o-tapu , New Zealand. *Bulletin of Volcanology*.

Gao, B. C., Montes, M. J., Davis, C. O., & Goetz, A. F. H. (2009). Atmospheric correction algorithms for hyperspectral remote sensing data of land and ocean. *Remote Sensing of Environment*, *113*(SUPPL. 1), S17–S24. https://doi.org/10.1016/j.rse.2007.12.015

Gao, B.-C., Ward, E., Bowles, J., & Yingling, A. (2020). A Systematic Sensitivity Study on Surface Pixel Shifts in High Spatial Resolution Satellite Images Resulting from Atmospheric Refraction in the Sensor to Surface Ray Path. *Sensors*, *20*(23), 6874. https://doi.org/10.3390/s20236874

Gemitzi, A., Dalampakis, P., & Falalakis, G. (2021). Detecting geothermal anomalies using Landsat 8 thermal infrared remotely sensed data. *International Journal of Applied Earth Observation and Geoinformation*, *96*(November 2020), 102283. https://doi.org/10.1016/j.jag.2020.102283

Gerard, V. B., & Lawrie, J. A. (1952). *Aeromagnetic surveys in New Zealand 1949–1952*.

Gewali, U. B., Monteiro, S. T., & Saber, E. (2018). *Machine learning based hyperspectral image analysis: A survey*. *February*. http://arxiv.org/abs/1802.08701

Ghamisi, P., Plaza, J., Chen, Y., Li, J., & Plaza, A. J. (2017). Advanced Spectral Classifiers for Hyperspectral Images: A review. *IEEE Geoscience and Remote Sensing Magazine*, *5*(1), 8–32. https://doi.org/10.1109/MGRS.2016.2616418

Ghamisi, P., Yokoya, N., Li, J., Liao, W., Liu, S., Plaza, J., Rasti, B., & Plaza, A. (2017). Advances in Hyperspectral Image and Signal Processing: A Comprehensive Overview of the State of the Art. *IEEE Geoscience and Remote Sensing Magazine*, *5*(4), 37–78. https://doi.org/10.1109/MGRS.2017.2762087

Ghosh, A., & Joshi, P. K. (2014). A comparison of selected classification algorithms for mappingbamboo patches in lower Gangetic plains using very high resolution WorldView 2 imagery. *International Journal of Applied Earth Observation and Geoinformation*, *26*(1), 298–311. https://doi.org/10.1016/j.jag.2013.08.011

Gianelli, G., & Grassi, S. (2001). Water–rock interaction in the active geothermal system of Pantelleria, Italy. *Chemical Geology*, *181*(1–4), 113–130. https://doi.org/10.1016/S0009-2541(01)00276-5

Giggenbach, W. F. (1984). Mass transfer in hydrothermal alteration systems-A conceptual approach. *Geochimica et Cosmochimica Acta*, *48*(12), 2693–2711. https://doi.org/10.1016/0016-7037(84)90317-X

Giggenbach, W. F. (1995). Variations in the chemical and isotopic composition of fluids discharged from the Taupo volcanic zone, New Zealand. *Journal of Volcanology and Geothermal Research*, *68*(95), 89–116.

Giggenbach, W. F., Sheppard, D. S., Robinson, B. W., Stewart, M. K., & Lyon, G. L. (1994). Geochemical structure and position of the Waiotapu geothermal field, New Zealand. *Geothermics*, *23*(5–6), 599–644.

Giggenbach, W., Sheppard, D., Robinson, B., Stewart, M., & Lyon, G. (1994). Geochemical structure and position of the Waiotapu geothermal field, New Zealand. *Geothermics*, *23*(5–6), 599–644. https://doi.org/10.1016/0375-6505(94)90022-1

Giordano, G., Pinton, A., Cianfarra, P., Baez, W., Chiodi, A., Viramonte, J., Norini, G., & Groppelli, G. (2013). Structural control on geothermal circulation in the Cerro Tuzgle-Tocomar

geothermal volcanic area (Puna plateau, Argentina). *Journal of Volcanology and Geothermal Research*, *249*, 77–94. https://doi.org/10.1016/j.jvolgeores.2012.09.009

Giovos, R., Tassopoulos, D., Kalivas, D., Lougkos, N., & Priovolou, A. (2021). Remote sensing vegetation indices in viticulture: A critical review. *Agriculture (Switzerland)*, *11*(5). https://doi.org/10.3390/agriculture11050457

Given, D. R. (1980). Vegetation on heated soils at Karapiti, Central North Island, New Zealand, And its relation to ground. *New Zealand Journal of Botany*, *18*(1), 1–13. https://doi.org/10.1080/0028825X.1980.10427227

Glime, J. M., & Iwatsuki, Z. (1990). Niche characteristics of Cladonia lichens associated with geothermal vents in Japan. *Ecological Research*, *5*(1), 131–141. https://doi.org/10.1007/BF02348468

Gobron, N., Pinty, B., Verstraete, M. M., & Widlowski, J. L. (2000). Advanced vegetation indices optimized for up-coming sensors: Design, performance, and applications. *IEEE Transactions on Geoscience and Remote Sensing*, *38*(6), 2489–2505. https://doi.org/10.1109/36.885197

Goetz, A. F. H., Vane, G., Solomon, J. E., & Rock, B. N. (1985). Imaging Spectrometry for Earth Remote Sensing. *Science*, *228*(4704), 1147–1153. https://doi.org/10.1126/science.228.4704.1147

Gomez, C., Lagacherie, P., & Coulouma, G. (2008). Continuum removal versus PLSR method for clay and calcium carbonate content estimation from laboratory and airborne hyperspectral measurements. *Geoderma*, *148*(2), 141–148. https://doi.org/10.1016/j.geoderma.2008.09.016

Gomez-Ortiz, D., Blanco-Montenegro, I., Arnoso, J., Martin-Crespo, T., Solla, M., Montesinos, F., Vélez, E., & Sánchez, N. (2019). Imaging Thermal Anomalies in Hot Dry Rock Geothermal Systems from Near-Surface Geophysical Modelling. *Remote Sensing*, *11*(6), 675. https://doi.org/10.3390/rs11060675

Gong, J., Munoz-Saez, C., Wilmeth, D. T., Myers, K. D., Homann, M., Arp, G., Skok, J. R., & van Zuilen, M. A. (2022). Morphogenesis of digitate structures in hot spring silica sinters of the El Tatio geothermal field, Chile. *Geobiology*, *20*(1), 137–155. https://doi.org/10.1111/gbi.12471

González-Acevedo, Z. I., García-Zarate, M. A., Núñez-Zarco, E. A., & Anda-Martín, B. I. (2018). Heavy metal sources and anthropogenic enrichment in the environment around the Cerro Prieto Geothermal Field, Mexico. *Geothermics*, *72*(May 2017), 170–181. https://doi.org/10.1016/j.geothermics.2017.11.004

Götze, C., Jung, A., Merbach, I., Wennrich, R., & Gläßer, C. (2010). Spectrometric analyses in comparison to the physiological condition of heavy metal stressed floodplain vegetation in a standardised experiment. *Central European Journal of Geosciences*, *2*(2), 132–137. https://doi.org/10.2478/v10085-010-0002-y

Govil, H. (2017). Prospecting for hydrothermal mineral deposits in the Himalaya using short-wave infrared spectroscopy. *Workshop on Hyperspectral Image and Signal Processing, Evolution in Remote Sensing*, *2015-June*, 1–4. https://doi.org/10.1109/WHISPERS.2015.8075363

Graf, T., & Therrien, R. (2009). Stable-unstable flow of geothermal fluids in fractured rock. *Geofluids*, *9*(2 SPEC. ISS.), 138–152. https://doi.org/10.1111/j.1468-8123.2008.00233.x

Grahn, H. F., & Geladi, P. (2007). Techniques and Applications of Hyperspectral Image Analysis. In *Techniques* (Vol. 22). https://doi.org/10.1002/9780470010884

Grange, L. (1937). The Geology of the Rotorua-Taupo Subdivision, Rotorua and Kaimanawa Divisions. *New Zealand Department of Scientific and Industrial Research Bulletin.*, *37*, 86–105.

Grant, M. A. (1982). *Geothermal Reservoir Engineering*.

Green, A. A., Berman, M., Switzer, P., & Craig, M. D. (1988). A transformation for ordering multispectral data in terms of image quality with implications for noise removal. *IEEE*

Transactions on Geoscience and Remote Sensing, *26*(1), 65–74. https://doi.org/10.1109/36.3001

Grindley, G., Mumme, T., & Kohn, B. (1994). Stratigraphy, paleomagnetism, geochronology and structure of silicic volcanic rocks, Waiotapu/Paeroa range area, New Zealand. *Geothermics*, *23*(5–6), 473–499. https://doi.org/10.1016/0375-6505(94)90014-0

Grindley, G. W. (1963). Geology and structure of Waiotapu geothermal field. *Department of Scientific and Industrial Research Bulletin*, *155*, 10–25.

Guanter, L., Kaufmann, H., Segl, K., Foerster, S., Rogass, C., Chabrillat, S., Kuester, T., Hollstein, A., Rossner, G., Chlebek, C., Straif, C., Fischer, S., Schrader, S., Storch, T., Heiden, U., Mueller, A., Bachmann, M., Mühle, H., Müller, R., … Sang, B. (2015). The EnMAP Spaceborne Imaging Spectroscopy Mission for Earth Observation. *Remote Sensing*, *7*(7), 8830–8857. https://doi.org/10.3390/rs70708830

Gupta, H., & Roy, S. (2007). Assessment and exploitation. *Geothermal Energy*, 121–164.

Gutiérrez, F. J., Lemus, M., Parada, M. A., Benavente, O. M., & Aguilera, F. A. (2012). Contribution of ground surface altitude difference to thermal anomaly detection using satellite images: Application to volcanic/geothermal complexes in the Andes of Central Chile. *Journal of Volcanology and Geothermal Research*, *237–238*, 69–80. https://doi.org/10.1016/j.jvolgeores.2012.05.016

Hacıoğlu, Ö., Başokur, A. T., & Diner, Ç. (2021). Geothermal potential of the eastern end of the Gediz basin, western Anatolia, Turkey revealed by three-dimensional inversion of magnetotelluric data. *Geothermics*, *91*(May 2020). https://doi.org/10.1016/j.geothermics.2020.102040

Hadfield, J., Nicole, D., Rosen, M., Wilson, C. J. L., & Morgenstern, U. (2001). Hydrogeology of Lake Taupo Catchment: Phase 1. In *Environment Waikato Technical Report ; 2001/01*.

Hamilton, A. R., Campbell, K., Guido, D., Dobson, M., Havig, J., Hamilton, T., Penrose, L., Drake, B., & Rowe, M. (2022). *Delineating Geothermal Upflow from Surface Features: A Waiotapu Case Study*.

Han, L., Liu, Z., Ning, Y., & Zhao, Z. (2018). Extraction and analysis of geological lineaments combining a DEM and remote sensing images from the northern Baoji loess area. *Advances in Space Research*, *62*(9), 2480–2493. https://doi.org/10.1016/j.asr.2018.07.030

Handley, K. M., Campbell, K. A., Mountain, B. W., & Browne, P. R. L. (2005). Abiotic-biotic controls on the origin and development of spicular sinter: In situ growth experiments, Champagne Pool, Waiotapu, New Zealand. *Geobiology*, *3*(2), 93–114. https://doi.org/10.1111/j.1472-4669.2005.00046.x

Hapke, B. (1993). *Combined Theory of Reflectance and Emittance Spectroscopy* (pp. 31–42).

Harris, A., Bryant, R. G., & Baird, A. J. (2005). Detecting near-surface moisture stress in Sphagnum spp. *Remote Sensing of Environment*, *97*(3), 371–381. https://doi.org/10.1016/j.rse.2005.05.001

Harvey, M. C., Rowland, J. V., & Luketina, K. M. (2016). Drone with thermal infrared camera provides high resolution georeferenced imagery of the Waikite geothermal area, New Zealand. *Journal of Volcanology and Geothermal Research*, *325*, 61–69. https://doi.org/10.1016/j.jvolgeores.2016.06.014

Harvey, M. C., Rowland, J. V., Chiodini, G., Rissmann, C. F., Bloomberg, S., Fridriksson, T., & Oladottir, A. A. (2017). CO 2 flux geothermometer for geothermal exploration. *Geochimica et Cosmochimica Acta*, *213*, 1–16. https://doi.org/10.1016/j.gca.2017.06.025

Harvey, M., & Luketina, K. (2014). Thermal Infrared Cameras and Drones: A Match Made in Heaven for Cost- Effective Geothermal Exploration, Monitoring and Development. *New Zealand Geothermal Workshop 2014 Proceedings*, *November*, 1–4.

Haselwimmer, C., & Prakash, A. (2013). Thermal Infrared Remote Sensing of Geothermal Systems. In *Remote Sensing and Digital Image processing* (pp. 453–473). https://doi.org/10.1007/978-94-007-6639-6_22

Haselwimmer, C., Prakash, A., & Holdmann, G. (2013). Quantifying the heat flux and outflow rate of hot springs using airborne thermal imagery: Case study from Pilgrim Hot Springs, Alaska. *Remote Sensing of Environment*, *136*, 37–46. https://doi.org/10.1016/j.rse.2013.04.008

Healy, J., & Hochstein, M. P. (1973). Horizontal flow in hydrothermal systems. *Journal of Hydrology (NZ)*, *12*(2), 71–82.

Heap, M. J., Gravley, D. M., Kennedy, B. M., Gilg, H. A., Bertolett, E., & Barker, S. L. L. (2019). Quantifying the role of hydrothermal alteration in creating geothermal and epithermal mineral resources: The Ohakuri ignimbrite (Taupō Volcanic Zone, New Zealand). *Journal of Volcanology and Geothermal Research*, *xxxx*, 106703. https://doi.org/10.1016/j.jvolgeores.2019.106703

Heap, M. J., Gravley, D. M., Kennedy, B. M., Gilg, H. A., Bertolett, E., & Barker, S. L. L. (2020). Quantifying the role of hydrothermal alteration in creating geothermal and epithermal mineral resources: The Ohakuri ignimbrite (Taupō Volcanic Zone, New Zealand). *Journal of Volcanology and Geothermal Research*, *390*, 106703. https://doi.org/10.1016/j.jvolgeores.2019.106703

Heap, M. J., Kennedy, B. M., Farquharson, J. I., Ashworth, J., Mayer, K., Letham-Brake, M., Reuschlé, T., Gilg, H. A., Scheu, B., Lavallée, Y., Siratovich, P., Cole, J., Jolly, A. D., Baud, P., & Dingwell, D. B. (2017). A multidisciplinary approach to quantify the permeability of the Whakaari/White Island volcanic hydrothermal system (Taupo Volcanic Zone, New Zealand). *Journal of Volcanology and Geothermal Research*, *332*, 88–108. https://doi.org/10.1016/j.jvolgeores.2016.12.004

Heasler, H., & Jaworowski, C. (2018). Hydrothermal monitoring of Norris Geyser Basin, Yellowstone National Park, USA, using airborne thermal infrared imagery. *Geothermics*, *72*(December 2017), 24–46. https://doi.org/10.1016/j.geothermics.2017.10.016

Hecker, C., der Meijde, M. van, & van der Meer, F. D. (2010). Thermal infrared spectroscopy on feldspars—Successes, limitations and their implications for remote sensing. *Earth-Science Reviews*, *103*(1–2), 60–70. https://doi.org/10.1016/j.earscirev.2010.07.005

Hecker, C., Hewson, R., Setianto, A., Saepuloh, A., & van der Meer, F. D. (2017). Multi-source remote sensing data analysis for geothermal targeting on Flores island. *Proceedings The 5th Indonesia International Geothermal Convention & Exhibition (IIGCE) 2017*, *August*, 1–7.

Hecker, C., Van Der Meijde, M., Van Der Werff, H., & Van Der Meer, F. D. (2008). Assessing the influence of reference spectra on synthetic SAM classification results. *IEEE Transactions on Geoscience and Remote Sensing*, *46*(12), 4162–4172. https://doi.org/10.1109/TGRS.2008.2001035

Hecker, C., van Ruitenbeek, F. J. A., Bakker, W. H., Fagbohun, B. J., Riley, D., van der Werff, H. M. A., & van der Meer, F. D. (2019). Mapping the wavelength position of mineral features in hyperspectral thermal infrared data. *International Journal of Applied Earth Observation and Geoinformation*, *79*(February), 133–140. https://doi.org/10.1016/j.jag.2019.02.013

Hedenquist, J. W. (1982). Fluid Flow in the Waiotapu Geothermal System, New Zealand: Implications for Its Potential. *Proceedings of the New Zealand Geothermal Workshop*, 61–67.

Hedenquist, J. W. (1991). Boiling and dilution in the shallow portion of the Waiotapu geothermal system , New Zealand. *Geochimica et Cosmochimica Acta*, *55*, 2753–2765.

Hedenquist, J. W., & Browne, P. R. L. (1989). The evolution of the Waiotapu geothermal system, New Zealand, based on the chemical and isotopic composition of its fluids, minerals and rocks. *Geochimica et Cosmochimica Acta*, *53*(9), 2235–2257. https://doi.org/10.1016/0016-7037(89)90347-5

Hedenquist, J. W., & Gulson, B. L. (1992). Intrusive and basement rock sources of lead in hydrothermal systems of the Taupo Volcanic Zone, New Zealand. *Geochimica et Cosmochimica Acta*, *56*(7), 2821–2829. https://doi.org/10.1016/0016-7037(92)90361-L

Hedenquist, J. W., & Henley, R. W. (1985). Hydrothermal eruptions in the Waiotapu geothermal system, New Zealand; their origin, associated breccias, and relation to precious metal mineralization. *Economic Geology*, *80*(6), 1640–1668. https://doi.org/10.2113/gsecongeo.80.6.1640

Hegan, B. D., Johnson, J. D., & Severne, C. (2001). Engineering and Development in Hazardous Terrain. Landslide Risk from the Hipaua Geothermal Area Near Waihi Village at the Southern End of Lake Taupo. *New Zealand Geotechnical Society 2001 Symposium*.

Heise, W., Caldwell, T. G., Bibby, H. M., & Bannister, S. C. (2008). Three-dimensional modelling of magnetotelluric data from the Rotokawa geothermal field, Taupo Volcanic Zone, New Zealand. *Geophysical Journal International*, *173*(2), 740–750. https://doi.org/10.1111/j.1365-246X.2008.03737.x

Heise, W., Caldwell, T. G., Bibby, H. M., & Bennie, S. L. (2010). Three-dimensional electrical resistivity image of magma beneath an active continental rift, Taupo Volcanic Zone, New Zealand. *Geophysical Research Letters*, *37*(10), 2–6. https://doi.org/10.1029/2010GL043110

Heller Pearlshtien, D., Pignatti, S., Greisman-Ran, U., & Ben-Dor, E. (2021). PRISMA sensor evaluation: A case study of mineral mapping performance over Makhtesh Ramon, Israel. *International Journal of Remote Sensing*, *42*(15), 5882–5914. https://doi.org/10.1080/01431161.2021.1931541

Hellman, M. J., & Ramsey, M. S. (2004). Analysis of hot springs and associated deposits in Yellowstone National Park using ASTER and AVIRIS remote sensing. *Journal of Volcanology and Geothermal Research*, *135*(1–2), 195–219. https://doi.org/10.1016/j.jvolgeores.2003.12.012

Henley, R. W., & Ellis, A. J. (1983). Geothermal systems ancient and modern: A geochemical review. *Earth Science Reviews*, *19*(1), 1–50. https://doi.org/10.1016/0012-8252(83)90075-2

Hetzer, A., Morgan, H. W., McDonald, I. R., & Daughney, C. J. (2007). Microbial life in Champagne Pool, a geothermal spring in Waiotapu, New Zealand. *Extremophiles*, *11*(4), 605–614. https://doi.org/10.1007/s00792-007-0073-2

Hewson, R., Mshiu, E., Hecker, C., van der Werff, H., van Ruitenbeek, F., Alkema, D., & van der Meer, F. (2020). The application of day and night time ASTER satellite imagery for geothermal and mineral mapping in East Africa. *International Journal of Applied Earth Observation and Geoinformation*, *85*(November 2019), 101991. https://doi.org/10.1016/j.jag.2019.101991

Heylen, R., Parente, M., & Gader, P. (2014). A review of nonlinear hyperspectral unmixing methods. *IEEE Journal of Selected Topics in Applied Earth Observations and Remote Sensing*, *7*(6), 1844–1868. https://doi.org/10.1109/JSTARS.2014.2320576

Hoang, N. T., & Koike, K. (2018). Comparison of hyperspectral transformation accuracies of multispectral Landsat TM, ETM+, OLI and EO-1 ALI images for detecting minerals in a geothermal prospect area. *ISPRS Journal of Photogrammetry and Remote Sensing*, *137*, 15–28. https://doi.org/10.1016/j.isprsjprs.2018.01.007

Hochstein, M. P. (2007). *Changes in geothermal manifestations and other surface features since the start of the thermal exploitation of the Mokai and Rotokawa Geothermal Fields, and an assessment of the Tokaanu-Waihi-Hipaua, Te Kopia and Reporoa Geothermal Fields and their Region*.

Hochstein, M. P., & Soengkono, S. (1997). Magnetic anomalies associated with high temperature reservoirs in the Taupo volcanic zone (New Zealand). *Geothermics*, *26*(1), 1–24. https://doi.org/10.1016/S0375-6505(96)00028-4

Hodder, D. T. (1970). Application of remote sensing to geothermal prospecting. *Geothermics*, *2*(PART 1). https://doi.org/10.1016/0375-6505(70)90035-0

Hong, H., Xiaoling, G., & Hua, Y. (2016). Variable selection using Mean Decrease Accuracy and Mean Decrease Gini based on Random Forest. *2016 7th IEEE International Conference on Software Engineering and Service Science (ICSESS)*, 219–224. https://doi.org/10.1109/ICSESS.2016.7883053

Honkavaara, E., Arbiol, R., Markelin, L., Martinez, L., Cramer, M., Bovet, S., Chandelier, L., Ilves, R., Klonus, S., Marshal, P., Schläpfer, D., Tabor, M., Thom, C., & Veje, N. (2009). Digital Airborne Photogrammetry—A New Tool for Quantitative Remote Sensing?—A State-of-the-Art Review On Radiometric Aspects of Digital Photogrammetric Images. *Remote Sensing*, *1*(3), 577–605. https://doi.org/10.3390/rs1030577

Hood, S. B., Cracknell, M. J., Gazley, M. F., & Reading, A. M. (2019). Element mobility and spatial zonation associated with the Archean Hamlet orogenic Au deposit, Western Australia: Implications for fluid pathways in shear zones. *Chemical Geology*, *514*(December 2018), 10–26. https://doi.org/10.1016/j.chemgeo.2019.03.022

Hook, S. J., Cawse-Nicholson, K., Barsi, J., Radocinski, R., Hulley, G. C., Johnson, W. R., Rivera, G., & Markham, B. (2020). In-Flight Validation of the ECOSTRESS, Landsats 7 and 8 Thermal Infrared Spectral Channels Using the Lake Tahoe CA/NV and Salton Sea CA Automated Validation Sites. *IEEE Transactions on Geoscience and Remote Sensing*, *58*(2), 1294–1302. https://doi.org/10.1109/TGRS.2019.2945701

Hook, S. J., Gabell, A. R., Green, A. A., & Kealy, P. S. (1992). A comparison of techniques for extracting emissivity information from thermal infrared data for geologic studies. *Remote Sensing of Environment*, *42*(2), 123–135. https://doi.org/10.1016/0034-4257(92)90096-3

Hook, S. J., & Rast, M. (1990). Mineralogic mapping using airborne visible infrared imaging spectrometer (AVIRIS), shortwave infrared (SWIR) data acquired over cuprite, Nevada. *Proceedings of the Second Airborne Visible/Infrared Imaging*.

Hope, A. S., Kimball, J. S., & Stow, D. A. (1993). The relationship between tussock tundra spectral reflectance properties and biomass and vegetation composition. *International Journal of Remote Sensing*, *14*(10), 1861–1874. https://doi.org/10.1080/01431169308954008

Hopkins, B., & Skellam, J. G. (1954). A new method for determining the type of distribution of plant individuals. *Annals of Botany*, *18*(2), 213–227. https://doi.org/10.1093/oxfordjournals.aob.a083391

Hou, L., Li, X., & Li, F. (2018). Hyperspectral-based Inversion of Heavy Metal Content in the Soil of Coal Mining Areas. *Journal of Environmental Quality*, *48*(1), 57–63. https://doi.org/10.2134/jeq2018.04.0130

Houghton, B. F., Wilson, C. J. N., McWilliams, M. O., Lanphere, M. A., Weaver, S. D., Briggs, R. M., & Pringle, M. S. (1995). Chronology and dynamics of a large silicic magmatic system: Central Taupo Volcanic Zone, New Zealand. *Geology*, *23*(3), 213–216. https://doi.org/10.1130/0091-7613(1995)023%3C0013:CADOAL%3E2.3.CO;2

Huang, C., Davis, L. S., & Townshend, J. R. G. (2002). An assessment of support vector machines for land cover classification. *International Journal of Remote Sensing*, *23*(4), 725–749. https://doi.org/10.1080/01431160110040323

Húdoková, H., Petrik, P., Petek-Petrik, A., Konôpková, A., Leštianska, A., Střelcová, K., Kmeť, J., & Kurjak, D. (2022). Heat-stress response of photosystem II in five ecologically important tree species of European temperate forests. *Biologia*, *77*(3), 671–680. https://doi.org/10.1007/s11756-021-00958-9

Hughes, M. R., & Fisher, T. J. (2022). *Introduction to Statistical Modeling*.

Hulley, G. C., Hook, S. J., & Baldridge, A. M. (2010). Investigating the effects of soil moisture on thermal infrared land surface temperature and emissivity using satellite retrievals and laboratory measurements. *Remote Sensing of Environment*, *114*(7), 1480–1493. https://doi.org/10.1016/j.rse.2010.02.002

Hunt, E. R., & Rock, B. N. (1989). Detection of changes in leaf water content using Near- and Middle-Infrared reflectances. *Remote Sensing of Environment*, *30*(1), 43–54. https://doi.org/10.1016/0034-4257(89)90046-1

Hunt, G. R. (1977). Spectral Signatures of Particulate Minerals in the Visible and Near Infrared. *Geophysics*, *42*, 501–513.

Hunt, G. R., & Ashley, R. P. (1979). *Altered Rock Spectra in the Visible and Near Infrared*.

Hunt, T. M., Glover, R. B., & Wood, C. P. (1994). Waimangu, Waiotapu, and Waikite Geothermal Systems, New Zealand: Backgound History. *Geothermics*, *23*(5), 379–400.

Hurst, T., Heise, W., Hreinsdottir, S., & Hamling, I. (2016). Geophysics of the Taupo Volcanic Zone: A review of recent developments. *Geothermics*, *59*, 188–204. https://doi.org/10.1016/j.geothermics.2015.09.008

Hutengs, C., Ludwig, B., Jung, A., Eisele, A., & Vohland, M. (2018). Comparison of Portable and Bench-Top Spectrometers for Mid-Infrared Diffuse Reflectance Measurements of Soils. *Sensors*, *18*(4), 993. https://doi.org/10.3390/s18040993

Idroes, R., Yusuf, M., Alatas, M., Subhan, Lala, A., Muhammad, Suhendra, R., Idroes, G. M., & Marwan. (2019). Geochemistry of Sulphate spring in the Ie Jue geothermal areas at Aceh Besar district, Indonesia. *IOP Conference Series: Materials Science and Engineering*, *523*(1), 012012. https://doi.org/10.1088/1757-899X/523/1/012012

Inskeep, W. P., Macur, R. E., Harrison, G., Bostick, B. C., & Fendorf, S. (2004). Biomineralization of As(V)-hydrous ferric oxyhydroxide in microbial mats of an acid-sulfate-chloride geothermal spring, Yellowstone National Park. *Geochimica et Cosmochimica Acta*, *68*(15), 3141–3155. https://doi.org/10.1016/j.gca.2003.09.020

Iriel, A., Lagorio, M. G., & Fernández Cirelli, A. (2015). Biosorption of arsenic from groundwater using Vallisneria gigantea plants. Kinetics, equilibrium and photophysical considerations. *Chemosphere*, *138*, 383–389. https://doi.org/10.1016/j.chemosphere.2015.06.053

Jaworowski, C., Heasler, H., Neale, C., Saravanan, S., & Masih, A. (2013). Temporal and seasonal variations of the hot spring basin hydrothermal system, Yellowstone National Park, USA. *Remote Sensing*, *5*(12), 6587–6610. https://doi.org/10.3390/rs5126587

Jaworowski, C., Heasler, H. P., Neale, C. M. U., & Sivarajan, S. (2010). Using thermal infrared imagery and LiDAR in Yellowstone geyser basins. *Yellowstone Science*, *18*(1), 8–19.

Jennejohn, D. (2009). Research and Development in Geothermal Exploration and Drilling. *Research and Development in Geothermal Exploration and Drilling*, *6*(13), 89–97.

Jensen, J. R. (2015). *Introductory Digital Image Processing: A Remote Sensing Perspective*. Pearson Education.

Jentsch, A., Jolie, E., Jones, D. G., Taylor-Curran, H., Peiffer, L., Zimmer, M., & Lister, B. (2020). Magmatic volatiles to assess permeable volcano-tectonic structures in the Los Humeros geothermal field, Mexico. *Journal of Volcanology and Geothermal Research*, *394*, 106820. https://doi.org/10.1016/j.jvolgeores.2020.106820

Jia, J., Wang, Y., Chen, J., Guo, R., Shu, R., & Wang, J. (2020). Status and application of advanced airborne hyperspectral imaging technology: A review. *Infrared Physics & Technology*, *104*, 103115. https://doi.org/10.1016/j.infrared.2019.103115

Jiang, Z., Li, P., Jiang, D., Dai, X., Zhang, R., Wang, Y., & Wang, Y. (2016). Microbial Community Structure and Arsenic Biogeochemistry in an Acid Vapor-Formed Spring in Tengchong Geothermal Area, China. *PLOS ONE*, *11*(1), e0146331. https://doi.org/10.1371/journal.pone.0146331

John, D. A., Sisson, T. W., Breit, G. N., Rye, R. O., & Vallance, J. W. (2008). Characteristics, extent and origin of hydrothermal alteration at Mount Rainier Volcano, Cascades Arc, USA: Implications for debris-flow hazards and mineral deposits. *Journal of Volcanology and Geothermal Research*, *175*(3), 289–314. https://doi.org/10.1016/j.jvolgeores.2008.04.004

Johnson, P. J., Stauffer, P. H., Omagbon, J., & Moore, C. R. (2022). Implications of rootless geothermal models: Missing processes, parameter compensation, and imposter convection. *Geothermics*, *102*, 102391. https://doi.org/10.1016/j.geothermics.2022.102391

Jolie, E., Scott, S., Faulds, J., Chambefort, I., Axelsson, G., Gutiérrez-Negrín, L. C., Regenspurg, S., Ziegler, M., Ayling, B., Richter, A., & Zemedkun, M. T. (2021). Geological controls on geothermal resources for power generation. *Nature Reviews Earth and Environment*, *2*(5), 324–339. https://doi.org/10.1038/s43017-021-00154-y

Jones, K. L., Schulenburg, N. W., & Wright, C. (2010). Hyperspectral remote sensing techniques for locating geothermal areas. *SPIE7687-Active and Passive Signatures*, *7687*, 76870J-76870J – 7. https://doi.org/10.1117/12.855444

Kabata-Pendias, A. (2010). Trace Elements in Soils and Plants. In *Angewandte Chemie International Edition, 6(11), 951–952.* CRC Press. https://doi.org/10.1201/b10158

Kamau, M., Hecker, C., & Lievens, C. (2020). Use of Short-Wave Infrared Reflectance (SWIR) Spectroscopy to Characterize Hydrothermal alteration minerals in Olkaria Geothermal System, Kenya. *Proceedings,45th Workshop on Geothermal Reservoir Engineering*, *Figure 1*, 1–15.

Kaya, E., Hochstein, M. P., Yeh, A., & Sullivan, M. J. O. (2015). Aspects of natural heat transfer of a geothermal system in moderate terrain: The greater Waiotapu geothermal system , New Zealand. *Proceedings World Geothermal Congress 2015*, *April*, 1–12.

Kaya, E., O'Sullivan, M. J., & Hochstein, M. P. (2014). A three dimensional numerical model of the Waiotapu, Waikite and Reporoa geothermal areas, New Zealand. *Journal of Volcanology and Geothermal Research*, *283*, 127–142. https://doi.org/10.1016/j.jvolgeores.2014.07.008

Kazberuk, W., Szulc, W., & Rutkowska, B. (2021). Use Bottom Sediment to Agriculture—Effect on Plant and Heavy Metal Content in Soil. *Agronomy*, *11*(6), 1077. https://doi.org/10.3390/agronomy11061077

Keesari, T., Chatterjee, S., Kumar, M., Mohokar, H., Sinha, U. K., Roy, A., Pant, D., & Patbhaje, S. D. (2022). Tracing thermal and non-thermal water circulations in shear zones of Eastern Ghats Mobile Belt zone, Eastern India- inferences on sustainability of geothermal resources. *Journal of Hydrology*, *612*, 128172. https://doi.org/10.1016/j.jhydrol.2022.128172

Kelley, K., & Lai, K. (2011). Accuracy in Parameter Estimation for the Root Mean Square Error of Approximation: Sample Size Planning for Narrow Confidence Intervals. *Multivariate Behavioral Research*, *46*(1), 1–32. https://doi.org/10.1080/00273171.2011.543027

Kelly, G. (2011). History and potential of renewable energy development in New Zealand. *Renewable and Sustainable Energy Reviews*, *15*(5), 2501–2509. https://doi.org/10.1016/j.rser.2011.01.021

Kennedy, B. M., Farquhar, A., Hilderman, R., Villeneuve, M. C., Heap, M. J., Mordensky, S., Kilgour, G., Jolly, A., Christenson, B., & Reuschlé, T. (2020). Pressure controlled permeability in a conduit filled with fractured hydrothermal Breccia reconstructed from ballistics from Whakaari (White island), New Zealand. *Geosciences (Switzerland)*, *10*(4). https://doi.org/10.3390/geosciences10040138

Kereszturi, G., Pullanagari, R. R., Mead, S., Schaefer, L. N., Procter, J., Schleiffarth, W. K., & Kennedy, B. (2018). Geological mapping of hydrothermal alteration on volcanoes from multi-sensor platforms. *International Geoscience and Remote Sensing Symposium (IGARSS)*, *2018-July*, 220–223. https://doi.org/10.1109/IGARSS.2018.8518818

Kereszturi, G., Schaefer, L. N., Miller, C., & Mead, S. (2020). Hydrothermal Alteration on Composite Volcanoes: Mineralogy, Hyperspectral Imaging, and Aeromagnetic Study of Mt Ruapehu, New Zealand. *Geochemistry, Geophysics, Geosystems*, *21*(9), 1–28. https://doi.org/10.1029/2020gc009270

Kereszturi, G., Schaefer, L. N., Schleiffarth, W. K., Procter, J., Pullanagari, R. R., Mead, S., & Kennedy, B. (2018). Integrating airborne hyperspectral imagery and LiDAR for volcano mapping and monitoring through image classification. *International Journal of Applied Earth*

Observation and Geoinformation, *73*(May), 323–339. https://doi.org/10.1016/j.jag.2018.07.006

Khaleghi, A., Naderi, R., Brunetti, C., Maserti, B. E., Salami, S. A., & Babalar, M. (2019). Morphological, physiochemical and antioxidant responses of Maclura pomifera to drought stress. *Scientific Reports*, *9*(1), 19250. https://doi.org/10.1038/s41598-019-55889-y

Khan, A., Khan, S., Khan, M. A., Qamar, Z., & Waqas, M. (2015). The uptake and bioaccumulation of heavy metals by food plants, their effects on plants nutrients, and associated health risk: A review. *Environmental Science and Pollution Research*, *22*(18), 13772–13799. https://doi.org/10.1007/s11356-015-4881-0

Khayatnezhad, M., & Gholamin, R. (2020). Study of Durum Wheat Genotypes' Response to Drought Stress Conditions. *HELIX*, *10*(5), 98–103. https://doi.org/10.29042/2020-10-5-98-103

King, P. L., Ramsey, M. S., McMillan, P. F., & Swayze, G. (2004). *LABORATORY FOURIER TRANSFORM INFRARED SPECTROSCOPY METHODS FOR GEOLOGIC SAMPLES*.

Kissling, W. M., & Weir, G. J. (2005). The spatial distribution of the geothermal fields in the Taupo Volcanic Zone, New Zealand. *Journal of Volcanology and Geothermal Research*, *145*(1–2), 136–150. https://doi.org/10.1016/j.jvolgeores.2005.01.006

Kokaly, R. F. (2001). Investigating a physical basis for spectroscopic estimates of leaf nitrogen concentration. *Remote Sensing of Environment*, *75*(2), 153–161. https://doi.org/10.1016/S0034-4257(00)00163-2

Kokaly, R. F., & Skidmore, A. K. (2015). Plant phenolics and absorption features in vegetation reflectance spectra near 1.66 μm. *International Journal of Applied Earth Observation and Geoinformation*, *43*, 55–83. https://doi.org/10.1016/j.jag.2015.01.010

Koon Koon, R., Marshall, S., Morna, D., McCallum, R., & Ashtine, M. (2020). A Review of Caribbean Geothermal Energy Resource Potential. *The West Indian Journal of Engineering*, *42*(2), 37–43.

Kovalevsky, A. L. (1987). *Biogeochemical Exploration for Mineral Deposits*.

Kraal, K., Ayling, B., Calvin, W., & Browning, D. (2018). Comparison of a Portable Field Spectrometer and Automated Imaging on Geothermal Drill Core: A Pilot Study. *GRC Transactions*, 13.

Kraal, K. O., Ayling, B. F., Blake, K., Hackett, L., Perdana, T. S. P., & Stacey, R. (2021). Linkages between hydrothermal alteration, natural fractures, and permeability: Integration of borehole data for reservoir characterization at the Fallon FORGE EGS site, Nevada, USA. *Geothermics*, *89*, 101946. https://doi.org/10.1016/j.geothermics.2020.101946

Kratt, C., Calvin, W., & Coolbaugh, M. (2004). Geothermal exploration with hyperspectral data in the Carson Sink, Nevada. *International Geoscience and Remote Sensing Symposium (IGARSS)*, *2*(C), 1304–1306. https://doi.org/10.1109/igarss.2004.1368656

Kratt, C., Calvin, W., & Coolbaugh, M. (2006). Geothermal exploration with Hymap hyperspectral data at Brady–Desert Peak, Nevada. *Remote Sensing of Environment*, *104*(3), 313–324. https://doi.org/10.1016/j.rse.2006.05.005

Kratt, C., Calvin, W. M., & Coolbaugh, M. F. (2010). Mineral mapping in the Pyramid Lake basin: Hydrothermal alteration, chemical precipitates and geothermal energy potential. *Remote Sensing of Environment*, *114*(10), 2297–2304. https://doi.org/10.1016/j.rse.2010.05.006

Kratt, C., Coolbaugh, M., Peppin, B., & Sladek, C. (2009). Identification of a new blind geothermal system with hyperspectral remote sensing and shallow temperature measurements at Columbus Salt Marsh, Esmeralda County, Nevada. *Geothermal Resources*, *33*, 481–485.

Krizhevsky, A., Sutskever, I., & Hinton, G. E. (2017). ImageNet classification with deep convolutional neural networks. *Communications of the ACM*, *60*(6), 84–90. https://doi.org/10.1145/3065386

Kruse, F. a. (2004). Comparison of ATREM, ACORN, and FLAASH Atmospheric Corrections Using Low-Altitude AVIRIS Data of Boulder, CO. *13th JPL Airborne Geoscience Workshop.*, *May*, 1–10.

Kruse, F. A. (2014). Combined SWIR and LWIR mineral mapping using MASTER/ASTER. *IEEE International Geoscience and Remote Sensing Symposium*, *4*(May), 2267–2269. https://doi.org/10.1109/IGARSS.2002.1026514

Kruse, F. A., Lefkoff, A. B., Boardman, J. W., Heidebrecht, K. B., Shapiro, A. T., Barloon, P. J., & Goetz, A. F. H. (1993). The spectral image processing system (SIPS)-interactive visualization and analysis of imaging spectrometer data. *Remote Sensing of Environment*, *44*(2–3), 145–163. https://doi.org/10.1016/0034-4257(93)90013-N

Kruse, F. A., Taranik, J. V., Coolbaugh, M., Michaels, J., Littlefield, E. F., Calvin, W. M., & Martini, B. A. (2011). Effect of reduced spatial resolution on mineral mapping using imaging spectrometry-examples using hyperspectral infrared imager (HyspIRI)-simulated data. *Remote Sensing*, *3*(8), 1584–1602. https://doi.org/10.3390/rs3081584

Kumari, W. G. P., & Ranjith, P. G. (2019). Sustainable development of enhanced geothermal systems based on geotechnical research – A review. *Earth-Science Reviews*, *199*(September), 102955. https://doi.org/10.1016/j.earscirev.2019.102955

Kuwatani, T., Yoshida, K., Ueki, K., Oyanagi, R., Uno, M., & Akaho, S. (2020). Sparse isocon analysis: A data-driven approach for material transfer estimation. *Chemical Geology*, *532*(June 2019), 119345. https://doi.org/10.1016/j.chemgeo.2019.119345

Lagat, J. (2007). Hydrothermal alteration mineralogy in geothermal fields with case examples from Olkaria domes geothermal field, Kenya. *Short Course II on Surface Exploration for Geothermal …*, 1–24.

Lamur, A., Kendrick, J. E., Eggertsson, G. H., Wall, R. J., Ashworth, J. D., & Lavallée, Y. (2017). The permeability of fractured rocks in pressurised volcanic and geothermal systems. *Scientific Reports*, *7*(1), 1–9. https://doi.org/10.1038/s41598-017-05460-4

Lassalle, G., Fabre, S., Credoz, A., Hédacq, R., Borderies, P., Bertoni, G., Erudel, T., Buffan-Dubau, E., Dubucq, D., & Elger, A. (2019). Detection and discrimination of various oil-contaminated

soils using vegetation reflectance. *Science of the Total Environment*, *655*, 1113–1124. https://doi.org/10.1016/j.scitotenv.2018.11.314

Lattanzi, P., Benesperi, R., Morelli, G., Rimondi, V., & Ruggieri, G. (2020). Biomonitoring Studies in Geothermal Areas: A Review. *Frontiers in Environmental Science*, *8*(x), 1–7. https://doi.org/10.3389/fenvs.2020.579343

Laukamp, C., Rodger, A., LeGras, M., Lampinen, H., Lau, I. C., Pejcic, B., Stromberg, J., Francis, N., & Ramanaidou, E. (2021). Mineral Physicochemistry Underlying Feature-Based Extraction of Mineral Abundance and Composition from Shortwave, Mid and Thermal Infrared Reflectance Spectra. *Minerals*, *11*(4), 347. https://doi.org/10.3390/min11040347

Lausch, A., Bastian, O., Klotz, S., Leitão, P. J., Jung, A., Rocchini, D., Schaepman, M. E., Skidmore, A. K., Tischendorf, L., & Knapp, S. (2018). Understanding and assessing vegetation health by in situ species and remote-sensing approaches. *Methods in Ecology and Evolution*, *9*(8), 1799–1809. https://doi.org/10.1111/2041-210X.13025

Lewis, A. J., Palmer, M. R., Sturchio, N. C., & Kemp, A. J. (1997). The rare earth element geochemistry of acid-sulphate and acid-sulphate-chloride geothermal systems from Yellowstone National Park, Wyoming, USA. *Geochimica et Cosmochimica Acta*, *61*(4), 695–706. https://doi.org/10.1016/S0016-7037(96)00384-5

Li, H., Zhou, B., Xu, F., & Wei, Z. (2022). Hyperspectral characterization and chlorophyll content inversion of reclaimed vegetation in rare earth mines. *Environmental Science and Pollution Research*. https://doi.org/10.1007/s11356-021-16772-4

Li, J., Sun, Y., Jiang, X., Chen, B., & Zhang, X. (2018). Arbuscular mycorrhizal fungi alleviate arsenic toxicity to Medicago sativa by influencing arsenic speciation and partitioning. *Ecotoxicology and Environmental Safety*, *157*(18), 235–243. https://doi.org/10.1016/j.ecoenv.2018.03.073

Li, J., Zhang, J., Chen, F., Zhao, K., & Zeng, D. (2022). Adaptive Material Matching for Hyperspectral Imagery Destriping. *IEEE Transactions on Geoscience and Remote Sensing*, *60*, 1–20. https://doi.org/10.1109/TGRS.2022.3158901

Li, S., Marsaglia, N., Garth, C., Woodring, J., Clyne, J., & Childs, H. (2018). Data Reduction Techniques for Simulation, Visualization and Data Analysis. *Computer Graphics Forum*, *37*(6), 422–447. https://doi.org/10.1111/cgf.13336

Li, X. C., Liu, L. L., & Huang, L. K. (2020). COMPARISON OF SEVERAL REMOTE SENSING IMAGE CLASSIFICATION METHODS BASED ON ENVI. *The International Archives of the Photogrammetry, Remote Sensing and Spatial Information Sciences*, *XLII-3/W10*, 605–611. https://doi.org/10.5194/isprs-archives-XLII-3-W10-605-2020

Li, Y., Tan, X., Zhang, W., Jiao, Q., Xu, Y., Li, H., Zou, Y., Yang, L., & Fang, Y. (2021). Research and Application of Several Key Techniques in Hyperspectral Image Preprocessing. *Frontiers in Plant Science*, *12*, 627865. https://doi.org/10.3389/fpls.2021.627865

Li, Y., Yang, K., Cheng, F., & Zhang, C. (2019). Development of a new heavy metal vegetation index for improving monitoring of copper and lead concentration in corn. *European Journal of Remote Sensing*, *52*(1), 632–639. https://doi.org/10.1080/22797254.2019.1700398

Lichtenthaler, H. K. (1996). Vegetation Stress: An Introduction to the Stress Concept in Plants. *Journal of Plant Physiology*, *148*(1–2), 4–14. https://doi.org/10.1016/s0176-1617(96)80287-2

Lillesand, T., Kiefer, R. W., & Chipman, J. W. (2015). *Remote Sensing and Image Interpretation* (7th ed.). Wiley.

Lillesand, T. M., & Kiefer, R. W. (1979). Remote sensing and image interpretation. In *Remote sensing and image interpretation.* https://doi.org/10.2307/634969

Lin, A., Chen, P., & Sado, K. (2018). Recurrent large earthquakes related with an active fault-volcano system, southwest Japan. *Scientific Reports*, *8*(1), 14081. https://doi.org/10.1038/s41598-018-32140-8

Littlefield, E. F., & Calvin, W. M. (2014). Geothermal exploration using imaging spectrometer data over Fish Lake Valley, Nevada. *Remote Sensing of Environment*, *140*, 509–518. https://doi.org/10.1016/j.rse.2013.09.007

Liu, J., Hu, J., Bürgmann, R., Li, Z., Sun, Q., & Ma, Z. (2021). A Strain-Model Based InSAR Time Series Method and Its Application to The Geysers Geothermal Field, California. *Journal of Geophysical Research: Solid Earth*, *126*(8). https://doi.org/10.1029/2021JB021939

Liu, J., Xie, J., Meng, T., & Dong, H. (2022). Organic matter estimation of surface soil using successive projection algorithm. *Agronomy Journal*, *114*(4), 1944–1951. https://doi.org/10.1002/agj2.20934

Liu, P., Zhang, H., & Eom, K. B. (2017). Active Deep Learning for Classification of Hyperspectral Images. *IEEE Journal of Selected Topics in Applied Earth Observations and Remote Sensing*, *10*(2), 712–724. https://doi.org/10.1109/JSTARS.2016.2598859

Liu, R., Zhu, T., Jiang, Y., Li, B., Yu, L., Du, Y., & Wang, Y. (2019). A predictive model correlating permeability to two-dimensional fracture network parameters. *Bulletin of Engineering Geology and the Environment*, *78*(3), 1589–1605. https://doi.org/10.1007/s10064-018-1231-8

Liu, S., Ye, C., Sun, Q., Xu, M., Duan, Z., Sheng, H., & Wan, J. (2021). Detection of Geothermal Anomaly Areas with Spatio-Temporal Analysis Using Multitemporal Remote Sensing Data. *IEEE Journal of Selected Topics in Applied Earth Observations and Remote Sensing*, *14*, 4866–4878. https://doi.org/10.1109/JSTARS.2021.3076162

Liu, W. J., Zhu, Y. G., Hu, Y., Williams, P. N., Gault, A. G., Meharg, A. A., Charnock, J. M., & Smith, F. A. (2006). Arsenic Sequestration in Iron Plaque, Its Accumulation and Speciation in Mature Rice Plants (Oryza Sativa L.). *Environmental Science & Technology*, *40*(18), 5730–5736. https://doi.org/10.1021/es060800v

Lloyd, E. F. (1959). The Hot Springs and Hydrothermal Eruptions of Waiotapu. *New Zealand Journal of Geology and Geophysics*, *2*(1), 141–176. https://doi.org/10.1080/00288306.1959.10431319

Lloyd, K., Beadel, S., Smith, D., Bycroft, C., Bawden, R., Harvey, M., Mcleod, J., & Luketina, K. (2016). *Ground and Aerial Photography of Geothermal Vegetation At Craters of the Moon Geothermal Area , Waikato*. *2016*(May).

Llugany, M., Poschenrieder, C., & Barceló, J. (2000). Assessment of barium toxicity in bush beans. *Archives of Environmental Contamination and Toxicology*, *39*(4), 440–444. https://doi.org/10.1007/s002440010125

Lopinto, E., & Ananasso, C. (2013). The Prisma Hyperspectral Mission. *European Space Agency, (Special Publication) ESA SP*, *SP-740*.

Loppi, S., & Bargagli, R. (1996). Lichen biomonitoring of trace elements in a geothermal area (central Italy). *Water, Air, and Soil Pollution*, *88*(1–2), 177–187. https://doi.org/10.1007/BF00157421

Lorenz, S., Ghamisi, P., Kirsch, M., Jackisch, R., Rasti, B., & Gloaguen, R. (2021). Feature extraction for hyperspectral mineral domain mapping: A test of conventional and innovative methods. *Remote Sensing of Environment*, *252*(October 2020), 112129. https://doi.org/10.1016/j.rse.2020.112129

Lund, J. W., Huttrer, G. W., & Toth, A. N. (2022). Characteristics and trends in geothermal development and use, 1995 to 2020. *Geothermics*, *105*, 102522. https://doi.org/10.1016/j.geothermics.2022.102522

Luo, G., Chen, G., Tian, L., Qin, K., & Qian, S. E. (2016). Minimum Noise Fraction versus Principal Component Analysis as a Preprocessing Step for Hyperspectral Imagery Denoising. *Canadian Journal of Remote Sensing*, *42*(2), 106–116. https://doi.org/10.1080/07038992.2016.1160772

Lv, W., & Wang, X. (2020). Overview of Hyperspectral Image Classification. *Journal of Sensors*, *2020*. https://doi.org/10.1155/2020/4817234

Lyapustin, A. I., & Kaufman, Y. J. (2001). Role of adjacency effect in the remote sensing of aerosol. *Journal of Geophysical Research: Atmospheres*, *106*(D11), 11909–11916. https://doi.org/10.1029/2000JD900647

Lynne, B. Y. (2012). Mapping vent to distal-apron hot spring paleo-flow pathways using siliceous sinter architecture. *Geothermics*, *43*, 3–24. https://doi.org/10.1016/j.geothermics.2012.01.004

Lynne, B. Y., & Campbell, K. A. (2004). Morphologic and mineralogic transitions from opal-A to opal-CT in low-temperature siliceous sinter diagenesis, Taupo Volcanic Zone, New Zealand. *Journal of Sedimentary Research*, *74*(4), 561–579. https://doi.org/10.1306/011704740561

Lyon, R. J. P., & Green, A. A. (1975). REFLECTANCE AND EMITTANCE OF TERRAIN IN THE MID-INFRARED (6-25μm) REGION. In *Infrared and Raman Spectroscopy of Lunar and Terrestrial Minerals* (pp. 165–195). Elsevier. https://doi.org/10.1016/B978-0-12-399950-4.50012-4

Lyons, M. B., Keith, D. A., Phinn, S. R., Mason, T. J., & Elith, J. (2018). A comparison of resampling methods for remote sensing classification and accuracy assessment. *Remote Sensing of Environment*, *208*(September 2017), 145–153. https://doi.org/10.1016/j.rse.2018.02.026

Macur, R. E., Langner, H. W., Kocar, B. D., & Inskeep, W. P. (2004). Linking geochemical processes with microbial community analysis: Successional dynamics in an arsenic-rich, acid-sulphate-chloride geothermal spring. *Geobiology*, *2*(3), 163–177. https://doi.org/10.1111/j.1472-4677.2004.00032.x

Madani, A. A., & Emam, A. A. (2011). SWIR ASTER band ratios for lithological mapping and mineral exploration: A case study from El Hudi area, southeastern desert, Egypt. *Arabian Journal of Geosciences*, *4*(1), 45–52. https://doi.org/10.1007/s12517-009-0059-8

Maes, W. H., & Steppe, K. (2019). Perspectives for Remote Sensing with Unmanned Aerial Vehicles in Precision Agriculture. *Trends in Plant Science*, *24*(2), 152–164. https://doi.org/10.1016/j.tplants.2018.11.007

Maghsoudi, Y., van der Meer, F., Hecker, C., Perissin, D., & Saepuloh, A. (2018). Using PS-InSAR to detect surface deformation in geothermal areas of West Java in Indonesia. *International Journal of Applied Earth Observation and Geoinformation*, *64*(November 2016), 386–396. https://doi.org/10.1016/j.jag.2017.04.001

Maity, J. P., Liu, C. C., Nath, B., Bundschuh, J., Kar, S., Jean, J. S., Bhattacharya, P., Liu, J. H., Atla, S. B., & Chen, C. Y. (2011). Biogeochemical characteristics of Kuan-Tzu-Ling, Chung-Lun and Bao-Lai hot springs in southern Taiwan. *Journal of Environmental Science and Health - Part A Toxic/Hazardous Substances and Environmental Engineering*, *46*(11), 1207–1217. https://doi.org/10.1080/10934529.2011.598788

Manzo, C., Salvini, R., Guastaldi, E., Nicolardi, V., & Protano, G. (2013). Reflectance spectral analyses for the assessment of environmental pollution in the geothermal site of Mt. Amiata (Italy). *Atmospheric Environment*, *79*, 650–665. https://doi.org/10.1016/j.atmosenv.2013.06.038

Mardiati, D., Setianto, A., & Harijoko, A. (2020). Revealing Geothermal Potential Areas with Remote Sensing Analysis for Surface Temperature and Lineament Density: Case Study in South Bajawa, NTT, Indonesia. *IOP Conference Series: Earth and Environmental Science*, *417*(1). https://doi.org/10.1088/1755-1315/417/1/012009

Marwan, Idroes, R., Yanis, M., Idroes, G. M., & Syahriza. (2021). A Low-Cost Uav Based Application for Identify and Mapping a Geothermal Feature in Ie Jue Manifestation, Seulawah Volcano, Indonesia. *International Journal of GEOMATE*, *20*(80), 135–142. https://doi.org/10.21660/2021.80.j2044

Mauriohooho, K., Barker, S. L. L., Rae, A. J., & Simpson, M. P. (2014). Hydrothermal Alteration of the Tauhara Geothermal Field, an active hydrothermal system. *AusIMM New Zealand Branch Annual Conference 2014, November*, 371–381.

Mäyrä, J., Keski-Saari, S., Kivinen, S., Tanhuanpää, T., Hurskainen, P., Kullberg, P., Poikolainen, L., Viinikka, A., Tuominen, S., Kumpula, T., & Vihervaara, P. (2021). Tree species classification from airborne hyperspectral and LiDAR data using 3D convolutional neural networks. *Remote Sensing of Environment*, *256*(February). https://doi.org/10.1016/j.rse.2021.112322

Maza, S., Collo, G., Morata, D., Cuña-Rodriguez, C., Taussi, M., & Renzulli, A. (2021). The Hydrothermal Alteration of the Cordón de Inacaliri Volcanic Complex in the Framework of the Hidden Geothermal Systems within the Pabelloncito Graben (Northern Chile). *Minerals*, *11*(11), 1279. https://doi.org/10.3390/min11111279

McKinley, J. M., Hron, K., Grunsky, E. C., Reimann, C., de Caritat, P., Filzmoser, P., van den Boogaart, K. G., & Tolosana-Delgado, R. (2016). The single component geochemical map: Fact or fiction? *Journal of Geochemical Exploration*, *162*, 16–28. https://doi.org/10.1016/j.gexplo.2015.12.005

McLachlan, G. J. (1992). *Discriminant Analysis and Statistical Pattern Recognition*. John Wiley & Sons, Inc. https://doi.org/10.1002/0471725293

McLellan, J. G., Oliver, N. H. S., Hobbs, B. E., & Rowland, J. V. (2010). Modelling fluid convection stability in continental faulted rifts with applications to the Taupo Volcanic Zone, New Zealand. *Journal of Volcanology and Geothermal Research*, *190*(1–2), 109–122. https://doi.org/10.1016/j.jvolgeores.2009.11.015

Melgani, F., & Bruzzone, L. (2004). Classification of hyperspectral remote sensing images with support vector machines. *IEEE Transactions on Geoscience and Remote Sensing*, *42*(8), 1778–1790. https://doi.org/10.1109/TGRS.2004.831865

Meng, F., Liang, X., Xiao, C., & Wang, G. (2021). Geothermal resource potential assessment utilizing GIS - based multi criteria decision analysis method. *Geothermics*, *89*(October 2020), 101969. https://doi.org/10.1016/j.geothermics.2020.101969

Meza, P., Parra, F., Torres, S. N., Pezoa, J. E., & Coelho, P. (2011). *A multidimensional approach for striping noise compensation in hyperspectral imaging devices* (P. D. LeVan, A. K. Sood, P. S. Wijewarnasuriya, M. Razeghi, J. L. Pau Vizcaíno, R. Sudharsanan, M. P. Ulmer, & T. Manzur, Eds.; p. 81550I). https://doi.org/10.1117/12.892246

Mia, M. B., Bromley, C. J., & Fujimitsu, Y. (2012a). Monitoring heat flux using Landsat TM/ETM+ thermal infrared data—A case study at Karapiti ('Craters of the Moon') thermal area, New Zealand. *Journal of Volcanology and Geothermal Research*, *235–236*, 1–10. https://doi.org/10.1016/j.jvolgeores.2012.05.005

Mia, M. B., Bromley, C. J., & Fujimitsu, Y. (2012). Monitoring heat flux using Landsat TM/ETM+ thermal infrared data—A case study at Karapiti ('Craters of the Moon') thermal area, New Zealand. *Journal of Volcanology and Geothermal Research*, *235–236*, 1–10. https://doi.org/10.1016/j.jvolgeores.2012.05.005

Mia, M. B., Bromley, C. J., & Fujimitsu, Y. (2013). Monitoring Heat Losses Using Landsat ETM + Thermal Infrared Data: A Case Study in Unzen Geothermal Field, Kyushu, Japan. *Pure and Applied Geophysics*, *170*(12), 2263–2271. https://doi.org/10.1007/s00024-013-0662-1

Mia, M. B., Nishijima, J., & Fujimitsu, Y. (2014). Exploration and monitoring geothermal activity using Landsat ETM+images. A case study at Aso volcanic area in Japan. *Journal of Volcanology and Geothermal Research*, *275*. https://doi.org/10.1016/j.jvolgeores.2014.02.008

Mielke, P., Bignall, G., & Sass, I. (2014). Predicting the Effect of Hydrothermal Alteration on Rock. *36th New Zealand Geothermal Workshop*, *November*.

Milicich, S. D., Mortimer, N., Villamor, P., Wilson, C. J. N., Sagar, M. W., Ireland, T. R., Milicich, S. D., Mortimer, N., Villamor, P., Wilson, C. J. N., Chambefort, I., Sagar, M. W., Ireland, T.

R., & Mesozoic, T. (2020). The Mesozoic terrane boundary beneath the Taupo Volcanic Zone , New Zealand , and potential controls on geothermal system characteristics The Mesozoic terrane boundary beneath the Taupo Volcanic Zone , New. *New Zealand Journal of Geology and Geophysics*, *0*(0), 1–12. https://doi.org/10.1080/00288306.2020.1823434

Mngadi, M., Odindi, J., Mutanga, O., & Sibanda, M. (2022). Estimating aboveground net primary productivity of reforested trees in an urban landscape using biophysical variables and remotely sensed data. *Science of The Total Environment*, *802*, 149958. https://doi.org/10.1016/j.scitotenv.2021.149958

Modriniak, N., & Studt, F. E. (1959). Geological structure and volcanism of the Taupo-Tarawera district. *New Zealand Journal of Geology and Geophysics*, *2*(4), 654–684. https://doi.org/10.1080/00288306.1959.10422763

Moeck, I. S. (2014). Catalog of geothermal play types based on geologic controls. *Renewable and Sustainable Energy Reviews*, *37*, 867–882. https://doi.org/10.1016/j.rser.2014.05.032

Molinaro, A. M., Simon, R., & Pfeiffer, R. M. (2005). Prediction error estimation: A comparison of resampling methods. *Bioinformatics*, *21*(15), 3301–3307. https://doi.org/10.1093/bioinformatics/bti499

Mongillo, M. A. (1994). Aerial Thermal Infrared Mapping of the Waimangu-Waiotapu Geothermal Region, New Zealand. *Geothermics*, *23*(5), 379–400.

Monteiro, F. A., Nogueirol, R. C., Carrijo Azevedo Melo, L., Guirado Artur, G. A., & da Rocha, F. (2011). Effect of barium on growth and macronutrient nutrition in Tanzania guineagrass grown in nutrient solution. *Communications in Soil Science and Plant Analysis*, *42*(13), 1510–1521. https://doi.org/10.1080/00103624.2011.581725

Moreno-Torres, J. G., Saez, J. A., & Herrera, F. (2012). Study on the impact of partition-induced dataset shift on k-fold cross-validation. *IEEE Transactions on Neural Networks and Learning Systems*, *23*(8), 1304–1312. https://doi.org/10.1109/TNNLS.2012.2199516

Morfopoulos, C., Müller, J. F., Stavrakou, T., Bauwens, M., De Smedt, I., Friedlingstein, P., Prentice, I. C., & Regnier, P. (2022). Vegetation responses to climate extremes recorded by remotely sensed atmospheric formaldehyde. *Global Change Biology*, *28*(5), 1809–1822. https://doi.org/10.1111/gcb.15880

Morifuji, Y., Fujimitsu, Y., Nishijima, J., Mia, M. B., & Onizuka, S. (2021). Analysis of Heat Discharge Rate in Geothermal Areas Using Remote Sensing Techniques: Case Study of Unzen Geothermal Area, Japan; Papandayan and Tangkuban Perahu Geothermal Area, Indonesia. *Pure and Applied Geophysics*, *178*(6), 2241–2256. https://doi.org/10.1007/s00024-021-02743-w

Mountrakis, G., Im, J., & Ogole, C. (2011). Support vector machines in remote sensing: A review. *ISPRS Journal of Photogrammetry and Remote Sensing*, *66*(3), 247–259. https://doi.org/10.1016/j.isprsjprs.2010.11.001

Moyersoen, B., & Beever, R. E. (2004). Abundance and characteristics of Pisolithus ectomycorrhizas in New Zealand geothermal areas. *Mycologia*, *96*(6), 1225–1232. https://doi.org/10.1080/15572536.2005.11832871

Müller, K., Daus, B., Mattusch, J., Vetterlein, D., Merbach, I., & Wennrich, R. (2013). Impact of arsenic on uptake and bio-accumulation of antimony by arsenic hyperaccumulator Pteris vittata. *Environmental Pollution*, *174*, 128–133. https://doi.org/10.1016/j.envpol.2012.10.024

Muriithi, F. K. (2015). Centered log-ratio (clr) transformation and robust principal component analysis of long-term NDVI data reveal vegetation activity linked to climate processes. *Climate*, *3*(1), 135–149. https://doi.org/10.3390/cli3010135

Mutua, J., Friese, a, Kuehn, F., Lopeyok, T., Mutonga, M., & Ochmann, N. (2013). High Resolution Airborne Thermal Infrared Remote Sensing Study , Silali Geothermal Prospect , Kenya. *Short Course VIII on Exploration for Geothermal Resources*, 1–10.

Muukkonen, P. (2005). Vegetation of geothermal areas on the North Island, New Zealand. *Terra*, *117*(4), 265–278.

Nairn, I. A., Hedenquist, J. W., Villamor, P., Berryman, K. R., & Shane, P. A. (2005). The ~AD1315 Tarawera and Waiotapu eruptions, New Zealand: Contemporaneous rhyolite and hydrothermal eruptions driven by an arrested basalt dike system? *Bulletin of Volcanology*, *67*(2), 186–193. https://doi.org/10.1007/s00445-004-0373-7

Nairn, I. A., Wood, C. P., & Bailey, R. A. (1994). The Reporoa Caldera, Taupo Volcanic Zone: Source of the Kaingaroa Ignimbrites. *Bulletin of Volcanology*, *56*(6–7), 529–537. https://doi.org/10.1007/BF00302833

Nash, G. D., Johnson, G. W., & Johnson, S. (2004). Hyperspectral detection of geothermal system-related soil mineralogy anomalies in Dixie Valley, Nevada: A tool for exploration. *Geothermics*, *33*(6), 695–711. https://doi.org/10.1016/j.geothermics.2004.06.002

Nash, G. D., Moore, J. N., & Sperry, T. (2003). Vegetal-spectral anomaly detection at the Cove Fort-Sulphurdale thermal anomaly, Utah, USA: Implications for use in geothermal exploration. *Geothermics*, *32*(2), 109–130. https://doi.org/10.1016/S0375-6505(03)00012-9

Nasruddin, Idrus Alhamid, M., Daud, Y., Surachman, A., Sugiyono, A., Aditya, H. B., & Mahlia, T. M. I. (2016). Potential of geothermal energy for electricity generation in Indonesia: A review. *Renewable and Sustainable Energy Reviews*, *53*, 733–740. https://doi.org/10.1016/j.rser.2015.09.032

Ndikubwimana, I., Mao, X., Niyonsenga, J. D., Zhu, D., & Mwizerwa, S. (2022). Water-rock interaction, formation and circulation mechanism of highly bicarbonate groundwater in the northwestern geothermal prospects of Rwanda. *Episodes*, *45*(1), 73–86. https://doi.org/10.18814/epiiugs/2021/021006

Nebeská, D., Auer Malinská, H., Erol, A., Pidlisnyuk, V., Kuráň, P., Medžová, A., Smaha, M., & Trögl, J. (2021). Stress Response of Miscanthus Plants and Soil Microbial Communities: A

Case Study in Metals and Hydrocarbons Contaminated Soils. *Applied Sciences*, *11*(4), 1866. https://doi.org/10.3390/app11041866

Neina, D. (2019). The Role of Soil pH in Plant Nutrition and Soil Remediation. *Applied and Environmental Soil Science*, *2019*, 1–9. https://doi.org/10.1155/2019/5794869

Neinavaz, E., Schlerf, M., Darvishzadeh, R., Gerhards, M., & Skidmore, A. K. (2021). Thermal infrared remote sensing of vegetation: Current status and perspectives. *International Journal of Applied Earth Observation and Geoinformation*, *102*, 102415. https://doi.org/10.1016/j.jag.2021.102415

New Zealand Institute of Economic Research. (2018). *Economic Impact of Meeting 2050 Emissions Targets—Stage 2 Modelling (NZIER)* (p. 47).

Nidamanuri, R. R. (2020). Hyperspectral discrimination of tea plant varieties using machine learning, and spectral matching methods. *Remote Sensing Applications: Society and Environment*, *19*(June), 100350. https://doi.org/10.1016/j.rsase.2020.100350

Niederau, J., Wellmann, J. F., & Börsing, N. (2019). Analyzing the influence of correlation length in permeability on convective systems in heterogeneous aquifers using entropy production. *Geothermal Energy*, *7*(1). https://doi.org/10.1186/s40517-019-0151-6

Ninomiya, Y., & Fu, B. (2019). Thermal infrared multispectral remote sensing of lithology and mineralogy based on spectral properties of materials. *Ore Geology Reviews*, *108*(February 2018), 54–72. https://doi.org/10.1016/j.oregeorev.2018.03.012

Ninomiya, Y., Fu, B., & Cudahy, T. J. (2005). Detecting lithology with Advanced Spaceborne Thermal Emission and Reflection Radiometer (ASTER) multispectral thermal infrared "radiance-at-sensor" data. *Remote Sensing of Environment*, *99*(1–2), 127–139. https://doi.org/10.1016/j.rse.2005.06.009

Nishar, A., Richards, S., Breen, D., Robertson, J., & Breen, B. (2016). Thermal infrared imaging of geothermal environments and by an unmanned aerial vehicle (UAV): A case study of the

Wairakei e Tauhara geothermal fi eld , Taupo , New Zealand. *Renewable Energy*, *86*, 1256–1264. https://doi.org/10.1016/j.renene.2015.09.042

Noomen, M. F., Skidmore, A. K., van der Meer, F. D., & Prins, H. H. T. (2006). Continuum removed band depth analysis for detecting the effects of natural gas, methane and ethane on maize reflectance. *Remote Sensing of Environment*, *105*(3), 262–270. https://doi.org/10.1016/j.rse.2006.07.009

Noorollahi, Y., Highway, Y. E., & Ghods, S. (2005). Application of Gis and Remote Sensing in Exploration and Environmental Management of Námafjall Geothermal Area , N-Iceland. In *Training* (Issue 1).

Notesco, G., Kopačková, V., Rojík, P., Schwartz, G., Livne, I., & Dor, E. (2014). Mineral Classification of Land Surface Using Multispectral LWIR and Hyperspectral SWIR Remote-Sensing Data. A Case Study over the Sokolov Lignite Open-Pit Mines, the Czech Republic. *Remote Sensing*, *6*(8), 7005–7025. https://doi.org/10.3390/rs6087005

Notesco, G., Ogen, Y., & Ben-Dor, E. (2016). Integration of hyperspectral shortwave and longwave infrared remote-sensing data for mineral mapping of Makhtesh Ramon in Israel. *Remote Sensing*, *8*(4). https://doi.org/10.3390/rs8040318

Nyahucho, D. (2020). *LWIR spectroscopy on feldspars from rock plugs for the detection of permeable zones in geothermal systems* . 1–67.

Okamoto, K., Imanishi, K., & Asanuma, H. (2022). Structures and fluid flows inferred from the microseismic events around a low-resistivity anomaly in the Kakkonda geothermal field, Northeast Japan. *Geothermics*, *100*, 102320. https://doi.org/10.1016/j.geothermics.2021.102320

Olofsson, P., Foody, G. M., Herold, M., Stehman, S. V., Woodcock, C. E., & Wulder, M. A. (2014). Good practices for estimating area and assessing accuracy of land change. *Remote Sensing of Environment*, *148*, 42–57. https://doi.org/10.1016/j.rse.2014.02.015

Orlovich, D. A., & Cairney, J. G. (2004). Ectomycorrhizal fungi in New Zealand: Current perspectives and future directions. *New Zealand Journal of Botany*, *42*(5), 721–738. https://doi.org/10.1080/0028825X.2004.9512926

Owotogbe, J. S., Ibiyemi, T. S., & Adu, B. A. (2019). *A COMPREHENSIVE REVIEW ON VARIOUS TYPES OF NOISE IN IMAGE PROCESSING*. *10*(11), 7.

Pan, S., Kong, Y., Wang, K., Ren, Y., Pang, Z., Zhang, C., Wen, D., Zhang, L., Feng, Q., Zhu, G., & Wang, J. (2021). Magmatic origin of geothermal fluids constrained by geochemical evidence: Implications for the heat source in the northeastern Tibetan Plateau. *Journal of Hydrology*, *603*, 126985. https://doi.org/10.1016/j.jhydrol.2021.126985

Pan, X., Li, F., Wu, Z., Zhang, Q., Lin, Z., Shi, X., & Qiao, Y. (2015). Near infrared spectroscopy model development and variable importance in projection assignment of particle size and lobetyolin content of Codonopsis radix. *Journal of Near Infrared Spectroscopy*, *23*(5), 327–335. https://doi.org/10.1255/jnirs.1175

Pascucci, S., Pignatti, S., Casa, R., Darvishzadeh, R., & Huang, W. (2020). Special Issue "Hyperspectral Remote Sensing of Agriculture and Vegetation." *Remote Sensing*, *12*(21), 3665. https://doi.org/10.3390/rs12213665

Pattathal, A., Sahoo, M. M., Porwal, A., & Karnieli, A. (2022). Deep-learning-based latent space encoding for spectral unmixing of geological materials. *ISPRS Journal of Photogrammetry and Remote Sensing*, *183*, 307–320. https://doi.org/10.1016/j.isprsjprs.2021.11.008

Patterson, J. W., Driesner, T., & Matthai, S. K. (2018). Self-Organizing Fluid Convection Patterns in an en Echelon Fault Array. *Geophysical Research Letters*, *45*(10), 4799–4808. https://doi.org/10.1029/2018GL078271

Pawluszek-Filipiak, K., & Borkowski, A. (2020). On the Importance of Train–Test Split Ratio of Datasets in Automatic Landslide Detection by Supervised Classification. *Remote Sensing*, *12*(18), 3054. https://doi.org/10.3390/rs12183054

Pippucci, A., Lorenzi, R., Spanò, C., & Sorce, C. (2015). Stress-induced changes to the flora in a geothermal field in central Italy. *Acta Physiologiae Plantarum*, *37*(10). https://doi.org/10.1007/s11738-015-1953-1

Pirajno, F. (2009). *Hydrothermal Processes and Mineral Systems* (Vol. 53). Springer Netherlands. http://link.springer.com/10.1007/978-1-4020-8613-7

Poblete, T., Camino, C., Beck, P. S. A., Hornero, A., Kattenborn, T., Saponari, M., Boscia, D., Navas-Cortes, J. A., & Zarco-Tejada, P. J. (2020). Detection of Xylella fastidiosa infection symptoms with airborne multispectral and thermal imagery: Assessing bandset reduction performance from hyperspectral analysis. *ISPRS Journal of Photogrammetry and Remote Sensing*, *162*(October 2019), 27–40. https://doi.org/10.1016/j.isprsjprs.2020.02.010

Pôças, I., Calera, A., Campos, I., & Cunha, M. (2020). Remote sensing for estimating and mapping single and basal crop coefficientes: A review on spectral vegetation indices approaches. *Agricultural Water Management*, *233*, 106081. https://doi.org/10.1016/j.agwat.2020.106081

Pope, J., & Brown, K. L. (2014). Geochemistry of discharge at Waiotapu geothermal area, New Zealand—Trace elements and temporal changes. *Geothermics*, *51*, 253–269. https://doi.org/10.1016/j.geothermics.2014.01.006

Poulet, F., Bibring, J. P., Mustard, J. F., Gendrin, A., Mangold, N., Langevin, Y., Arvidson, R. E., Gondet, B., Gomez, C., Berthe, M., Erard, S., Forni, O., Manaud, N., Poulleau, G., Soufflot, A., Combes, M., Drossart, P., Encrenaz, T., Fouchet, T., … Forget, F. (2005). Phyllosilicates on Mars and implications for early martian climate. *Nature*, *438*(7068), 623–627. https://doi.org/10.1038/nature04274

Pour, A. B., Zoheir, B., Pradhan, B., & Hashim, M. (2021). Editorial for the Special Issue: Multispectral and Hyperspectral Remote Sensing Data for Mineral Exploration and Environmental Monitoring of Mined Areas. *Remote Sensing*, *13*(3), 519. https://doi.org/10.3390/rs13030519

Prakash, A. (2000). Thermal remote sensing: Concepts, issues and applications. *Archives of Photogrammetry and Remote Sensing*, *XXXIII*, 239–243.

Preston, L. J., Benedix, G. K., Genge, M. J., & Sephton, M. A. (2008). A multidisciplinary study of silica sinter deposits with applications to silica identification and detection of fossil life on Mars. *Icarus*, *198*(2), 331–350. https://doi.org/10.1016/j.icarus.2008.08.006

Procesi, M., Ciotoli, G., Mazzini, A., & Etiope, G. (2019). Sediment-hosted geothermal systems: Review and first global mapping. *Earth-Science Reviews*, *192*, 529–544. https://doi.org/10.1016/j.earscirev.2019.03.020

Pullagurala, V. L. R., Rawat, S., Adisa, I. O., Hernandez-Viezcas, J. A., Peralta-Videa, J. R., & Gardea-Torresdey, J. L. (2018). Plant uptake and translocation of contaminants of emerging concern in soil. *Science of The Total Environment*, *636*, 1585–1596. https://doi.org/10.1016/j.scitotenv.2018.04.375

Pullanagari, Kereszturi, G., Yule, I. J., & Ghamisi, P. (2017). Knowledge-based decision tree approach for mapping spatial distribution of rice crop using C- band synthetic aperture radar-derived information Knowledge-based decision tree approach for mapping spatial distribution of rice crop using C-band synthetic ap. *J. Appl. Remote Sens*, *11*(4). https://doi.org/10.1117/1.JRS.11

Pullanagari, R. R., Kereszturi, G., & Yule, I. J. (2016). Mapping of macro and micro nutrients of mixed pastures using airborne AisaFENIX hyperspectral imagery. *ISPRS Journal of Photogrammetry and Remote Sensing*, *117*, 1–10. https://doi.org/10.1016/j.isprsjprs.2016.03.010

Purkis, S., & Klemas, V. (2011). *Remote Sensing and Global Environmental Change*.

Putri, D. R., Ismail, N., Idroes, R., Rizal, S., Nur, S., & Nanda, M. (2021). Analysis of Land Surface Temperature (LST) in Bur Ni Geureudong Geothermal Field, Aceh, Indonesia Using Landsat 8 OLI / TIRS Images. *Chiang Mai University Journal of Natural Sciences*, *20*(4). https://doi.org/10.12982/CMUJNS.2021.084

Qian, S.-E. (2021). Hyperspectral Satellites, Evolution, and Development History. *IEEE Journal of Selected Topics in Applied Earth Observations and Remote Sensing*, *14*, 7032–7056. https://doi.org/10.1109/JSTARS.2021.3090256

Qin, Q., Zhang, N., Nan, P., & Chai, L. (2011). Geothermal area detection using Landsat ETM+ thermal infrared data and its mechanistic analysis-A case study in Tengchong, China. *International Journal of Applied Earth Observation and Geoinformation*, *13*(4), 552–559. https://doi.org/10.1016/j.jag.2011.02.005

Qu, L., Han, W., Lin, H., Zhu, Y., & Zhang, L. (2014). Estimating vegetation fraction using hyperspectral pixel unmixing method: A case study of a Karst area in China. *IEEE Journal of Selected Topics in Applied Earth Observations and Remote Sensing*, *7*(11), 4559–4565. https://doi.org/10.1109/JSTARS.2014.2361253

Qudsi, I., & Noor, M. R. (2022). Geothermal Surface Manifestation Identification Using Airborne Hyperspectral Imagery Case Study: Davis-Schrimpf Geothermal Field, Salton Sea, California. *Indonesian Journal on Geoscience*, *9*(1), 119–130. https://doi.org/10.17014/IJOG.9.1.119-130

Queißer, M., Burton, M., & Kazahaya, R. (2019). Insights into geological processes with CO2 remote sensing – A review of technology and applications. *Earth-Science Reviews*, *188*(November 2018), 389–426. https://doi.org/10.1016/j.earscirev.2018.11.016

Rajan Girija, R., & Mayappan, S. (2019). Mapping of mineral resources and lithological units: A review of remote sensing techniques. *International Journal of Image and Data Fusion*, *10*(2), 79–106. https://doi.org/10.1080/19479832.2019.1589585

Rajesh, H. M. (2004). Application of remote sensing and GIS in mineral resource mapping — An overview. *Journal of Mineralogical and Petrological Sciences*, *99*, 83–103.

Ramdhan, M. R. (2019). *The investigation of geothermal temperature anomalies and structures using airborne TIR and LiDAR data: A case study in Bajawa area , Indonesia The investigation of*

geothermal temperature anomalies and structures using airborne TIR and LiDAR data: A cas.

Ramsey, M., & Flynn, I. (2020). The Spatial and Spectral Resolution of ASTER Infrared Image Data: A Paradigm Shift in Volcanological Remote Sensing. *Remote Sensing*, *12*(4), 738. https://doi.org/10.3390/rs12040738

Rascio, N., & Navari-Izzo, F. (2011). Heavy metal hyperaccumulating plants: How and why do they do it? And what makes them so interesting? *Plant Science*, *180*(2), 169–181. https://doi.org/10.1016/j.plantsci.2010.08.016

Rasti, B., Chang, Y., Dalsasso, E., Denis, L., & Ghamisi, P. (2021). *Image Restoration for Remote Sensing: Overview and Toolbox* (arXiv:2107.00557). arXiv. http://arxiv.org/abs/2107.00557

Rasti, B., Scheunders, P., Ghamisi, P., Licciardi, G., & Chanussot, J. (2018). Noise Reduction in Hyperspectral Imagery: Overview and Application. *Remote Sensing*, *10*(3), 482. https://doi.org/10.3390/rs10030482

Rasti, B., Ulfarsson, M. O., & Sveinsson, J. R. (2016). Hyperspectral Feature Extraction Using Total Variation Component Analysis. *IEEE Transactions on Geoscience and Remote Sensing*, *54*(12), 6976–6985. https://doi.org/10.1109/TGRS.2016.2593463

Rathod, P. H., Brackhage, C., Müller, I., Van der Meer, F. D., & Noomen, M. F. (2018). Assessing Metal-Induced Changes in the Visible and Near-Infrared Spectral Reflectance of Leaves: A Pot Study with Sunflower (Helianthus annuus L.). *Journal of the Indian Society of Remote Sensing*, *3*(3). https://doi.org/10.1007/s12524-018-0846-3

Rathod, P. H., Brackhage, C., Van Der Meer, F. D., Müller, I., Noomen, M. F., Rossiter, D. G., & Dudel, G. E. (2015). Spectral changes in the leaves of barley plant due to phytoremediation of metals—Results from a pot study. *European Journal of Remote Sensing*, *48*, 283–302. https://doi.org/10.5721/EuJRS20154816

Rathod, P. H., Rossiter, D. G., Noomen, M. F., & van der Meer, F. D. (2013). Proximal Spectral Sensing to Monitor Phytoremediation of Metal-Contaminated Soils. *International Journal of Phytoremediation*, *15*(5), 405–426. https://doi.org/10.1080/15226514.2012.702805

Rattenbury, M., Martin, A., Baisden, T., Turnbull, R., & Rogers, K. (2018). Geochemical baseline soil surveys for understanding element and isotope variation across New Zealand. *New Zealand Journal of Agricultural Research*, *61*(3), 347–357. https://doi.org/10.1080/00288233.2018.1426616

Reath, K. A., & Ramsey, M. S. (2013). Exploration of geothermal systems using hyperspectral thermal infrared remote sensing. *Journal of Volcanology and Geothermal Research*, *265*, 27–38. https://doi.org/10.1016/j.jvolgeores.2013.08.007

Reeves, R., Bromley, C., & Milloy, S. (2015). *Using Time-Series Aerial Thermal Infrared Surveys to Determine Near-Surface Thermal Processes at the Ohaaki Geothermal Field, New Zealand*. 7.

Reeves, R., & Rae, L. (2016). Changes in aerial thermal infrared signature over the Rotorua Geothermal Field, New Zealand: 1990–2014. *Geothermics*, *64*, 262–270. https://doi.org/10.1016/j.geothermics.2016.06.007

Reeves, R., & Sanders, F. (2019). *2019 Thermal infrared survey of the Waiotapu Geothermal Field* (p. 29). GNS Science. https://doi.org/10.21420/ZD6D-GD88

Reich, M., Román, N., Barra, F., & Morata, D. (2020). Silver-Rich Chalcopyrite from the Active Cerro Pabellón Geothermal System, Northern Chile. *Minerals*, *10*(2), 113. https://doi.org/10.3390/min10020113

Reyes, A. G. (1990). Petrology of Philippine geothermal systems and the application of alteration mineralogy to their assessment. *Journal of Volcanology and Geothermal Research*, *43*(1–4), 279–309. https://doi.org/10.1016/0377-0273(90)90057-M

Richter, R. (1998). Correction of satellite imagery over mountainous terrain. *Applied Optics*, *37*(18), 4004. https://doi.org/10.1364/AO.37.004004

Richter, R., & Schläpfer, D. (2016). ATCOR-4 User Guide. *German Aerospace Center, Germany*, *7.0.3*(March), 565–01.

Riese, F. M., Keller, S., & Hinz, S. (2020). Supervised and semi-supervised self-organizing maps for regression and classification focusing on hyperspectral data. *Remote Sensing*, *12*(1). https://doi.org/10.3390/RS12010007

Rincheval, M. (2019). Biogeochemical mapping of metal contamination from mine tailings using field-portable XRF. *Science of the Total Environment*, 10.

Ripley, R. D. (1979). *Tests of "Randomness" for Spatial Point Patterns*. https://doi.org/10.1111/j.2517-6161.1979.tb01091.x

Risk, G., Caldwell, T., & Bibby, H. (1994). Deep resistivity surveys in the Waiotapu-Waikite-Reporoa region, New Zealand. *Geothermics*, *23*(5–6), 423–443. https://doi.org/10.1016/0375-6505(94)90012-4

Ritchie, A. B. H. (1996). *Volcanic Geology and Geochemistry of Waiotapu Ignimbrite, Taupo Volcanic Zone, New Zealand.*

Robinson, B., Kim, N., Marchetti, M., Moni, C., Schroeter, L., van den Dijssel, C., Milne, G., & Clothier, B. (2006). Arsenic hyperaccumulation by aquatic macrophytes in the Taupo Volcanic Zone, New Zealand. *Environmental and Experimental Botany*, *58*(1–3), 206–215. https://doi.org/10.1016/j.envexpbot.2005.08.004

Rock, G., Gerhards, M., Gattung, T., Hecker, C., Udelhoven, T., Schlerf, M., & Werner, W. (2017). Species discrimination using emissive thermal infrared imaging spectroscopy. *Workshop on Hyperspectral Image and Signal Processing, Evolution in Remote Sensing*, *2014-June*, 16–26. https://doi.org/10.1109/WHISPERS.2014.8077500

Rodger, A. (2011). SODA: A new method of in-scene atmospheric water vapor estimation and post-flight spectral recalibration for hyperspectral sensorsApplication to the HyMap sensor at two locations. *Remote Sensing of Environment*, *115*(2), 536–547. https://doi.org/10.1016/j.rse.2010.09.022

Rodriguez-Gomez, C., Kereszturi, G., Reeves, R., Rae, A., Pullanagari, R., Jeyakumar, P., & Procter, J. N. (2021). Lithological mapping of Waiotapu Geothermal Field (New Zealand) using hyperspectral and thermal remote sensing and ground exploration techniques. *Geothermics*, *96*(June), 102195. https://doi.org/10.1016/j.geothermics.2021.102195

Romaguera, M., Vaughan, R. G., Ettema, J., Izquierdo-Verdiguier, E., Hecker, C. A., & van der Meer, F. D. (2018). Detecting geothermal anomalies and evaluating LST geothermal component by combining thermal remote sensing time series and land surface model data. *Remote Sensing of Environment*, *204*(September 2017), 534–552. https://doi.org/10.1016/j.rse.2017.10.003

Rosas-Chavoya, M., López-Serrano, P. M., Hernández-Díaz, J. C., Wehenkel, C., & Vega-Nieva, D. J. (2021). Analysis of Near-Surface Temperature Lapse Rates in Mountain Ecosystems of Northern Mexico Using Landsat-8 Satellite Images and ECOSTRESS. *Remote Sensing*, *14*(1), 162. https://doi.org/10.3390/rs14010162

Rosipal, R. (2003). Kernel partial least squares for nonlinear regression and discrimination. *Neural Network World*, *13*(3), 291–300.

Rosipal, R., & Trejo, L. J. (2002). Kernel Partial Least Squares Regression in Reproducing Kernel Hilbert Space. *CrossRef Listing of Deleted DOIs*, *1*, 97–123. https://doi.org/10.1162/15324430260185556

Rossel, R. A. V., Jeon, Y. S., Odeh, I. O. A., & McBratney, A. B. (2008). Using a legacy soil sample to develop a mid-IR spectral library. *Australian Journal of Soil Research*, *46*(1), 1–16. https://doi.org/10.1071/SR07099

Rowan, L. C., Schmidt, R. G., & Mars, J. C. (2006). Distribution of hydrothermally altered rocks in the Reko Diq, Pakistan mineralized area based on spectral analysis of ASTER data. *Remote Sensing of Environment*, *104*(1), 74–87. https://doi.org/10.1016/j.rse.2006.05.014

Rowland, J. V., & Sibson, R. H. (2004). Structural controls on hydrothermal flow in a segmented rift system, Taupo Volcanic Zone, New Zealand. *Geofluids*, *4*(4), 259–283. https://doi.org/10.1111/j.1468-8123.2004.00091.x

Rowland, J. V., & Simmons, S. F. (2012). Hydrologic, magmatic, and tectonic controls on hydrothermal flow, Taupo Volcanic Zone, New Zealand: Implications for the formation of epithermal vein deposits. *Economic Geology*, *107*(3), 427–457. https://doi.org/10.2113/econgeo.107.3.427

Rowland, J. V., Simmons, S. F., & Sepulveda, F. (2007). Structural Controls on Regional and Reservoir Scale. *29th New Zealand Geothermal Workshop*.

Rowland, J. V., Wilson, C. J. N., & Gravley, D. M. (2010). Spatial and temporal variations in magma-assisted rifting, Taupo Volcanic Zone, New Zealand. *Journal of Volcanology and Geothermal Research*, *190*(1–2), 89–108. https://doi.org/10.1016/j.jvolgeores.2009.05.004

Roy, P. S. (1989). Spectral reflectance characteristics of vegetation and their use in estimating productive potential. *Proceedings: Plant Sciences*, *99*(1), 59–81. https://doi.org/10.1007/BF03053419

Rudemo, M. (1982). Empirical Choice of Histograms and Kernel Density Estimates. *Scandinavian Journal of Statistics*, *9*(2), 65–78.

Ruff, S. W., Christensen, P. R., Barbera, P. W., & Anderson, L. (1997). Quantitative thermal emission spectroscopy of minerals: A laboratory technique for measurement and calibration. *Journal of Geophysical Research*, *102*(B7), 899–913.

Runge, M. G., Bebbington, M. S., Cronin, S. J., Lindsay, J. M., & Moufti, M. R. (2015). Sensitivity to volcanic field boundary. *Journal of Applied Volcanology*, *4*(1). https://doi.org/10.1186/s13617-015-0040-z

Runge, M. G., Bebbington, M. S., Cronin, S. J., Lindsay, J. M., & Moufti, M. R. (2016). Integrating geological and geophysical data to improve probabilistic hazard forecasting of Arabian Shield volcanism. *Journal of Volcanology and Geothermal Research*, *311*, 41–59. https://doi.org/10.1016/j.jvolgeores.2016.01.007

Russell, M. J., & Hall, A. J. (1997). The emergence of life from iron monosulphide bubbles at a submarine hydrothermal redox and pH front. *Journal of the Geological Society*, *154*(3), 377–402. https://doi.org/10.1144/gsjgs.154.3.0377

Rye, R. O., Bethke, P. M., & Wasserman, M. D. (1992). The stable isotope geochemistry of acid sulfate alteration. *Economic Geology*, *87*(2), 225–262. https://doi.org/10.2113/gsecongeo.87.2.225

Ryu, J. H., Jeong, H., & Cho, J. (2020). Performances of vegetation indices on paddy rice at elevated air temperature, heat stress, and herbicide damage. *Remote Sensing*, *12*(16). https://doi.org/10.3390/RS12162654

Sabins, F. F. (1999). Remote sensing for mineral exploration. *Ore Geology Reviews*, *14*(3–4), 157–183. https://doi.org/10.1016/S0169-1368(99)00007-4

Saepuloh, A., Dewi, W. C., Harto, A. B., & Agustan. (2021). Occurrence of Geothermal Features Based on Surface Roughness and Geobotanical Analyses derived by ALOS-2 PALSAR-2 and Sentinel-2 Images. *2021 7th Asia-Pacific Conference on Synthetic Aperture Radar (APSAR)*, 1–6. https://doi.org/10.1109/APSAR52370.2021.9688361

Saepuloh, A., Haeruddin, H., Heriawan, M. N., Kubo, T., Koike, K., & Malik, D. (2018). Application of lineament density extracted from dual orbit of synthetic aperture radar (SAR) images to detecting fluids paths in the Wayang Windu geothermal field (West Java, Indonesia). *Geothermics*, *72*(November 2017), 145–155. https://doi.org/10.1016/j.geothermics.2017.11.010

Sahoo, M. M., V., A. P., & Porwal, A. (2021). Support Vector Machines for Unmixing Geological Mixtures. *2021 11th Workshop on Hyperspectral Imaging and Signal Processing: Evolution in Remote Sensing (WHISPERS)*, 1–6. https://doi.org/10.1109/WHISPERS52202.2021.9484054

Salisbury, J. W., Walter, L. S., Vergo, N., & D'Aria, D. M. (1991). *Infrared (2.1–25 Am) spectra of minerals*. Johns Hopkins Uni- versity Press.

Salje, E., Guttler, B., & Ormerod, C. (1989). Determination of the degree of Al, Si order QOD in kinetically disordered albite using hard mode infrared spectroscopy. *Physics and Chemistry*.

Sammut, C., & Webb, G. I. (2011). Mean Absolute Error. In *Encyclopedia of Machine Learning*. Springer. https://doi.org/10.1007/978-0-387-30164-8_525

San, B., & Süzen, M. (2010). Evaluation of different atmospheric correction algorithms for EO-1 Hyperion imagery. *International Archives of the Photogrammetry Remote Sensing and Spatial Information Sciences*, *38*, 392–397.

Sanches, I. D., Souza Filho, C. R., Magalhães, L. A., Quitério, G. C. M., Alves, M. N., & Oliveira, W. J. (2013). Unravelling remote sensing signatures of plants contaminated with gasoline and diesel: An approach using the red edge spectral feature. *Environmental Pollution*, *174*, 16–27. https://doi.org/10.1016/j.envpol.2012.10.029

Sand, W. (2003). Microbial life in geothermal waters. *Geothermics*, *32*(4), 655–667. https://doi.org/10.1016/S0375-6505(03)00058-0

Santaga, F. S., Agnelli, A., Leccese, A., & Vizzari, M. (2021). Using Sentinel-2 for Simplifying Soil Sampling and Mapping: Two Case Studies in Umbria, Italy. *Remote Sensing*, *13*(17), 3379. https://doi.org/10.3390/rs13173379

Santilano, A., Manzella, A., Gianelli, G., Donato, A., Gola, G., Nardini, I., Trumpy, E., & Botteghi, S. (2015). Convective, intrusive geothermal plays: What about tectonics? *Geothermal Energy Science*, *3*(1), 51–59. https://doi.org/10.5194/gtes-3-51-2015

Sasaki, K., Morita, J., Iwaki, C., & Ueda, A. (2021). Geochemical evaluation of geothermal resources in Toyama Prefecture, Japan, based on the chemical and isotopic characteristics of hot spring waters. *Geothermics*, *93*, 102071. https://doi.org/10.1016/j.geothermics.2021.102071

Savage, S., Lawrence, R., Custer, S., Jewett, J., Powell, S., & Shaw, J. (2010). Review of alternative methods for estimating terrestrial Emittance and Geothermal Heat Flux for Yellowstone National Park Using Landsat Imagery. *GIScience and Remote Sensing*, *47*(4), 460–479. https://doi.org/10.2747/1548-1603.47.4.460

Savitri, K. P., Hecker, C., van der Meer, F. D., & Sidik, R. P. (2021). VNIR-SWIR infrared (imaging) spectroscopy for geothermal exploration: Current status and future directions. *Geothermics*, *96*(January), 102178. https://doi.org/10.1016/j.geothermics.2021.102178

Savitzky, A., & Golay, M. J. E. (1964). Smoothing and Differentiation of Data by Simplified Least Squares Procedures. *Analytical Chemistry*, *36*(8), 1627–1639. https://doi.org/10.1021/ac60214a047

Saxena, J., Jain, A., & Krishna, P. R. (2020). A Review on Applicability of Deep Learning for Remote Sensing Applications. *Solid State Technology*, *63*(6), 10.

Schaefer, L. N., Kereszturi, G., Kennedy, B., & Villenueve, M. (2020). Characterizing lithological, weathering, and hydrothermal alteration influences on volcanic rock properties via spectroscopy and laboratory testing: A case study of Mt. Ruapehu volcano, New Zealand. *ESSOar*.

Schaefer, L. N., Kereszturi, G., Villeneuve, M., & Kennedy, B. (2021). Determining physical and mechanical volcanic rock properties via reflectance spectroscopy. *Journal of Volcanology and Geothermal Research*, *420*, 107393. https://doi.org/10.1016/j.jvolgeores.2021.107393

Schläpfer, D., & Richter, R. (2002). Geo-atmospheric processing of airborne imaging spectrometry data. Part 1: Parametric orthorectification. *International Journal of Remote Sensing*, *23*(13), 2609–2630. https://doi.org/10.1080/01431160110115825

Schmid, M., Rath, D., & Diebold, U. (2022). Why and How Savitzky–Golay Filters Should Be Replaced. *ACS Measurement Science Au*, *2*(2), 185–196. https://doi.org/10.1021/acsmeasuresciau.1c00054

Schmidt, C., Laag, C., Whitehead, M., Profe, J., Aka, F., Hasegawa, T., & Kereszturi, G. (2022). The complexities of assessing volcanic hazards along the Cameroon Volcanic Line using spatial distribution of monogenetic volcanoes. *Journal of Volcanology and Geothermal Research*, *427*(November 2021), 107558. https://doi.org/10.1016/j.jvolgeores.2022.107558

Schodlok, M. C., Green, A., & Huntington, J. (2016). A reference library of thermal infrared mineral reflectance spectra for the HyLogger-3 drill core logging system. *Australian Journal of Earth Sciences*, 1–9. https://doi.org/10.1080/08120099.2016.1234508

Schwertmann, U., & Murad, E. (1983). Effect of pH on the formation of goethite and hematite from ferrihydrite. *Clays & Clay Minerals*, *31*(4), 277–284. https://doi.org/10.1346/CCMN.1983.0310405

Scott, K. M., & Yang, K. (1997). *Spectral Reflectance Studies of White Micas*. *03*, 41p.

Seebeck, H., Nicol, A., Villamor, P., Ristau, J., & Pettinga, J. (2014). Structure and kinematics of the Taupo Rift, New Zealand. *Tectonics*, *33*(6), 1178–1199. https://doi.org/10.1002/2014TC003569

Sekertekin, A., & Arslan, N. (2019). Monitoring thermal anomaly and radiative heat flux using thermal infrared satellite imagery – A case study at Tuzla geothermal region. *Geothermics*, *78*(July 2018), 243–254. https://doi.org/10.1016/j.geothermics.2018.12.014

Sellers, P. J. (1985). Canopy reflectance, photosynthesis and transpiration. *International Journal of Remote Sensing*, *6*(8), 1335–1372. https://doi.org/10.1080/01431168508948283

Sengelen, X., Robion, P., Ledésert, B., Hébert, R., Regnet, J.-B., Bourquin, S., Gasparrini, M., Margueret, S., & Barnes, C. (2019). *Petrophysical characterization of Triassic and basement formations for geothermal purposes in the Paris basin: From sub-surface data to reservoir outcrop analogue*. 10.

Sepulcre-Cantó, G., Zarco-Tejada, P. J., Jiménez-Muñoz, J. C., Sobrino, J. A., Miguel, E. D., & Villalobos, F. J. (2006). Detection of water stress in an olive orchard with thermal remote sensing imagery. *Agricultural and Forest Meteorology*, *136*(1–2), 31–44. https://doi.org/10.1016/j.agrformet.2006.01.008

Sepúlveda, F., Rosenberg, M. D., Rowland, J. V, & Simmons, S. F. (2012). Kriging predictions of drill-hole stratigraphy and temperature data from the Wairakei geothermal field, New

Zealand: Implications for conceptual modeling. *Geothermics*, *42*, 13–31. https://doi.org/10.1016/j.geothermics.2012.01.002

Serrano, L., Peñuelas, J., & Ustin, S. L. (2002). Remote sensing of nitrogen and lignin in Mediterranean vegetation from AVIRIS data: Decomposing biochemical from structural signals. *Remote Sensing of Environment*, *81*(2–3), 355–364. https://doi.org/10.1016/S0034-4257(02)00011-1

Seward, A., Ashraf, S., Reeves, R., & Bromley, C. (2018). Improved environmental monitoring of surface geothermal features through comparisons of thermal infrared, satellite remote sensing and terrestrial calorimetry. *Geothermics*, *73*(July 2017), 60–73. https://doi.org/10.1016/j.geothermics.2018.01.007

Seward, A., Reeves, R., & Alcaraz, S. (2022). Assessment of the surface heat loss from Waimangu Geothermal Valley: Comparison of terrestrial based assessment techniques with remote sensing. *Journal of Volcanology and Geothermal Research*, *430*(July), 107630. https://doi.org/10.1016/j.jvolgeores.2022.107630

Seward, T. M., Williams-Jones, A. E., & Migdisov, A. A. (2014). *The Chemistry of Metal Transport and Deposition by Ore-Forming Hydrothermal Fluids* (Vol. 13).

Shahid, M., Dumat, C., Khalid, S., Schreck, E., Xiong, T., & Niazi, N. K. (2017). Foliar heavy metal uptake, toxicity and detoxification in plants: A comparison of foliar and root metal uptake. *Journal of Hazardous Materials*, *325*, 36–58. https://doi.org/10.1016/j.jhazmat.2016.11.063

Shao, Y., & Lunetta, R. S. (2012). Comparison of support vector machine, neural network, and CART algorithms for the land-cover classification using limited training data points. *ISPRS Journal of Photogrammetry and Remote Sensing*, *70*, 78–87. https://doi.org/10.1016/j.isprsjprs.2012.04.001

Shi, T., Liu, H., Chen, Y., Wang, J., & Wu, G. (2016). Estimation of arsenic in agricultural soils using hyperspectral vegetation indices of rice. *Journal of Hazardous Materials*, *308*, 243–252. https://doi.org/10.1016/j.jhazmat.2016.01.022

Shoedarto, R. M., Tada, Y., Kashiwaya, K., Koike, K., & Iskandar, I. (2020). Specifying recharge zones and mechanisms of the transitional geothermal field through hydrogen and oxygen isotope analyses with consideration of water-rock interaction. *Geothermics*, *86*, 101797. https://doi.org/10.1016/j.geothermics.2019.101797

Shoedarto, R. M., Tada, Y., Kashiwaya, K., Koike, K., Iskandar, I., Malik, D., & Bratakusuma, B. (2021). Investigation of meteoric water and parent fluid mixing in a two-phase geothermal reservoir system using strontium isotope analysis: A case study from Southern Bandung, West Java, Indonesia. *Geothermics*, *94*(March), 102096. https://doi.org/10.1016/j.geothermics.2021.102096

Shortall, R., Davidsdottir, B., & Axelsson, G. (2015). Geothermal energy for sustainable development: A review of sustainability impacts and assessment frameworks. *Renewable and Sustainable Energy Reviews*, *44*, 391–406. https://doi.org/10.1016/j.rser.2014.12.020

Shtangeeva, I., Bali, R., & Harris, A. (2011). Bioavailability and toxicity of antimony. *Journal of Geochemical Exploration*, *110*(1), 40–45. https://doi.org/10.1016/j.gexplo.2010.07.003

Sillitoe, R. H., & Hedenquist, J. W. (2003). Linkages between Volcanotectonic Settings , Ore-Fluid Compositions , and Epithermal Precious Metal Deposits. *Society of Economic Geologists - Special Publication*, *10*(November 2017), 315–343. https://doi.org/10:315-343

Silvestri, M., Romaniello, V., Hook, S., Musacchio, M., Teggi, S., & Buongiorno, M. F. (2020). First Comparisons of Surface Temperature Estimations Between ECOSTRESS, ASTER and Landsat 8 over Italian Volcanic and Geothermal Areas. *Remote Sensing*, *12*(1), 1–11. https://doi.org/10.3390/RS12010184

Simmons, S. F., Brown, K. L., Browne, P. R. L., & Rowland, J. V. (2016). Gold and silver resources in Taupo Volcanic Zone geothermal systems. *Geothermics*. https://doi.org/10.1016/j.geothermics.2015.07.009

Simmons, S. F., Brown, K. L., & Tutolo, B. M. (2016). Hydrothermal Transport of Ag, Au, Cu, Pb, Te, Zn, and Other Metals and Metalloids in New Zealand Geothermal Systems: Spatial

Patterns, Fluid-Mineral Equilibria, and Implications for Epithermal Mineralization. *Economic Geology*, *111*(3), 598–618.

Simpson, M. P., & Bignall, G. (2016). Undeveloped high-enthalpy geothermal fields of the Taupo Volcanic Zone, New Zealand. *Geothermics*, *59*, 325–346. https://doi.org/10.1016/j.geothermics.2015.08.006

Simpson, M. P., & Rae, A. J. (2018). Short-wave infrared (SWIR) reflectance spectrometric characterisation of clays from geothermal systems of the Taupō Volcanic Zone, New Zealand. *Geothermics*, *73*(February), 74–90. https://doi.org/10.1016/j.geothermics.2018.01.006

Sims, D. A., & Gamon, J. A. (2002). Relationships between leaf pigment content and spectral reflectance across a wide range of species, leaf structures and developmental stages. *Remote Sensing of Environment*, *81*(2–3), 337–354. https://doi.org/10.1016/S0034-4257(02)00010-X

Singer, D. A., & Kouda, R. (2001). Some simple guides to finding useful information in exploration geochemical data. *Natural Resources Research*, *10*(2), 137–147. https://doi.org/10.1023/A:1011552810482

Sishodia, R. P., Ray, R. L., & Singh, S. K. (2020). Applications of Remote Sensing in Precision Agriculture: A Review. *Remote Sensing*, *12*(19), 3136. https://doi.org/10.3390/rs12193136

Sleimi, N., Kouki, R., Hadj Ammar, M., Ferreira, R., & Pérez-Clemente, R. (2021). Barium effect on germination, plant growth, and antioxidant enzymes in Cucumis sativus L. plants. *Food Science and Nutrition*, *9*(4), 2086–2094. https://doi.org/10.1002/fsn3.2177

Slonecker, T., Haack, B., & Price, S. (2009). Spectroscopic analysis of arsenic uptake in Pteris ferns. *Remote Sensing*, *1*(4), 644–675. https://doi.org/10.3390/rs1040644

Smale, M. C., & Fitzgerald, N. B. (2015). *Geothermal vegetation types of the Taupō Volcanic Zone* (Vol. 4355). Waikato Regional Council.

Smale, M. C., Wiser, S. K., Bergin, M. J., & Fitzgerald, N. B. (2018). A classification of the geothermal vegetation of the Taupō Volcanic Zone, New Zealand. *Journal of the Royal Society of New Zealand*, *48*(1), 21–38. https://doi.org/10.1080/03036758.2017.1322619

Smith, C. L., Ficklin, W. H., & Thompson, J. M. (1987). Concentrations of arsenic, antimony, and boron in steam and steam condensate at The Geysers, California. *Journal of Volcanology and Geothermal Research*, *32*(4), 329–341. https://doi.org/10.1016/0377-0273(87)90083-7

Smith, E. G. C., Scott, B. J., & Latter, J. H. (1984). The Waiotapu earthquake of 1983, December 14. *Bulletin of the New Zealand National Society for Earthquake Engineering*, *17*(4), 272–279.

Smith, L. (1988). A tutorial on Principal Components Analysis. *Communications in Statistics - Theory and Methods*, *17*(9), 3157–3175. https://doi.org/10.1080/03610928808829796

Sobrino, J. A., Jiménez-Muñoz, J. C., Zarco-Tejada, P. J., Sepulcre-Cantó, G., & de Miguel, E. (2006). Land surface temperature derived from airborne hyperspectral scanner thermal infrared data. *Remote Sensing of Environment*, *102*(1–2), 99–115. https://doi.org/10.1016/j.rse.2006.02.001

Soengkono, S. (2001). Interpretation of magnetic anomalies over the Waimangu geothermal area, Taupo volcanic zone, New Zealand. *North*, *30*, 443–459.

Soengkono, S. (2011). Deep interpretation of gravity and airborne magnetic data of the Central Taupo volcanic zone. *New Zealand Geothermal Workshop Proceedings (21-23 November 2011)*, *1955*.

Soengkono, S. (2016). Airborne Magnetic Surveys to Investigate High Temperature Geothermal Reservoirs. In *Advances in Geothermal Energy*. InTech. https://doi.org/10.5772/61651

Soltani, M., Moradi Kashkooli, F., Souri, M., Rafiei, B., Jabarifar, M., Gharali, K., & Nathwani, J. S. (2021). Environmental, economic, and social impacts of geothermal energy systems. *Renewable and Sustainable Energy Reviews*, *140*(May 2020), 110750. https://doi.org/10.1016/j.rser.2021.110750

Somers, B., Asner, G. P., Tits, L., & Coppin, P. (2011). Endmember variability in Spectral Mixture Analysis: A review. *Remote Sensing of Environment*, *115*(7), 1603–1616. https://doi.org/10.1016/j.rse.2011.03.003

Sonobe, R., Yamashita, H., Mihara, H., Morita, A., & Ikka, T. (2021). Hyperspectral reflectance sensing for quantifying leaf chlorophyll content in wasabi leaves using spectral pre-processing techniques and machine learning algorithms. *International Journal of Remote Sensing*, *42*(4), 1311–1329. https://doi.org/10.1080/01431161.2020.1826065

Sridhar, B. B. M., Diehl, S. V., Han, F. X., Monts, D. L., & Su, Y. (2005). Anatomical changes due to uptake and accumulation of Zn and Cd in Indian mustard (Brassica juncea). *Environmental and Experimental Botany*, *54*(2), 131–141. https://doi.org/10.1016/j.envexpbot.2004.06.011

Sridhar, B. B. M., Han, F. X., & Su, Y. (2022). Monitoring the process of phytoremediation of heavy metals using spectral reflectance and remote sensing. In *Phytoremediation Technology for the Removal of Heavy Metals and Other Contaminants from Soil and Water* (pp. 219–243). Elsevier. https://doi.org/10.1016/B978-0-323-85763-5.00001-5

Stafford, A. D., Kusumo, B. H., Jeyakumar, P., Hedley, M. J., & Anderson, C. W. N. (2018). Cadmium in soils under pasture predicted by soil spectral reflectance on two dairy farms in New Zealand. *Geoderma Regional*, *13*(March), 26–34. https://doi.org/10.1016/j.geodrs.2018.03.001

Stavros, E. N., Chrone, J., Cawse-Nicholson, K., Freeman, A., Glenn, N. F., Guild, L., Kokaly, R., Lee, C., Luvall, J., Pavlick, R., Poulter, B., Schollaert Uz, S., Serbin, S., Thompson, D. R., Townsend, P. A., Turpie, K., Yuen, K., Thome, K., Wang, W., … Schimel, D. (2023). Designing an Observing System to Study the Surface Biology and Geology (SBG) of the Earth in the 2020s. *Journal of Geophysical Research: Biogeosciences*, *128*(1). https://doi.org/10.1029/2021JG006471

Stehman, S. V., & Foody, G. M. (2019). Key issues in rigorous accuracy assessment of land cover products. *Remote Sensing of Environment*, *231*, 111199. https://doi.org/10.1016/j.rse.2019.05.018

Steiner, A. (1963). The rocks penetrated by drillholes in the Waiotapu thermal area, and their hydrothermal alteration. In Waiotapu Geothermal Field. *New Zealand Department of Scientific and Industrial Research Bulletin.*, *155*, 26–35.

Stewart, M. K. (1994). Groundwater contributions to Waikite geothermal fluids. *16th NZ Geothermal Workshop*, 109–114.

Su, T. C. (2016). A filter-based post-processing technique for improving homogeneity of pixel-wise classification data. *European Journal of Remote Sensing*, *49*, 531–552. https://doi.org/10.5721/EuJRS20164928

Suherlina, L., Newson, J., Kamah, Y., & Brehme, M. (2022). The dynamic evolution of the Lahendong geothermal system in North-Sulawesi, Indonesia. *Geothermics*, *105*, 102510. https://doi.org/10.1016/j.geothermics.2022.102510

Sun, B., Schafer, M., Ehrlich, A., Jakel, E., & Wendisch, M. (2021). Influence of atmospheric adjacency effect on top-of-atmosphere radiances and its correction in the retrieval of Lambertian surface reflectivity based on three-dimensional radiative transfer. *Remote Sensing of Environment*, *263*(May). https://doi.org/10.1016/j.rse.2021.112543

Sun, J., Liu, K., He, Q., Yu, T., & Deng, Y. (2022). Thermal infrared remote sensing and soil gas radon for detecting blind geothermal area. *Geothermics*, *105*, 102534. https://doi.org/10.1016/j.geothermics.2022.102534

Suwa, R., Jayachandran, K., Nguyen, N. T., Boulenouar, A., Fujita, K., & Saneoka, H. (2008a). Barium toxicity effects in soybean plants. *Archives of Environmental Contamination and Toxicology*, *55*(3), 397–403. https://doi.org/10.1007/s00244-008-9132-7

Suwa, R., Jayachandran, K., Nguyen, N. T., Boulenouar, A., Fujita, K., & Saneoka, H. (2008b). Barium toxicity effects in soybean plants. *Archives of Environmental Contamination and Toxicology*, *55*(3), 397–403. https://doi.org/10.1007/s00244-008-9132-7

Swayze, G. A., Clark, R. N., Goetz, A. F. H., Livo, K. E., Breit, G. N., Kruse, F. A., Sutley, S. J., Snee, L. W., Lowers, H. A., Post, J. L., Stoffregen, R. E., & Ashley, R. P. (2014). Mapping advanced argillic alteration at Cuprite, Nevada, using imaging spectroscopy. *Economic Geology*, *109*(5), 1179–1221. https://doi.org/10.2113/econgeo.109.5.1179

Thompson, A. J. B., Thompson, J. F. H., Allen, R. L., Barrett, T. J., Browne, P. R. L., Clemson, J. E., Dunne, K. P. E., Ettlinger, A. D., Gibson, H. L., Groat, L. A., Hannington, M. D., Hawke, M. M., Jowett, E. C., Lang, J. R., Leitch, C. H. B., Lentz, D. R., Macdonald, A. J., McLeod, M., Martin, R. F., … Zeigler, J. F. (1996). *Atlas of Alteration: A Field and Petrographic Guide to Hydrothermal Alteration Minerals*.

Thompson, D. R., Cawse-Nicholson, K., Erickson, Z., Fichot, C. G., Frankenberg, C., Gao, B.-C., Gierach, M. M., Green, R. O., Jensen, D., Natraj, V., & Thompson, A. (2019). A unified approach to estimate land and water reflectances with uncertainties for coastal imaging spectroscopy. *Remote Sensing of Environment*, *231*, 111198. https://doi.org/10.1016/j.rse.2019.05.017

Tian, B., Wang, L., Kashiwaya, K., & Koike, K. (2015). Combination of well-logging temperature and thermal remote sensing for characterization of geothermal resources in Hokkaido, northern Japan. *Remote Sensing*, *7*(3), 2647–2667. https://doi.org/10.3390/rs70302647

Tian, X., Zhang, C., Li, J., Fan, S., Yang, Y., & Huang, W. (2021). Detection of early decay on citrus using LW-NIR hyperspectral reflectance imaging coupled with two-band ratio and improved watershed segmentation algorithm. *Food Chemistry*, *360*(May), 130077. https://doi.org/10.1016/j.foodchem.2021.130077

Timperley, J. (2020). What can the world learn from New Zealand on climate? *The Lancet Planetary Health*, *4*(5), e176–e177. https://doi.org/10.1016/S2542-5196(20)30109-1

Torres, I., & Amigo, J. M. (2020). An overview of regression methods in hyperspectral and multispectral imaging. *Data Handling in Science and Technology*, *32*, 205–230. https://doi.org/10.1016/B978-0-444-63977-6.00010-9

Torres-Alvarado, I. S., & Satir, M. (1998). Geochemistry of hydrothermally altered rocks from Los Azufres geothermal field, Mexico. *Geofisica Internacional*, *37*(3), 201–213. https://doi.org/10.22201/igeof.00167169p.1998.37.3.393

Tortini, R., van Manen, S. M., Parkes, B. R. B., & Carn, S. A. (2017). The impact of persistent volcanic degassing on vegetation: A case study at Turrialba volcano, Costa Rica. *International Journal of Applied Earth Observation and Geoinformation*, *59*, 92–103. https://doi.org/10.1016/j.jag.2017.03.002

Tsai, F., & Philpot, W. (1998). Derivative analysis of hyperspectral data. *Remote Sensing of Environment*, *66*(1), 41–51. https://doi.org/10.1016/S0034-4257(98)00032-7

Tschan, M., Robinson, B. H., & Schulin, R. (2009). Antimony in the soil—Plant system—A review. *Environmental Chemistry*, *6*(2), 106–115. https://doi.org/10.1071/EN08111

Tucker, C. J. (1979). Remote sensing of leaf water content in the near infrared. *Remote Sensing of Environment*, *10*, 23–32.

Tuominen, J., & Lipping, T. (2014). *ATMOSPHERIC CORRECTION OF HYPERSPECTRAL DATA USING COMBINED EMPIRICAL AND MODEL BASED METHOD*. 6.

Tut Haklidir, F. S., & Haklidir, M. (2020). Prediction of Reservoir Temperatures Using Hydrogeochemical Data, Western Anatolia Geothermal Systems (Turkey): A Machine Learning Approach. *Natural Resources Research*, *29*(4), 2333–2346. https://doi.org/10.1007/s11053-019-09596-0

Ubeynarayana, N., Jeyakumar, P., Bishop, P., Pereira, R. C., & Anderson, C. W. N. (2021). Effect of soil cadmium on root organic acid secretion by forage crops. *Environmental Pollution*, *268*, 115839. https://doi.org/10.1016/j.envpol.2020.115839

Uchimiya, M., Bannon, D., Nakanishi, H., McBride, M. B., Williams, M. A., & Yoshihara, T. (2020). Chemical Speciation, Plant Uptake, and Toxicity of Heavy Metals in Agricultural Soils. *Journal of Agricultural and Food Chemistry*, *68*(46), 12856–12869. https://doi.org/10.1021/acs.jafc.0c00183

Ulusoy, İ. (2016). Temporal radiative heat flux estimation and alteration mapping of Tendürek volcano (eastern Turkey) using ASTER imagery. *Journal of Volcanology and Geothermal Research*, *327*, 40–54. https://doi.org/10.1016/j.jvolgeores.2016.06.027

Ünal Ercan, H., Işık Ece, Ö., Schroeder, P. A., & Gülmez, F. (2022). Characteristics and evolution of the Etili silica sinter epithermal deposits, Çanakkale – Turkey: Relation to alkali chloride vs acid-sulfate fluids. *Ore Geology Reviews*, *142*, 104726. https://doi.org/10.1016/j.oregeorev.2022.104726

van der Linden, S., Rabe, A., Held, M., Jakimow, B., Leitão, P., Okujeni, A., Schwieder, M., Suess, S., & Hostert, P. (2015). The EnMAP-Box—A Toolbox and Application Programming Interface for EnMAP Data Processing. *Remote Sensing*, *7*(9), 11249–11266. https://doi.org/10.3390/rs70911249

van der Meer, F. (2004). Analysis of spectral absorption features in hyperspectral imagery. *International Journal of Applied Earth Observation and Geoinformation*, *5*(1), 55–68. https://doi.org/10.1016/j.jag.2003.09.001

Van der Meer, F. D. (2018). Near-infrared laboratory spectroscopy of mineral chemistry: A review. *International Journal of Applied Earth Observation and Geoinformation*, *65*(October 2017), 71–78. https://doi.org/10.1016/j.jag.2017.10.004

van der Meer, F. D., van der Werff, H. M. A., van Ruitenbeek, F. J. A., Hecker, C. A., Bakker, W. H., Noomen, M. F., van der Meijde, M., Carranza, E. J. M., de Smeth, J. B., & Woldai, T. (2012). Multi and hyperspectral geologic remote sensing: A review. *International Journal of Applied Earth Observation and Geoinformation*, *14*(1), 112–128. https://doi.org/10.1016/j.jag.2011.08.002

van der Meer, F., & de Jong, S. M. (2001). *Imaging Spectrometry*.

van der Meer, F., Hecker, C., van Ruitenbeek, F., van der Werff, H., de Wijkerslooth, C., & Wechsler, C. (2014). Geologic remote sensing for geothermal exploration: A review. *International Journal of Applied Earth Observation and Geoinformation*, *33*(1), 255–269. https://doi.org/10.1016/j.jag.2014.05.007

van der Meer, F., Kopačková, V., Koucká, L., van der Werff, H. M. A., van Ruitenbeek, F. J. A., & Bakker, W. H. (2018). Wavelength feature mapping as a proxy to mineral chemistry for investigating geologic systems: An example from the Rodalquilar epithermal system. *International Journal of Applied Earth Observation and Geoinformation*, *64*(February 2018), 237–248. https://doi.org/10.1016/j.jag.2017.09.008

Van Manen, S. M., & Reeves, R. (2012). An assessment of changes in kunzea ericoides var. Microflora and other hydrothermal vegetation at the Wairakei-Tauhara geothermal field, New Zealand. *Environmental Management*, *50*(4), 766–786. https://doi.org/10.1007/s00267-012-9899-1

van Ruitenbeek, F. J. A., Debba, P., van der Meer, F. D., Cudahy, T., van der Meijde, M., & Hale, M. (2006). Mapping white micas and their absorption wavelengths using hyperspectral band ratios. *Remote Sensing of Environment*, *102*(3–4), 211–222. https://doi.org/10.1016/j.rse.2006.02.012

Varshney, P., & Arora, M. (2004). *Image Processing Techniques for Remotely Sensed Hyperspectral Data*. Springer. https://doi.org/10.1007/978-3-662-05605-9

Vaughan, R. G., Calvin, W. M., & Taranik, J. V. (2003). SEBASS hyperspectral thermal infrared data: Surface emissivity measurement and mineral mapping. *Remote Sensing of Environment*, *85*(1), 48–63. https://doi.org/10.1016/S0034-4257(02)00186-4

Vaughan, R. G., Hungerford, J. D. G., & Keller, W. (2020). A Newly Emerging Thermal Area in Yellowstone. *Frontiers in Earth Science*, *8*, 204. https://doi.org/10.3389/feart.2020.00204

Vaughan, R. G., Keszthelyi, L. P., Davies, A. G., Schneider, D. J., Jaworowski, C., & Heasler, H. (2010). Exploring the limits of identifying sub-pixel thermal features using ASTER TIR data. *Journal of Volcanology and Geothermal Research*, *189*(3–4), 225–237. https://doi.org/10.1016/j.jvolgeores.2009.11.010

Vaughan, R. G., Keszthelyi, L. P., Lowenstern, J. B., Jaworowski, C., & Heasler, H. (2012). Use of ASTER and MODIS thermal infrared data to quantify heat flow and hydrothermal change at Yellowstone National Park. *Journal of Volcanology and Geothermal Research*, *233–234*, 72–89. https://doi.org/10.1016/j.jvolgeores.2012.04.022

Vaughan, R., Hook, S., Calvin, W., & Taranik, J. (2005). Surface mineral mapping at Steamboat Springs, Nevada, USA, with multi-wavelength thermal infrared images. *Remote Sensing of Environment*, *99*(1), 140–158.

Vermote, E., Tanre, D., Deuze, J., Herman, M., & Morcrette, J.-J. (2006). *Second simulation of a satellite signal in the solar spectrum-vector (6SV).*

Virtue, J., Turner, D., Williams, G., Zeliadt, S., McCabe, M., & Lucieer, A. (2021). Thermal Sensor Calibration for Unmanned Aerial Systems Using an External Heated Shutter. *Drones*, *5*(4), 119. https://doi.org/10.3390/drones5040119

Wallace, A., Mueller, R. T., & Wood, R. A. (1980). Arsenic Phytotoxicity and Interactions in Bush Bean Plants Grown in Solution Culture. *Journal of Plant Nutrition*, *2*(1–2), 111–113. https://doi.org/10.1080/01904168009362747

Wang, C., Xu, M., Jiang, Y., Deng, G., Lu, Z., Zhang, G., & Cui, H. (2022). Hyperspectral Image Stripe Removal Network With Cross-Frequency Feature Interaction. *IEEE Transactions on Geoscience and Remote Sensing*, *60*, 1–15. https://doi.org/10.1109/TGRS.2021.3138740

Wang, F., Gao, J., & Zha, Y. (2018). Hyperspectral sensing of heavy metals in soil and vegetation: Feasibility and challenges. *ISPRS - Journal of Photogrammetry and Remote Sensing*, *136*, 73–84.

Wang, L., Han, M., Li, X., Zhang, N., & Cheng, H. (2021). Review of Classification Methods on Unbalanced Data Sets. *IEEE Access*, *9*, 64606–64628. https://doi.org/10.1109/ACCESS.2021.3074243

Wang, M., Zhou, X., Liu, Y., Xu, H., Wu, Y., & Zhuo, L. (2020). Major, trace and rare earth elements geochemistry of geothermal waters from the Rehai high-temperature geothermal field in Tengchong of China. *Applied Geochemistry*, *119*, 104639. https://doi.org/10.1016/j.apgeochem.2020.104639

Wang, P., Lombi, E., Sun, S., Scheckel, K. G., Malysheva, A., McKenna, B. A., Menzies, N. W., Zhao, F. J., & Kopittke, P. M. (2017). Characterizing the uptake, accumulation and toxicity of silver sulfide nanoparticles in plants. *Environmental Science: Nano*, *4*(2), 448–460. https://doi.org/10.1039/c6en00489j

Wang, S., Li, A., Wen, K., & Wu, X. (2020). Robust kernels for kernel density estimation. *Economics Letters*, *191*, 109138. https://doi.org/10.1016/j.econlet.2020.109138

Wang, W., Geilert, S., Wei, H.-Z., & Jiang, S.-Y. (2021). Competition of equilibrium and kinetic silicon isotope fractionation during silica precipitation from acidic to alkaline pH solutions in geothermal systems. *Geochimica et Cosmochimica Acta*, *306*, 44–62. https://doi.org/10.1016/j.gca.2021.05.022

Wang, W., & Lu, Y. (2018). Analysis of the Mean Absolute Error (MAE) and the Root Mean Square Error (RMSE) in Assessing Rounding Model. *IOP Conference Series: Materials Science and Engineering*, *324*, 012049. https://doi.org/10.1088/1757-899X/324/1/012049

Wang, Y., Li, P., Guo, Q., Jiang, Z., & Liu, M. (2018). Environmental biogeochemistry of high arsenic geothermal fluids. *Applied Geochemistry*, *97*(July), 81–92. https://doi.org/10.1016/j.apgeochem.2018.07.015

Wang, Y., Sharp, B., Poletti, S., & Nam, K.-M. (2022). Economic and land use impacts of net zero-emission target in New Zealand. *International Journal of Urban Sciences*, *26*(2), 291–308. https://doi.org/10.1080/12265934.2020.1869582

Ward, J., Burns, B., Johnson, V., & Simmons, D. G. (2000). *Interactions Between Tourists and the Natural Environment: Impacts of Tourist Trampling on Geothermal Vegetation and Tourist Experiences at Geothermal Sites in Rotorua*. *16*.

Warner, T., Nellis, M., & Foody, G. (2009). *The SAGE handbook of remote sensing*. https://doi.org/10.4135/9780857021052

Waskom, M. (2021). Seaborn: Statistical Data Visualization. *Journal of Open Source Software*, *6*(60), 3021. https://doi.org/10.21105/joss.03021

Watson, F. G. R., Lockwood, R. E., Newman, W. B., Anderson, T. N., & Garrott, R. A. (2008). Development and comparison of Landsat radiometric and snowpack model inversion techniques for estimating geothermal heat flux. *Remote Sensing of Environment*, *112*(2), 471–481. https://doi.org/10.1016/j.rse.2007.05.010

Way, W., & Hall, S. (2001). Cost-effective vegetation anomaly mapping for geotherma exploration. *PROCEEDINGS: Twenty-Sixth Workshop on Geothermal Reservoir Engineering Stanford University, Stanford, California, January 29-30, 2001 SGP-TR-168, 2*.

Wei, L., Pu, H., Wang, Z., Yuan, Z., Yan, X., & Cao, L. (2020). Estimation of soil arsenic content with hyperspectral remote sensing. *Sensors (Switzerland)*, *20*(14), 1–16. https://doi.org/10.3390/s20144056

Wei, M., Qiao, B., Zhao, J., & Zuo, X. (2020). The area extraction of winter wheat in mixed planting area based on Sentinel-2 a remote sensing satellite images. *International Journal of Parallel, Emergent and Distributed Systems*, *35*(3), 297–308. https://doi.org/10.1080/17445760.2019.1597084

Wei, Z.-A., Shao, H., Tang, L., Deng, B., Li, H., & Wang, C. (2021). Hydrogeochemistry and geothermometry of geothermal waters from the Pearl River Delta region, South China. *Geothermics*, *96*, 102164. https://doi.org/10.1016/j.geothermics.2021.102164

Weissberg, B. G. (1969). Gold-Silver Ore-Grade Precipitates from New Zealand Thermal Waters. *Economic Geology*, *64*, 95–108.

Weldeyohannes, T. T., Hailu, B. T., Muluneh, A. A., & Kidane, T. (2022). Detection of geothermal anomalies in the Northern Lake Abaya geothermal field, Main Ethiopian Rift. *Journal of Volcanology and Geothermal Research*, *430*, 107638. https://doi.org/10.1016/j.jvolgeores.2022.107638

Weng, Q. (2009). Thermal infrared remote sensing for urban climate and environmental studies: Methods, applications, and trends. *ISPRS Journal of Photogrammetry and Remote Sensing*, *64*(4), 335–344. https://doi.org/10.1016/j.isprsjprs.2009.03.007

White, N. C., & Hedenquist, J. W. (1990). Epithermal environments and styles of mineralization: Variations and their causes, and guidelines for exploration. *Journal of Geochemical Exploration*, *36*(1–3), 445–474. https://doi.org/10.1016/0375-6742(90)90063-G

Whiteford, P. C. (1995). Repeat Measurements of Seismic Noise at the Waiotapu Geothermal Area, North Island, NZ. *Proceedings 17th NZ Geothermal Workshop 1995*.

Willmott, C., & Matsuura, K. (2005). Advantages of the mean absolute error (MAE) over the root mean square error (RMSE) in assessing average model performance. *Climate Research*, *30*, 79–82. https://doi.org/10.3354/cr030079

Wilson, C. J. N., Houghton, B. F., McWilliams, M. O., Lanphere, M. A., Weaver, S. D., & Briggs, R. M. (1995). Volcanic and structural evolution of Taupo Volcanic Zone, New Zealand: A review. *Journal of Volcanology and Geothermal Research*, *68*(1–3), 1–28. https://doi.org/10.1016/0377-0273(95)00006-G

Wilson, C. J. N., & Rowland, J. V. (2016). The volcanic, magmatic and tectonic setting of the Taupo Volcanic Zone, New Zealand, reviewed from a geothermal perspective. *Geothermics*, *59*, 168–187. https://doi.org/10.1016/j.geothermics.2015.06.013

Wilson, N., Webster-Brown, J., & Brown, K. (2012). The behaviour of antimony released from surface geothermal features in New Zealand. *Journal of Volcanology and Geothermal Research*, *247–248*, 158–167. https://doi.org/10.1016/j.jvolgeores.2012.08.009

Wilson, S. C., Lockwood, P. V., Ashley, P. M., & Tighe, M. (2010). The chemistry and behaviour of antimony in the soil environment with comparisons to arsenic: A critical review. *Environmental Pollution*, *158*(5), 1169–1181. https://doi.org/10.1016/j.envpol.2009.10.045

Wilson, S. H. (1963). Chemical Investigations at Waiotapu. In *NZ DSIR Bulletin* (pp. 87–118).

Wisian, K. W., Blackwell, D. D., & Richards, M. (2001). Correlation of Surface Heat loss and Total Energy Production for Geothermal Systems. *Geothermal Resources Council Transactions*, *25*, 331–336.

Wójcik, M., Sugier, P., & Siebielec, G. (2014). Metal accumulation strategies in plants spontaneously inhabiting Zn-Pb waste deposits. *Science of The Total Environment*, *487*, 313–322. https://doi.org/10.1016/j.scitotenv.2014.04.024

Wold, S., Sjöström, M., & Eriksson, L. (2001). PLS-regression: A basic tool of chemometrics. *Chemometrics and Intelligent Laboratory Systems*, *58*(2), 109–130. https://doi.org/10.1016/S0169-7439(01)00155-1

Wood, C. P. (1994). Aspects of the geology of Waimangu, Waiotapu, Waikite and Reporoa geothermal systems, Taupo Volcanic Zone, New Zealand. *Geothermics*, *23*(5–6), 401–421. https://doi.org/10.1016/0375-6505(94)90011-6

Worku, G., Teferi, E., & Bantider, A. (2021). Assessing the effects of vegetation change on urban land surface temperature using remote sensing data: The case of Addis Ababa city, Ethiopia. *Remote Sensing Applications: Society and Environment*, *22*(May), 100520. https://doi.org/10.1016/j.rsase.2021.100520

World Health Organization, W. H. O. (2016). *Barium in Drinking-Water.*

Wyering, L. D., Villeneuve, M. C., Wallis, I. C., Siratovich, P. A., Kennedy, B. M., Gravley, D. M., & Cant, J. L. (2014). Mechanical and physical properties of hydrothermally altered rocks, Taupo Volcanic Zone, New Zealand. *Journal of Volcanology and Geothermal Research*, *288*, 76–93. https://doi.org/10.1016/j.jvolgeores.2014.10.008

Xia, X., Li, X., Wang, C., Liu, X., & Liu, M. (2014). A hyperspectral index sensitive to subtle changes in the canopy chlorophyll content under arsenic stress. *International Journal of Applied Earth Observation and Geoinformation*, *36*, 41–53. https://doi.org/10.1016/j.jag.2014.10.017

Xie, Q., Dash, J., Huete, A., Jiang, A., Yin, G., Ding, Y., Peng, D., Hall, C. C., Brown, L., Shi, Y., Ye, H., Dong, Y., & Huang, W. (2019). Retrieval of crop biophysical parameters from Sentinel-2 remote sensing imagery. *International Journal of Applied Earth Observation and Geoinformation*, *80*, 187–195. https://doi.org/10.1016/j.jag.2019.04.019

Xie, R., Darvishzadeh, R., Skidmore, A. K., Heurich, M., Holzwarth, S., Gara, T. W., & Reusen, I. (2021). Mapping leaf area index in a mixed temperate forest using Fenix airborne hyperspectral data and Gaussian processes regression. *International Journal of Applied Earth Observation and Geoinformation*, *95*, 102242. https://doi.org/10.1016/j.jag.2020.102242

Xu, T., Liang, X., Xia, Y., Jiang, Z., & Gherardi, F. (2022). Performance evaluation of the Habanero enhanced geothermal system, Australia: Optimization based on tracer and induced micro-seismicity data. *Renewable Energy*, *181*, 1197–1208. https://doi.org/10.1016/j.renene.2021.09.111

Xue, J., & Su, B. (2017). Significant remote sensing vegetation indices: A review of developments and applications. *Journal of Sensors*, *2017*. https://doi.org/10.1155/2017/1353691

Yan, X., Li, Z., Luo, N., Shi, W., Zhao, W., Yang, X., & Jin, J. (2018). A minimum albedo aerosol retrieval method for the new-generation geostationary meteorological satellite Himawari-8. *Atmospheric Research*, 14.

Yang, K., Huntington, J. F., Browne, P. R. L., & Ma, C. (2000). An infrared spectral reflectance study of hydrothermal alteration minerals from the Te Mihi sector of the Wairakei geothermal system, New Zealand. *Geothermics*, *29*(3), 377–392. https://doi.org/10.1016/S0375-6505(00)00004-3

Yang, M., Hu, Y., Tian, H., Khan, F. A., Liu, Q., Goes, J. I., Gomes, H. do R., & Kim, W. (2021). Atmospheric Correction of Airborne Hyperspectral CASI Data Using Polymer, 6S and FLAASH. *Remote Sensing*, *13*(24), 5062. https://doi.org/10.3390/rs13245062

Yin, F., Wu, M., Liu, L., Zhu, Y., Feng, J., Yin, D., Yin, C., & Yin, C. (2021). Predicting the abundance of copper in soil using reflectance spectroscopy and GF5 hyperspectral imagery. *International Journal of Applied Earth Observation and Geoinformation*, *102*, 102420. https://doi.org/10.1016/j.jag.2021.102420

Young, S. J., Johnson, B. R., & Hackwell, J. A. (2002). An in-scene method for atmospheric compensation of thermal hyperspectral data. *Journal of Geophysical Research Atmospheres*, *107*(24), 1–20. https://doi.org/10.1029/2001JD001266

Zaini, N., Yanis, M., Abdullah, F., Van Der Meer, F., & Aufaristama, M. (2022). Exploring the geothermal potential of Peut Sagoe volcano using Landsat 8 OLI/TIRS images. *Geothermics*, *105*(November 2021), 102499. https://doi.org/10.1016/j.geothermics.2022.102499

Zeng, Y., Chen, M., Hao, D., Damm, A., Badgley, G., Rascher, U., Johnson, J. E., Dechant, B., Siegmann, B., Ryu, Y., Qiu, H., Krieger, V., Panigada, C., Celesti, M., Miglietta, F., Yang, X., & Berry, J. A. (2022). Combining near-infrared radiance of vegetation and fluorescence spectroscopy to detect effects of abiotic changes and stresses. *Remote Sensing of Environment*, *270*(December 2021), 112856. https://doi.org/10.1016/j.rse.2021.112856

Zhang, M., Hu, C., English, D., Carlson, P., Muller-Karger, F. E., Toro-Farmer, G., & Herwitz, S. R. (2015). Atmospheric Correction of AISA Measurements Over the Florida Keys Optically Shallow Waters: Challenges in Radiometric Calibration and Aerosol Selection. *IEEE Journal of Selected Topics in Applied Earth Observations and Remote Sensing*, *8*(8), 4189–4196. https://doi.org/10.1109/JSTARS.2015.2437326

Zhang, M., Salje, E. K. H., Carpenter, M. A., Parsons, I., Kroll, H., Reed, S. J. B., & GraemeBarber, A. (1997). Exsolution and Al–Si disorder in alkali feldspars: Their analysis by infrared spectroscopy. *American Mineralogist*, *82*, 849–857.

Zhang, X., & Li, P. (2014). Lithological mapping from hyperspectral data by improved use of spectral angle mapper. *International Journal of Applied Earth Observation and Geoinformation*, *31*(1), 95–109. https://doi.org/10.1016/j.jag.2014.03.007

Zhang, Y., Hui, J., Qin, Q., Sun, Y., Zhang, T., Sun, H., & Li, M. (2021). Transfer-learning-based approach for leaf chlorophyll content estimation of winter wheat from hyperspectral data. *Remote Sensing of Environment*, *267*(July), 112724. https://doi.org/10.1016/j.rse.2021.112724

Zhao, D., Li, H. B., Xu, J. Y., Luo, J., & Ma, L. Q. (2015). Arsenic extraction and speciation in plants: Method comparison and development. *Science of the Total Environment*, *523*, 138–145. https://doi.org/10.1016/j.scitotenv.2015.03.051

Zhou, C., Xia, J., Pang, J., Cheng, F., Chen, X., Xi, C., Zhang, H., Liu, Y., Ning, L., Dai, T., Mi, B., & Zhou, C. (2021). Near-Surface Geothermal Reservoir Imaging based on the Customized Dense Seismic Network. *Surveys in Geophysics*, *42*(3), 673–697. https://doi.org/10.1007/s10712-021-09642-8

Zhou, W. N., White, J. F., Soares, M. A., Torres, M. S., Zhou, Z. P., & Li, H. Y. (2015). Diversity of fungi associated with plants growing in geothermal ecosystems and evaluation of their capacities to enhance thermotolerance of host plants. *Journal of Plant Interactions*, *10*(1), 305–314. https://doi.org/10.1080/17429145.2015.1101495

Zhu, K., Sun, Z., Zhao, F., Yang, T., Tian, Z., Lai, J., Zhu, W., & Long, B. (2021). Relating hyperspectral vegetation indices with soil salinity at different depths for the diagnosis of winter wheat salt stress. *Remote Sensing*, *13*(2), 1–21. https://doi.org/10.3390/rs13020250

Zouzias, D., Miliaresis, G. C., & St. Seymour, K. (2011). Probable regional geothermal field reconnaissance in the Aegean region from modern multi-temporal night LST imagery. *Environmental Earth Sciences*, *62*(4), 717–723. https://doi.org/10.1007/s12665-010-0560-0

Zweifel, R., Rigling, A., & Dobbertin, M. (2009). Species-specific stomatal response of trees to drought—A link to vegetation dynamics? *Journal of Vegetation Science*, *20*(3), 442–454. https://doi.org/10.1111/j.1654-1103.2009.05701.x